EVALUATION OF AN INTEGRATED PTSC/THERMAL ENERGY STORAGE SYSTEM USING NANO-FLUID PARTICLES

by

Adnan Alashkar

A Thesis Presented to the Faculty of the
American University of Sharjah
College of Engineering
in Partial Fulfillment
of the Requirements
for the Degree of

Master of Science in
Mechanical Engineering

Sharjah, United Arab Emirates

January 2016

Approval Signatures

We, the undersigned, approve the Master's Thesis of Adnan Alashkar.

Thesis Title: Evaluation of an Integrated PTSC/Thermal Energy Storage System Using Nano-Fluid Particles.

Signature **Date of Signature**

_____ _____

Dr. Mohamed Gadalla
Professor, Department of Mechanical Engineering
Thesis Advisor

_____ _____

Dr. Rachid Chebbi
Professor, Department of Chemical Engineering
Thesis Committee Member

_____ _____

Dr. Thomas Gally
Senior Lecturer, Department of Mechanical Engineering
Thesis Committee Member

_____ _____

Dr. Mamoun Abdel-Hafez
Head, Department of Mechanical Engineering

_____ _____

Dr. Mohamed El Tarhuni
Associate Dean, College of Engineering

_____ _____

Dr. Leland Blank
Dean, College of Engineering

_____ _____

Dr. Khaled Assaleh
Interim Vice Provost for Research and Graduate Studies

Acknowledgments

Firstly, I would like to thank my advisor, Professor Mohamed Gadalla, whose patience, encouragement, and academic experience were vital in the completion of this thesis. I would also like to thank him for his unlimited support and understanding during the preparation and presentation of the thesis.

Secondly, I would like to thank my committee members, Professor Saad Ahmed, Professor Rachid Chebbi, and Dr. Thomas Gally for their time, feedback, and insightful comments.

Lastly, I would like to express my gratitude to the American University of Sharjah, for providing me with the facilities and resources to carry out the research.

Dedication

To my parents, who if it was not for their unlimited support and sacrifice, I would not be where I am today. To my sisters and my brothers-in-law, who provided me with endless support and encouragement. To my nephews and niece, who bring joy to my life as I watch them grow. To my grandparents, for their unconditional love. To my friends, who always helped me throughout writing my thesis.

Abstract

Daily increase in the use of electricity and fossil fuels in the world raises the need for a renewable source of energy to accommodate the needs and power requirements for different sectors. Concentrated Solar Power (CSP) is the leading technology in harvesting the solar radiation, which paves the way for a sustainable energy production that can replace conventional power generation methods. Parabolic Trough Solar Collectors (PTSC) are the most efficient and advanced type of CSPs. However, the efficiency and heat loss while storing are two major drawbacks in using PTSC. Adding nanoparticles to a conventional heating fluid will increase the thermal conductivity of that fluid, which will enhance the performance of the PTSC, and improve the overall performance of a PTSC/Thermal Energy Storage (TES) integrated system. In this thesis, the effect of using nanofluids as a heating fluid in an integrated PTSC/TES System is evaluated. Two metallic nanoparticles: Copper (Cu) and Alumina(Al_2O_3), and one non-metallic: Single Walled Carbon Nanotubes($SWCNT$) are dispersed into Therminol VP-1 and Syltherm 800. The thermophysical properties of the resulting nanofluids are studied for different volume fractions, and their effect on the convective heat transfer coefficient is analyzed. Further, the improvement in performance of the PTSC is investigated, and the effect of that improvement on the performance and the cost of different configurations of an integrated PTSC/TES system for different modes of operation (no storage, 7.5 hours and 10 hours) are examined. The results show that adding nanoparticles to a base fluid will increase the thermal conductivity as well as the overall heat transfer inside the absorber tube of the PTSC. It was seen that $SWCNT$-based nanofluids showed the highest improvement of 6-8% in the PTSC efficiency. The effect of the nanofluids on the performance and cost of the PTSC/TES system depends on the mode of operation, where different nanofluids showed different enhancements on the annual energy and net saving of the PTSC/TES system. It was concluded that the 2ndmode of operation with a storage period of 7.5 hours is the most efficient and cost effective mode for the PTSC/TES system to operate on.

Search terms: Concentrated Solar Power, Parabolic Trough Solar Collector, Thermal Energy Storage, nanofluids, SWCNT, Therminol VP-1, Syltherm 800**.**

Table of Contents

List of Figures 12
List of Tables 16
Nomenclature 17
Chapter 1: Introduction 24
1.1 Problem Statement 24
1.2 Significance of the Research 25
1.3 Scope and Objectives 26
1.4 Research Methods and Materials 27
1.5 Thesis Organization 28
Chapter 2: Literature Review 29
2.1 PTSC modeling and applications 29
2.2 Thermal Energy Storage 34
2.2.1 Thermal energy storage types. 35
2.2.2 Thermal energy storage experimental studies. 38
2.3 Nanofluids and their applications 39
2.3.1 Thermophysical properties enhancements. 39
2.3.1.1 Experimental properties enhancements 39
2.3.1.1.1 Thermal conductivity 39
2.3.1.1.2 Specific heat capacity 49
2.3.1.1.3 Viscosity. 50
2.3.1.2 Analytical properties enhancements. 51
2.3.1.2.1 Thermal conductivity 51
2.3.1.2.2 Viscosity. 56
2.3.2 Heat transfer characteristics and heat transfer coefficient enhancements. 57
2.3.2.1 Experimental studies on heat transfer characteristics. 58
2.3.2.2 Analytical studies on heat transfer characteristics. 61
2.3.3 Applications of nanofluids in solar energy. 68
2.3.3.1 Direct Absorption Collector (DAC) 68
2.3.3.2 Flat Plate Solar Collector (FPSC) 72
2.3.3.3 Parabolic Trough Solar Collector (PTSC) 73
2.3.4 Applications of nanofluids in Thermal Energy Storage. 75
Chapter 3: System Configurations and Modeling 78

3.1 Nanofluids Modeling 78
3.1.1 Base fluids. 78
3.1.1.1 Therminol-VP1. 78
3.1.1.2 Syltherm 800. 79
3.1.2 Nanoparticles. 79
3.1.2.1 Metallic nanoparticles. 80
3.1.2.1.1 Copper. 80
3.1.2.1.2 Alumina. 80
3.1.2.2 Non-metallic nanoparticles. 80
3.1.2.2.1 Single Walled Carbon Nanotubes. 81
3.1.3 Density of nanofluids. 81
3.1.4 Specific heat capacity of nanofluids. 82
3.1.5 Viscosity of the nanofluids. 82
3.1.6 Thermal Conductivity of the nanofluids. 84
3.2 Convective Heat Transfer 91
3.2.1 Base fluids. 91
3.2.1.1 Reynolds Number of base fluids. 92
3.2.1.2 Prandtl Number of base fluids. 92
3.2.1.3 Nusselt Number of base fluids. 92
3.2.1.4 Convective heat transfer coefficient of base fluids. 94
3.2.2 Nanofluids. 94
3.2.2.1 Reynolds Number of nanofluids. 94
3.2.2.2 Prandtl Number of nanofluids. 94
3.2.2.3 Nusselt Number of nanofluids. 95
3.2.2.4 Convective heat transfer coefficient of nanofluids. 96
3.3 PTSC Modeling 96
3.3.1 Collector. 97
3.3.1.1 Angle of incidence. 97
3.3.1.2 Optical efficiency. 99
3.3.2 Receiver. 100
3.3.3 Glass cover. 101
3.3.4 PTSC energy model. 102
3.3.5 PTSC exergy model. 104
3.4 Integrated Solar-Rankine Cycle model (ISRC) 105

3.4.1 Steam turbine. 107
3.4.2 Condenser. 107
3.4.3 Pump. 107
3.4.4 Heat exchanger. 108
3.4.5 Efficiency. 110
3.5 Integrated Solar-Regenerative Rankine Cycle model (ISRRC) 110
3.5.1 Open feed water heater. 112
3.5.2 Steam turbine. 113
3.5.3 Condenser. 113
3.5.4 Pumps. 113
3.5.5 Heat exchanger. 114
3.6 Thermal Energy Storage 114
3.6.1 Modes of operation. 115
3.6.2 ISRC/TES and ISRRC/TES systems. 116
Chapter 4: Results and Discussion 122
4.1 Meteorological data 122
4.2 Heating fluid and Thermal Storage material selection 125
4.2.1 Heating fluid selection. 125
4.2.2 TES material selection. 126
4.3 Nanofluids properties 126
4.3.1 Base fluids properties. 127
4.3.2 Nanoparticles properties. 129
4.3.3 Nanofluids density. 132
4.3.4 Nanofluids specific heat capacity. 135
4.3.5 Nanofluids viscosity. 138
4.3.6 Nanofluids thermal conductivity. 141
4.3.6.1 Comparison of models. 141
4.3.6.2 Effect of radius, length and nanolayer thickness. 144
4.3.6.3 Effect of nanoparticles shape. 147
4.3.6.4 Effect of volume fraction. 148
4.4 Convective heat transfer coefficient 152
4.4.1 Reynolds number. 152
4.4.2 Prandtl number. 155

4.4.3 Heat transfer coefficient. 157
4.4.3.1 Model validation. 157
4.4.3.2 Effect of the nanofluids on the convective heat transfer coefficient. 160
4.4.3.3 Effect of the temperature on the convective heat transfer coefficient. 162
4.4.3.4 Effect of the flow type on the convective heat transfer coefficient. 164
4.5 Parabolic Trough Solar Collector (PTSC) 165
4.5.1 Effect of the mass flow rate on the PTSC performance. 165
4.5.2 Effect of the volume fraction on the PTSC performance. 169
4.5.3 Effect of the concentration ratio on the PTSC performance. 171
4.5.4 Effect of the beam radiation on the PTSC performance. 173
4.6 Integrated Solar-Rankine Cycle (ISRC) and Integrated Solar- Regenerative Rankine Cycle (ISRRC) 185
4.6.1 Comparison between ISRC and ISRRC. 185
4.6.2 Effect of the mass flow rate on the performance of the ISRRC. 187
4.6.3 Effect of the mass flow rate for different nanofluids and modes of operation. 189
4.6.4 Effect of the nanofluids on the performance of the ISRRC for different modes of operation. 196
4.6.4.1 Effect of the nanofluids on the performance of the ISRRC for the 1st Mode of operation 196
4.6.4.2 Effect of the nanofluids on the performance of the ISRRC for the 2nd Mode of operation 198
4.6.4.3 Effect of the nanofluids on the performance of the ISRRC for the 3rd Mode of operation 201
4.6.4.4 Comparison of the effect of the modes of operation on the performance of the ISRRC 203
Chapter 5: Economic Evaluation of the ISRRC 208
5.1 Economic model 209
5.1.1 Steam Turbine. 209
5.1.2 Heat Exchangers. 209
5.1.3 Pumps. 210
5.1.4 Condenser. 210
5.1.5 PTSC Field. 211
5.1.6 Auxiliary Equipment. 212
5.1.7 Equipment Installation. 212
5.1.8 Water Treatment Facility. 213

5.1.9 Operating Cost. 213
5.1.10 Civil Engineering. 213
5.1.11 Project Engineering and Contingencies. 213
5.1.12 Decommissioning cost. 214
5.1.13 Labor cost 214
5.1.14 Maintenance cost. 214
5.1.15 Net Present Value (NVP). 215
5.1.16 Net Saving ($\boldsymbol{NS}$). 216
5.1.17 Levelized Cost of Electricity (LEC). 216
5.2 Effect of the nanofluids on the cost of the ISRRC for different modes of operation 217
5.2.1 Effect of the nanofluids on the economic-performance of the ISRRC for the 1st mode of operation. 217
5.2.2 Effect of the nanofluids on the economic-performance of the ISRRC for the 2nd mode of operation. 218
5.2.3 Effect of the nanofluids on the economic-performance of the ISRRC for the 3rdmode of operation. 219
5.2.4 Comparison of the effect of the nanofluids on the economic-performance of the ISRRC for different modes of operation. 220
5.2.5 Effect of the optimum mode of operation on the TES. 224
Chapter 6: Conclusion and Recommendations 230
6.1 Conclusion 230
6.2 Recommendations 234
References 235
Vita 255

List of Figures

Figure 1: Effect of the volume fraction on the efficiency for different nanofluids [145] 70
Figure 2: Difference between a PSC and NSPSC [146] 71
Figure 3: PTSC Schematic Diagram 96
Figure 4: Relation between tilt angle and aperture azimuth angle [170] 99
Figure 5: ISRC Schematic Diagram 106
Figure 6: T-S diagram for the ISRC 106
Figure 7: Shell and Tube Heat Exchanger Schematic Diagram [172] 108
Figure 8: ISRRC Schematic Diagram 111
Figure 9: T-S diagram for the ISRRC 111
Figure 10: ISRC/TES Charging Cycle Schematic Diagram for (a) Full load, and (b) Partial load 118
Figure 11: ISRC/TES Discharging Cycle Schematic Diagram for (a) Full load, and (b) Partial load 119
Figure 12: ISRRC/TES Charging Cycle Schematic Diagram for (a) Full load, and (b) Partial load 120
Figure 13: ISRRC/TES Discharging Cycle Schematic Diagram for (a) Full load, and (b) Partial load 121
Figure 14: Effect of time on the beam radiation 123
Figure 15: Maximum and average beam radiation 123
Figure 16: Effect of time on the dry bulb temperature 124
Figure 17: Maximum and average dry bulb temperatures 124
Figure 18: Effect of temperature on the density of the base fluids 127
Figure 19: Effect of temperature on the specific heat capacity of the base fluids 128
Figure 20: Effect of temperature on the thermal conductivity of the base fluids 129
Figure 21: Effect of temperature on the dynamic viscosity of the base fluids 129
Figure 22: Effect of temperature on the specific heat capacity of $Al2O3$ and Cu nanoparticels 130
Figure 23: Effect of temperature on the thermal conductivity of $Al2O3$ and Cu nanoparticels 131
Figure 24: Effect of temperature on the thermal conductivity of $SWCNT$ nanoparticles for different lengths 131
Figure 25: Effect of volume fraction on the density of (a) Therminol-based nanofluids and (b) Syltherm-based nanofluids 133
Figure 26: Effect of temperature on the density of (a) Therminol-based nanofluids and (b) Syltherm-based nanofluids ($\varphi = 5\%$) 134
Figure 27: Effect of volume fraction on the specific heat capacity of (a) Therminol-based nanofluids and (b) Syltherm-based nanofluids 136
Figure 28: Effect of temperature on the specific heat capacity of (a) Therminol-based nanofluids and (b) Syltherm-based nanofluids ($\varphi = 5\%$) 137
Figure 29: Effect of temperature on the dynamic viscosity of Therminol-based nanofluids for different viscosity models($\varphi = 3\ \%$) 139
Figure 30: Effect of temperature on the dynamic viscosity of Therminol-based nanofluids for different nanoparticle radii ($\varphi = 3\%$) 139

Figure 31: Effect of temperature on the dynamic viscosity of (a) Therminol-based nanofluids, and (b) Syltherm-based nanofluids for different volume fractions 140
Figure 32: Comparison of experimental data [30] and various models for the thermal conductivity of EG/Cu nanofluids 142
Figure 33: Comparison of experimental data [31] and various models for the thermal conductivity of Water/$Al2O3$ nanofluids 143
Figure 34: Comparison of experimental data [86] and various models for the thermal conductivity of Oil/CNT nanofluids 143
Figure 35: Comparison of experimental data and various CNT-based models for the thermal conductivity of Oil/CNT nanofluids 144
Figure 36: Effect of nanoparticle's radius on the thermal conductivity ratio of $Al2O3$/Therminol nanofluids for different nanolayer thicknesses 145
Figure 37: Effect of volume fraction on the thermal conductivity ratio of $SWCNT$/Therminol nanofluids for different lengths 146
Figure 38: Effect of volume fraction on the thermal conductivity ratio of $SWCNT$/ Therminol nanofluids for different diameters 146
Figure 39: Effect of volume fraction on the thermal conductivity ratio of $Al2O3$ /Therminol nanofluids for different nanoparticles shapes 147
Figure 40: Effect of volume fraction on the thermal conductivity ratio of (a) Therminol-based nanofluids, and (b) Syltherm-based nanofluids 149
Figure 41: Effect of temperature on the thermal conductivity of Cu-based nanofluids 150
Figure 42: Effect of temperature on the Reynolds number for (a) Therminol-based nanofluids, and (b) Syltherm-based nanofluids 153
Figure 43: Effect of the volume fraction on the Reynolds number for (a) Therminol-based nanofluids, and (b) Syltherm-based nanofluids 154
Figure 44: Effect of temperature on the Prandtl number for (a) Therminol-based nanofluids, and (b) Syltherm-based nanofluids 156
Figure 45: Effect of volume fraction on the Prandtl number for (a) Therminol-based nanofluids, and (b) Syltherm-based nanofluids 157
Figure 46: Effect of Reynolds number on the Nusselt number for Cu/water, compared to [103] 158
Figure 47: Effect of Reynolds number on the Nusselt number for $Al2O3$/ water, compared to [129] 159
Figure 48: Effect of Reynolds number on the heat transfer coefficient for CNT/ water, compared to [111] 160
Figure 49: Effect of volume fraction on the convective heat transfer coefficient for (a) Therminol-based nanofluids, and (b) Syltherm-based nanofluids 161
Figure 50: Effect of temperature on the convective heat transfer coefficient for (a) Therminol-based nanofluids, and (b) Syltherm-based nanofluids 163
Figure 51: Effect of Reynolds number on the heat transfer coefficient for Therminol-based nanofluids (turbulent flow) 164
Figure 52: Effect of Reynolds number on the heat transfer coefficient for Therminol-based nanofluids (laminar flow) 165

Figure 53: Effect of mass flow rate on the power output of the PTSC for (a) Therminol-based nanofluids, and (b) Syltherm-based nanofluids 166
Figure 54: Effect of mass flow rate on the efficiency of the PTSC for (a) Therminol-based nanofluids, and (b) Syltherm-based nanofluids 168
Figure 55: Effect of volume fraction on the power output of the PTSC for (a) Therminol-based nanofluids, and (b) Syltherm-based nanofluids 170
Figure 56: Effect of mass flow rate on the power output of the PTSC for different concentration for (a) Therminol, (b) 5% $Al2O3$/Therminol, (c) 5% Cu/Therminol, and (d) 5% $SWCNT$/Therminol 172
Figure 57: Effect of mass flow rate on the power output of the PTSC for different concentration for (a) Syltherm, (b) 5% $Al2O3$/Syltherm, (c) 5% Cu/Syltherm, and (d) 5% $SWCNT$/Syltherm 173
Figure 58: Effect of beam radiation on the power output of the PTSC on a monthly basis for (a) Therminol-based nanofluids and (b) Syltherm-based nanofluids 174
Figure 59: Effect of time on the beam radiation for a day in the month of August 176
Figure 60: Effect of time on the (a) power output, (b) efficiency, (c) exergetic efficiency, and (d) entropy generation of the PTSC for Therminol-based nanofluids for a day in August 177
Figure 61: Effect of time on the (a) power output, (b) efficiency, (c) exergetic efficiency, and (d) entropy generation of the PTSC for Syltherm-based nanofluids for a day in August 178
Figure 62: Effect of beam radiation on the power output of the PTSC on a monthly basis for (a) Therminol and $SWCNT$/Therminol fluids and (b) Syltherm and $SWCNT$/Syltherm fluids 180
Figure 63: Effect of beam radiation on the efficiency of the PTSC on a monthly basis for (a) Therminol and $SWCNT$/Therminol fluids and (b) Syltherm and $SWCNT$/Syltherm fluids 182
Figure 64: Effect of beam radiation on the exergetic efficiency of the PTSC on a monthly basis for (a) Therminol and $SWCNT$/Therminol fluids and (b) Syltherm and $SWCNT$/Syltherm fluids 183
Figure 65: Effect of beam radiation on the entropy generation of the PTSC on a monthly basis for (a) Therminol and $SWCNT$/Therminol fluids and (b) Syltherm and $SWCNT$/Syltherm fluids... 184
Figure 66: Effect of feed water pressure on the efficiency of the ISRRC 185
Figure 67: Effect of feed water pressure on the flash factor of the ISRRC 186
Figure 68: Effect of inlet turbine temperature on the efficiencies of the ISRC and ISRRC 187
Figure 69: Effect of time on the mass flow rate for a day in August for Therminol 188
Figure 70: Effect of beam radiation on the mass flow rates of the power plant on a monthly basis for Therminol 189
Figure 71: Effect of time on the mass flow rates of the ISRRC for the 1st mode of operation for (a) Therminol, (b) 5% $Al2O3$/Therminol, (c) 5% Cu/Therminol, and (d) 5% $SWCNT$/Therminol . 190
Figure 72: Effect of time on the mass flow rates of the ISRRC for the 1st mode of operation for (a) Syltherm, (b) 5% $Al2O3$/Syltherm, (c) 5% Cu/Syltherm, and (d) 5% $SWCNT$/Syltherm 191
Figure 73: Effect of time on the mass flow rates of the ISRRC for the 2nd mode of operation for (a) Therminol, (b) 5% $Al2O3$/Therminol, (c) 5% Cu/Therminol, and (d) 5% $SWCNT$/Therminol 192
Figure 74: Effect of time on the mass flow rates of the ISRRC for the 2nd mode of operation for (a) Syltherm, (b) 5% $Al2O3$/Syltherm, (c) 5% Cu/Syltherm, and (d) 5% $SWCNT$/Syltherm 193

Figure 75: Effect of time on the mass flow rates of the ISRRC for the 3rd mode of operation for (a) Therminol, (b) 5% $Al2O3$/Therminol, (c) 5% Cu/Therminol, and (d) 5% $SWCNT$/Therminol 194
Figure 76: Effect of time on the mass flow rates of the ISRRC for the 3rd mode of operation for (a) Syltherm, (b) 5% $Al2O3$/Syltherm, (c) 5% Cu/Syltherm, and (d) 5% $SWCNT$/Syltherm 195
Figure 77: Variation of the month on the energy output of the ISRRC for (a) Therminol-based nanofluids, and (b) Syltherm-based nanofluids for 1st mode of operation 197
Figure 78: Variation of the month on the energy output of the ISRRC for (a) Therminol-based nanofluids, and (b) Syltherm-based nanofluids for 2ndmode of operation 200
Figure 79: Variation of the month on the energy output of the ISRRC for (a) Therminol-based nanofluids, and (b) Syltherm-based nanofluids for 3rdmode of operation 202
Figure 80: Effect of modes of operation on the power output of the ISRRC for (a) Therminol-based nanofluids, and (b) Syltherm-based nanofluids 204
Figure 81: Effect of modes of operation on the annual energy of the ISRRC for (a) Therminol-based nanofluids, and (b) Syltherm-based nanofluids 205
Figure 82: Effect of modes of operation on the thermal output from the field of the ISRRC for (a) Therminol-based nanofluids, and (b) Syltherm-based nanofluids 206
Figure 83: Effect of modes of operation on the LEC of the ISRRC for (a) Therminol-based nanofluids, and (b) Syltherm-based nanofluids 221
Figure 84: Effect of modes of operation on the net savings of the ISRRC for (a) Therminol-based nanofluids, and (b) Syltherm-based nanofluids 223
Figure 85: Schematic diagram of the charging cycle of the ISRRC with the new TES system for (a) Full load, and (b) Partial load 227
Figure 86: Schematic diagram of the discharging cycle of the ISRRC with the new TES system for (a) Full load, and (b) Partial load 228

List of Tables

Table 1: Storage Medias used for sensible heat storage [20] 36
Table 2: Properties of latent heat storage Medias [20] 37
Table 3: Potential materials for thermocline storage [20] 38
Table 4: Thermophysical properties of the base fluids and nanoparticles 81
Table 5: Receiver, Glass cover and Collector specifications 98
Table 6: PTSC energy model design parameters 104
Table 7: Location and Solar Field Design parameters 107
Table 8: Heat Exchanger Overall Heat Transfer coefficient 110
Table 9: ISRC and ISRRC Input Design Parameters 112
Table 10: TES design parameters for the 2nd mode of operation 115
Table 11: TES design parameters for the 3rd mode of operation 116
Table 12: Comparison between HTFs 125
Table 13: Comparison between different Salts for TES material 126
Table 14: Thermophysical properties of nanofluids for different temperatures and volume fractions 151
Table 15: Average enhancement in PTSC efficiency and power output ($\boldsymbol{\varphi = 5\%}$) 169
Table 16: Comparison between Therminol-based and Syltherm-based nanofluids regarding the performance of the PTSC for a day in the month of August 179
Table 17: Comparison between Therminol-based and Syltherm-based nanofluids regarding the performance of the ISRRC for 1st mode of operation 198
Table 18: Comparison between Therminol-based and Syltherm-based nanofluids regarding the performance of the ISRRC for 2ndmode of operation 199
Table 19: Comparison between Therminol-based and Syltherm-based nanofluids regarding the performance of the ISRRC for 3rd mode of operation 201
Table 20: Input data and design parameters for the economic model 212
Table 21: Plant positions, salary, and number of employees needed [177] 214
Table 22: Comparison between Therminol-based and Syltherm-based nanofluids regarding the costs of the ISRRC for 1st mode of operation 218
Table 23: Comparison between Therminol-based and Syltherm-based nanofluids regarding the costs of the ISRRC for 2ndmode of operation 219
Table 24: Comparison between Therminol-based and Syltherm-based nanofluids regarding the costs of the ISRRC for 3rd mode of operation 220
Table 25: Most suitable nanofluid to replace the base fluids for different modes of operation 224
Table 26: Input design parameters for the new TES for the 2nd mode of operation 225

Nomenclature

A	Area (m^2)
A_a	Reflective aperture area (m^2)
A_c	Glass cover area (m^2)
A_r	Receiver area (m^2)
A_{SA}	Solar field area (m^2)
C	Concentration ratio (-)
$C_{Al_2O_3}$	Alumina nanoparticles price $(US\$/gram)$
C_{cu}	Copper nanoparticles price $(US\$/gram)$
C_{el}	Electricity sale price $(US\$/kWh)$
C_p	Specific heat capacity $(kJ/kg \cdot K)$
C_{SWCNT}	Single Walled Carbon Nanotubes price $(US\$/gram)$
D	Diameter (mm)
D_{co}	Glass cover outer diameter(mm)
D_{ri}	Absorber tube inner diameter(mm)
D_{ro}	Absorber tube outer diameter(mm)
F_R	Heat removal factor (-)
F_{RS}	Shading factor (-)
F'	Efficiency factor (-)
f	Fanning friction factor (-)
f_D	Darcy friction factor (-)
h	Enthalpy (kJ/kg)
h_{crin}	Convective heat transfer coefficient inside the absorber tube (W/m^2K)
h_{rca}	Radiation heat transfer coefficient between glass cover and ambient (W/m^2K)

h_{rcr}	Radiation heat transfer coefficient between glass cover and receiver (W/m^2K)
h_{cca}	Convective heat transfer coefficient between glass cover and ambient(W/m^2K)
I_B	Normal beam radiation (W/m^2)
i	Loan interest rate (%)
$K(\theta)$	Incident angle modifier (-)
k	Thermal conductivity $(W/m \cdot K)$
k_{air}	Air thermal conductivity $(W/m \cdot K)$
k_B	Boltzmannconstant ($1.381 \times 10^{-23} J/K$)
k_r	Thermal conductivity of the receiver $(W/m \cdot K)$
k_s	Thermal conductivity of the glass cover $(W/m \cdot K)$
L	Length of collector assembly (m)
L_c	Collector length (m)
l_s	$SWCNT$ length (μm)
$\dot{m}_f$	Fluid mass flow rate (kg/s)
$\dot{m}_s$	Steam mass flow rate (kg/s)
N_c	Number of collectors (-)
N_l	Number of loops (-)
N_m	Number of modules (-)
Nu	Nusselt Number (-)
Nu_c	Nusselt Number of glass cover (-)
P	Pressure (kPa)
P_c	Condenser pressure(bar)
P_f	Feed water pressure(bar)

P_{st}	Steam turbine pressure(bar)
Pr	Prandtl Number (-)
$\dot{Q}_u$	Useful power collected by the PTSC (kW)
q_c	Specific heat rejected (kW/kg)
Re	Reynolds Number (-)
Re_c	Reynolds Number of glass cover (-)
R_k	Kaptiza Resistance ($8 \times 10^{-8} m^2K/$)
r	Radius (nm)
r_{ins}	Insurance rate (%)
$\dot{S}_{gen}$	Entropy generated rate in the PTSC(kW/K)
T	Fluid temperature (℃)
T_{amb}	Ambient temperature (℃)
T_c	Glass cover temperature (℃)
T_i	Inlet temperature (℃)
T_m	Mean temperature (℃)
T_o	Outlet temperature (℃)
T_r	Receiver temperature (℃)
T_s	Sun temperature (K)
t_{opt}	Operating hours of the plant $(hour/year)$
U_L	Overall heat loss coefficient (W/m^2K)
U_o	Overall heat transfer coefficient (W/m^2K)
V	Fluid velocity (m/s)
V_{wind}	Wind velocity (m/s)
v	Specific volume (m^3/kg)
w	Collector width (m)

w_p	Specific pump work (kW/kg)
w_{st}	Specific turbine work (kW/kg)
$\dot{W}_{net}$	Net power output (MW)
$\dot{X}_{in,PTSC}$	Exergy input rate to the PTSC (kW)
$\dot{X}_{out,PTSC}$	Exergy output rate from the PTSC (kW)
$\dot{X}_{des,PTSC}$	Exergy destruction rate in the PTSC (kW)
y	Flash factor (-)
y_{con}	Construction years of the plant $(years)$
y_{dec}	Decommissioning years of the plant $(years)$
y_{opt}	Plant life time cycle $(years)$
Z_C	Capital investment cost of the condenser $(US\$)$
Z_{CE}	Capital investment cost of the civil engineering works $(US\$)$
Z_{con}	Cost of contingency issues $(US\$)$
Z_{ct}	Capital investment cost of the cooling tower $(US\$)$
Z_{dec}	Cost of decommissioning the plant $(US\$)$
Z_{eq}	Equipment capital investment cost $(US\$)$
$Z_{eq,ins}$	Equipment installation capital investment cost $(US\$)$
Z_{FW}	Capital investment cost of the feed water heater $(US\$)$
$Z_{HE,1}$	Capital investment cost of the heat exchanger between the PTSC Field and the TES system$(US\$)$
$Z_{HE,2}$	Capital investment cost of the heat exchanger between the TES and the power block $(US\$)$
Z_{ic}	Cost of indirect factors (planning, permitting) $(US\$)$
Z_{labor}	Labor cost $(US\$)$
Z_m	Maintenance cost of the plant $(US\$)$

Z_{opt}	Operating cost of the plant ($US\$$)
Z_{PCST}	Capital investment cost of the cold storage tank pump ($US\$$)
Z_{PFWH}	Capital investment cost of feed pump ($US\$$)
Z_{PHTF}	Capital investment cost of the heating fluid pump ($US\$$)
Z_{PHST}	Capital investment cost of the hot storage tank pump ($US\$$)
Z_{PW}	Capital investment cost of the water pump ($US\$$)
Z_{PTSC}	Capital investment cost of the PTSC field($US\$$)
Z_{sc}	Capital investment cost of the steam condenser($US\$$)
Z_{st}	Capital investment cost of the steam turbine ($US\$$)
$Z_{st,aux}$	Capital investment cost of the auxiliary equipment of the steam turbine ($US\$$)
Z_{wt}	Capital investment cost of the water treatment facility($US\$$)

GREEK LETTERS

ρ	Density (kg/m^3)
ρ_{air}	Air density (kg/m^3)
ρ_{cl}	Mirror reflectance (-)
μ	Dynamic viscosity ($mPa \cdot s$)
μ_{air}	Air dynamic viscosity ($mPa \cdot s$)
ν	Kinematic viscosity (mm^2/s)
φ	Volume fraction (%)
ε	Nanolayer thickness (nm)
ε_c	Glass cover emissivity (-)
ε_c	Receiver emissivity (-)
γ	Nanolayer thickness ratio (-)
θ	Angle of Incidence (rad)
λ	Tilt angle (rad)
Ω	Aperture azimuth angle (rad)

a	Solar altitude angle (rad)
β	Solar azimuth angle (rad)
η_o	Collector optical efficiency (-)
η_r	Receiver efficiency (-)
η_{PTSC}	Energetic efficiency of the PTSC (%)
η_{ex}	Exergetic efficiency of the PTSC (%)
η_{ISRC}	Energetic efficiency of the ISRC (%)
η_{ISRRC}	Energetic efficiency of the ISRRC (%)
η_{st}	Isentropic efficiency of the Steam Turbine (%)
η_p	Isentropic efficiency of the Pump (%)
α_r	Receiver absorptance (-)
α_c	Glass cover absorptance (-)
τ_C	Glass cover transmittance (-)
σ	Stefan-Boltzmann Constant ($5.67 \times 10^{-8}\ W/m^2K^4$)

SUBSCRIPTS

f	Base fluid
nf	Nanofluid
p	Nanoparticle

ABBREVIATIONS

CNT	Carbon Nanotubes
CSP	Concentrated Solar Power
$DWCNT$	Double Walled Carbon Nanotubes
EES	Engineering Equation Solver
EG	Ethylene Glycol
$ISRC$	Integrated Solar Rankine Cycle
$ISRRC$	Integrated Solar Regenerative Rankine Cycle
LEC	Levelized Cost of Electricity
NPV	Net Present Value
NS	Net Saving

$MWCNT$	Multi Walled Carbon Nanotubes
$PTSC$	Parabolic Trough Solar Collector
SAM	System Advisory Model
$SWCNT$	Single Walled Carbon Nanotubes
TES	Thermal Energy Storage

Chapter 1: Introduction

The daily increase in the use of the electricity and fossil fuels in the United Arab Emirates raises the necessitates for finding a renewable source of energy to accommodate the needs and power requirements for different sectors. Solar Energy is one of the renewable sources that provide a clean, reliable and uninterrupted source of power that can replace conventional power generation methods. Concentrated Solar Power (CSP) is the leading technology in harvesting the solar radiation, which paves the way for a sustainable energy production. Different types of CSP's are used in the industry for power generation, but Parabolic Trough Solar Collectors (PTSCs) are the most common technology deployed in power plants. However, the efficiency of the PTSC and heat loss during storage times are two major drawbacks while using the PTSC in solar energy harvesting. Recent discoveries suggested that adding nanoparticles to a conventional heating fluid increases the thermal conductivity and then enhances the thermophysical properties and heat transfer characteristics of that fluid. The nanofluid produced will then have a positive effect on the performance of the PTSC and Thermal Energy Storage system (TES).

1.1 Problem Statement

The demand for energy is growing daily at an unexpected rate, and conventional power plants running on fossil fuels are struggling to equate the increasing load of electricity needed.

Renewable energy, specifically solar energy, can be used for power generation, desalination and many other applications. CSP is the most promising and efficient method of harnessing solar radiation. PTSCs are available commercially for power production usage because of their relatively low cost compared to other solar collectors. Nonetheless, PTSCs integrated with TES have a low storage capacity depending on the heating fluid used and a high maintenance cost. Also, the PTSCs efficiency is limited to around 60%, and thermal losses are considered to be an issue.

The performance of the PTSCs ought to be enhanced if solar energy is to replace the conventional power production methods. The heating fluid inside the receiver of a

PTSC is one of the major parameters that affect the PTCS, TES and power cycle of a power production plant. Thus, enhancing the heat transfer characteristics and thermophysical properties of the heating fluid can give a positive effect on the performance of the PTSC; this could be done by using nanofluids which consist of the conventional heating fluids with the addition of nanoparticles.

This research aims at studying the effect of using nanofluids as heating fluids on the performance of a PTSC, and an integrated PTSC/TES system.

1.2 Significance of the Research

The rate of the increase in the global demand for fossil fuel will lead to a shortage in the fossil fuel sources, while the annual production will fall short in supplying the worldwide demand. It is expected that in the next 40 years, crude oil and natural gas resources will be completely depleted.

Solar energy provides clean, secure and efficient energy. It is the most reliable source of energy to help countries reach their sustainable development objectives. Switching to solar energy reduces the CO_2emissions and the use of fossil fuels which in its turn benefits the environment. Nationally, the United Arab Emirates has already taken a huge step in the renewable energy path by constructing SHAMS 1; the first CSP solar plant in the United Arab Emirates [1]. In addition, building Masdar city, a planned city in Abu Dhabi which is run solely on solar and renewable energy resources, confirms the United Arab Emirates vision of clean, reliable and sustainable energy [2]. Moreover, several other projects are undergoing the planning phase and are to be launched soon, with reports stating that the United Arab Emirates is planning to meet 25% of its energy demand by the end of the decade by relying on non-conventional energy sources [3].

The United Arab Emirates' vision for sustainable development can be reached by the use of renewable energy. In order to help the UAE thrive to that vision and accomplish its objective of achieving around 7% renewable energy power generation capacity by 2020 [4], the conventional PTSCs are to be improved and the integration between the PTSC and TES is to be enhanced. The use of nanofluids will increase the power output, efficiency and enhance the performance of PTSCs, subsequently lowering

the load on the TES. From an economic point of view, the use of nanofluids will decrease the levelized electricity cost of the power plant and decrease the variable costs on the long run. However, running PTSC on nanofluids is considered to be a new idea, and a lot of research and experimental work are needed in order to commercialize a nanofluid based parabolic trough solar collector.

1.3 Scope and Objectives

The scope of this research is combining different nanoparticles with different heating fluids and studying their effect on the thermophysical properties and heat transfer characteristics, then evaluating the performance and the cost of an integrated PTSC/TES system using nanofluids as a heating fluid for different modes of operation.

The main objective of this research is to provide a nanofluid that enhances the performance of a PTSC/TES system, and can potentially replace the conventional heating fluids in order to optimize the characteristics of a power plant.

The research specifically aims to:

1. Carry out an in-depth literature survey
2. Investigate the integration between PTSC and TES.
3. Determine the appropriate heating fluids used in operating the PTCS, and appropriate storage materials for the TES.
4. Study the effect of adding nanoparticles on different thermophysical properties and heat transfer coefficient of the heating fluids by applying different models and correlations.
5. Conduct parametric studies to examine the effect of nanoparticle size, shape, and type and volume fraction on the thermophysical properties of the nanofluids, and the convective heat transfer coefficient inside the absorber tube of the PTSC.
6. Study the effect of using nanofluids as a heating fluid on the performance of the PTSC in terms of energy and exergy.
7. Choose the most adequate nanofluids according to the United Arab Emirates weather data and conditions, and specific design inputs and parameters.

8. Compare two different configurations which are the Integrated Solar Rankine Cycle (ISRC) and the Integrated Solar Regenerative Rankine Cycle in order to choose the most efficient cycle.
9. Study the effect of the storage on the PTSC/TES system by varying the modes of operation, and using conventional heating fluids versus nanofluids.
10. Study the effect of using the nanofluids on the performance of the integrated system for different modes of operation.
11. Carry a thermo-economic evaluation of the effect on nanofluids on the performance of the integrated system from an economic point of view.
12. Choose the most suitable nanofluid to replace the conventional heating fluid for different modes of operation of the integrated system.
13. Choose the most efficient and cost effective mode of operation of the integrated system to operate at.

1.4 Research Methods and Materials

The methodology behind this research starts with selecting the nanoparticles and base fluids to carry out the analysis. Two metallic: Copper (Cu) and Alumina (Al_2O_3) and one non-metallic: Single Walled Carbon Nanotubes ($SWCNT$) nanoparticles are selected, while Therminol VP-1 and Syltherm 800 are chosen as the heating fluids. The thermophysical properties of the different nanofluids are calculated using different models and correlations for the thermal conductivity, viscosity and the Nusselt number. Afterwards, the effect of the properties on the convective heat transfer coefficient is numerically investigated using MATLAB. Parametric studies are carried to study the effect of the shape, size, type and volume fraction on the heat transfer coefficient. Further, the use of nanofluids as a heating fluid in a PTSC is investigated; using MATLAB again to analyze the effect of using different nanofluids on the efficiency, power output and performance of a PTSC. Another parametric study is done to examine the effect the concentration ratio, and volume fraction on the performing parameters of the PTSC.

Engineering Equation Solver (EES) is used to analytically compare two different configurations for the integrated system (ISRC and ISRRC) in terms of efficiency. Next the Solar Advisory Model (SAM) is used to evaluate the performance and cost

parameters of the chosen PTSC/TES power production plant configuration. The nanofluids properties are imported to SAM from MATLAB, and the performance and cost analysis of the full integrated system are studied for different modes of operation.

Finally, comparison between the conventional heating fluids and the nanofluids is presented, and the most suitable fluid for enhancing the performance and cost of a PTSC/TES is chosen for different modes of operation.

1.5 Thesis Organization

The thesis consists of six main chapters. Chapter 1 provided an introduction to the thesis, the significance of the research and the problem statement. Furthermore, it outlined the scope and objectives of the thesis followed by the research methods and methodology used in the analysis.

Chapter 2 provides an in-depth literature survey about the experimental and analytical enhancement of thermal conductivity and heat transfer characteristic of nanofluids, and the use of nanofluids in solar energy and TES systems. Chapter 3 presents the modeling equations, correlations and thermophysical properties' models used in the prediction and calculation of different parameters. Chapter 4 provides the results of the study; it includes graphs, tables and discussion of the obtained results, while Chapter 5 presents an economic evaluation of the proposed systems. Final conclusions, recommendations and remarks are provided in Chapter 6.

Chapter 2: Literature Review

In this chapter, an in-depth literature survey about the PTSC modeling, TES operation and types, nanofluids thermophysical properties and enhancements, and nanofluids application in solar energy and thermal energy storage is presented.

2.1 PTSC modeling and applications

Solar energy can be harnessed using different mechanisms and applications. The Concentrated Solar Power (CSP) has proved to be the most efficient since the radiation is absorbed, and then reflected to focus on a smaller area in order to maximize the amount of heat captured. Different types of CSP can be found, such as: Fresnel Reflectors, Dish Sterling, Solar Power Tower, and Parabolic Trough Solar Collector (PTSC) which is the most studied, and most available in the literature. The PTSC simply consists of a parabola shaped sheet, mostly made of aluminum, which acts as a reflector. The sheet is usually called a collector as it is the area where the solar radiation is collected, then reflected. The sun rays are reflected onto a metal tube placed in the center of the collector, which is called the receiver. The heating fluid flows through the receiver and it is heated by the solar radiation reflected from the collector. The receiver is surrounded by a glass cover in order to minimize the heat loss, due to convection and radiation. Review of the literature on the modeling and the applications of PTSC are provided as follows.

Kalogirou [5] provided a detailed thermal model of a parabolic trough solar collector (PTSC). The model presented takes into account all the modes of heat transfer; convection into the receiver pipe, convection in the annulus between the receiver and the glass cover, and convection from the glass cover to the ambient air; conduction through the metal receiver pipe and class cover walls; and radiation from the metal receiver pipe and glass cover surfaces to the glass cover and sky respectively. The model was validated by comparing the results of the efficiency and heat loss with the data provided from Sandia National Laboratories. The performance of the model yielded very close and satisfactory results.

Reddy et al. [6] carried out exergetic and energetic analysis for the components of the solar thermal power plant system in both the cities of Delhi and Jodhpur. The solar

system consisted of two subsystems, the collector – receiver subsystem, and Rankine heat engine subsystem. The collector-receiver subsystem contains a set of parabolic trough mirrors installed in arrays, and an energy storage system that pumps Therminol VP-1 to the system. The analysis showed that the main energetic losses took place in the heat engine circuit through the condenser, followed by the collector-receiver system. However for the exergetic losses, the solar collector-receiver is the main area where the exergetic power loss is the greatest. It was also shown that by increasing the operating pressure from 90 to 105 bar, the energetic and exergetic efficiencies are increased by 1.49% and 1.51% respectively.

Kumaresan et al. [7] experimentally investigated the performance of a solar parabolic trough collector system integrated with a storage unit. The system consisted of a parabolic trough collector, a thermal storage tank and a positive displacement pump to force Therminol 55 which is the heating fluid from the storage tank to the trough. The experimental study was conducted until the storage tank was capable of storing the heat during the day. It was concluded that firstly, the instantaneous efficiency of the PTC depends on both the incident beam radiation and the useful heat gain. Secondly, the peak instantaneous efficiency is around 63%. Thirdly, the decrease in the insolation rate and increase in the heat loss decreases the overall efficiency and that minimizing the heat loss alone can lead to an acceptable performance of the PTSC.

Feldhoff et al. [8] described and compared two power plants' design, performance and investment. The first plant uses synthetic oil and includes a two-tank molten salt storage system, while the other plant is a direct steam generation (DSG) plant with a phase change material for the latent heat storage, and molten salt for the sensible thermal energy storage system. To make sure the two plants are comparable, they both shared the same electrical capacity of 100 MW, same TES capacity of 9 hours and the same solar multiple of the collector field. Results showed that the efficiency of the DSG plant is about 8% more than the synthetic oil plant, but its project investment is 10% higher which causes the levelized electricity cost (LEC) to be higher by 6%. The main reason for the high LEC is the storage system used in the DSG plant. If no storage system is used, then the LEC is about 5-8% less than that of the oil plant.

Lobón et al. [9] introduced a computational fluid dynamic (CFD) simulation approach to predict the behavior of a multiphase fluid in a parabolic trough solar collector. The simulation results show a reliably close agreement with experimental time series data for different categories of transients which include variation in solar radiation, inlet mass water flow and outlet steam temperature. The overall mean squared error for temperature values is less than 6%. Valenzuela et al. believe that this work [9] supports the applicability of using CFD modeling to study dynamics of DSG in parabolic trough solar collector.

Al-Ansary and Zeitoun [10] introduced a promising technique to bridge the cost and performance gap between receivers with vacuum annuli and receivers with air- filled annuli. This is done by fitting a heat- resistant thermal insulation material in the portion of the receiver annulus that does not receive concentrated sunlight. It is expected that the presence of this insulation material would decrease not only the convection heat losses but also the radiation heat losses. The simulation results showed that the combined conduction and convection heat loss of the proposed model is 25% less than a receiver with an air-filled annulus when fiber glass insulation is used. However, since the thermal conductivity of the insulating material increases with the increase of temperature, thus reducing the benefit of the proposed concept at high temperature, it was concluded that the proposed model could be a suitable replacement for receivers with air-filled annuli or an economical alternative to the evacuated receivers that only operate at low temperatures.

Padilla et al. [11] performed a detailed one dimensional numerical heat transfer analysis on a PTCS. Finite element method was used by dividing the receiver and the envelope into several segments, then applying mass and energy balance in each segment. In addition, improvements in convective and radiative heat transfer correlations were also presented. The model was compared to the experimental data obtained from Sandia National Laboratory (SNL) and other models. The simulation results show that the presented model provides a better agreement with the experimental data compared to other models in terms of efficiency, heat and thermal losses.

Yilmaz and Söylemez [12] performed a comprehensive thermo-mathematical analysis for a PTSC. Solar, optical and thermal models were developed using differential and non-algebraic correlations. Then, the obtained solution was fed into Engineering Equation Solver (EES) software to be solved simultaneously. The simulated results were compared to experimental data of SNL and yielded satisfactory results showing good consistency with respect to other models studied. The following conclusions were made: The most variable and effective parameter on the collector efficiency is the optical loss, and variation in the radiative properties of the optical materials with incidence angle less than 20 ℃ can be considered insignificant. Moreover, it was reported that the annulus condition has a considerable effect on the thermal efficiency, where the heat loss can be minimized by vacuuming the annulus but then the maintenance of the receiver becomes problematic. Further, increasing the mass flow rate will result in increasing the pumping power; therefore an optimum optimal value of the mass flow is needed to keep the pumping work at minimum for the sake of raising the thermal efficiency. Finally, it was observed that the heating fluid type has no significant effect on the enhancement of the thermal efficiency.

Li and Wang [13] measured the heating efficiency and temperature of two types of solar evacuated tube parabolic trough solar collectors with heating fluids of water and Nitrogen (N_2). Experimental results demonstrated that both evacuated tubes presented good heat transfer with water as the heating fluid. Where the heating efficiency ranges from 70-80%, but the water easily boils when the mass flow rate is less than 0.0046 kg/s. However, for Nitrogen, the heating efficiency is around 40%, and the gas temperature reaches 320-460℃. A model is built to further analyze the evacuated tube heated by solar trough concentrating system, and the results showed that the model agrees with experimental data with an accuracy of 5.2%.

Tyagi et al. [14] evaluated the exergetic performance of concentrating type solar collector, and carried a parametric study using hourly solar radiation. The results showed that most of the performance parameters such as the exergy output, exergetic and thermal efficiencies, stagnations temperature, inlet temperature all increase with the increase of the solar intensity, however the exergy output and the exergetic and thermal efficiencies

are found to be the increasing function of the mass flow rate at a constant solar intensity. Moreover, for low value of solar intensity, the exergetic efficiency first increases and then decreases as the concentration ratio is increased. Finally, it is recommenced that mass flow is chosen carefully because it is a critical parameter for a concentrating solar collector.

Öztürk et al. [15] investigated the geometry of a parabolic trough reflector and the characteristics of solar radiation to the reflecting surface. The energy into the receiver was also calculated. Moreover, a parabolic trough collector is analyzed with respect to the energy and exergy models for meteorological specification of different months in Isparta/ Turkey. The simulated results show that the first law efficiency reaches its highest peak in July where the solar intensity is at its highest. , The second law efficiency also follows the same trend and reaches the highest peak in July, and the maximum first and second law efficiencies are around 76% and 27% respectively.

PTSCs can be used in cooling, heating, power generation and desalination as provided in the following literature. Mazloumi et al. [16] simulated a solar single effect lithium-bromide absorption cooling system running on a parabolic trough solar collector with an insulated thermal storage tank. A thermodynamic model was used to simulate the absorption cycle and the parabolic trough solar collector, running on water and for a load of 17.5 kW, which is the average load for a household. The simulation results showed that the mass flow rate of the collector has a negligible effect on the minimum required collector area, but a significant effect on the optimum capacity of the storage tank. In addition, the thermal stratification in the storage tank tends toward the well-mixed situation, when the mass flow rate of the collector is high and storage tank volume is low. It was also concluded that the optimal capacity of the storage tank increased extremely when the operation of the absorption system continued after sunset.

Cabrera et al. [17] summarized the existing experiences, and reviewed the available papers on the applications of the parabolic trough solar collector in solar cooling systems. The use of the PTSC as an occasional alternative to other solar collectors in air conditioning applications was evaluated. The results showed that the PTSC is suitable to be used in process heat and absorption cooling, but the rate of the

growth of the PTSC is still low. Compared to other solar technologies, the PTSC showed the highest solar fraction compared to the Flat Plate Solar Collector, Evacuated Tube Solar Collector and Concentrated Power Solar Collector.

Abueidda and Gadalla [18] performed a thermodynamic analysis on an integrated solar-based multi-flash stage desalination/Rankine cycle system. Energy and exergy models for the solar field are presented and the first and second law efficiencies are calculated. The simulation results show that the first-law and second law efficiencies of the solar field are 61.7% and 31.7% respectively.

Al-Sulaiman et al. [19] assessed the exergetic performance of a novel trigeneration system using parabolic trough solar collector (PTSC) and an organic Rankine cycle (ORC). The trigeneration system considered is examined using three modes of operations. First, solar mode during the low-solar radiation time of the day, second solar and storage mode during the high-solar radiation time of the day, and third storage mode during night time, where the storage mode is operated through the heat collected in a thermal storage tank during the solar and storage mode. The simulated results show that the maximum electrical-exergy efficiencies for the solar mode, solar and storage mode and storage mode are 7%, 3.5% and 3% respectively. However, when trigeneration is used, the maximum efficiencies of the modes become noticeably higher with 20%, 8% and 7% for the solar mode, solar and storage mode and storage mode. Further, it was shown the maximum exergy destruction happens in the solar collectors and the evaporators of the ORC. Therefore, a careful selection and design of these components is vital for the reduction of the exergy destruction.

2.2 Thermal Energy Storage

Thermal energy, after being collected by the solar field, has to be stored for later use. It is vital that the storage of the thermal energy is done efficiently, thus the design of the thermal energy storage system needs to be studied carefully. The main aspects of designing a solar thermal energy storage system are the technical properties, cost effectiveness and environmental impact.

2.2.1 Thermal energy storage types.

Thermal energy storage systems can be classified into two types: active and passive. In case of the active TES, the storage medium is a fluid and it is able to flow between the tanks, while in the case of the passive TES, the storage media is a solid and the fluid only enters the tank for charging or discharging. Moreover, the TES can be classified into two main categories. The first one is the direct storage, where the heating fluid from the solar field is the same fluid stored in the storage tank; for example, steam is accumulated in pressure vessel for later use. The second is the indirect storage which is widely used and it is classified into three main mechanisms as follows:

a) Sensible heat storage:

The sensible heat storage is the most developed technology but it has the lowest storage capacity leading to an increase in the storage system size. The energy stored in the sensible heat storage could either be solid-state or liquid- state storage media. Table 1 shows the most common storage media used for sensible heat storage [20]. The mechanism behind the sensible heat storage is a direct heat exchange between two media, whether it is liquid-liquid or liquid-solid, meaning that the fluid undergoes no phase change. With regard to Table 1, the best option for sensible heat storage is the use of molten salts, because of their excellent stability under high temperature, low viscosity and high thermal conductivity. Add to that, the non-flammability and non-toxicity makes molten salt environmentally safe.

b) Latent heat Storage:

The main idea behind the latent heat storage mechanism is the use of phase change materials (PCMs). The PCMs can store or release a large amount of heat when changing their phase structure whether it is melting or solidification. Compared to the sensible materials, the enthalpy of PCMs is almost a 100-200 times higher leading to a smaller storage size. Table 2 shows the thermophysical properties of some commercial latent heat storage materials [20]. The main disadvantage in implementing the latent heat storage is the low thermal conductivity, and the cost of

ranging from 0.5$/kg to 5$/kg is remarkably cheaper than that of the latent heat storage ranging from 4.28 $/kg to 334 $/kg [21].

Table 1: Storage Medias used for sensible heat storage [20]

Parameter	T_{cold}	T_{hot}	Material	k	ρ	C_p	Medium
Unit	(℃)	(℃)	-	(W/mK)	(kg/m^3)	(kJ/kgK)	-
	200	300	Sand-rock-oil	1	1700	1.3	Solid
	200	400	Reinforced Concrete	1.5	2200	0.85	Solid
	200	400	Cast Iron	37	7200	0.56	Solid
	200	500	NaCl	7	2160	0.85	Solid
	200	700	Cast Steel	40	7800	0.6	Solid
	200	700	Silica fire bricks	1.5	1820	1	Solid
	200	1200	Magnesia fire bricks	5	3000	1.15	Solid
	250	350	Synthetic Oil	0.11	900	2.3	Liquid
	250	450	Nitrate Salt	0.57	1825	1.5	Liquid
	270	530	Liquid Sodium	71	853	1.3	Liquid
	300	400	Silicon Oil	0.1	900	2.1	Liquid
	180	1300	Lithium Liquid Salt	38.1	510	4.19	Liquid
	15	400	Dowtherm A	0.1171	867	2.2	Liquid
	120	500	HitecXL	0.52	1992	1.4	Liquid

Table 2: Properties of latent heat storage Medias [20]

Parameter	Material	Phase change Temperature	k	ρ	Latent heat
Unit	-	℃	(w/mK)	(kg/m^3)	(kJ/kg)
	$NaNo_3$	307	0.5	2260	172
	KNO_3	333	0.5	2110	226
	KOH	380	0.5	2044	149.7
	$AlSi_{12}$	576	1.6	2700	560
	$NaCl$	800	5	2160	492
	Na_2Co_3	854	2	2533	275.7
	K_2CO_3	897	2	2290	235.8

c) Thermocline heat storage:

The idea behind this mechanism is relying on chemical reactions, because some chemicals can absorb or release a large amount of thermal energy when they break or form certain chemical bonds. Based on this idea, this storage heat mechanism makes use of the chemical heat. The main constraint while using the thermocline heat storage is the design criteria. Hence storage materials with excellent chemical reversibility, large chemical enthalpy change and simple reaction condition is needed. Table 3 provides a list of potential materials for thermocline heat storage [20].

Table 3: Potential materials for thermocline storage [20]

Parameter	Material	Temperature Range	Enthalpy Change	Chemical Reaction
Unit	-	℃	GJ/m^3	-
	Iron Carbonate	180	2.6	$FeCO_3 \leftrightarrow FeO + CO_2$
	Metal Hydrides	200-300	4	$(Metal\ xH_2 \leftrightarrow Metal\ yH_2 + (x-y)H)_2$
	Ammonia	400-500	$67\ kJ/mol$	$NH_3 + \Delta H \leftrightarrow 1/2\ N_2 + 3/2\ H_2$
	Hydroxides	500	3	$Ca(OH)_2 \leftrightarrow CaO + CO_2$
	Calcium Carbonate	800-900	4.4	$CaCO_3 \leftrightarrow Ca + CO_2$

2.2.2 Thermal energy storage experimental studies.

Zhao and Wu et al. [22] experimentally investigated the use of a novel ternary nitrate molten salt as a heat transfer fluid through a parabolic trough solar collector instead of synthetic oil. The molten salt is a mixture of 50-80 wt. % KNO_3, 0-25 wt. % $LiNO_3$ and 10-45 wt. %$Ca(NO_3)_2$, and the results indicated that the mixture exhibited excellent thermal properties such as, a low melting point of 100 ℃, robust reliability, temperature stability up to 500 ℃ and a low viscosity of 5 cP at 190 ℃. Add to that, the cost of manufacturing these salts is considerably lower than that of the existing heat transfer fluids, concluding that these salts are an excellent replacement to synthetic oil which is widely used.

Hermann et al. [23] investigated the use of molten salt as a two direct tank storage systems instead of using the heating transfer fluid flowing through a PTSC directly. The experimental results showed that the LEC reduces by 10% for a 12 hour full load capacity. In addition, it was measured that the specific cost of a two tank molten salt storage system is in the range of 30-40 \$/kWh_{th} depending on the storage size.

2.3 Nanofluids and their applications

Nanofluids are defined as fluids with nanoparticles dispersed inside them. The nanoparticles enhance the thermophysical properties of the fluid, and the heat transfer characteristics. Therefore, using nanofluids can improve the output parameters of almost any application. Nanofluids can be used in different energy harvesting systems in order to increase the amount of energy captured. , They can be also used for cooling as some of them enhance the specific heat capacity of the base fluid. In general, nanofluids can be used in application that requires fluid motion whether it is for cooling and heating, or it is mechanical or even electrical work that is being done. However, in this literature review the effect of adding nanoparticles to the properties of the fluid such as the thermal conductivity, viscosity and specific heat capacity are shown, as well as the enhancement in the convective heat transfer coefficient and heat transfer characteristics. In addition to, the effect of nanofluids on solar systems such as Flat Plate Solar Collector (FPSC), Direct Absorption Solar Collector (DASC), and Parabolic Trough Solar Collectors (PTSC), and finally the effect on the performance and the size of the TES are seen.

2.3.1 Thermophysical properties enhancements.

The following section shows literature on the effect of adding nanoparticles on the thermal conductivity, viscosity, and specific heat capacity of the fluid. It is divided into experimental work, and analytical literature.

2.3.1.1 Experimental properties enhancements.

2.3.1.1.1 Thermal conductivity.

The term nanofluids was first presented by Choi et al. [24], where carbon nanotubes were added to oil to study the enhancement of the thermal conductivity. Masuda et al. [25], and Xuan and Li [26] all experimentally showed that the addition of nanoparticles with small volume fractions (1% to 5%), results in an enhancement of the thermal conductivity up to 20%.

Eastman et al. [27] carried some preliminary experiments to study the effect of suspending $Al_2O_3, CuO\ and\ Cu$ nanoparticles in water and HE-200 oil. The results

showed that for a volume fraction of 5% of CuO dipped in water, the thermal conductivity increased by 60%.

Wang et al. [28] and Lee et al. [29] experimentally studied the effect of dispersing CuO and Al_2O_3 nanoparticles in water and ethylene glycol. The results revealed that the thermal conductivity of the nanofluids increases with the increase of the volume fraction. In addition, it was reported that the enhancement of the thermal conductivity of CuO/water with a volume fraction of 10% is around 34%, while for CuO/EG nanofluid with a volume fraction of 15%, the enhancement was around 50%. Moreover, an enhancement of 12% in thermal conductivity was reported for Al_2O_3/water nanofluid for a volume fraction of 3%.

Choi et al. [24] carried the first experimental analysis to show the enhancement of the thermal conductivity of CNT-based nanofluids. It was discovered that the measured thermal conductivity of the CNT-based nanofluids was anomalously greater than theoretical predictions, and it was nonlinear with respect to nanotube loading. In addition, the authors suggested physical concepts in order to understand the anomalous behavior of the nanotubes. The experimental results showed that by adding CNT with a volume fraction of less than 1% in oil, the thermal conductivity increased by 150%. The previous results suggest that nanotubes provide the highest thermal conductivity enhancement in fluids, opening the door for a wide range of carbon nanotubes applications.

Eastman et al. [30] studied the effective thermal conductivity of Cu/EG nanofluids, and measured a 40% increase in thermal conductivity for a volume fraction of 0.3% and a nanoparticle size of less than 10 nm. The experimental results were found to be anomalous based on previous theoretical studies that suggest a strong effect of the particles shape on the effective thermal conductivity of nanofluids, but also suggests no effect of the particle size and the particle thermal conductivity.

Xie et al. [31] examined the effect of the base fluid on the enhancement of the effective thermal conductivity, and concluded that base fluids with lower thermal conductivity will lead to a higher thermal conductivity enhancement. In addition, the authors studied the effect of the particle shape on the enhancement of the effective

thermal conductivity. It was established that elongated particles provide better enhancements. For instance a 26 nm spherical and 600 nm cylindrical particles of SiC were dispersed in ethylene glycol at a volume fraction of 3%, and the experiment showed that the ratio of thermal conductivity enhancement for the spherical and cylindrical particles was 1.10 and 1.16 respectively.

Biercuk et al. [32] experimentally measured the enhancement of the thermal properties of industrial epoxy caused by the addition of $SWCNT$. The experimental results showed an enhancement of 70% in thermal conductivity at a temperature of 40 K, rising to 125% at room temperature for a weight percent on 1% only. In addition, the electrical conductivity showed a percolation threshold between a weight percent of 0.1% and 0.2% of $SWCNT$ loading. Moreover, the Vickers hardness increased up to a factor of 3.5 at a weight percent of 2%.

Xie et al. [33] experimentally investigated the addition of multi walled carbon nanotubes ($MWCNT$) to deionized water, ethylene glycol and decene. The $MWCNT$ were treated by using a concentrated nitric acid to disentangle the CNT's in order for them to be dispersed into the fluids. Also oxygen-containing functional groups were introduced on the CNT surfaces to enable the production of a more homogenous and stable CNT-based nanofluids. It was measured that the thermal conductivity of $MWCNT$/DE, $MWCNT$/EG and $MWCNT$/DW increased by 19.6%, 12.7% and 7.0% respectively at a volume fraction of 1%. In addition, it was observed that the enhancement in the thermal conductivity decreases with the increase in the thermal conductivity of the base fluids. Finally, a comparison between the experimental and theoretical data provided that there is a strong dependency between the thermal conductivity and the interfacial nanolayer existing between the nanoparticles and the base fluid.

Patel et al. [34] studied the dispersion of gold (Au) and silve (Ag) nanoparticles with nanoparticle diameter between 10-20 nm in water and toluene. It was shown that for a very small volume fraction of 0.00026 of Ag in water, the thermal conductivity was enhanced by 5%-21%. In addition, for a volume fraction of 0.011 of Au in water, the thermal conductivity was enhanced by 7%-14%. In addition, the effective thermal

conductivity decreased as the nanoparticle diameter increased, pointing to the different factors that the thermal conductivity enhancement depends on. Moreover, it was pointed out that a direct contact between the metal surface and the solvent is vital to improve enhancement.

Wen and Ding [35] investigated the effect of the temperature on the enhancement of the thermal conductivity of $MWCNT$/water nanofluids. The stable nanofluids were made using sodium dodecylbenzenesulfonate as the dispersant. The results showed that the enhancement in the thermal conductivity increases with the increase of the concentration with a nonlinear dependency even at low concentrations, which was not the case for metal-based and metal oxides-based nanofluids where a linear relation was present. In addition, the effect of the temperature on the thermal conductivity of nanofluids was studied, and a directly proportional relation was present. For example, it was found that the thermal conductivity increases by 23.7% and 31% at a concentration of 0.84% for a temperature of 20 ℃ and 45 ℃ respectively.

Assael et al. [36] measured the enhancement of the thermal conductivity of $MWCNT$ and Double Walled Carbon Nanotubes ($DWCNT$) water based nanofluids. In order to enhance the thermal conductivity enhancement, Hexadecyltrimethyl ammonium bromide and Nanosperse AQ were employed as dispersants. The thermal conductivity of the nanofluids was measured by using the conventional hot wire method, and all measurements were taken at an ambient temperature. It was provided that the maximum enhancement was 34% at a volume fraction of 0.6%.

Hong et al. [37] experimentally investigated the addition of Fe nanoparticles to ethylene glycol and Fe nanocrystalline powder synthesized by a chemical vapor condensation process. The dispersion of the nanoparticles was improved by the use of sonication with high-powered pulses .The results showed an 18% increase in the thermal conductivity of Fe/EG nanofluids for a volume fraction of 0.55%. By comparing Fe-based nanofluids and Cu-based nanofluids, it was concluded that the suspension of highly thermally conductive materials is not always effective to improve thermal transport property of nanofluids.

Murshed et al. [38] experimentally investigated the dispersion of rod shaped ($\emptyset 10\ x\ 40$) and spherical shaped ($\emptyset\ 15$)TiO_2 nanoparticles in deionized water. The transient hot-wired method integrated with a correlation model was used to measure the thermal conductivity more conveniently. The experimental results showed a directly proportional relation between the measured thermal conductivity and the volume fraction. In addition, it was found that the thermal conductivity is dependent on the shape of the nanoparticles. For example, it was observed that thermal conductivity was enhanced by 33% and 30% for the rod shaped and spherical shaped nanoparticles respectively for a volume fraction of 5%.

Liu et al. [39] experimentally measured the thermal conductivity enhancement of $MWCNT$ dispersed into ethylene glycol and synthetic engine oil. The results show that the $MWCNT$ nanofluid exhibits higher thermal conductivity than that of the EG and engine oil base fluids. In addition, for the $MWCNT$/EG nanofluid and for a volume fraction of 1% the enhancement of the thermal conductivity is around 12.4%. On the other hand, for the $MWCNT$/Oil nanofluid and for a volume fraction of 2%, the thermal conductivity enhancement is around 30%. Although the increase rate of the thermal conductivity is different for different base fluids, it was observed that Oil based nanofluids display a higher thermal conductivity enhancement than that of the EG based nanofluids.

Li and Peterson [40] conducted experiments on the effect of the volume fraction, temperature and particle size on the effective thermal conductivity of Al_2O_3 and CuO water based nanofluids. It was shown that the effective thermal conductivity of Al_2O_3/water nanofluid increased up to three times by increasing the temperature from 27 to 34.7 ℃.

Liu et al. [41] dispersed Cu nanoparticles in EG, water and engine oil and studied their effects on the thermal conductivity. Experimental results showed that for Cu/water nanofluid with a volume fraction of 0.1%, the thermal conductivity is increased by 23.8%.

Chopkar et al. [42] experimentally measured the effective thermal conductivity of nanocrystalline$Al_{70}Cu_{30}$ particles dispersed in ethylene glycol. The nanofluids were prepared by adding particles from 0.2 up to 2% to the base fluid, and the thermal conductivity of the mixture is measured using a modified thermal comparator. The results showed that the thermal conductivity of the nanofluid with a 1.5% of $Al_{70}Cu_{30}$ particles increased up to 200% when compared to the base fluid. Moreover, by applying a simple quenching experiment on the nanofluid, it was observed that the heat removal rate of the nanofluid is better than the base fluid at low temperatures.

Hwang et al. [43] produced four kinds of nanofluids such as $MWCNT$/Water, CuO/Water, SiO_2/Water and CuO/EG, and measured their thermal conductivity using the transient hot-wire method. The experimental results showed that for a volume fraction of 1%, the thermal conductivity of $MWCNT$/Water nanofluid increased by 11.3%, which is the highest enhancement compared to the remaining nanofluids. It was concluded that the higher the thermal conductivity of the nanoparticles, the higher the enhancement in the effective thermal conductivity is.

Hwang et al. [44] also produced different kinds of nanofluids, using $MWCNT$, fullerene,Cuo,SiO_2 and Ag as nanoparticles and DI water, ethylene glycol, oil, silicon oil and poly-α-Olefin oil as basefluids. The results demonstrated that the lower the thermal conductivity of the base fluid, the higher the enhancement in the thermal conductivity of the nanofluid with the same nanoparticles. For example, for a volume fraction of 1% the enhancement in thermal conductivity of the $MWCNT$/Water nanofluid is around 7% while for the $MWCNT$/oil nanofluid with a volume fraction of 0.5% the enhancement is around 9%. In addition, it was shown that the enhancement in thermal conductivity increases with the increase of the volume fraction given that the thermal conductivity of the nanoparticles is higher than that of the base fluid. In the case of fullerene/water nanofluid, for instance, it was noticed that the enhancement in the thermal conductivity decreases with the increase of the volume fraction, and that was attributed to the fact that the thermal conductivity of fullerene ($0.4\ W/mk$) is less than that of water ($0.613\ W/mK$).

Pop et al. [45] measured the thermal conductivity of suspended metallic single walled carbon nanotubes ($SWCNT$) by extracting its thermal properties from its high-bias (I-V) electrical characteristics over the 300-800 K temperature range. A correlation for the thermal conductivity of SWCNT was provided by linearly fitting the experimental data. It was established that the thermal conductivity of the SWCNT depends on the temperature and the length of the SWCNT. In addition, it was shown that the thermal conductivity is about 3500 W/mK at room temperature for a length of $2.6\,\mu m$. Moreover, the thermal conductivity increases with the increase of length and decreases with the increase in temperature.

Jana et al. [46] studied the enhancement of$C\ NT$, copper and gold nanoparticles as well as their hybrids such as $CNT-Cu$ and $CNT-Au$ on the thermal conductivity of water as the base fluid. It was observed that with a small volume fraction of 0.3% for Cu nanoparticles, the thermal conductivity was enhanced by 70%.

Kim et al. [47] experimentally measured the thermal conductivity of $AL_2O_3, TiO_2 and\ ZnO$ nanoparticles dispersed in water and EG. The effect of the particle size was analyzed and it was measured that for TiO_2/EG nanofluid with a volume fraction of 3% and nanoparticle size of 10 nm the thermal conductivity enhancement was around 16%, which is halved when nanoparticles of size 70 nm are used.

Yoo et al. [48] studied experimentally the effect of adding Fe nanoparticles to ethylene glycol on the thermal conductivity. The nanofluids were prepared in a two-step procedure by dispersing nanoparticles into the base fluid. In addition, a cell disrupter generating high power pulses is used to break the clusters formed by the nanoparticles and to improve the dispersion of the nanoparticles. It was shown that the thermal conductivity increased by 16.5% for a volume fraction of 0.3%. This enhancement exceeds the theoretical expectation of two-component mixture system.

Amrollahi et al. [49] experimentally measured the thermal conductivity of CNT/EG nanofluids using a thin layer technique as a function of time of ultra-sonication, temperature and volume fraction. It was observed that by using the ultrasonic disrupter the number of nanoparticles in a cluster was decreased, leading to an increase in the

thermal conductivity. In addition, a strong dependency was found between the thermal conductivity, temperature and volume fraction. This dependency can be attributed to the presence of the Brownian motion which influences the particle motion. It was provided that for a volume fraction of 2.5% the thermal conductivity enhancement was 20%.

Chen et al. [50] studied the effect of the volume fraction on the thermal conductivity of $MWCNT$ nanoparticles dispersed in water and EG. It was observed that the thermal conductivity enhancement increases with the increase of the volume fraction. It was also measured that for a volume fraction of 1%, the enhancement in thermal conductivity was about 175%.

Xie and Chen [51] produced stable and homogenous $MWNCT$/EG nanofluids, and measured the thermal conductivity enhancement with respect to the temperature and nanotube loading. The results showed that increasing the volume fraction of $MWCNT$ increases the thermal conductivity enhancement. For example, at a volume fraction of 0.006%, the enhancement is around 18%, while for a 0.01% volume fraction, the enhancement is around 27%. Moreover, the increase of the temperature and the milling time increases the enhancement of the thermal conductivity. For instance, by increasing the milling time from 28 hours to 38 hours, the enhancement of the thermal conductivity increased from 10.4 % to 12.8 %.

Warrier and Teja [52] presented a one-parameter model that takes into account the decrease in the thermal conductivity of metal nanoparticles with decreasing size. The effect of the size of the particle on the effective thermal conductivity of nanofluids could not be elucidated from the data, although these data were fitted using the model. Therefore, the thermal conductivity of six nanofluids containing silver nanoparticles of different sizes and volume fractions are reported experimentally. The results show that the size of the silver nanoparticles dispersed in ethylene glycol affects the effective thermal conductivity of the nanofluids. It was observed that the thermal conductivity decreases with the decrease in particle size.

Kameya and Hanamura [53] experimentally concluded that adding 0.1% of Ni in alkyl naphthalene increases the solar absorption by a remarkable amount, concluding that

the addition of nanoparticles to a base fluid will increase the thermal properties of that fluid.

Liu et al. [54] investigated the enhancement of thermal conductivities of ethylene glycol, water and synthetic engine oil in the presence of Cu, CuO and $MWCNT$. The nanofluids were prepared using the physical mixing method, however for the Cu/water nanofluid, the chemical reduction method was used. The experimental results showed that the thermal conductivity of the nanofluids is considerably higher than the thermal conductivity of the base fluids, even for small volume fractions. For CuO/EG nanofluid with a volume fraction of 5%, the thermal conductivity increase was 22.4%. As for the $MWCNT$-based nanofluids, $MWCNT$/EG nanofluid with a volume fraction of 1%, $MWCNT$/Water nanofluid with a volume fraction of 1.5%, and $MWCNT$/Oil nanofluid with a volume fraction of 2% showed enhancement in the thermal conductivity by 12.4%, 17% and 30% respectively when compared with their respected base fluids.

Colangelo et al. [55] assessed the potential of using $CuO, Al_2O_3, Zn\ and\ Cu$ dipped in water and diathermic oil as a heating fluid in high temperature solar collectors by measuring their thermal conductivity. The results showed that the thermal conductivity enhancement in diathermic oil was higher than that of water for the same nanoparticles, volume fraction and conditions. Moreover, it was found that the thermal conductivity enhancement is reduced by the increase of the particle size.

Gan and Qiao [56] investigated the optical properties of $MWCNT$, carbon and aluminum dispersed in ethanol. It was concluded that $MWCNT$ has the highest absorption compared to carbon and aluminum. The authors [57] also established that the radiation absorption of Al_2O_3/ethanol is higher than that of Al/ethanol.

Barbés et al. [58] experimentally measured the thermal conductivity and specific heat capacity of AL_2O_3nanoparticles dispersed in both water and ethylene glycol. The experimental analysis was done on a temperature range from 298 K to 338 K, and different volume fractions up to 10%. It was observed that the thermal conductivity of both nanofluids increases with the increase of the temperature and volume fraction, however since the thermal conductivity of water is higher than the thermal conductivity

of ethylene glycol. It was shown that the AL_2O_3/water nanofluid had higher thermal conductivity than the AL_2O_3/EG nanofluid Nevertheless, AL_2O_3/EG nanofluid showed higher thermal conductivity enhancement than AL_2O_3/water nanofluid. , For example, at a temperature of 310 K, the enhancement was around 1.18 for a volume fraction of 6% of AL_2O_3 in EG, and around 1.12 for a volume fraction of 7.3% for AL_2O_3 in water.

Tesfamicha and Woldeyo [59] investigated the effect of the size and type of the nanoparticle and the volume fraction of water based nanofluids. The model used in the analysis was the modified Hamilton and Crosser model using the interfacial shell concept to study the size effect of the nanoparticle. The results showed that the used model under predict the effective thermal conductivity of water based nanofluids when compared to data from the literature. Moreover, it was observed that as the particle size increases, the effective thermal conductivity decreases. In addition, Cu/water nanofluids showed higher thermal conductivity enhancement than Al_2O_3/water at any given volume fraction.

Gu et al. [60] experimentally measured the effective thermal conductivity of three water based nanofluids with high aspect ratio fillers. Multi-walled carbon nanotubes, silver nanowires and copper nanowires were the nanoparticles used in the experiment. The experimental results showed that the enhancement of the thermal conductivity was highest for the silver nanowires/water nanofluids, while CNT/water and Copper nanowires/water nanofluids showed almost the same enhancement at the same volume fraction. It was concluded that thermal conductivity of the nanoparticles is not the decisive factor in the predication of the effective thermal conductivity, i.e. the nanoparticles with the highest thermal conductivity will not necessarily produce nanofluids with the highest thermal conductivity enhancement. The experimental results determined that the shape factor has a substantial effect on the enhancement of the thermal conductivity of nanofluids.

Haddad et al. [61] summarized the methods of preparing nanofluids reported by different investigators to create a stable nanofluid. Different methods are discussed depending on the type of the nanoparticles, whether it is metallic or non-metallic, and the type of the fluid. It was concluded that there are three major methods to prepare a stable nanofluid. First, it is the sonication method. It was shown that an optimum time of

sonication is a major variable to be accounted for. Some nanofluids were sonicated just to be kept stable for the duration of the experiment. The second is the PH control method. It was concluded that the PH needs to be adjusted for small volume fraction because of its effect on the zeta potential. Third is the surfactants. It was concluded that a critical miscell concentration should be respected to avoid speedy sedimentation of the nanoparticles.

Sadri et al. [62] provided experimental data on the effects of ultra-sonication, temperature and surfactant on the thermo-physical properties of multi walled carbon nanotubes. The surfactants used in the experiment were namely, gum Arabic (GA), sodium dodecyl benzene (SDBS) and sodium dodecyl sulfate (SDS). The experimental results showed that the use of GA surfactant in nanofluids led to a higher thermal conductivity compared to using SDBS and SDS, with distillated water as the base fluid. Moreover, it was concluded that the sonication time affects the thermal conductivity and viscosity of nanofluids. The thermal conductivity was enhanced with the increase in sonication time. The highest thermal conductivity enhancement measured was 22.31% at a temperature of 45℃ , sonication time of 40 minutes, $MWCNT$ 0.5 wt. % and 0.25% GA

2.3.1.1.2 Specific heat capacity.

Starace et al. [63] experimentally measured the heat capacities of 13 different nanofluids combinations, and compared them to their respected base fluids. Five base fluids were used in the analysis, which were poly-αolefin, mineral oil, ethylene glycol, a mixture of ethylene glycol and water and calcium nitrate tetrahydrate. As for the nanoparticles used, they were inert metals and metal oxides that did not go any phase transitions over the temperature range. It was concluded that nanoparticles with lower heat capacity than the base fluid will result in decreasing the effective heat capacity of the nanofluid, while an increase in the effective heat capacity of the nanofluid will occur if the heat capacity of the nanoparticle is higher than that of the base fluid, which is not the case for most metallic and metallic oxide particles.

Shin and Banerjee [64] experimentally measured the specific heat capacity of silica nanoparticles (SiO_2) dispersed into eutectic of lithium carbonate and potassium carbonate (62:38 by molar ratio) at a 1.5% concentration. Experiment results show that

the specific heat capacity of silica nanocomposites (Solid phase) was enhanced by 38-54% and the specific heat capacity of the silica nanofluid (liquid phase) by 118-124% over that of the pure eutectic.

2.3.1.1.3 Viscosity.

Mishra et al. [65] reviewed the effect of the nanoparticles on the viscosity of the nanofluids and reported different findings than those provided by the literature. Regarding the particle size, some experimental work studied the viscosity of TiO_2/water nanofluids at different particle sizes and reported that the viscosity of the nanofluids increases with the increase in particle size. However, many other researchers reported that the viscosity of the nanofluids increases with the decrease in the particle size. Moreover, with respect to the shape of the particle, it was reported that elongated particles increase the viscosity more than spherical ones. In addition, when studying the effect of the volume fraction, all the researchers agreed that the viscosity of the nanofluids increases with the increase of the volume fraction.

Shokrlu and Babadagli [66] carried a different set of experiments to clarify the mechanism of additional viscosity reduction of heavy oil/bitumen using nano-size metal particles during steam injection techniques. The first set of experiments was aimed to study the effect of metal particles on the viscosity of the produced oil at a low temperature below a 100℃, while the second was aimed to study their effect in the presence of aqueous phase at high temperature of around 300 ℃ to simulate the steam stimulation process. Finally the third set of experiments was aimed to study the effect of micro and nano-sized particles on the enhancement of the heat transfer within the oil phase. The results showed that at low temperature the particles reduce the heavy oil viscosity after being mixed with the oil phase and that amount of reduction is a function of the particle concentration. In addition, an optimum concentration of the particle yielding the maximum reduction was studied by observing the trend of the viscosity and the concentration which is a function of the particle type, size and temperature. Regarding the steam injection conditions, it was shown that the same trend applies for the low temperature, but the reduction of viscosity is considerably larger. For the third set of

experiments, it was concluded that using the metal particle at their optimum concentration yielded no significant enhancement in the heat transfer.

2.3.1.2 Analytical properties enhancements.

2.3.1.2.1 Thermal conductivity.

Thermal Conductivity is the most critical property for analyzing the heat transfer of nanofluids. Different models are presented in the literature, starting with the Maxwell [67]. He provided the oldest model used to calculate the thermal conductivity of solid-liquid mixtures; it is used for spherical particles and for volume fractions less than 1%.

Bruggeman [68] considered the interaction of spherical particles in his analysis and provided a model for predicting the effective thermal conductivity.

Hamilton and Crosser [69] modified the Maxwell model by introducing an empirical shape factor n to account for different particles shapes. This model led to the study of different particle shapes and their effect on the effective thermal conductivity of nanofluids.

Jeffery [70] considered a composite material of infinite range, and imposed an undistributed linear temperature field on it. The analysis was applied to spherical inclusions and a model for the calculation if effective thermal conductivity was produced.

Yamada and Ota [71], proposed a predictive model for calculating the effective thermal conductivity of nanofluids. The model accounts for spherical and cylindrical shaped nanoparticles. The model was proposed through analyzing experimental data, numerical results and data obtained with the electrolytic-bath. The proposed formula was found to have a wider range of applicability compared to previous formulas.

Davis [72] updated Jeffery's model by adding the ensemble-averaged dipole strength of a single fixed sphere, and by using a decaying temperature field. Those modifications resulted in encountering only convergent integrals, and removing the renormalization factor as it is no longer needed. The model presented depends on the thermal conductivities of the particle and the liquid, the volume fraction and a function$f(\alpha)$, where this function is introduced by the use of renormalization technique.

Kumar et al. [73] proposed a model for the prediction of the effective thermal conductivity of nanofluids and its strong temperature dependence. The model took into account the Brownian motion, however it was established that it might not be accurate for high particle concentrations.

Xuan et al. [74] developed a theoretical model to predict the effective thermal conductivity of nanofluids based on the theory of Brownian motion and the diffusion-limited aggregation model. The model also considers the physical properties of both the base liquid and the nanoparticles, as well as the structure of the nanoparticles. The predictive model consisted of two terms where the first term is simply the Maxwell model, while the second term adds the contribution of the random motion on the effective thermal conductivity of nanofluids. The predications obtained show a satisfactory agreement with experimental data, especially ones where the nanoparticle aggregation is taken into account. In addition, it was observed that the thermal conductivity of a nanofluid increases with the fluid temperature. Moreover, it was established that nanoparticle aggregation reduced the efficiency of energy transport enhancement.

Yu and Choi [75] studied the effect of the liquid nanolayer formed between the spherical nanoparticles and renovated the Maxwell model. Their model was the first to take into account the nanolayer formation.

Xie et al. [76] derived a model for calculating the enhanced thermal conductivity of the nanofluids by taking into account the effect of the nanolayer structure formed between the nanoparticle and the base fluid. In addition, an expression to calculate the thermal conductivity of the nanolayer was derived. The results showed that nanolayer thickness, nanoparticle size, volume fraction, the thermal conductivity of the nanoparticles and the base fluid all influence the effective thermal conductivity of the nanofluids. It was observed that the effective thermal conductivity increases with the decrease of the particle size and an increase in the nanolayer thickness, and that effect plays a major role in the manipulation of the enhanced thermal conductivity, especially at small particle sizes. Further, the model proposed fits quite well when compared to the available experimental data.

Leong et al. [77] proposed a model to calculate the effective thermal conductivity of nanofluids based on the theory of the interfacial layer between the nanoparticles and the base fluid. In this model, the thermal conductivity of the nanolayer is considered to be twice or three time the thermal conductivity of the base fluid. Moreover, the model accounts for the effects of the particle size, interfacial layer thickness, volume fraction and thermal conductivity of the nanoparticles, base fluid and nanolayer. The predicted results showed that the model is in a good agreement with most of the experimental data and it was concluded that the interfacial layer is significant in enhancing the thermal conductivity.

Xuan et al. [78] developed a theoretical model for the prediction of the effective thermal conductivity based on Langevin equation of the Brownian motion and the concept of the stochastic thermal process. The model also describes the temperature fluctuation of the nanoparticles suspended in the base fluid. The predicted results from the model coincide well with the experimental data reported by researchers. It was observed that the thermal conductivity of the nanofluids increases with the increase of the volume fraction and with the decrease of the particle size. Moreover, the model provides that the Brownian motion is the basis of the enhancement in the heat transfer coefficient. It is shown that the term representing the Brownian motion in the model becomes more dominant with the decrease of the particle size or the increase in temperature and volume fraction implying that the Brownian motion is an important factor in the energy transport enhancement.

Prasher et al. [79] developed a model to predict the effective thermal conductivity of nanofluids. The model accounted for the Brownian motion of the nanoparticles inside the base fluid, which according to the authors plays a major role in the enhancement of the thermal conductivity. The developed model was compared to experimental data and other models and the results showed excellent agreement. The model predicted the right trend with respect to different parameters, such as the nanoparticles volume fraction, diameter and temperature.

Gao and Zhou [80] presented a differential effective medium theory to estimate the effective thermal conductivity of nanofluids. The model considered both the physical

and geometrical anisotropy. It was found that the adjustment of the particle shape is very supportive to achieve appreciable enhancement of the effective thermal conductivity. Moreover, the model applied to CNT/oil nanofluids showed good agreement with the experimental data.

Murshed and de Castro [81] developed an improved Brownian-based thermal conductivity model with the addition of a renovated Brownian motion term. The model also takes into account the particle size, interfacial layer and temperature as they are believed to intensify the enhancement of thermal conductivity. It was found that the enhancement in the thermal conductivity is due to the static and dynamic contribution, while the dynamic contribution is presented by the Brownian motion. However, this contribution is more significant for nanofluids with small size nanoparticles and low concentration.

Xiao et al. [82] proposed a model to calculate the effective thermal conductivity of nanofluids, including the effect of Brownian motion and using fractal geometry. The effective thermal conductivity predicted by the model is in a close agreement with experimental data thus verifying the accuracy of the model. In addition, the results showed that the effective thermal conductivity increases with the increase of the volume fraction, and that the small sized nanoparticles yielded out higher thermal conductivity than the larger nanoparticles.

Jiang et al. [83] developed a model to predict the effective thermal conductivity of nanofluids. An interfacial nano-shell between the nanoparticle and the fluid was used to derive an expression of the effective thermal conductivity of nanofluids. This analysis yielded that the thermal conductivity of the nanofluids is not only a function of the conductivities of the nanoparticles and based fluid, and their respected volume fraction, but also a function of the nanoparticle radius and the thermal conductivity and thickness of the interfacial nano-shell. The results showed that the model fits quite well when compared with experimental data, for both water and oil based nanofluids and metallic and non-metallic nanoparticles. In addition, the effect of the radius of the nanoparticle and the thickness of the nano-shell layer on the effective thermal conductivity is studied.

All the above models predict the thermal conductivity of spherical or cylindrical shape nanoparticles which is the case in a lot of nanoparticles suspended in fluids. However, when it comes to SWCNT, the shape is two dimensional and not only one: meaning that the previous models will not be able to predict the thermal conductivity accurately.

Nan et al. [84] presented a model to calculate the effective thermal conductivity of CNT-based nanofluids. The model analyzed the thermal transport behavior in heterogeneous media using the various effective medium approaches to determine the effective thermal conductivity. In addition, the model accounted for the high aspect ratio of $CNTs$ and the thermal conductivities in the axial and transverse directions. The results show that the model overestimates the enhancement of CNT-based nanofluids when compared to experimental data. In the previous model, the Kaptiza resistance was neglected which led to an over predication when compared to the experimental effective thermal conductivity. Nan et al. [85] took these considerations into account and reformulated the analytical model to include the interfacial resistance.

Xue [86] presented a simple model to calculate the effective thermal conductivity of CNT-based nanofluids. The very large axial ratio and the space distribution of $CNT's$ were considered in order to formulate the model. Also, based on the Maxwell theory, two formulas of calculating the effective thermal conductivity of CNT-based composites are given. The model showed that the dispersion of small traces of CNT can lead to a remarkable enhancement in the effective thermal conductivity. In addition, the model was applied to a CNT/Oil nanofluids and the results showed reasonable agreement with the experimental data; the model did however overestimate the effective thermal conductivity.

Patel et al. [87] presented a model to calculate the effective thermal conductivity of CNT-based nanofluids. The model predicts the thermal behavior of oil and water based $CNTs$, accounting for the novelty of this model. The model considers two paths for heat flow in the CNT nanofluid; one through the base fluid, and the other through the $CNTs$ particles. Two continuous media were considered in the analysis, since the paths were assumed to be parallel. The predicted effective thermal conductivity calculated

using the model was compared to experimental data, and the Hamilton-Crosser model. It was found that the present model overestimates the thermal conductivity enhancement of both oil and water based CNT nanofluids. In addition, the model correctly predicted the linear variation of the thermal conductivity of CNT nanofluids with volume fraction.

Pasrija and Srivastava [88] formulated a model to predict the thermal conductivity of carbon nanotube nanorefrigerants based on the concept of interfacial layer. The empirical formulation presented for the interfacial layer was assuming the thermal conductivity at the inner surface to be equal to the thermal conductivity of the nanoparticles, and at the outer surface to be equal to the thermal conductivity of the base fluid. The results show that the concept of interfacial layer and the concept of convective heat transfer due to Brownian motion of the fluid particles play a major role in explaining the anomalous enhancement in thermal conductivity of the CNT-based nanofluids. Moreover, the present model predicted the enhancement of the thermal conductivity with a mean deviation of 1.5%.

2.3.1.2.2 Viscosity.

There are different models to calculate the effective viscosity of nanofluids. Starting with Einstein [89] in 1906, the model is based on the kinetic theory and it is the oldest model used to determine the viscosity of nanofluids; it is valid for spherical particles and volume fractions less than 2%.

Brinkman [90] developed a model that is used widely to calculate the viscosity of nanofluids and is valid for high particle concentrations.

Krieger [91] developed a formula for the calculation of shear viscosity for randomly monodispersed spherical particles.

Frankel and Acrivos [92] developed a mathematical expression for the calculation of the effective viscosity.

Lundgren [93] proposed an equation as a Taylor series expansion of the volume fraction. This equation is referred to as the reduction of Einstein's formula.

Batchelor [94] modified Einstein's model and included the effect of Brownian motion in the fluid. The model was developed by taking into account the isotropic suspension of rigid and spherical particles.

Graham [95] developed a generalized form of the Franken and Acrivos model by introducing the effect of the particle radius and inter-particle spacing. The model is well in accordance with Einstein's formula for small volume fraction.

Kitano et al. [96] proposed a formula to calculate the viscosity of a two phase mixture.

Pak and Cho [97] developed a viscosity model based on the particle volume fraction taken at room temperature as a reference.

Avsec and Oblac [98] derived a viscosity model with the help of the represented formula of Ward and the Einstein model. The model is also known as the renewed ward model.

Nguyen et al. [99] derived an expression of a temperature-dependent viscosity model for particle volume fractions of 1% to 4%.

All the previous literature regarding the thermophysical properties of the nanofluids, whether analytical or experimental, shows the wide range of applications that can be improved by using nanofluids. This thesis aims to study the different models provided by the literature, and to select the most suitable model for the thermal conductivity and viscosity, in order to optimize the thermophysical properties of the nanofluids to be used as a heating fluid in the PTSC/TES integrated system. Moreover, the conventional heating fluids for solar applications are used as the base fluids, which is a contribution towards the research of using nanofluids in solar applications as most of the fluids used in the experimental studies are water or EG.

2.3.2 Heat transfer characteristics and heat transfer coefficient enhancements.

In order to implement the use of nanofluids in PTSC, the effect of the enhancement of the thermophysical properties on the convective heat transfer coefficient is to be studied. Hence, the increase in the heat transfer coefficient will cause an increase

in the amount of the heat captured inside the PTSC receiver, which increases or which results in increasing the output parameters of the PTSC. This section shows experimental and analytical literature done to study the effect of nanofluids on the convective heat transfer.

2.3.2.1 Experimental studies on heat transfer characteristics.

Pak and Cho [97] performed experiments on turbulent heat transfer performance for Al_2O_3/water and TiO_2/water nanofluids and measured that the heat transfer coefficient of the nanofluid at volume fraction of 0.03% is 12% less than that of pure water.

Tsai et al. [100], [101] investigated the thermal resistance of a disk shaped heat pipe with Au/water nanofluids. It was concluded that the presence of Au dramatically decreases the thermal resistance to values of 0.17-0.215 K/W, giving the nanofluid the potential to replace conventional heating fluids.

Wen and Ding [102] experimentally studied the convective heat transfer of Al_2O_3/water nanofluids in a copper tube in the laminar region. It was concluded that adding Al_2O_3nanoparticles enhanced the heat transfer coefficient, and that enhancement increases with the volume fraction and Reynolds number, but decreases with the axial distance.

Xuan and Li [103] investigated experimentally the effect of adding 2% volume fraction Cu nanoparticles to water on the Nusselt number. The study was done on a laminar flow in a small hydraulic diameter flat tube, and a 39% enhancement of the Nusselt number was measured. In addition, the effect of the volume fraction was analyzed, and it was provided that by increasing the volume fraction from 0.5% to 2%, the Nusselt enhancement ratio increased from 1.06 to 1.39.

Zeinali Heris et al. [104] carried experimental analysis with Al_2O_3 and CuO nanoparticles in water under laminar flow and up to turbulence. The results showed that the heat transfer was enhanced to more than 40% for Al_2O_3 particles with thermal conductivity enhancement of 15%.

Yang et al. [105] studied the enhancement of the convective heat transfer of graphite nanofluid flowing through a circular tube in the laminar region. Disk shaped graphite nanoparticles were used in the analysis, and the results showed that the enhancement in the convective heat transfer coefficient is less than the enhancement in the thermal conductivity. It was determined that the particle shape and size play a major role in the enhancement of the heat transfer coefficient.

Lai et al. [106] studied experimentally the flow behavior of Al_2O_3/water nanofluids flowing in the laminar region through a millimeter sized stainless steel tube subjected to a constant heat flux. It was provided that the maximum enhancement in the Nusselt number was 8% at a volume fraction of 1%.

Ding et al. [107] experimentally investigated the heat transfer behavior of aqueous suspensions of multi-walled carbon nanotubes flowing through a horizontal tube. The enhancement of the heat transfer characteristics depended on the flow condition, the $MWCNT$ concentration and to some extent the pH level. It was concluded that the enhancement of the heat transfer coefficient is a function of the axial distance from the inlet to the test section. The enhancement increases at first reaching a maximum value then decreases with the increase of the axial distance. Regarding the maximum enhancement, it was around 350% for a Reynolds number of 800 and 0.5 wt. %, which took place at an axial distance of 110 times the tube diameter.

Zeinali Heris et al. [108] experimentally investigated the convictive heat transfer of Al_2O_3/water nanofluids in the laminar region flowing through a tube subject to a constant wall temperature. It was shown that the heat transfer coefficient increases with the increase of the volume fraction, and the maximum enhancement was 22%.

Anoop et al. [109] experimentally investigated the convective heat transfer of Al_2O_3/water nanofluids in the laminar developing region of a tube subjected to a constant heat flux. The experimental results showed that for both a 45 nm and 150 nm nanoparticles sizes, the heat transfer coefficient in the developing region is higher than that of the base fluid, but the nanoparticles of size 45 nm showed a higher enhancement compared to the 150 nm ones.

Hojjat et al. [110] experimentally investigated the forced convective heat transfer of nanofluids through a uniformly heated circular tube under turbulent flow conditions. The nanoparticles used in the experiment were $Al_2O_3, CuO\ and\ TiO_2$, and were all dispersed in an aqueous solution of carboxymethyl Cellulose (CMC). The experimental results reveal that the local and average heat transfer coefficients of the nanofluids are larger than the base fluid, and that the enhancement of the heat transfer coefficient increases with the increase in the volume fraction. In addition, for a given nanoparticle concentration and Peclet number, the local heat transfer coefficient of the base fluid and the nanofluids decreases with the axial distance from the tube inlet. Finally a new correlation is proposed to predict the Nusselt number of non-Newtonian nanofluids as a function of the Reynolds and Prandtl numbers.

Cárdenas Gómez et al. [111] experimentally evaluated the thermal- hydraulic performance of CNT nanoparticles dispersed in water in single-phase flow in a horizontal tube. Moreover, the heat transfer coefficient and pressure drop were determined for turbulent and transition phase flow. The experimental results showed that the heat transfer coefficient as a function of the Reynolds number showed an increase of 30% compared to water for a CNT volume fraction of 0.5%. Further, nanofluids experienced pressure drops between 5% and 8.7% greater than that of the base fluid.

Sun et al. [112] experimentally analyzed the flow and convective heat transfer characteristics of Fe_2O_3/water nanofluids inside inner-grooved copper and smooth copper tubes. Different dispersants were added to improve the stability of nanofluids with volume fractions of 0.1% to 0.4%. The experimental results showed that the dispersants enhance the stability of the nanofluids significantly, especially when sodium dodecyl benzene sulfonate (SDBS) was used. Moreover, the convective heat transfer performance was better in the inner-grooved copper tube when compared to the smooth copper tube. Further, the increase in the mass fraction of the nanoparticles enhances the pressure and the value of the convective heat transfer coefficient.

Mehrali et al. [113] experimentally investigated the heat transfer coefficient and entropy generation of graphenenanoplatelets (GNP) nanofluids under laminar forced convection conditions inside a circular stainless steel tube subjected to constant wall heat

flux. The experimental results showed that the thermal conductivity of GNP is 12% to 28% higher when compared to the base fluid. Moreover, the convective heat transfer coefficient was found to be 15% higher than that of the base fluid. Further and for a constant velocity flow, the entropy generation was found to be less than that of the base fluid and that the entropy generation decreases with the increase in velocity. Finally, it was demonstrated that GNP nanofluids with concentrations of 0.075 wt. % and 0.1 wt. % is more energy efficient compared to other concentrations.

Venkatachalapathy et al. [114] carried an experimental study to analyze the thermal performance of a cylindrical mesh wick heat pipe using CuO/water nanofluids. The studies were done by varying the heat pipe inclination angle and heat input. The experimental results show that the thermal resistance is reduced by 23.83% and 10.43% respectively for 1 wt. % and 1.5 wt. % of CuO in water. Further, the maximum enhancement in the evaporation and condensation heat transfer coefficient is 30.5% and 23.54% respectively for an optimum tilt angle of 60°.

2.3.2.2 Analytical studies on heat transfer characteristics.

Roy et al. [115] numerically studied the heat transfer of Al_2O_3/water nanofluids in a radial cooling system. It was concluded that the addition of Al_2O_3 nanoparticles increases the heat transfer rate considerably; a 10% volume fraction led to a two-fold increase in the heat transfer rate.

Maïga et al. [116] provided a solution for the forced convection of nanofluids flowing in a tube under constant and uniform heat flux. The analysis was done for Al_2O_3/water and Al_2O_3/EG nanofluids for both laminar and turbulent flow. Thermal conductivity correlations were provided alongside viscosity, density and specific heat capacity. Maïga et al. [117] developed a numerical method to study the heat transfer enhancements in convective heat transfer using nanofluids. A uniformly heated tube with a laminar flow was considered for the analysis, with Al_2O_3/water and Al_2O_3/EG nanofluids. Two correlations for the determination of the Nusselt number for a tube flow subjected to a constant heat flux and a constant wall temperature were developed by studying the effect of the particle volume fraction and the flow Reynolds number.

Khaled and Vafai [118] studied heat transfer enhancements for fully developed laminar flow in a two dimensional channel by controlling the thermal dispersion effects inside the flow. The flow was subjected to a constant heat flux, and the energy equations were solved numerically and analytically by neglecting axial conduction. It was shown that the distribution of the dispersive elements that maximizes the heat transfer is governed by the flow and the thermal conditions.

Buongiorno [119] considered seven slip mechanisms that can produce a relative velocity between the nanoparticles and the base fluid to test the assumption that the increase of the heat transfer coefficient is generally attributed to thermal dispersion and intensified turbulences. Those seven mechanisms were: Inertia, Brownian diffusion, thermophoresis, diffusiophoresis, Magnus effect, fluid drainage and gravity. The results showed that only Brownian diffusion and thermophoresis are considered to be important slip mechanisms in nanofluids. Based on these findings, an explanation for the abnormal heat transfer coefficient increase is proposed, which states that the nanofluids properties may vary significantly within the boundary layer because of the effect of the temperature gradient and thermophoresis. Hence, for a heated fluid, this effect can decrease the viscosity significantly leading to the increase of the heat transfer coefficient.

Maïga et al. [120] studied the heat transfer enhancement of turbulent flow in a tube subjected to a constant heat flux. After considering the effect of the particle volume fraction of AL_2O_3/water nanofluids and solving the energy equation, a correlation for the determination of the Nusselt number is provided.

Heris et al. [121] provided a solution for the enhancement of laminar forced convection in tube subjected to a constant wall temperature. The two-phase approach was used, and the energy equations were solved. The solution agrees with experimental finding when compared for $Al_2O_3, Cu\ and\ CuO$ water based nanofluids.

Behzadmehr et al. [122] provided a solution for the prediction of turbulent forced convection of nanofluids in a tube subjected to constant wall heat flux by the use of the two-phase approach. The provided solution was compared to a single-phase solution for a

1% Cu in water, and the comparison showed that the two-phase model is more accurate than the single-phase one.

Mansour et al. [123] theoretically investigated the effect of the Maxwell and Hamilton-Crosser thermal conductivity models to predict the thermophysical properties of Al_2O_3/water nanofluids and their effect on the performance of a fully developed laminar and turbulent flow through a tube subjected to a constant heat flux. The results showed that both models predicted an increase in the heat transfer coefficient with the increase of the volume fraction.

Bianco et al. [124] numerically investigated a developing laminar forced convection flow of Al_2O_3/water nanofluid in a circular tube subjected to a constant and uniform heat flux. A single and two phase model is employed with either constant or temperature dependent properties, and for a nanoparticle size equal to 100 nm. The results show that the maximum difference in the average heat transfer coefficient between single and two phase models is about 11% for a volume fraction of 4%, and for both models the convective heat transfer coefficient is larger than that of the base fluid. In addition, it was observed that the heat transfer coefficient increases with the increase of the volume fraction and the Reynolds number, but this is accompanied by an increase of shear stress.

Ayatollahi et al. [125] analyzed the effect of adding Ag nanoparticles to water on the improvements of free convection heat transfer of a vertical plane with two kinds of boundary conditions including uniform heat flux and uniform wall temperature. Four different viscosity models were used to predict the effective viscosity of the Ag/water nanofluids. It was concluded that adding Ag nanoparticles had a positive effect on the convective heat transfer coefficient as it increases with the increase of the volume fraction up to 4%, while for the viscosity models it was shown that the Brinkman's, Einstein's and Brownian movement models all share the same trend and are in precise calculation. Regarding the Park and Cho model, it was concluded that the model is in discrepancy with the other models.

Vajjha and Das [126] carried a comprehensive analysis to study the effect of varying the density, specific heat capacity, viscosity and thermal conductivity on the performance of the nanofluids, and the convective heat transfer characteristics. Two metallic oxides Al_2O_3 and CuO, and one non-metallic oxide SiO_2dispersed in EG/Water mixture were used as nanofluids for the analysis. Different viscosity, thermal conductivity and Nusselt number models and correlations were studied, analyzed and compared based on their applicability. The results show that the addition of nanoparticles into the base fluid increases the viscosity, thermal conductivity and density while decreasing the specific heat capacity. For example, Al_2O_3-based nanofluids, compared to the EG/Water base fluid, showed a 91% increase in viscosity, a 22.4% increase in thermal conductivity, a 13.9% increase in density and a 13.2 % decrease in specific heat capacity for a volume fraction of 6% and a temperature of 293 K. Moreover, the Prandtl number of the nanofluids increases as the volume fraction increases, but it decreases with the increase in temperature, while, the Reynolds number of the nanofluids for a specified velocity increases with the increase in temperature, but decreases with the increase in volume fraction. In addition, the convective heat transfer coefficient increases with the increase in the volume fraction and temperature. For example, Al_2O_3-based nanofluids show a 31.9% increase in the heat transfer coefficient for a volume fraction of 1% only. Finally, the pumping power needed for nanofluids is less than that of the base fluid. Once again pumping power required for a 2% Al_2O_3-based nanofluid under constant heat rate is 83.3% less than that of the EG/Water base fluid.

Salman et al. [127] numerically investigated laminar convective heat transfer in a two-dimensional micro tube with 50 μm in diameter and 250 μm in length with constant heat flux. In the analysis, different nanoparticles Al_2O_3, Cuo, SiO_2 and ZnO with different diameters of 25, 45, 65 and 80 nm, and different volume fractions from 1% to 4% are all dispersed in ethylene glycol base fluid. The results show that SiO_2/EG nanofluids have the highest Nusselt number yielding the highest heat transfer coefficient, followed by ZnO/EG, CuO/EG and Al_2O_3/EG. It was also established that the Nusselt number for all nanofluids increases with the increase in the volume fraction, Reynolds number, and the decrease in the nanoparticle diameter.

Azimi and Kalbasi [128] considered the forced convective heat transfer of nanofluid in the developing laminar flow in a circular tube subjected to a constant wall temperature. The nanofluids used were Al_2O_3/water and the thermal conductivity was considered as two parts: Static and dynamic. The simulated results showed that the dynamic part of the thermal conductivity due to the Brownian motion has a negligible effect on the heat transfer coefficient, while the static part due to the nanolayer surrounding the nanoparticles has a considerable effect on the heat transfer coefficient.

Moghadassi et al. [129] presented a CFD model to study the effect of nanofluids on the laminar convective heat transfer coefficient in a circular horizontal tube. Al_2O_3 and $Al_2O_3 - Cu$ hybrid nanoparticles were added to water at a volume fraction of 0.1%, and nanoparticles size of 15 nm to carry the analysis. The solutions of the model were based on both the single- and two- phase approaches. The numerical results showed that the hybrid based nanofluids showed a higher heat transfer coefficient enhancement compared to Al_2O_3-based nanofluids and pure water, the average Nusselt number increase was around 4.73% and 13.46% compared to Al_2O_3-based nanofluids and pure water respectively. Further, the single-phase approach showed a better agreement with the experimental data.

Turkyilmazoglu [130] numerically investigated the convective heat transfer of nanofluids in circular concentric pipes under the influence of partial velocity slips on the surfaces and the resulting anomalous heat transfer enhancement. The single-phase model was employed to the fully developed laminar flow and temperature fields accounting for the thermal boundary conditions of both the inner and outer walls. The results indicate that the velocity slip enhances the rate of heat transfer from the surface of the pipes into the fluid.

Hassan and Harmand [131] studied the effect of using nanofluids on the heat transfer, liquid film thickness, and performance of a rotating heat pipe. Water was used as the base fluid with the addition of $Cu, Cuo\ and\ Al_2O_3$ nanoparticles at different volume fractions and for different nanoparticles sizes. The analysis was carried for different rotation speeds, temperature differences, and masses of the working fluid of the heat pipe. The results showed that the heat transfer by rotating pipe increases with the increase in

the temperature difference, volume fraction, radius of the nanoparticles, and the decrease in the condenser taper angle. In addition, rotating heat pipes with Cu/water nanofluids showed the highest heat transfer enhancement compared to Cuo/water and Al_2O_3/water nanofluids. The maximum heat transfer enhancement of 56% due to Cu nanoparticles happened at a temperature difference of 20℃, rotational speed of 300 rpm, a volume fraction of 0.04%, and nanoparticles size of 5 nm.

Saha and Paul [132] applied the Eulerian-Eulerian multi-phase mixture model to numerically analyze the turbulent flow and heat transfer behavior of water based Al_2O_3 and TiO_2 nanofluids in a pipe. Further, analysis of entropy generation is provided to investigate the condition that optimizes the thermal system. The results show that nanofluids with a volume fraction of 6% and nanoparticles diameter of 6 nm, display the highest thermal performance factor and minimized the entropy generation. In addition, TiO_2-based nanofluids were found to be more energy efficient coolant than Al_2O_3-based nanofluids.

Zadeh et al. [133] aimed to develop an efficient modeling of a PTSC absorber tube with non-uniform heat flux, fully developed mixed convection flow using Al_2O_3/synthetic oil nanofluids. A hybrid optimization method involving genetic algorithm and sequential quadratic programming is introduced in the optimization process. The results show that the presence of nanofluids enhances the heat transfer inside the tube, and that the heat transfer coefficient is increased with the increase in the volume fraction. Further and for a given Reynolds number, the enhancement in the heat transfer coefficient caused by nanoparticles is decreased as the operational temperature of the tube increased.

Moghaddami et al. [134] estimated the entropy generation of Al_2O_3/water and Al_2O_3/EG nanofluids flowing in a circular tube subjected to a constant heat flux under both laminar and turbulent flow. The results determined that adding nanoparticles decreases the entropy generation for any given Reynolds number in the laminar flow, however an optimum Reynolds number exists for which the entropy generation is minimized in the turbulent flow. Moreover, for the EG mixtures it was found that adding

nanoparticles at any Reynolds number increases the entropy generation, and that could be attributed to the viscous effects that are dominant in the base fluid. Finally, it was concluded that adding nanoparticles is only useful when the fluid friction contribution to entropy generation is less than the contribution of the heat transfer to the entropy generation.

Ghanbarpour and Khodabandeh [135] analytically investigated the effect of the nanofluids on different sources of entropy generation in heat pipe caused by heat transfer between hot and cold reservoirs. Moreover, the effect of the nanofluids on the frictional losses and pressure drop in the liquid and vapor flow along heat pipe is studied. Water with additives of TiO_2 and Al_2O_3 at different concentrations was chosen as the working fluids. The results showed a 3-13.5% reduction in the entropy generation in heat pipes where nanofluids are the working fluid. In addition, heat pipes with Al_2O_3-based nanofluids are found to have less entropy generation compared to TiO_2-based nanofluids.

Mwesigye and Huan [136] thermodynamically investigated a fully developed turbulent forced convection in a circular tube with Al_2O_3/water nanofluids using the entropy generation minimization method. The entropy generation rates were determined numerically from the temperature and velocity fields obtained during the CFD fluid dynamic analysis. The cross section area of the circular tube, Reynolds number and volume fractions were all varied in order to carry the analysis. The results showed that for every cross section area there is an optimal Reynolds number where the entropy generation is minimized. In addition, at every Reynolds number there is an optimum tube cross section area for which the entropy generation is minimized. The optimal cross section area increases as the Reynolds number increases.

All the preceding literature discusses the enhancement of the convective heat transfer coefficient in circular tubes and for different flow types and conditions. In this thesis, a temperature dependent model is proposed for the prediction of the convective heat transfer coefficient of nanofluids inside the PTSC absorber tube. The model is simply proposed by choosing the most suitable correlations provided in the literature for the convective heat transfer, and using the temperature dependent correlations for the calculation of the thermophysical properties of the nanofluids. The model is specifically

tailored for the calculation of the convective heat transfer coefficient of the nanofluids inside the absorber tube of the PTSC. Moreover, the effect of the volume fraction, shape and size of the nanoparticles, and the temperature on the connective heat transfer is studied.

2.3.3 Applications of nanofluids in solar energy.

The effect of using nanofluids on different output parameters of different solar energy harvesting devices is shown in the following literatures.

2.3.3.1 Direct Absorption Collector (DAC)

Tyagi et al. [137] theoretically investigated the effect of the nanoparticles volume fraction and nanoparticles size on the efficiency of a low-temperature nanofluid direct absorption solar collector. The volume fraction of Aluminum nanoparticles dispersed in water was varied from 0.1% till 5%, and the results showed that an increase in the volume fraction below 2% yields a remarkable increase in the solar collector's efficiency. However, increasing the volume fraction above 2% has no significant impact on the collector's efficiency. In addition, increasing the particle size showed a positive effect on the efficiency of the solar collector, where it increased by a small amount as the nanoparticle size increased.

He et al. [138] experimentally investigated the light-heat conversion characteristics of TiO_2/water and CNT/water nanofluids in a vacuum tube solar collector. The results showed a very good light-heat characteristics for the CNT/water nanofluids with a concentration of 0.5% only. In addition, the CNT/water nanofluids showed a better light-heat characteristics compared to TiO_2/water nanofluids, therefore, yielding a higher temperature making it more suitable to be utilized in a vacuum tube solar collector.

Li et al. [139] studied the effect of water based nanofluids on the performance of a tubular solar collector. A comparison was done between Al_2O_3/water, ZnO/water and MgO/water nanofluids, and it was concluded that the ZnO/water nanofluids with a volume fraction of 0.2% is the best heating fluid for the solar collector.

Taylor et al. [140] studied the optical property characterization of different nanofluids to test their potential as heating fluid in a direct absorption solar collector. Graphite, Silver, Copper, Gold and Aluminum nanoparticles were dispersed in both water and Therminol VP1. The results showed that over 95% of the incoming sunlight can be absorbed with a very low volume fraction of 10 ppm.

Otanicar and Golden [141] carried a comparative analysis between a conventional and a nanofluid based solar collector in terms of the environmental and economic aspects. The economic analysis showed that for the nanofluid based solar collector, the capital and maintenance cost are more by 120$ and 20$ respectively. However, due to the higher efficiency and annual solar fraction of the nanofluid based solar collector, the fuel cost savings per year for both electricity and natural gas are greater than that of the conventional collector. Regarding the environmental analysis, it was concluded that the nanofluid based solar collector saves up to 50 kg of CO_2emission when compared to the conventional collector.

Saidur et al. [142] analyzed the effect of water based Aluminum nanofluids on a direct solar collector. The extinction coefficient was investigated and evaluated by varying nanoparticles size and volume fraction. It was shown that Al nanoparticles have a very strong extinction coefficient at short wavelength with a peak at $0.3\mu m$, and that it can be used to enhance the light absorption ability of water at the visible and lower wavelength region despite a lower extinction coefficient at longer wavelengths. Furthermore, it was concluded that the particle diameter has no effect on the extinction coefficient but it is advised to keep it below $20\mu\, m$, in order for Rayleigh scattering to take place.

Taylor et al. [143] indicated that power tower solar collectors can benefit from efficiency improvements arising from the use of nanofluids. Theoretical analysis showed efficiency improvements up to 10% when solar concentrations are in the range of 100-1000. Further analysis showed that Graphite nanofluids with volume fractions on the order of 0.001% are suitable for 10-100MW power plants. The findings are used to compare the energy and revenue generated in a conventional solar thermal plant to a nanofluid-based one. It is found that a 100 MW capacity solar thermal power tower

operating in a solar resource similar to Tucson, AZ, could generate around 3.5$ million more per year by incorporating a nanofluid receiver.

Ladjevardi et al. [144] investigated the application of nanofluids in direct absorption of solar radiation in a volumetric solar collector. The efficiency of the solar receiver's impacts on the harvested solar energy, irradiation spectrum distribution and irradiation energy level versus the depth of the flow was studied with the variation of the diameter and volume fractions of Graphite nanoparticles. Results showed that with only a volume fraction of 0.000025% of graphite in water, it will be possible to absorb more than 50% of incident irradiation energy by a cost increase of 0.0045$/L.

Otanicar et al. [145] reported experimental results on a solar collector based on nanofluids made out of a variety of nanoparticles (Carbon Nanotubes, Graphite, and Silver). Results demonstrated efficiency improvements up to 5% in the solar thermal collector. The experimental and numerical results demonstrated an initial rapid increase in the efficiency with the increase in the volume fraction, followed by a leveling off in efficiency as volume fractions increase. Figure 1 shows the variation of the volume fraction on the efficiency of the collector with respect to different nanofluids.

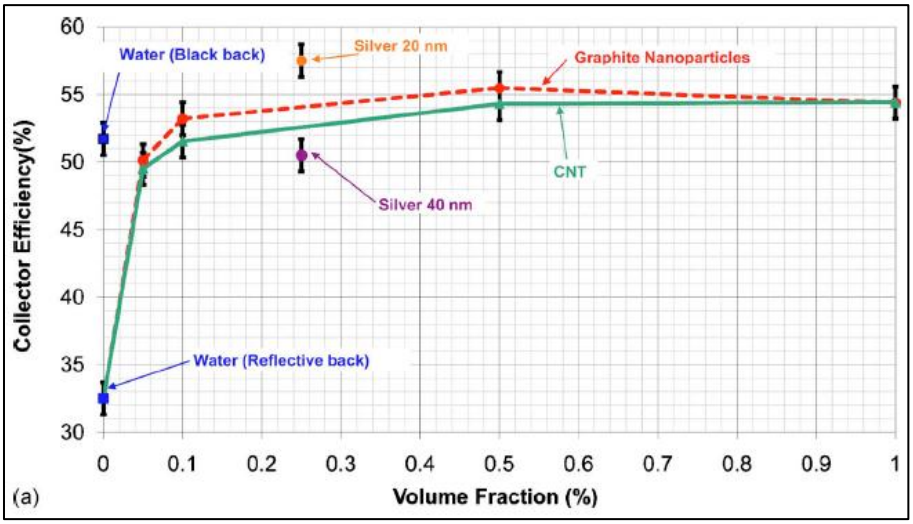

Figure 1: Effect of the volume fraction on the efficiency for different nanofluids [145]

Khullar et al. [146] attempted to introduce the idea of harvesting solar radiant energy through the use of nanofluid-based concentrating parabolic solar collector

(NCPSC). The NCPSC was modeled mathematically, and the governing equations were solved using finite difference method. Figure 2 shows the difference between a conventional parabolic collector and a NCPSCS. The results showed that the NCPSC has about 5-10% higher efficiency as compared to the conventional parabolic solar collector. The theoretical results indicate that the NSPSC has the potential to harness solar radiant energy more efficiently than a conventional parabolic solar collector.

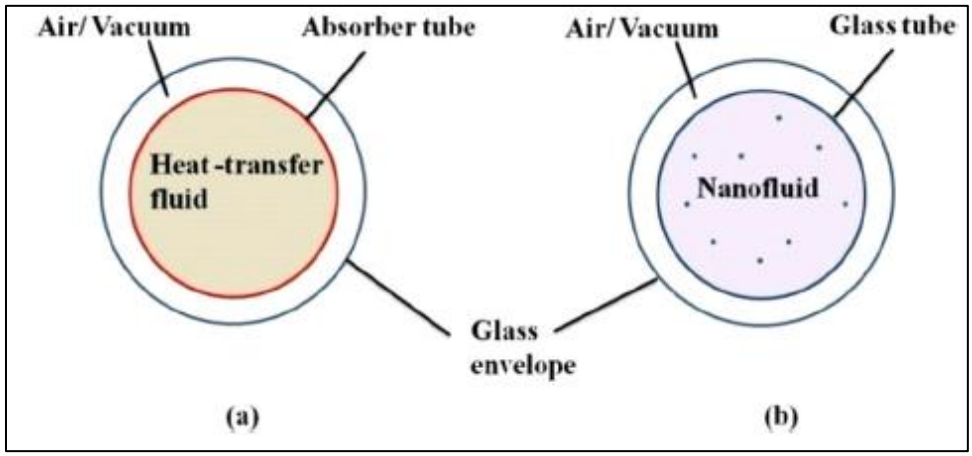

Figure 2: Difference between a PSC and NSPSC [146]

Karami et al. [147] introduced alkaline functionalized Carbon Nanotubes ($f-CNT$) nanoparticles in water, as a working fluid in a direct absorption solar collector. Dispersion stability and optical properties of the nanofluids were estimated. The relative stability of the prepared nanofluids versus the sediment time was confirmed by the spectral absorbance analysis. The extinction coefficient of the $f-CNT$ shows remarkable improvements compared to the base fluid even at low particle readings. Moreover, thermal conductivity improvements up to 32% were demonstrated only by adding 150 ppm of $f-CNT$ to water.

Mercatelli et al. [148] investigated the scattering and absorption properties of nanofluids consisting of Single Walled Carbon Nanohorns in aqueous suspension. The characteristics of these fluids were analyzed in order to use them in direct absorption solar collectors. The investigation was carried out for nanohorns of different morphologies and for suspension prepared with different amounts of surfactant. The results showed that the obtained values of the scattering albedo were always lower than

0.05; indicating that the amount of light directly absorbed was as high as 95%. In addition, the values of scattering albedo decreased with increasing the wavelength, meaning that the value of the absorbed light increases with the increase of the wavelength.

Paul et al. [149] prepared nanoparticles enhanced Ionic Liquid (NEILs) by dispersing 0.5% Al_2O_3nanoparticle (Whiskers and Spherical) in ionic liquid. Viscosity, heat capacity and thermal conductivity of NEILs were measured experimentally and compared to theoretical models. Results demonstrated that the thermal conductivity of NEILs was enhanced by 3% for spherical and 5% for whiskers, heat capacity enhanced by 14% for spherical and 20% for whiskers. In addition, viscosity of the NEILs showed higher values compared to the base IL within investigated temperature range. Further, the heat transfer coefficient of NEIL is enhanced compared to IL; this enhancement is mainly due to the enhancement in the thermal conductivity and particle migration behavior in the boundary layer.

Khullar and Tyagi [150] examined the potential of the nanofluid-based concentrating solar water heating system (NCSWHS) as an alternative to systems based on fossil fuels. The analysis revealed that a considerable emission reduction of about 2200 kg of CO_2/household/year if fuel savings can be achieved if the NCSWHS are adopted.

2.3.3.2 Flat Plate Solar Collector (FPSC)

Yousefi et al. [151] experimentally investigated the effect of Al_2O_3/water nanofluids on the efficiency of a flat plate solar collector. The experiment was done by varying the weight fraction of the nanoparticles from 0.2% to 0.4%, and the mass flow rate of the nanofluids. The nanofluids were prepared by the researchers and surfactant was used to create a stable and homogenous mixture. The results show that with using 0.2 wt. % nanoparticles, the efficiency of the plate increased by 28.3 %. Moreover, the use of the surfactant enhances the heat transfer characteristics. The authors [152] also experimentally investigated the effect of $MWCNT$/Water nanofluids on the efficiency of a flat plate solar collector. The experiment was also done by varying the weight fraction of the nanoparticles from 0.2% to 0.4%, and the mass flow rate of the nanofluids. In

addition, surfactant was added. The results showed that using the 0.2 wt. % $MWCNT$-based nanofluid without surfactant decreases the efficiency, and that the presence of the surfactant causes an increase in the efficiency. However, in the case of the 0.4 wt. % the efficiency increases without the use of the surfactant.

Said et al. [153] carried a theoretical analysis on the entropy generation, heat transfer enhancement capabilities and pressure drop for a flat-plate solar collector operated with $SWCNT$ based nanofluids as the absorbing medium. The analysis results showed that the thermal properties of $SWCNT$-based nanofluids is better than that of metal or metal oxide based nanofluids, leading to a higher increase in the convective heat transfer coefficient compared to conventional fluids at the same Reynolds number. Moreover, the analytical outcome revealed the $SWCNT$/water nanofluids reduce the entropy generation by 4.34% and enhance the heat transfer coefficient by 15.33% compared to water. However, using the nanofluid leads to a pumping power penalty of 1.2%.

Alim et al. [154] analyzed theoretically the entropy generation, heat transfer enhancement capabilities and pressure drop of an absorbing medium with suspended nanoparticles ($Al_2O_3, CuO, SiO_2, TiO_2$) dispersed in water inside a flat plate solar collector. It was concluded that the dispersed nanoparticles improve the heat transfer phenomena and that with increasing the nanoparticles volume percentage, the heat transfer features improved. Analytical results showed that the CuO-bases nanofluids could reduce the entropy generation by 4.34% and enhance the heat transfer coefficient by 22.15% theoretically compared to water as an absorbing fluid, however it had a pumping power penalty of 1.58%. Moreover, it was established thatCuO-based nanofluids might be a good option in laminar flow condition.

2.3.3.3 Parabolic Trough Solar Collector (PTSC)

Sokhansefat et al. [155] numerically studied a three dimensional fully developed turbulent mixed convection heat transfer of Al_2O_3/Syltherm 800 nanofluids in a tube of a parabolic trough solar collector. The effect of Al_2O_3 nanoparticles volume fraction on the rate of the heat transfer from the absorber tube was also investigated. The results display that nanoparticles enhance the heat transfer coefficient of the working fluid, and that it is increased by increasing the concentration of the nanoparticles in the base fluid.

Moreover, for a given Reynolds's number the enhancement in the heat transfer coefficient decreases as the operational temperature of the absorber tube is increased.

Khullar and Tyagi [156] mathematically modeled the heat transfer and flow aspects of a Al/water nanofluids in a linear parabolic solar collector. The collector has been modeled as a two dimensional steady state system, and the equations were solved by using the finite difference method. A comparison between a conventional collector and a nanofluid based collector was done. The results show that the nanofluid based collector performs better than the conventional one even for small volume fractions (1%). By dispersing Aluminum nanoparticles into water, the optical efficiency increased by almost 60%, while thermal efficiency increased by almost 55%.

de Risi et al. [157] proposed and investigated the possibility of using gas-based nanofluids in a transparent parabolic trough collector. Transparent receivers combined with gas-based nanofluids were found to be able to directly absorb solar radiation due to very high total surface area of the nanoparticles. The gas used is Nitrogen with a mixture of CuO and Ni nanoparticles. Numerical results showed that the maximum solar to thermal efficiency was 62.5% for an outlet temperature of 650℃ and a volume fraction of 0.3%. Moreover, it was established that the gas-based nanofluid can be an effective alternative to conventional systems, such as molten salt and synthetic oil.

Kasaeian et al. [158] designed and manufactured a pilot trough collector with a width of 0.7 m, a reflector height of 2 m and a new shape design of the receiver coupling. The transient response time and the optical and thermal performances of the collector were compared using different types of receivers: a blacked painted vacuumed steel tube, a copper bare tube with black chrome coating, a glass enveloped non-evacuated copper tube with black chrome coating, and a vacuumed copper tube with black coating. For the experimental part a 0.2% and a 0.3% CNT/oil nanofluids were prepared and tested in the pilot trough with the black chrome coated vacuumed copper absorber tube. The results show that the vacuumed absorbed tube has a higher efficiency of 11% when compared to the bare absorber tube which is due to convection losses. Moreover, with the addition of 0.2% and 0.3% CNT nanoparticles, the global efficiency of the trough collector increased by 4-5% and 5-7% respectively.

Ghasemi and Ahangar [159] studied numerically the effect of Cu/water nanofluid as the heat transfer fluid on the performance of a parabolic solar collector. In addition, the conventional parabolic collectors and the nanofluid based collectors were compared in terms of the temperature field, thermal efficiency and mean outlet temperatures. Moreover, the effect of the fluid velocity, volume fraction of nanoparticles, concentration ratio and receiver length have been studied. The results demonstrated that the nanofluid based solar collector showed a higher efficiency and temperature outlet compared to the conventional parabolic solar collector. It was concluded that by increasing the volume fraction of the nanoparticles, the performance of the solar parabolic collector are enhanced.

The previous literature, considering the use of nanofluids in a PTSC, all fail to study the magnitude of enhancement in the efficiency and power output caused by the use of nanofluids. This thesis studies the effect of using nanofluids on the efficiency and power output of a PTSC for different beam radiations, volume fractions and nanoparticles. An energy and exergy models are proposed, and the evaluation of the PTSC performance is done accordingly. The use of conventional heating fluids as a base fluid allows for a comparison between the nanofluids based PTSC and conventional PTSC's, in order to study the magnitude of enhancement.

2.3.4 Applications of nanofluids in Thermal Energy Storage.

Wu et al. [160] numerically investigated the melting processes of Cu/paraffine nanofluids PCMs. The results showed that for a concentration of only 1 wt. %, the melting time can be saved by 13.1%. Hence, the conclusion is that adding nanoparticles leads to enhancing the heat transfer in latent heat thermal energy storage systems.

Jo and Banerjee [161] investigated the enhancement of the thermal properties of various high temperature nanofluids using Carbon Nanotubes (CNT) for solar thermal energy storage applications. A eutectic mixture of Lithium Carbonate and Potassium Carbonate is used as the base fluid. Results showed that the specific heat capacities of carbonate eutectic/CNT nanofluids were linearly increased as the temperature increased, with enhancement up to 20% for a concentration of 1%. In addition, increasing the surfactant concentration from 1% to 5% resulted in a higher enhancement of the specific

heat values. Moreover, it was established that better theoretical models are required to predict thermophysical properties of nanofluids, since the models used in [161] failed to predict the enhancement of the specific heat for some cases.

Kwak et al. [162] studied the specific heat enhancement of Silicon dioxide nanoparticles dispersed in both Molten Salt and Therminol VP-1, and the applicability of such nanofluids materials for solar thermal storage applications was explored. Results showed that the sensible heat capacity of Therminol VP-1 was enhanced by 5.41% when doped in silica nanoparticles at 1% by weight, whereas, the sensible heat capacity of nanofluids containing 2.5% by weight of silica nanoparticles in alkali metal salt carbonate eutectic was enhanced by 14.59%.

Dudda and Shin [163] synthesized molten salt nanomaterials by dispersing Silica nanoparticles in selected molten salts, and evaluated the use of molten salt nanomaterials as heating fluid in CSP. The study showed that the specific heat capacity enhancements of the 5nm and 30 nm sized SiO_2 nanoparticles at 1 wt. % concentration to be in an increasing order.

Zabalegui et al. [164] experimentally investigated the use of multi walled carbon nanotubes dispersed in paraffin on the latent heat of fusion, and presented a finite element model as a method of quantifying nanofluid phase change material (PCM) energy storage system. The experimental results demonstrated that smaller diameter nanoparticle in suspension causes an increase in the magnitude of the latent heat reduction. Three possible mechanism- the interfacial liquid layering, Brownian motion and particle clustering were examined to attribute further reduction in the latent heat of fusion. Although additional research is required to discover each mechanism, experimental evidence suggests that the interfacial layering and the Brownian motion cannot explain the degree of latent heat reduction observed. Regarding the analysis of the thermal energy storage system, the thermal properties based on the modified effective medium theory and an empirical relation for latent heat of fusion were applied as model parameters to determine the energy stored and extracted over a period of time. It was shown that nanoparticles in PCMs provide no significant improvements in TES performance. The reason is that with smaller nanoparticles, the enhancement in thermal conductivity is not

significant enough to overcome the reduction in latent heat of fusion, and less energy is stored over the PCM charge period. In addition, it was concluded that since the model parameters depend on the material properties, the storage performance may vary with the variation of the nanofluids.

Wang et al. [165] experimentally investigated the thermal energy storage characteristics of Cu/H_2O nanofluids as a new PCM for cooling systems, and experimentally studied the influence of the nanoparticle agent on super cooling of water PCMs. The experimental results showed that the Cu/H_2O nanofluids have a remarkably lower supercooling degree than water PCMs, and as the mass fraction of Cu increases the freezing time of Cu/H_2O nanofluid gets lower than that of water PCMs. For instance, the super cooling degree was reduced by 20.5% and the total freezing time was lowered by 19.2% when a 0.1 wt. % of Cu nanoparticles was added to water.

Choi et al. [166] experimentally measured the thermal conductivity of PCM with carbon additives, and evaluated the effect of Poly Vinyl Pyrrolidone (PVP) as a dispersion stabilizer on the thermal conductivity of Multi-walled Carbon Nanotubes, Graphite and Graphene PCMs. The experimental results showed that the heat transfer rate enhances up to 3.35 times in the case of Graphite at a volume fraction of 5%. Finally, it was concluded that although Graphene showed the highest thermal conductivity enhancement of 21.5% at a volume fraction of 0.1%, Graphite is the most promising candidate for heat transfer enhancement of stearic acid with carbon additives.

From the previous literature, It is seen that the addition of nanoparticles in some base fluids increases the thermal energy performance, however, none of the studies studied the effect of the nanofluids on the size of the storage tanks. In this thesis, an integrated PTSC/TES system is studied and the effect of the nanofluids on the performance of the whole system is investigated, accounting for the novelty of this work. In addition, the effect of the nanofluids on the volume of the storage tanks is evaluated, as well as the effect of nanofluids on different modes of operation and different storage periods for the PTSC/TES integrated system.

Chapter 3: System Configurations and Modeling

In order to assess the feasibility and possibility of using nanofluids as a heating fluid in an integrated PTSC/TES system, the thermophysical properties, heat transfer parameters and PTSC outputs are to be studied and analyzed. In this following section, the modeling equations and correlations used for the calculation of the thermophysical properties and different parameters of the nanofluids are shown. Moreover, the equations for the calculation of the convective heat transfer coefficient are presented, as well as the modeling equations of the PTSC. Further, the configurations of the integrated PTSC/TES systems are provided.

3.1 Nanofluids Modeling

First the correlations for the thermophysical properties of the nanoparticles are provided, along with the correlations of the properties of the base fluids. Second, different models for the prediction of the specific heat capacity, density, viscosity and thermal conductivity of the nanofluids are presented and discussed based on their applicability and accuracy.

3.1.1 Base fluids.

The heating fluids used in the PTSC have a major impact on the efficiency and power output of the system. Synesthetic oil and molten salts are commonly used in the industry as heating fluid. In this analysis Therminol VP-1 and Syltherm 800 are considered as the heating fluid for the PTSC system.

3.1.1.1 Therminol-VP1.

Therminol VP-1 is an ultra-high temperature synthetic heat transfer fluid that can work in both liquid and vapor phase. It is widely used in parabolic solar collectors because of its low viscosity and high operating temperatures (up to 400℃). The following equations provide the correlations for the density, specific heat capacity, thermal conductivity and viscosity of Therminol-VP1, and they are obtained from [167].

$$\rho = 0.90797T + 0.00078116T^2 - 2.36 * 10^{-6}T^3 + 1083.25 \quad (3.1)$$

$$C_p = 0.002414T + 5.9591 * 10^{-6}T^2 - 2.9879 * 10^{-8}T^3 + 1.498 \quad (3.2)$$

$$k = -8.19477 * 10^{-5}T - 1.92257 * 10^{-7}T^2 + 2.5034 * 10^{-11}T^3 + 0.137743 \quad (3.3)$$

$$\nu = e^{(\frac{544.149}{T+114.43} - 2.59578)} \quad (3.4)$$

3.1.1.2 Syltherm 800.

"Syltherm 800 is a highly stable, long lasting silicone fluid designed specifically for liquid phase operation" [168]. It can sustain high temperatures up to 400℃. The following equations provide the correlations for the density, specific heat capacity, thermal conductivity and viscosity of Syltherm 800, and they are obtained from [168].

$$\rho = -6.061657 * 10^{-4}T^2 - 4.1535 * 10^{-1}T + 1.1057 * 10^{-3} \quad (3.5)$$

$$C_p = 0.001708T + 1.107798 \quad (3.6)$$

$$k = -5.7535 * 10^{-10}T^2 - 1.875266 * 10^{-4}T + 1.9002 * 10^{-1} \quad (3.7)$$

$$\mu = 6.67 * 10^{-7}T^4 - 1.56 * 10^{-3}T^3 + 1.38T^2 - 5.541 * 10^2T + 8.848 * 10^4 \quad (3.8)$$

where $283\ K \leq T \leq 673\ K$ and $373\ K \leq T \leq 673\ K$ for equation (3.8).

3.1.2 Nanoparticles.

The addition of the nanoparticles is one of the main research topics in this thesis; therefore, the thermophysical properties of the nanoparticles, such as the density, specific heat capacity, and most importantly thermal conductivity are to be calculated in order to predict the behavior and thermophysical properties of the nanofluids. Since the heat transfer coefficient is to be increased in order to enhance the heat transfer characteristics of the base fluids, metallic nanoparticles are selected because of the relatively high thermal conductivity of metals. However, non-metallic nanoparticles and especially $SWCNT$ are selected because of their extraordinary high thermal conductivity. The properties of the nanoparticles are obtained for different temperatures, since all of the thermophysical properties are temperature dependent. The nanoparticles are divided into two categories: metallic and non-metallic.

3.1.2.1 Metallic nanoparticles.

Two metallic nanoparticles are used in the analysis: Copper (Cu) and Alumina (Al_2O_3).

3.1.2.1.1 Copper.

Copper is a metallic chemical element with a very high thermal and electrical conductivity. It is used in different applications as nanoparticles, especially with water as a base fluid. The only disadvantage of using Cu nanoparticles is the process of preparing them, as it is quite hard and costly to not oxidize the metal while preparing it. The following equations present the density, specific heat capacity and thermal conductivity of copper and are obtained from [169].

$$\rho = 8933 \tag{3.9}$$

$$C_p = 316.21 + 0.3177T - 3.4936 * 10^{-4}T^2 + 1.667 * 10^{-7}T^3 \tag{3.10}$$

$$k = 420.75 - 6.8493 * 10^{-2}T \tag{3.11}$$

3.1.2.1.2 Alumina.

Alumina or Aluminum Oxide (Al_2O_3), is a chemical compound of Aluminum and Oxygen. It is metallic, has a relatively high thermal conductivity, and a very high melting point (around 2072℃). Since the Aluminum is oxidized, the preparation method is fairly simple. The following equations present the density, specific heat capacity and thermal conductivity of Alumina and are obtained from [155].

$$\rho = 3850 \tag{3.12}$$

$$C_p = 1.046 + 1.74 * 10^{-4}T - 2.79 * 10^{4}T^{-2} \tag{3.13}$$

$$k = 5.5 + 34.5e^{(-0.0033*(T-273))} \tag{3.14}$$

3.1.2.2 Non-metallic nanoparticles.

One non-metallic nanoparticle was used in this analysis, which is: Single Walled Carbon Nanotubes ($SWCNT$).

3.1.2.2.1 Single Walled Carbon Nanotubes.

Carbon nanotubes are cylindrical shaped allotropes of carbon with a length-to-diameter ratio of around 132,000,000:1 in general. Single walled carbon nanotubes have recently been used in solar technologies because of their extraordinary high thermal conductivity. They are available in the market, but they are costly compared to other nanoparticles. The following equations provide the correlations of the density, specific heat capacity which are obtained from [153] and [128] respectively, and thermal conductivity obtained from [45].

$$\rho = 1400 \tag{3.15}$$

$$C_p = 1.38 \tag{3.16}$$

$$k = \left[3.7 * 10^{-7}T + 9.7 * 10^{-10}T^2 + 9.3\left(1 + \frac{0.5}{l_s}\right)T^{-2}\right]^{-1} \tag{3.17}$$

where l_s is the length of the $SWCNT$ in micrometers, and T is the temperature in K.

The thermophysical properties of the base fluids and nanoparticles at room temperature are shown in Table 4. It is seen that the thermal conductivity of $SWCNT$ is the highest among other nanoparticles ($l_s = 1.5\mu m$), and the viscosity of Syltherm is more than two times the viscosity of Therminol.

Table 4: Thermophysical properties of the base fluids and nanoparticles

Parameter	Temperature	ρ	C_p	k	μ
Unit	℃	kg/m^3	kJ/kgK	W/mK	$mPa \cdot s$
Therminol VP-1	25	1061	1.5605	0.1355	3.91
Syltherm	25	936	1.6168	0.1341	9.1
Al_2O_3	25	3850	0.38	37	-
Cu	25	8933	0.78	400	-
$SWCNT$	25	1400	1.38	2976	-

3.1.3 Density of nanofluids.

The density of the nanofluids can be calculated based on the assumption that the nanoparticles and the base fluid form a homogenous, thermodynamically stable fluid. The

model used assumes an equilibrium state between the particles and the fluid; it is obtained from [155] and it is as follows:

$$\rho_{nf} = \rho_f(1-\varphi) - \rho_p\varphi \tag{3.18}$$

Where the subscripts f and p stand for fluid and nanoparticle respectively, and φ is the volume fraction which is the concentration of the nanoparticles in the nanofluid.

3.1.4 Specific heat capacity of nanofluids.

The specific heat capacity of the nanofluids can be calculated using two different models. The first is the same as the density assumes an equilibrium state of a homogeneous, thermodynamically stable fluid consisting of the base fluid and the nanoparticles. The model is obtained from [155] and it is as follows:

$$C_{p_{nf}} = C_{p_f}(1-\varphi) - C_{p_p}\varphi \tag{3.19}$$

The second model is based on the balance of the density and the specific heat capacity of the nanoparticles, base fluids and nanofluids. It is most widely used in the predication of entropy generation models; it is also obtained from [155] and it is as follows:

$$C_{p_{nf}} = \frac{\rho_f C_{p_f}(1-\varphi) - \rho_p C_{p_p}\varphi}{\rho_{nf}} \tag{3.20}$$

For the purpose of this analysis and for simplicity, Equation (3.19) is used for the calculation of the specific heat capacity of nanofluids.

3.1.5 Viscosity of the nanofluids.

There are different models to calculate the effective viscosity of the nanofluids. Starting with the Einstein model [89], the model is based on the kinetic theory and it is the oldest model used to determine the viscosity of nanofluids; it is valid for spherical particles and volume fractions which are less than 2%. The model is represented below:

$$\mu_{nf} = \mu_f(1+2.5\varphi) \tag{3.21}$$

Brinkman [90] developed a model that is used widely to calculate the viscosity of nanofluids and is valid for high particle concentrations, and it is given below:

$$\mu_{nf} = \frac{\mu_f}{(1-\varphi)^{2.5}} \tag{3.22}$$

Krieger and Dougherty [91] developed a formula for the calculation of shear viscosity for randomly monodispersed spherical particles, the formula is as follows:

$$\mu_{nf} = \mu_f \left[1 - \frac{\varphi}{\varphi_m}\right]^{-\eta\varphi_m} \tag{3.23}$$

where φ_m is the maximum particle packing factor. It varies from 0.495 to 0.54, and η is the intrinsic viscosity and its value is 2.5.

Franken and Acrivos [92] developed a mathematical expression for the calculation of the effective viscosity described below:

$$\mu_{nf} = \mu_f \frac{9}{8}\left[\frac{\left(\frac{\varphi}{\varphi_m}\right)^{\frac{1}{3}}}{\frac{(\varphi_m-\varphi)^{\frac{1}{3}}}{\varphi_m^{\frac{1}{3}}}}\right] \tag{3.24}$$

Lundgren [93] proposed an equation as a Taylor series expansion of the volume fractionφ. This equation is referred to as the reduction of Einstein's formula [65], and it is as follows:

$$\mu_{nf} = \mu_f \left[1 + 2.5\varphi + \frac{25}{4}\varphi^2 + f(\varphi^3)\right] \tag{3.25}$$

Batchelor [94] modified Einstein's model and included the effect of the Brownian motion in the fluid. The model was developed by taking into account the isotropic suspension of rigid and spherical particles. The model is as follows:

$$\mu_{nf} = \mu_f(1 + 2.5\varphi + 6.5\varphi^2) \tag{3.26}$$

Graham [95] developed a generalized form of the Franken and Acrivos model by introducing the effect of the particle radius and inter-particle spacing. The model is well in accordance with Einstein's formula for small volume fractions; it is as follows:

$$\mu_{nf} = \mu_f \left(1 + 2.5\varphi + 4.5 \left[\frac{1}{\left(\frac{h}{d_p}\left(2+\frac{h}{d_p}\right)\right)\left(1+\frac{h}{d_p}\right)^2} \right] \right) \quad (3.27)$$

Kitano et al. [96] proposed a formula to calculate the viscosity of a two- phase mixture; the formula is as follows:

$$\mu_{nf} = \frac{\mu_f}{\left[1-\left(\frac{\varphi}{\varphi_m}\right)\right]^2} \quad (3.28)$$

Pak and Cho [97] developed a viscosity model based on the particle volume fraction taken at room temperature as a reference, the model is given as:

$$\mu_{nf} = \mu_f(1 + 39.11\varphi + 533.9\varphi^2) \quad (3.29)$$

Avsec and Oblac [98] derived a viscosity model with the help of the represented formula of Ward and the Einstein model. The model is also known as the renewed ward model; it is given by:

$$\mu_{nf} = \mu_f[\, 1 + 2.5\left(\varphi_{eff} + 2.5\varphi_{eff} + 2.5\varphi_{eff}^2\right) \,] \quad (3.30)$$

where φ_{eff} is the effective volume fraction and can be calculated by using the following equation:

$$\varphi_{eff} = \varphi\left(1 + \frac{\gamma}{r_p}\right)^3 \quad (3.31)$$

where $\gamma \; and \; r_p$ represent the nanolayer thickness and nanoparticle radius respectively.

Nguyen et al. [99] derived an expression of a temperature-dependent viscosity model for particle volume fractions of 1-4%, and it is presented below:

$$\mu_{nf} = \mu_f(2.1275 - 0.0215T + 0.00027T^2) \quad (3.32)$$

3.1.6 Thermal Conductivity of the nanofluids.

Thermal Conductivity is the most critical property for analyzing the heat transfer of nanofluids. Different models are presented in the literature and discussed in this section, starting with the Maxwell model [67], it is the oldest model used to calculate the

thermal conductivity of solid-liquid mixtures; it is used for spherical particles and for a volume fraction φless than 1%; the model is as follows:

$$k_{nf} = k_f \frac{k_p+2k_f+2\varphi(k_p-k_f)}{k_p+2k_f-\varphi(k_p-k_f)} \tag{3.33}$$

Bruggeman [68] considered the interaction between spherical particles and presented a model for the prediction of the thermal conductivity of nanofluids, which is as follows:

$$k_{nf} = k_f \frac{(3\varphi-1)\frac{k_p}{k_f}+\{3(1-\varphi)-1\}+\sqrt{\Delta}}{4} \tag{3.34}$$

where $\Delta = [(3\varphi - 1)\frac{k_p}{k_f} + \{3(1-\varphi)-1\}]^2 + 8\frac{k_p}{k_f}$ (3.35)

Hamilton and Crosser [69] modified the Maxwell model by introducing an empirical shape factor n to account for different particles shapes. The model is valid for all the shapes by accounting for their sphericity $\emptyset$. Sphericity is a measure of how round an object is; it is the ratio of the surface area of a sphere to the surface area of the particle provided that they share the same volume.

$$\emptyset = \frac{\pi^{\frac{1}{3}}(6V_p)^{\frac{2}{3}}}{A_p} \tag{3.36}$$

where $V_p$and A_p are the particle's volume and surface area, respectively.

The model is as follows:

$$k_{nf} = k_f \frac{k_p+(n-1)k_f+(n-1)\varphi(k_p-k_f)}{k_p+(n-1)k_f-\varphi(k_p-k_f)} \tag{3.37}$$

where n=$\frac{3}{\emptyset}$, and the sphericity is 1 and 0.5 for spherical and cylindrical particles respectively.

Jeffery [70] considered a composite material of infinite range, and imposed an undistributed linear temperature field on it. The analysis was applied to spherical

inclusions and the model for the prediction of the effective thermal conductivity is as follows:

$$k_{nf} = k_f[1 + 3b\varphi + \left(3b^2 + \frac{3b^2}{4} + \frac{9b^3}{16}\frac{1+2\alpha}{2+3\alpha} + \frac{3b^4}{2^6}\right)\varphi^2 \quad (3.38)$$

where, $b = \frac{(1-\alpha)}{(1+2\alpha)}$ and$\alpha = k_f/k_p$.

Yamada and Ota [71] proposed a predictive model for calculating the effective thermal conductivity of nanofluids. The model accounts for spherical and cylindrical shaped nanoparticles, and it is as follows:

$$k_{nf} = k_f\left[\frac{1+2\alpha\varphi^{-0.2}+2(1-\alpha)\varphi^{0.8}}{1+2\alpha\varphi^{-0.2}-(1-\alpha)\varphi}\right] \quad (3.39)$$

Davis [72] updated Jeffery's model by adding the ensemble-averaged dipole strength of a single fixed sphere, and by using a decaying temperature field. Those modifications resulted in encountering only convergent integrals, and removing the renormalization factor as it is no longer needed. The model is as follows:

$$k_{nf} = k_f\left\{1 + \frac{3(1-\alpha)\varphi}{(1+2\alpha-(1-\alpha)\varphi}[\varphi + f(\alpha)\varphi^2 + O(\varphi^3)]\right\} \quad (3.40)$$

Xuan et al. [74] studied the effective thermal conductivity of nanofluids, by considering Brownian motion and clustering of nanoparticles. The predictive model is as follows:

$$k_{nf} = k_f\frac{k_p+2k_f+2\varphi(k_p-k_f)}{k_p+2k_f-\varphi(k_p-k_f)} + \frac{\rho_p\varphi c_p}{2}\sqrt{\frac{k_BT}{3\pi r_{cl}\mu_f}} \quad (3.41)$$

where r_{cl} is the apparent radius of the cluster which is determined by experiment ($r_{cl} = r_p$ when a cluster conations only one nanoparticle). $T$is the temperature and k_B is the Boltzmann constant. The first term of the right hand side of Equation (3.41) is simply the Maxwell model, while the second term adds the contribution of the random motion on the effective thermal conductivity of nanofluids.

Yu and Choi [75] studied the effect of the liquid nanolayer formed between the spherical nanoparticles and renovated the Maxwell model. The model considered the

interaction between the nanoparticles and the base fluid happening in the layer formed between them. The model is presented below:

$$k_{nf} = k_f \frac{k_p+2k_f+2\varphi(k_p-k_f)(1+\gamma)^3}{k_p+2k_f-2\varphi(k_p-k_f)(1+\gamma)^3} \tag{3.42}$$

where γ is the ratio of the nano-layer thickness to the original particle radius$\gamma = \frac{\varepsilon}{r_p}$ and mostly it is assumed to be 0.1.

Xie et al. [76] developed a model for the effective thermal conductivity by taking into account the nanolayer structure formed between the nanoparticles and the base fluid. It was assumed that the layer has its own thermal conductivity which is between the thermal conductivity of the fluid and the nanoparticles. The layer thermal conductivity is given by:

$$k_l = \frac{k_f M^2}{(M-\gamma)\ln(1+M)+\gamma M} \tag{3.43}$$

where $M = \varepsilon_p(1+\gamma) - 1, and \ \varepsilon_p = \frac{k_p}{k_f}$.

Xie et al. [76] provided a formula to calculate the total volume fraction of the original nanoparticle:

$$\varphi_T = \varphi(1+\gamma)^3 \tag{3.44}$$

The effective thermal conductivity is given by the following model:

$$k_{nf} = k_f \left[3\theta\varphi_T + \frac{3\theta^2\varphi_T^2}{1-\theta\varphi_T} \right] + k_f \tag{3.45}$$

where $\theta = \frac{\beta_{lf}\left[(1+\gamma)^3 - \frac{\beta_{pl}}{\beta_{fl}}\right]}{(1+\gamma)^3+2\beta_{pl}\beta_{fl}}$

and

$$\beta_{lf} = \frac{k_l-k_f}{k_l+2k_f} \tag{3.46}$$

$$\beta_{pl} = \frac{k_p - k_l}{k_p + 2k_l} \tag{3.47}$$

$$\beta_{fl} = \frac{k_f - k_l}{k_f + 2k_l} \tag{3.48}$$

Leong et al. [77] also studied the effect of the interfacial layer between the solid particles and the base fluid. The derived model for the effective thermal conductivity is as follows:

$$k_{nf} = \frac{(k_s - k_l)\varphi k_l[2\beta_1^3 - \beta^3 + 1] + (k_s + 2k_l)\beta_1^3[\varphi\beta^3(k_l - k_f) + k_f]}{\beta_1^3(k_s + 2k_l) - (k_s - k_l)\varphi[\beta_1^3 + \beta^3 - 1]} \tag{3.49}$$

where $\beta = 1 + \gamma, and \beta_1 = 1 + \frac{\gamma}{2}$

In Xie et al. [76] model, the thermal conductivity of the interfacial layer is calculated using Equation (3.43), where in Leong et al. [77] model, the thermal conductivity of the interfacial nanolayer is considered to be twice or three times as the thermal conductivity of the base fluid.

Xuan et al. [78] developed a model by adopting the concepts of the Langevin equation of the Brownian motion and the concept of stochastic thermal process to describe the temperature fluctuation of spherical nanoparticles dispersed in base fluids. The model is as follows:

$$k_{nf} = k_f \frac{k_p + 2k_f + 2\varphi(k_p - k_f)}{k_p + 2k_f - \varphi(k_p - k_f)} + \frac{18\varphi HAk_B T}{\pi^2 \rho_p d_p^6}\tau \tag{3.50}$$

where H is the overall heat transfer coefficient between the nanoparticles and the fluid, A is the heat transfer area, and $\tau$is the comprehensive relaxation time constant.

All the above models predict the thermal conductivity of spherical or cylindrical shape which is the case in a lot of nanoparticles suspended in fluids, however when it comes to $SWCNT$, the shape and the structure is more complicated; meaning that the previous models will not be able to predict the thermal conductivity accurately. Nan et al. [84], developed a model to calculate the effective thermal conductivity of CNT's medium

composites based on theory of scattering. The CNT's are assumed to be randomly dispersed in the matrix. The model of the effective thermal conductivity is as follows:

$$k_{nf} = k_m \frac{3+2\varphi[B_x(1-L_x)+B_z(1-L_z)]}{3-\varphi(2B_xL_x+B_ZL_z)} \tag{3.51}$$

Where k_m is the thermal conductivity of the matrix and,

$$B_x = \frac{k_x-k_m}{k_m+L_x(k_c-k_m)} \tag{3.52}$$

$$B_z = \frac{k_x-k_m}{k_m+L_z(k_c-k_m)} \tag{3.53}$$

where $k_x and k_z$ are the thermal conductivities of the CNT along the transverse and longitudinal directions respectively.$L_x and l_z$ are geometric factors dependent on the aspect ratio of the CNT (p) and given by:

$$L_x = \frac{p^2}{2(p^2-1)} - \frac{p}{2(p^2-1)^{\frac{3}{2}}}\cosh^{-1} p \tag{3.54}$$

$$L_z = 1 - 2L_x \tag{3.55}$$

For high p over 100, $L_x = 0.5\ and\ L_z = 0$, which reduces the effective thermal conductivity model to:

$$k_{nf} = k_m \frac{3\left(\frac{k_x}{k_m}+1\right)+\varphi\left[2\left(\frac{k_x}{k_m}-1\right)+\left(\frac{k_x}{k_m}+1\right)\left(\frac{k_z}{k_m}-1\right)\right]}{3\left(\frac{k_x}{k_m}+1\right)-2\varphi\left(\frac{k_x}{k_m}-1\right)} \tag{3.56}$$

In the previous model, the Kaptiza resistance (a_k) was neglected which led to an over predication of the nanofluids thermal conductivity when compared to the experimental data. Nan et al. [85] took these considerations into account and reformulated the analytical model to include the interfacial resistance between the nanoparticles and the base fluid. The modified thermal conductivity model is expressed as:

$$k_{nf} = \frac{3+\varphi(B_{11}+B_{33})}{3-\varphi B_{11}} k_f \tag{3.57}$$

where

$$B_{11} = \frac{2(k_{11}^c - k_f)}{k_{11}^c + k_f} \tag{3.58}$$

$$B_{33} = \frac{k_{33}^c}{k_f} - 1 \tag{3.59}$$

The parameters k_{11}^c, k_{33}^c are the thermal conductivities along the transverse and longitudinal axes of the interfacial thermal barriers layer and are represented by:

$$k_{11}^c = \frac{k_p}{1 + \frac{2a_k k_p}{d_s\ k_f}} \tag{3.60}$$

$$k_{33}^c = \frac{k_p}{1 + \frac{2a_k k_p}{l_s\ k_f}} \tag{3.61}$$

where $d_s and\ l_s$ are the diameter and the length of the CNT respectively, a_k is the Kaptiza radius defined as:

$$a_k = R_k k_f \tag{3.62}$$

Where R_k is $8\ \times 10^{-8} m^2 K/W$.

Xue [86] developed a model to express the thermal conductivity of CNTs-based composites. A distribution function $P(B_j)$ is defined to account for the dispersion of the CNT's in the base fluid. For CNT's that are assumed to be randomly distributed in the base fluid, the normal-like distribution function is:

$$P(B_j) = \frac{2}{\pi\sqrt{B_j(1 - B_j)}} \tag{3.63}$$

When substituting the function in the equivalent field factor, and assuming that the thermal conductivity of the CNT's is isotropic, the effective thermal conductivity of the nanofluids can be predicted by the model as follows:

$$k_{nf} = k_f \frac{1 - \varphi + (4\varphi/\pi)\sqrt{k_p/k_f}\, arctg\left(\frac{\pi}{\sqrt[4]{k_p/k_f}}\right)}{1 - \varphi + (4\varphi/\pi)\sqrt{k_f/k_p}\, arctg\left(\frac{\pi}{\sqrt[4]{k_p/k_f}}\right)} \tag{3.64}$$

Xue [86] pointed out that the CNT's distribution can hugely affect the effective thermal conductivity of nanofluids. For instance, the thermal conductivity of randomly distributed CNT's in a base fluid differs from CNT's distributed according to distribution function shown in Equation (3.63). Two conditions are ought to be satisfied in order to choose a distribution function. The conditions are as follows:

$0 < B_j < 1/2$

$\int_0^{1/2} P(B_j) dB_j = 1.$

For Comparison, it is assumed that the distribution function is set to be $P(B_j) = 2$, which satisfies the two conditions. In that case, the effective thermal conductivity model is given by:

$$k_{nf} = k_f \frac{1-\varphi+2\varphi\frac{k_p}{k_p-k_f} ln\frac{k_p+k_f}{2k_f}}{1-\varphi+2\varphi\frac{k_f}{k_p-k_f} ln\frac{k_p+k_f}{2k_f}} \quad (3.65)$$

Patel et al. [87] presented a model to predict the thermal conductivity of CNT based nanofluids for both water and oil base fluids. The model takes into account the radius of the fluid and nanoparticles; it is presented as follows:

$$k_{nf} = k_f \left[1 + \frac{k_p \varphi r_f}{k_f (1-\varphi) r_p} \right] \quad (3.66)$$

3.2 Convective Heat Transfer

This section presents the equations and correlations used to calculate the convective heat transfer coefficient of fluids inside the PTSC receiver tube. The Nusselt number is the most critical parameter to calculate. Different correlations were used for the predication of the Nusselt number assuming a flow in a circular pipe subjected to constant heat flux. The equations for the base fluids and nanofluids are shown in the following sections.

3.2.1 Base fluids.

The equations and different correlations for the calculation of the convective heat transfer coefficient of the base fluids (Therminol, Syltherm) are shown below.

3.2.1.1 Reynolds Number of base fluids.

The Reynolds number is a dimensionless number that indicates the flow type of a fluid, whether it is laminar or turbulent; Reynolds number above 5000 usually shows a turbulent flow. The equation of the Reynolds number is provided as follows:

$$Re_f = \frac{\rho_f V D_{ri}}{\mu_f} \tag{3.67}$$

where μ_f is the dynamic viscosity, calculated from the following equation:

$$\nu_f = \frac{\mu_f}{\rho_f} \tag{3.68}$$

3.2.1.2 Prandtl Number of base fluids.

The Prandtl number is a dimensionless number that measures the ratio of the momentum diffusivity to the thermal diffusivity. The Prandtl number is given by:

$$Pr_f = \frac{\mu_f C_{p_f}}{k_f} \tag{3.69}$$

3.2.1.3 Nusselt Number of base fluids.

The Nusselt number is a dimensionless number that measures the ratio of convective to conductive heat transfer. It depends on the flow type, boundary and geometry of the surface, Reynolds number and Prandtl number. Different correlations for the Nusselt number of the base fluids are presented in this analysis, starting with Kalogirou [5] where a model for the Nusselt number of the fluid in the PTSC absorber tube is presented as follows:

$$Nu_f = \frac{f}{\frac{8\left(Re_f - 1000\right)Pr_f}{1+12.7\sqrt{f/8}\left(Pr_f^{\frac{2}{3}}-1\right)}\left(\frac{Pr_f}{Pr_p}\right)} \tag{3.70}$$

Where Pr_p is the Prandtl number evaluated at the inner absorber temperature and all other parameters are evaluated at the fluid temperature.

f_D is the Darcy friction factor given by:

$$f_D = \left[1.82\ln\left(Re_f\right) - 1.64\right]^{-2}$$

(3.71)

The previous model is valid for $0.5 < Pr_f < 2000\ and\ 2300 < Re_f < 5x10^6$.

Yilmaz and Söylemez [12] presented another model to calculate the Nusselt number of the heating fluid in a PTSC absorber tube. The model is given by:

$$Nu_f = \frac{\sqrt{f/8}Re_f \mathrm{Pr_f}}{12.48Pr_f^{\frac{2}{3}} - 7.8853Pr_f^{\frac{1}{3}} + 3.613\ln\left(Pr_f^{\frac{1}{3}}\right) + 5.8 + C} \quad (3.72)$$

where $C = 2.78\ln(\sqrt{f/8}\,Re_f/90)$ and f is the Fanning friction factor for smooth pipes given by:

$$f = \left[0.79\ln\left(Re_f\right) - 1.64\right]^{-2} \quad (3.73)$$

The previous model is valid for $0.5 < Pr_f < 2000\ and\ 10^4 < Re_f < 5 \times 10^6$.

Another correlation that is widely used is the Dittus-Boelter equation. The equation is tailored for smooth tubes and shows a bit of discrepancy when a large range of temperature difference is present. The equation is as follows:

$$Nu_f = 0.023Re_f^{0.8}Pr_f^{0.4} \quad (3.74)$$

The previous equation is valid for $0.6 < Pr_f < 160\ and\ Re_f > 4000$.

The famous Gnielinski's correlation can be also used to calculate the Nusselt number of a fluid inside a PTSC absorber tube. The correlation is as follows:

$$Nu_f = \frac{\left(f/8\right)(Re_f - 1000)Pr_f}{1 + 1.27\left(f/8\right)^{\frac{1}{2}}(Pr_f^{\frac{2}{3}} - 1)} \quad (3.75)$$

where f is the Fanning friction factor given by Equation (3.73), and the correlation is valid for $0.5 < Pr_f < 2000\ and\ 3000 < Re_f < 5 \times 10^6$.

All the above Nusselt number correlations are for turbulent flow, but in case of Laminar flow the Nusselt number for a flow through a circular tube with constant heat flux is simply given as:

$$Nu_{f\,laminar} = 4.36 \tag{3.76}$$

3.2.1.4 Convective heat transfer coefficient of base fluids.

The overall convective heat transfer coefficient of a fluid flow through the absorber tube of a PTSC can be calculated using the following equation:

$$h_{crin} = \frac{Nu_f k_f}{D_{ri}} \tag{3.77}$$

3.2.2 Nanofluids.

The equations and different correlations for the calculation of the convective heat transfer coefficient of nanofluids are shown below.

3.2.2.1 Reynolds Number of nanofluids.

The Reynolds number for nanofluids is calculated by using the same equation as the base fluids; however the nanofluids properties are to be used. The Reynolds number is an important parameter to calculate because it gives an indication of whether the flow is laminar or turbulent. Laminar flow, which usually takes place for a Reynolds number less than 3000, is characterized to be a smooth flow at lower speeds. The turbulent flow is characterized by a fluid flow that is subjected to turbulences because of the high speeds of the fluid. For an improved heat transfer between a fluid and a surface, it is recommended to keep the flow turbulent, as the random movement of the molecules of the fluid caused a higher heat transfer between the fluid and absorber tube. The equation of the Reynolds number of nanofluids is provided as follows:

$$Re_{nf} = \frac{\rho_{nf} V D_{ri}}{\mu_{nf}} \tag{3.78}$$

3.2.2.2 Prandtl Number of nanofluids.

The Prandtl number for nanofluids is calculated by using the same equation as the base fluids, but with the use of nanofluids properties. The Prandtl number is important to calculate because it is a key parameter for the calculation of the Nusselt number and the

convective heat transfer coefficient, as well as many other parameters that deal with the performance of the PTSC. The Prandtl number for nanofluids is given by:

$$Pr_{nf} = \frac{\mu_{nf} C_{p_{nf}}}{k_{nf}} \tag{3.79}$$

3.2.2.3 Nusselt Number of nanofluids.

The Nusselt number for nanofluids cannot be calculated using the equations provided in section 3.2.1.3, but proper models and correlations are to be implemented for the prediction of the Nusselt number of nanofluids for turbulent and laminar flows. Different models are provided in the literature as seen from section 2.3.4; however plenty of them are not applicable for the type of analysis done here, since some are tailored only for water based nanofluids or a certain type of nanoparticles. Nevertheless, some models can be used in this analysis, starting with Maïga et al. [117] where a model for the prediction of the Nusselt number of nanofluids flow through a circular tube was presented. The model is for laminar flow and it is as follows:

$$Nu_{nf} = 0.086 Re_{nf}^{0.55} Pr_{nf}^{0.5} \tag{3.80}$$

The above correlation is valid for $6 < Pr_{nf} < 753$ and $\phi < 10$.

Maïga et al. [120] also provided a model for the prediction of the Nusselt number of nanofluids flow through a circular tube. The model is for turbulent flow and it is as follows:

$$Nu_{nf} = 0.085 Re_{nf}^{0.71} Pr_{nf}^{0.35} \tag{3.81}$$

The above correlation is valid for $10^4 < Re_{nf} < 5x10^6$ and $\phi < 10$.

Vajjha and Das [126] also provided a model for the prediction of the Nusselt number of nanofluids flow through a circular tube. The difference in this model is that it takes into account the volume fraction of the nanoparticles. The model is for turbulent flow and it is as follows:

$$Nu_{nf} = 00.65(Re_{nf}^{0.65} - 60.22)(1 + 0.0169\varphi^{0.15}) Pr_{nf}^{0.542} \tag{3.82}$$

3.2.2.4 Convective heat transfer coefficient of nanofluids.

The overall convective heat transfer coefficient of nanofluids flow through the absorber tube of a PTSC can be calculated using the following equation:

$$h_{nf,crin} = \frac{Nu_{nf} k_{nf}}{D_{ri}} \tag{3.83}$$

3.3 PTSC Modeling

The following section covers the mathematical modeling of a PTSC based on an energy and exergy analysis. The PTSC unit consists of an absorber tube or a receiver fixed along the center of the focal length of the collector. The absorber tube is a metal tube painted black to absorb more heat; it is covered by glass cover to reduce the heat loss due to convection and radiation. The collector is in the shape of a parabola and it serves as a reflective surface where the parallel rays on it are reflected onto the absorber tube. The energy model used in the analysis is based on the following assumptions:

1. The system operates at steady state conditions.
2. The porous medium properties have a cylindrical symmetry.
3. All phases are continuously in thermal and chemical local equilibrium.
4. The glass tube temperature is uniform at any given time.

The model of the PTSC is done by analyzing the collector, receiver and glass cover separately, then combing the parameters to analyze the energetic and exergetic performances of the PTSC. Figure 3 shows the schematic diagram of a PTSC, and how the rays of sunlight are reflected by the collector onto the receiver.

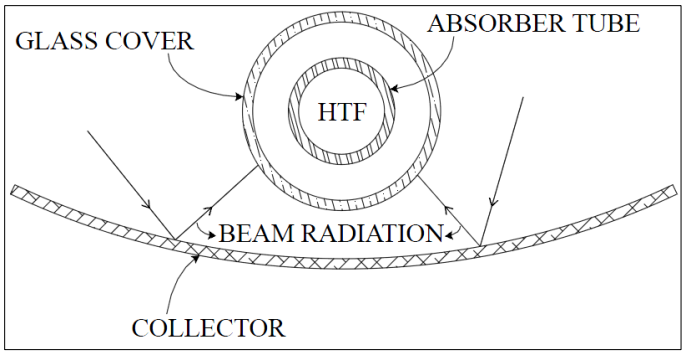

Figure 3: PTSC Schematic Diagram

3.3.1 Collector.

The collector is a metal sheet shaped as a parabola in order to catch the maximum amount of sun rays and reflect it onto the absorber tube centered at the focal line of the collector. The specifications of the collector used in the analysis are presented in Table 5.

3.3.1.1 Angle of incidence.

The angle of incidence is the angle between the ray incident on the collector and the line perpendicular to the collector surface. Calculating the angle of incidence is important because it affects the amount of solar energy received by the collector. The equation of the incident angle is given by:

$$\cos\theta = \sin a \cos\lambda + \cos a \sin\lambda \cos(\Omega - \beta) \tag{3.84}$$

where λ is the tilt is angle and Ω is the aperture azimuth angle. Figure 4 shows the relation between the two angles. a and β are the solar altitude angle and solar azimuth angle respectively The solar altitude angle is the angle between the solar rays and the horizontal plane on the surface of the earth, where the solar azimuth angle is the angle between the horizontal projection of the sun rays and the due-south direction line. The angles can be calculated from the following equations:

$$a = \sin^{-1}(\sin\delta \sin\Phi + \cos\delta \cos\Phi \cos w) \tag{3.85}$$

$$\beta = cos^{-1}\left(\frac{\sin\delta \cos\Phi - \cos\delta \sin\Phi \cos w}{\cos a}\right) \tag{3.86}$$

where w is the hour angle given by:

$$w = 15[t_s - 12] \tag{3.87}$$

and $t_s$is the solar time (hour), calculated by:

$$t_s = LCT + \left(\frac{EOT}{60}\right) - LC - DLS \tag{3.88}$$

where LCT, DLS are the local clock time and the correction for daylight saving which is one hour.

Table 5: Receiver, Glass cover and Collector specifications

Receiver			
Parameter	Symbol	Unit	Value
Type	-	-	Schott PTR70 2008
Absorber tube inner diameter	D_{ri}	mm	66
Absorber tube outer diameter	D_{ro}	mm	70
Receiver efficiency	η_r	%	75
Receiver emissivity	ε_r	-	0.92
Receiver absorptance	α_r	-	0.96
Receiver Area	A_r	m^2	22
Absorber material type	-	-	Stainless steel 304L
Glass Cover			
Glass cover inner diameter	D_{ci}	mm	115
Glass cover outer diameter	D_{co}	mm	120
Glass cover emissivity	ε_C	-	0.86
Glass cover absorptance	α_C	-	0.02
Glass cover transmittance	τ_C	-	0.963
Glass cover area	A_c	m^2	37.7
Collector			
Type	-	-	Solargenix SGX-1
Collector width	w	m	5
Collector length	L_c	m	8.3333
Length of collector assembly	L	m	100
Number of modulus	N_m	-	12
Number of collectors	N_c	-	1
Reflective Aperture Area	A_a	m^2	470.3
Tracking error	$e_{tracking}$	-	0.994
Mirror reflectance	ρ_{cl}	-	0.935
Collector optical efficiency	η_o	%	85.66

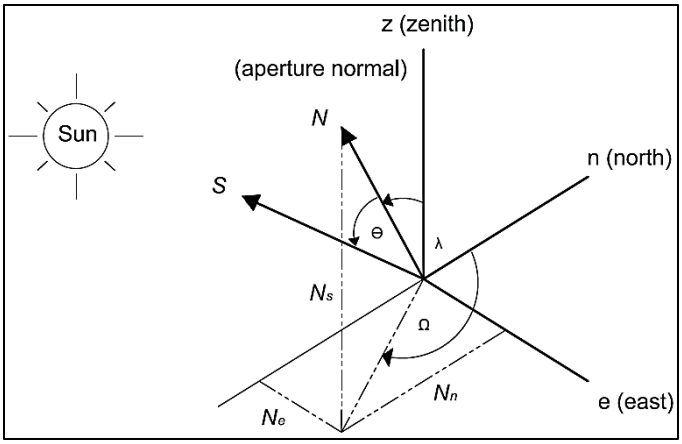

Figure 4: Relation between tilt angle and aperture azimuth angle [170]

$$EOT = 0.285\cos x - 7.416\sin x - 3.648\cos 2x - 9.228\sin 2x \tag{3.89}$$

and

$$x = \frac{360(N-1)}{365.242} \tag{3.90}$$

where N is the day number.

LC is the longitude correction given by:

$$LC = \frac{(Longitude\ of\ standard\ time\ zone\ meridan - Local\ longititude)}{15} \tag{3.91}$$

and δ is the solar declination angle, which is the angle between the earth sun line and the equatorial plane and it varies from $-23.5\,°$ to $23.5\,°$ from the summer to the winter season. The angle can be calculated using the following equation:

$$\sin\delta = 0.39795\cos[0.98563\ (N-173)] \tag{3.92}$$

The latitude angle Φ is measured from the center of the earth. It specifies the location on the earth surface. The latitude angle also affects the solar radiation and contributes to climate zones on earth.

3.3.1.2 Optical efficiency.

The optical efficiency of the collector can be calculated using the following equation:

$$\eta_o = F_{RS} K(\theta) \rho_m (\tau_{CG} a_c)_e \gamma_n \quad (3.93)$$

where ρ_m is the average specular mirror reflectance, τ_{CG} is the glass envelope transmittance, $a_c$is the surface coating absorptance, $(\tau_{CG} a_c)_e$ is the effective product of $\tau_{CG}\ and\ a_c$, γ_n is the intercept factor, $K(\theta)$ is the incident angle modifier given by [99]:

$$K(\theta) = \cos\theta - 2.859621 \times 10^{-5}\theta^2 - 5.25097 \times 10^{-4} \quad (3.94)$$

and F_{RS} is the shading factor given by:

$$F_{RS} = \frac{(W_e)_t}{W_t} \quad (3.95)$$

where W_t and $(W_e)_t$ are the total aperture width of the solar field and the total effective width for all solar collectors respectively.

3.3.2 Receiver.

The receiver of the PTSC consists of the absorber tube where the beam radiation is centered, which is usually painted black in order to absorb more heat. Typically the receiver material is stainless or copper. In this analysis, the receiver material chosen is stainless steel 304L. The thermal conductivity of the receiver can be calculated from the following equation obtained from [5]:

$$k_r = 0.013T_r + 15.2 \quad (3.96)$$

The area of the receiver can be calculated using the following equation:

$$A_r = \pi D_{ro} L \quad (3.97)$$

The heat transfer coefficient of the fluid inside the receiver pipe can be calculated from the equations provided in the previous sections (3.2.1.3, 3.2.1.4, 3.2.2.3, 3.2.2.4) depending on the base fluid or nanofluids used, and with respect to the Nusselt number correlation chosen. Table 5 shows the specifications of the receiver and absorber used in this analysis.

3.3.3 Glass cover.

The glass cover is a tube envelope surrounding the receiver tube; it limits the heat losses due to convection and radiation. The annulus is the space between the receiver and the glass cover and it is usually filled with air or vacuumed. For the simplicity of the calculation, it is assumed that the annulus is air filled. The area of the glass cover is calculated using the following equation:

$$A_c = \pi D_{co} L \tag{3.98}$$

The radiation heat transfer coefficient between the glass cover and the ambient is given by:

$$h_{rca} = \varepsilon_c \sigma (T_c + T_{amb})(T_c^2 + T_{amb}^2) \tag{3.99}$$

While the radiation heat transfer coefficient between the glass cover and the receiver is given by:

$$h_{rcr} = \frac{\sigma (T_c + T_r)(T_c^2 + T_r^2)}{\left(\frac{1}{\varepsilon_r} + \frac{A_r}{A_c}\right)\left(\frac{1}{\varepsilon_c} - 1\right)} \tag{3.100}$$

The convective heat transfer coefficient between the glass cover and the ambient is given by:

$$h_{cca} = \frac{Nu_c k_{air}}{D_{co}} \tag{3.101}$$

where the Nusselt number for the glass cover can be calculated using the following correlations provided by [171]:

$$Nu_c = 0.4 + 0.54(Re_c)^{0.6} \tag{3.102}$$

For $0.1 < Re_c < 2300$

$$Nu_c = 0.3(Re_c)^{0.6} \tag{3.103}$$

For $Re_c > 4000$

The Reynolds number for the flow around the glass cover is defined as:

$$Re_c = \frac{\rho_{air} V_{wind} D_{co}}{\mu_{air}} \tag{3.104}$$

where the properties of the air are calculated at the atmospheric pressure and mean temperature. The mean temperature is the average temperature of the glass cover given by:

$$T_m = \frac{T_c + T_{amb}}{2} \tag{3.105}$$

The specifications of the glass cover are also presented in Table 5.

3.3.4 PTSC energy model.

The analysis for the PTSC is done under steady state conditions as mentioned in the assumptions; the rate of useful energy produced by the PTSC is the difference between the amount of heat absorbed by the heating fluid and the direct or indirect losses from the surface to the surroundings. The useful energy collected by the PTSC is given by:

$$\dot{Q}_u = F_R[I_B A_a - A_r U_L (T_i - T_{amb})] N_l N_m N_c \tag{3.106}$$

where the aperture area A_a is defined as:

$$A_a = (w - D_{co}) L \tag{3.107}$$

The concentration ratio of the PTSC is defined as the ratio of the aperture area to the receiver area, it is as follows:

$$C = \frac{A_a}{A_r} \tag{3.108}$$

The PTSC can utilize only a portion of the total sun radiation. This portion is called the beam radiation and it is absorbed by the receiver, therefore it depends on the receiver efficiency. The beam radiation is given by:

$$I_B = I_D \eta_r \tag{3.109}$$

The heat removal factor is the ratio of the actual heat delivered to the heat delivered if the collector plate was at a uniform temperature equal to the temperature of the entering fluid. The heat removal factor is as follows:

$$F_R = \dot{m}_f \frac{C_{pf}}{A_r U_L}\left[1 - e\left(-\frac{A_r U_L F'}{\dot{m}_f C_{pf}}\right)\right] \tag{3.110}$$

A new model for the overall heat transfer coefficient and the overall heat loss coefficient is presented in this thesis. The overall heat transfer coefficient depends on the overall heat loss coefficient, convective heat transfer coefficient inside the absorber tube of the PTSC, and the conduction heat transfer coefficient of the heating fluid through the absorber tube of the PTSC. On the other hand, the heat loss coefficient was modeled based on the following assumptions and heat transfer mechanisms:

1. Conduction heat transfer through the receiver.
2. Conduction heat transfer through the glass cover.
3. Convective hear transfer between the glass cover and the ambient.
4. Radiation heat transfer between the receiver and the glass cover.
5. Radiation heat transfer between the glass cover and the ambient.

According to the previous assumptions and by adding the thermal resistances of each heat transfer mechanisms, the overall heat loss coefficient and heat transfer coefficient are as follows:

$$U_L = \left(\frac{A_r}{A_c(h_{cca}+h_{rca})} + \frac{1}{h_{rcr}} + \frac{D_{ro}}{k_r} + \frac{D_{co}}{k_s}\right)^{-1} \tag{3.111}$$

$$U_o = \left(\frac{1}{U_L} + \frac{D_{ro}}{h_{crin}D_{ri}} + \left(\frac{D_{ro}}{2k_f} ln\frac{D_{ro}}{D_{ri}}\right)\right)^{-1} \tag{3.112}$$

The collector efficiency factor F' is the ratio of the actual useful energy gain to the useful energy gain produced if the collector absorbing surface is at the local fluid temperature. The efficiency factor is defined as:

$$F' = \frac{U_o}{U_L} = \frac{\frac{1}{U_L}}{\frac{1}{U_L}+\frac{D_{ro}}{h_{crin}D_{ri}}+\left(\frac{D_{ro}}{2k_f}ln\frac{D_{ro}}{D_{ri}}\right)} \quad (3.113)$$

In order to carry out the analysis, the glass cover temperature is assumed and the parameters are calculated. To check the accuracy of the assumption, the cover temperature can be calculated and checked as follows:

$$T_c = \frac{A_r h_{rcr} T_r + A_c(h_{rca}+h_{cca})T_{amb}}{A_r h_{rcr} + A_c(h_{rca}+h_{cca})} \quad (3.114)$$

The efficiency of the PTSC can be calculated from the following equation:

$$\eta_{PTSC} = \frac{\dot{Q}_u}{I_B A_a N_c N_m N_l} \quad (3.115)$$

Table 6 shows the design input parameters for the analysis of the energy model of the PTSC.

3.3.5 PTSC exergy model.

The exergetic analysis done on the PTSC is fairly simple; the exergetic efficiency is the ratio of the output exergy to the input exergy. In case of the PTSC, the exergy output is the exergy stored by the fluid that passes through the receiver tube, while the exergy input is the exergy of the solar radiation absorbed by the PTSC.

Table 6: PTSC energy model design parameters

Parameter	Symbol	Unit	Value
Inlet temperature	T_i	℃	293
Outlet temperature	T_o	℃	391
Receiver temperature	T_r	℃	334
Glass cover temperature	T_c	℃	105
Ambient Temperature	T_{amb}	℃	25
Sun Temperature	T_s	K	5770
Beam radiation	I_B	W/m^2	560
Wind Velocity	v_{wind}	m/s	5

The exergy efficiency is as follows:

$$\eta_{ex} = \frac{\dot{X}_{out,PTSC}}{\dot{X}_{in,PTSC}} \tag{3.116}$$

Where the exergy output and exergy input are given as follows:

$$\dot{X}_{out,PTSC} = Q_u \left(1 - \frac{T_{amb}}{T_r}\right) \tag{3.117}$$

$$\dot{X}_{in,PTSC} = A_a I_B \left[1 + \frac{1}{3}\left(\frac{T_{amb}}{T_s}\right)^4 - \frac{4}{3}\left(\frac{T_{amb}}{T_s}\right)\right] \tag{3.118}$$

The exergy destruction is the difference between the input and the output exergy, and it can be calculated using the following equation:

$$\dot{X}_{des,PTSC} = \dot{X}_{in,PTSC} - \dot{X}_{out,PTSC} \tag{3.119}$$

The entropy generation can be simply calculated using the following equation:

$$\dot{S}_{gen} = \frac{\dot{X}_{des,PTSC}}{T_{amb}} \tag{3.120}$$

3.4 Integrated Solar-Rankine Cycle model (ISRC)

The energy produced by the PTSC is utilized for power production by integrating the PTSC with a conventional Rankine cycle. The conventional Rankine cycle typically consists of a boiler, steam turbine, condenser and a pump, however in the case of an ISRC; the boiler is substituted by the solar field and a heat exchanger in order to exchange the heat between the heating fluid and the water/steam in order to run the Rankine cycle. Figure 5 shows the schematic diagram of the ISRC, while Figure 6 shows the T-S diagram of the ISRC. The heating fluid is heated by solar field. Then, it is passed through the heat exchanger where it heats up the water until it changes phase into steam. The superheated steam is then directed into the steam turbine where electricity is produced. While the steam passes through the steam turbine, its temperature and pressure drop before entering the condenser. Inside the condenser the steam temperature drops and heat is rejected. The drop in temperature causes the steam to change phase and exit the condenser as saturated liquid. The saturated liquid enters the pump and the pressure is

increased to match the pressure of the heating fluid pumped from the solar field and into the heat exchanger. The water is pumped into the heat exchanger and the closed cycle is repeated again. The thermodynamic analysis of the Rankine cycle is shown in the following sections, and the design input parameters for the ISRC are shown in Table 7.

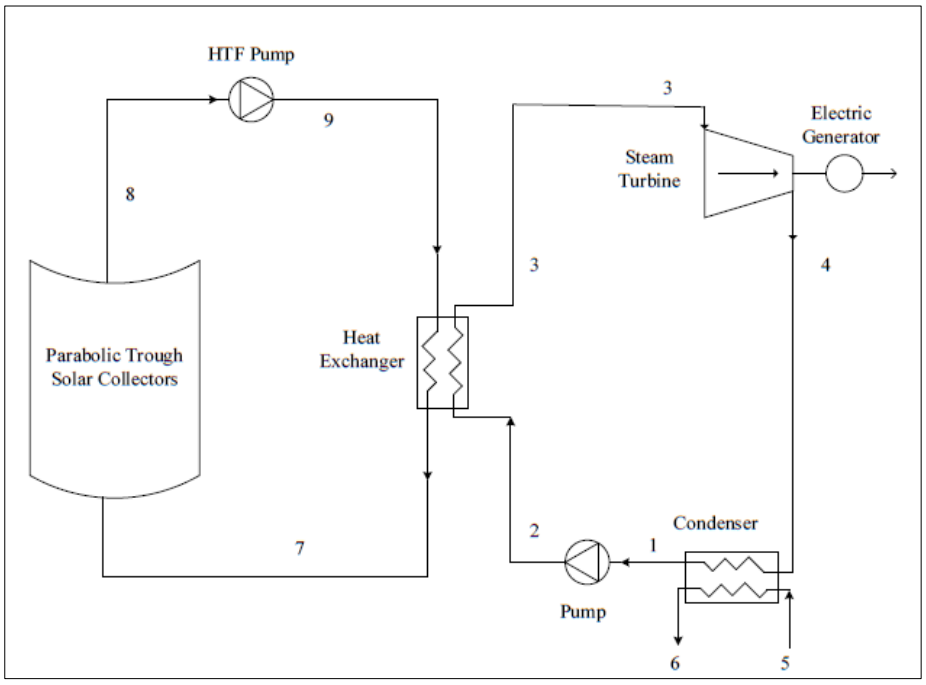

Figure 5: ISRC Schematic Diagram

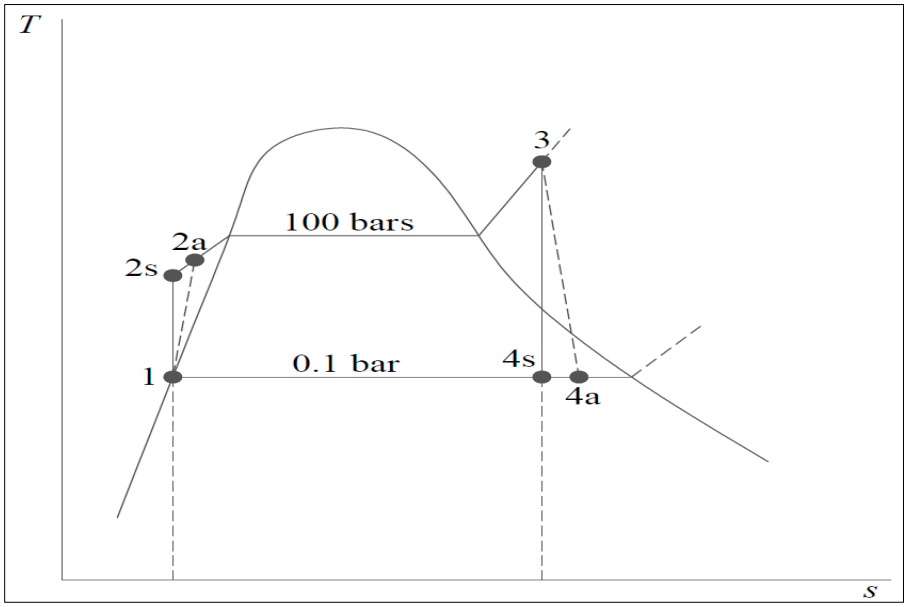

Figure 6: T-S diagram for the ISRC

Table 7: Location and Solar Field Design parameters

Weather Data for the City of Abu Dhabi		
Parameter	Unit	Value
Latitude	-	24.43 °N
Longitude	-	54.65 °E
Elevation	m	27
Direct Normal Irradiance	$kWh/m^2/day$	6.29
Global Horizontal Irradiance	$kWh/m^2/day$	6.04
Average Dry Temperature	℃	27.1
Average wind speed	m/s	3.6
Solar Field		
Solar Aperture Area	m^2	877000
Solar Multiple	-	2
Number of Loops	-	311
Beam radiation at design I_B	W/m^2	560

3.4.1 Steam turbine.

The specific work produced by the steam turbine can be calculated from the following equation:

$$w_{st} = (h_3 - h_4) \tag{3.121}$$

3.4.2 Condenser.

The specific heat rejected by the condenser can be calculated from the following equation:

$$q_c = (h_4 - h_1) \tag{3.122}$$

3.4.3 Pump.

The specific ideal work done by the pump can be calculated from the following equation:

$$w_p = (h_2 - h_1) \tag{3.123}$$

Another equation to calculate the ideal pump work is provided as follows:

$$w_p = v_1(P_2 - P_1) \tag{3.124}$$

where v_1 is the specific volume of the saturated water.

3.4.4 Heat exchanger.

In this analysis, a shell and tube heat exchanger is used. The heat transfer happens between the heating fluid which is in liquid phase and the water that is heated to steam. The following equation shows the energy balance done on the heat exchanger:

$$\dot{m}_f C_{pf}(T_o - T_i) = \dot{m}_s(h_3 - h_2) \tag{3.125}$$

where

$$\dot{m}_s = \frac{\dot{W}_{net}}{w_{net}} \tag{3.126}$$

and $\dot{w}_{net}$ is the specific net work of the cycle given by:

$$w_{net} = w_{st} - w_p \tag{3.127}$$

The shell and tube heat exchanger, as the name suggests, consists of the shell side and a bundle of tubes inside it as seen from Figure 7. The water from the cycle fills the shell, while the heating fluid passes through the tubes, heating the water in the shell to steam temperature. The flow of the heating fluid and the water are opposite, implying a counter flow arrangement to maximize the heat transfer between both fluids.

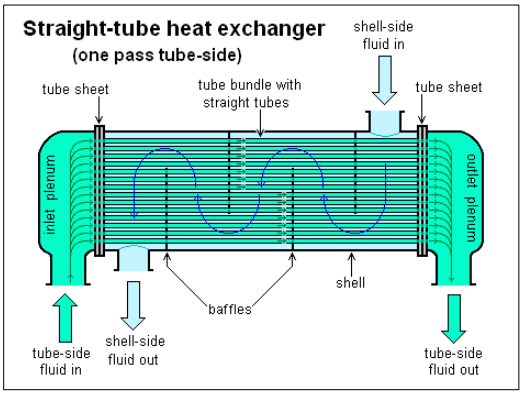

Figure 7: Shell and Tube Heat Exchanger Schematic Diagram [172]

The design equations of the heat exchanger are provided below, where the effectiveness –NTU method is used to calculate the temperature differences, area and rated capacity of the heat exchanger. In general, the NTU , which stands for the number of heat transfer units, can be calculated from the following equation obtained from [172]:

$$NTU = \frac{U_{he}A_{he}}{C_{min}} \tag{3.128}$$

where U_{he} and A_{he} are the overall heat transfer coefficient and the area of the heat exchanger respectively.

$$C_{min} = \min(C_h, C_c) \tag{3.129}$$

where C_h and C_c are the hot and cold capacity rates respectively. $C_{min}$is simply the smaller capacity rate, and C_{max} is the larger capacity rate. The hot and cold capacity rates are given by:

$$C_h = \dot{m}_h C_{ph} \tag{3.130}$$

$$C_c = \dot{m}_c C_{pc} \tag{3.131}$$

The effectiveness of the heat exchanger for counter flow arrangement can be calculated from the following equation:

$$\in = \frac{C_h(T_{h,in} - T_{h,out})}{C_{min}\,(T_{h,in} - T_{c,in})} = \frac{C_c(T_{c,out} - T_{c,in})}{C_{min}\,(T_{h,in} - T_{c,in})} \tag{3.132}$$

The NTU for counter flow arrangement can be calculated using the equation provided by [172]:

$$NTU = \frac{\ln\left(\frac{1 - \in C_{min}/C_{max}}{1 - \in}\right)}{1 - C_{min}/C_{max}} \tag{3.133}$$

The area of the heat exchanger can be calculated from the following equation:

$$A_{he} = NTU\,\frac{C_{min}}{U_{he}} \tag{3.134}$$

The overall heat transfer coefficient of the heat exchanger depends on the hot and cold fluids. Table 8 shows the overall heat transfer coefficient for some fluids used in the analysis.

Table 8: Heat Exchanger Overall Heat Transfer coefficient

Parameter	Hot Fluid	Cold Fluid	U_{he}
Unit	-	-	$(W.m^2K)$
	Oil	Water	370-730
	Oil	Molten Salt	50-200
	Molten Salt	Oil	150-300

3.4.5 Efficiency.

The efficiency of the ISRC is simply the output which is the net work produced by the Rankine cycle, over the input which is the energy produced by the PTSC. The efficiency of the ISRC is defined as:

$$\eta_{ISRC} = \frac{\dot{W}_{net}}{\dot{Q}_{PTSC}} \tag{3.135}$$

3.5 Integrated Solar-Regenerative Rankine Cycle model (ISRRC)

The Integrated Solar-Regenerative Rankine Cycle (ISRRC) consists of the solar power input which is the PTSC and a regenerative Rankine Cycle. The regenerative Rankine cycle mainly consists of a boiler, steam turbine, condenser, pump, open feed water heater and a feed pump. In case of the solar integration, the boiler is substituted by a solar field and a heat exchanger to carry the heat from the heating fluid to the water as shown in Figure 8. Figure 9 shows the T-S diagram of the ISRRC. The heating fluid is heated in the solar field until the required design temperature where it is then pumped into the heat exchanger to heat the water. The water exits the heat exchanger as steam and it is directed to a steam turbine where a fraction of it is used for power production, and a fraction is extracted and directed towards the open feed water heater which works as a heat exchanger. The portion of the steam that was not extracted expands completely and it is led to the condenser where the pressure drops and the steam changes phase to saturated liquid as it exits the condenser. The saturated liquid is then pumped to the feed

water heater pressure where it mixes directly with steam extracted from the turbine. The feed water heater is called an open feed water heater because of the direct mixing that takes place. In the ideal case, the mixture leaves the feed water heater as saturated liquid with no pressure loss. The saturated liquid is directed to the feed pump where it is pumped to match the heating fluid pressure in order for the heat exchange to take place. The water leaves the heat exchanger as steam and the cycle is repeated.

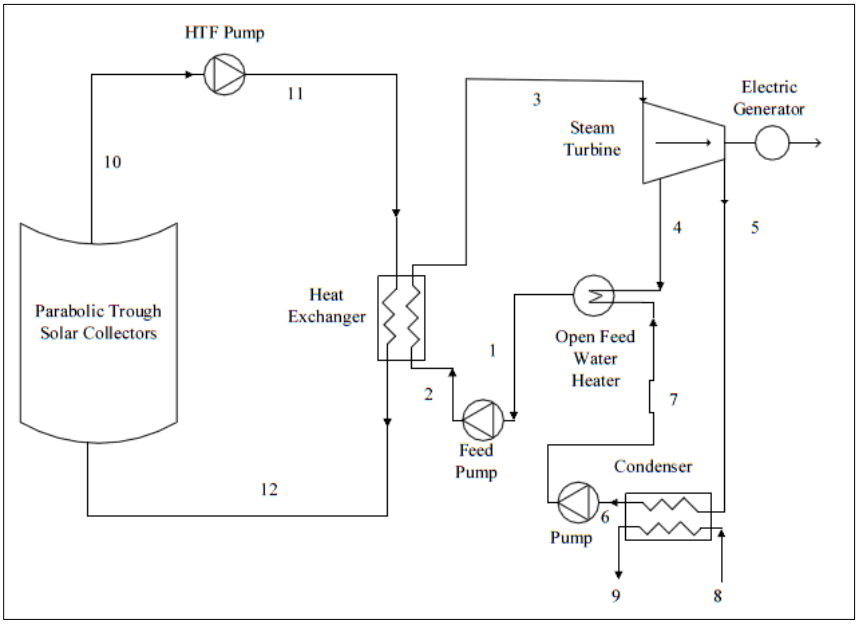

Figure 8: ISRRC Schematic Diagram

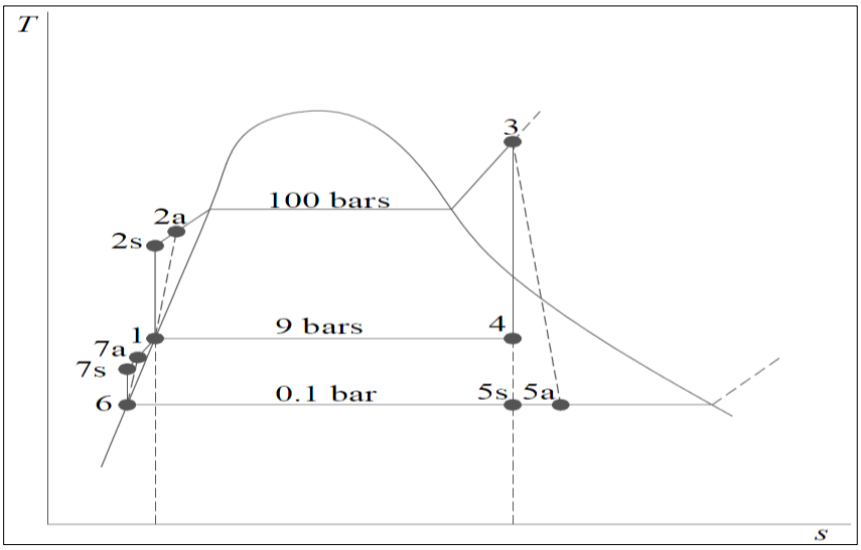

Figure 9: T-S diagram for the ISRRC

When comparing between the ISRC and ISRRC, the thermal efficiency of the ISRRC cycle is higher than that of the ISRC. The increase in the temperature of the turbine inlet reduces the work of the turbine for a set power output, therefore increasing the efficiency of the cycle. The pressure of the feed water heater and the amount of steam extracted affects the performance of the cycle greatly. The optimization of the feed water pressure is shown in the results section. The thermodynamic analysis of the ISRRC is shown below. Table 9 shows the design input parameters for both the ISRC and ISRRC cycles.

Table 9: ISRC and ISRRC Input Design Parameters

Power Cycles				
Parameter	Symbol	Unit	Value	
Cycle Type	-	-	ISRC Conventional Rankine Cycle	ISRRC Regenerative Rankine Cycle
Net Power Output	$\dot{W}_{net}$	MWe	150	150
Steam turbine efficiency	η_{st}	%	85	85
Pumps efficiency	η_p	%	78	78
Steam Turbine Pressure	P_{st}	bar	100	100
Feed water Pressure	P_f	bar	-	9
Condenser Pressure	P_c	bar	0.1	0.1

3.5.1 Open feed water heater.

The mass balance and energy balance on the open feed water heater yields the following equations:

$$\dot{m}_s = \dot{m}_4 + \dot{m}_7 \tag{3.136}$$

$$\dot{m}_s h_1 = \dot{m}_4 h_4 + (\dot{m}_s - \dot{m}_4) h_7 \tag{3.137}$$

The fraction of steam extracted from the turbine y is given as:

$$y = \frac{\dot{m}_4}{\dot{m}_s} = \frac{h_1 - h_7}{h_4 - h_7} \tag{3.138}$$

The previous equation means that for every kg of steam that enters the steam turbine a mass fraction y is going to be extracted and directed to the open feed water heater.

3.5.2 Steam turbine.

The specific work output of the turbine can be calculated using the following equation:

$$w_{st,RRC} = h_3 - h_4 + (1 - y)(h_4 - h_5) \tag{3.139}$$

3.5.3 Condenser.

The specific heat rejected by the condenser is described by the following equation:

$$q_{c,RRC} = (1 - y)(h_5 - h_6) \tag{3.140}$$

3.5.4 Pumps.

The specific work of the pumps is calculated given by the following equation:

$$w_{p,RRC} = w_{fp,RRC} + (1 - y)w_{cp,RRC} \tag{3.141}$$

where $w_{cp,RRC}$ is the specific ideal work of the condenser pump given by:

$$w_{cp,RRC} = v_6(P_5 - P_6) \tag{3.142}$$

where v_6 is the specific volume of the saturated water, $P_5\ and\ P_6$ are the pressures of the feed water heater and the condenser respectively.

The feed pump ideal work $w_{fp,RRC}$ is calculated from the following equation:

$$w_{fp,RRC} = v_1(P_3 - P_5) \tag{3.143}$$

where v_6 is the specific volume of the saturated water, $P_5\ and\ P_3$ are the pressures of the feed water heater and the steam turbine respectively.

3.5.5 Heat exchanger.

The design of the heat exchanger is the same as section 3.4.4; the mass flow rate of the steam can be also calculated from Equation (3.126). However the net specific work of the ISRRC can be calculated from the following equation:

$$w_{net,RRC} = w_{st,RRC} - w_{p.RRC} \tag{3.144}$$

3.6 Thermal Energy Storage

The thermal energy storage allows for flexible working hours and can increase the production of the plant, however integrating the TES will lead to a decrease in the efficiency because of the thermal losses. In this analysis a two tank molten salt storage is used as a TES, with a full load storage capacity of 7.5 hours or 10 hours depending on the mode of the operation discussed in the following section. Another heat exchanger is added after the PTSC and it can be modeled using the equations from section 3.4.4. The heat exchanger is supplied in order to exchange the heat between the heating fluid and the molten salt in the tanks. The energy balance on that heat exchanger is provided as follows:

$$\dot{m}_f C_{pf}(T_o - T_i) = \dot{m}_{salt} C_{psalt}(T_{hot} - T_{cold}) \tag{3.145}$$

where T_{hot}, T_{cold} are the design temperatures of the two tanks presented in Tables 10 and 11. Along with the input design parameters and the storage volume calculated on SAM (Solar Advisory Model) based on the previous data provided in Table 6 and Table 9, the storage salt used is Hitec Salt and it operates between the temperatures of 142 and 538℃. The volume of tank is considered to be the volume needed to fill one tank completely while the other one is empty. Nonetheless, a minimum amount of salt is required to be present in both tanks at any given time. The efficiency of the ISRC/TES can be calculated using the following equation:

$$\eta_{ISRC/TES} = \frac{\dot{W}_{net}}{\dot{Q}_{PTSC} + \dot{Q}_{tank}} \tag{3.146}$$

3.6.1 Modes of operation.

In the analysis, three modes of operation are examined. In the 1st mode, no thermal energy storage is used. The operation time is limited to the PTSC working hours, and the energy produced is directly utilized for power production.

The 2nd mode of operation allows for 7.5 hour storage period, meaning that the fluid is stored during the charging cycle, and after the PTSC is shut, the fluid is discharged starting the discharging cycle. Table 10 shows the input design parameters for the 2nd mode of operation.

The 3rd mode of operation allows for a longer storage period of 10 hour. The fluid stored in the two tank molten salt storage systems will be discharged for a longer period of time compared to the 2nd mode of operation. However, because of that higher storage time period, the volume of the storage tank increases as seen from Table 11, where the input design parameters for the 3rd mode of operation are presented. The increase in the volume will naturally lead to an increase in the cost of the storage system.

Table 10: TES design parameters for the 2nd mode of operation

Parameter	Symbol	Unit	Value
Storage Media Type	-	-	Sensible
Storage Media	-	-	Hitec Salt
Cold Tank Temperature	T_{cold}	℃	250
Hot Tank Temperature	T_{hot}	℃	365
TES Density	ρ_{salt}	kg/m^3	1829.31
TES Specific heat	$C_{p_{salt}}$	kJ/kgK	1.56
Storage Volume	V_{TES}	m^3	43726.2
Tank Height	h_{tank}	m	20
Tank Diameter	D_{tank}	m	53
TES Thermal Capacity	$\dot{Q}_{tank}$	MWh	2981
TES Capacity	$t_{storage}$	$hour$	7.5

Table 11: TES design parameters for the 3rd mode of operation

	Symbol	Unit	Value
Storage Media Type	-	-	Sensible
Storage Media	-	-	Hitec Salt
Cold Tank Temperature	T_{cold}	℃	250
Hot Tank Temperature	T_{hot}	℃	365
TES Density	ρ_{salt}	kg/m^3	1829.31
TES Specific heat	$C_{p_{salt}}$	kJ/kgK	1.56
Storage Volume	V_{TES}	m^3	58301.6
Tank Height	h_{tank}	m	20
Tank Diameter	D_{tank}	m	61
TES Thermal Capacity	$\dot{Q}_{tank}$	MWh	3975
TES Capacity	$t_{storage}$	$hour$	10

3.6.2 ISRC/TES and ISRRC/TES systems.

The Integrated Solar Rankine Cycle/TES system and the Integrated Solar Regenerative Rankine Cycle/TES system can be divided into three main subsystems: The solar field, power block, and storage system. The solar field is basically the PTSC field, while the power block is the conventional Rankine cycle for the ISRC and the Regenerative Rankin Cycle for the ISRRC. The TES System consists of two tanks filled with Hitec salt. The properties of the Hitec salt shown in Tables 10 and 11 differ depending on the modes of operation. The ISRC and ISRRC will operate on either a full load operation, or a partial load operation depending on the beam radiation.

In the charging cycle and for the full load operation during the hours where the demand by the power cycle is met by operating the PSTC alone. The heating fluid from the PTSC field by passes the TES system and is directed toward the power cycle heat exchanger to heat up the water as seen in Figure 10 (a) for the ISRC/TES system and Figure 12 (a) for the ISRRC/TES system. While operating on partial load, when the mass flow rate from the PTSC field exceeds the designed flow rate for solar energy production,

i.e. during high solar radiation periods; the excess flow rate from the solar field will pass through the storage tank heat exchanger to charge the two tank Hitec salt storage system as seen in Figure 10 (b) and Figure 12 (b). The salt from the cold tank is heated and then directed to the hot tank where it is stored for later use. The system is controlled by the three way open valves placed between the PTSC solar field and the TES system. During the charging cycle the valves are open to let the heating fluid enter the heat exchanger and charge the system.

In the discharging cycle and for full load operation during the night hours where the PTSC is not in operation. The salt flows from the hot tank into the heat exchanger where it heats the water to steam, then the Hitec salt is directed back to the cold storage tank to be stored as seen in Figure 11 (a) for the ISRC/TES system and Figure 13 (a) for the ISRRC/TES system. While operating on partial load, during the low beam radiation hours mostly before sunset, both the TES system and the PTSC are in operation. The water from the power cycle is first heated up by the Hitec salt flowing from the hot storage tank, and then it is heated by the heating fluid from the PTSC field as seen in Figure 11 (b) and Figure 13 (b). The three way valves are used to regulate the flow between the PTSC field and TES system.

The same thermal storage salt is used in both integrated cycles, the molten salt used is Hitec and it possess great performance parameters; however there are still concerns about the freezing temperature of the salt in the tanks. Most molten salts freeze at high temperatures around100℃; in the Hitec case the freezing temperature is 142℃ , which might occur if the temperature in the cold tank drops during long periods of charging. Therefore, it is suggested to add a set of auxiliary heaters to maintain the design point temperature and heat the salt in case of temperature drop.

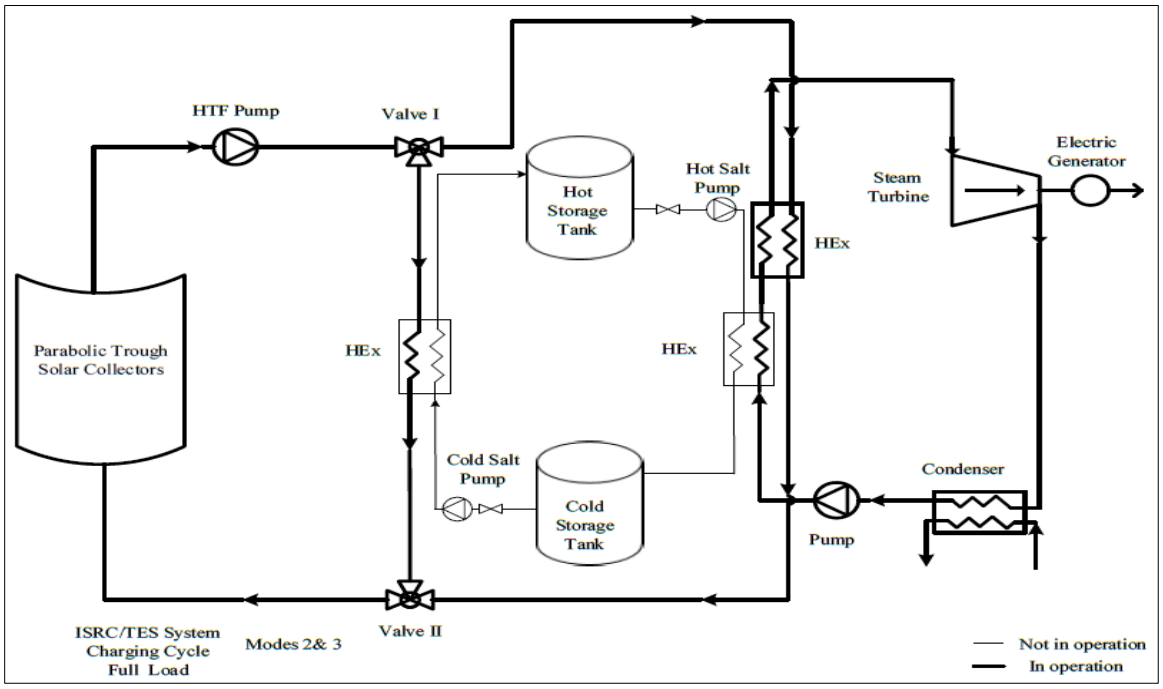

(a)

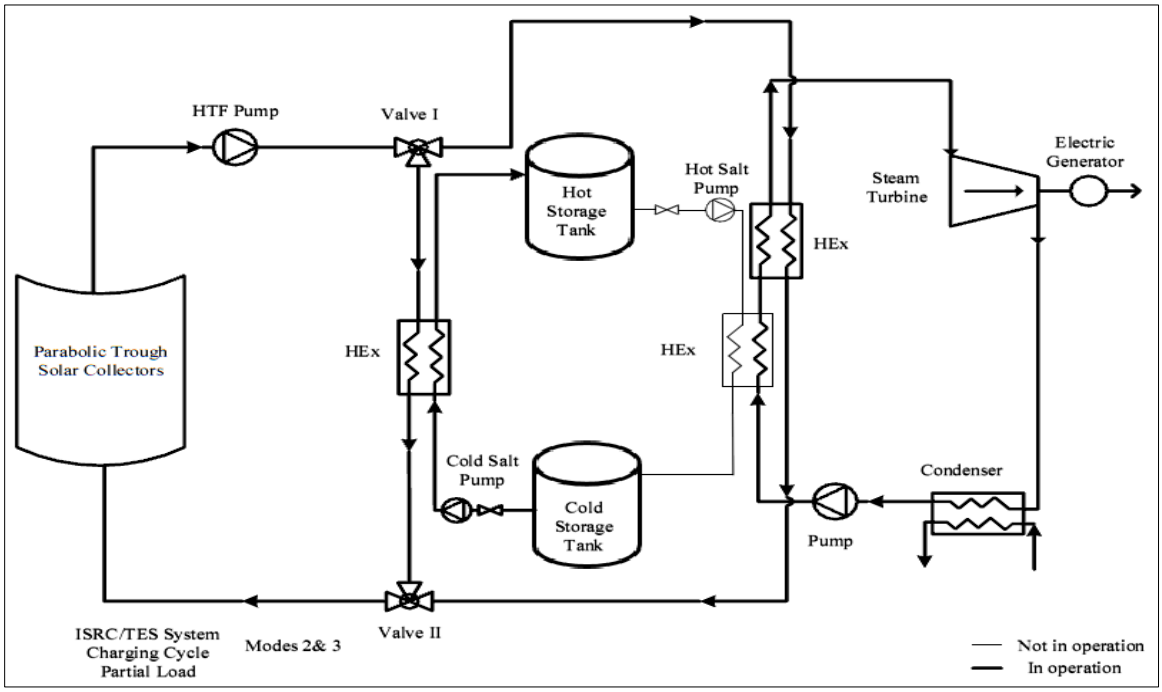

(b)

Figure 10: ISRC/TES Charging Cycle Schematic Diagram for (a) Full load, and (b) Partial load

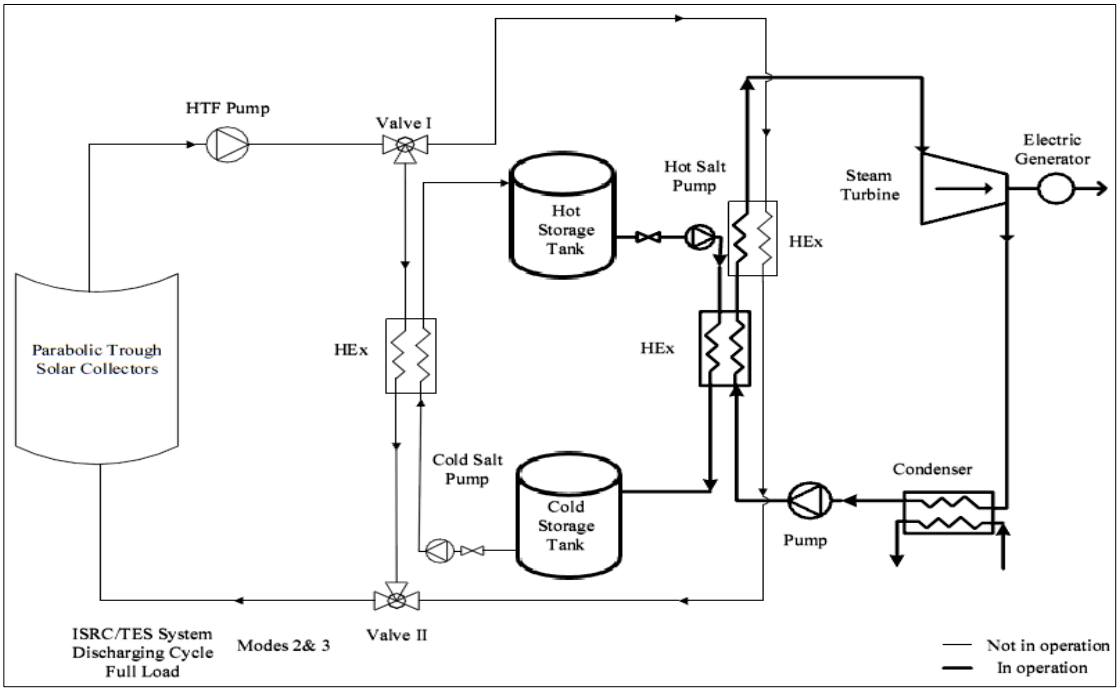

(a)

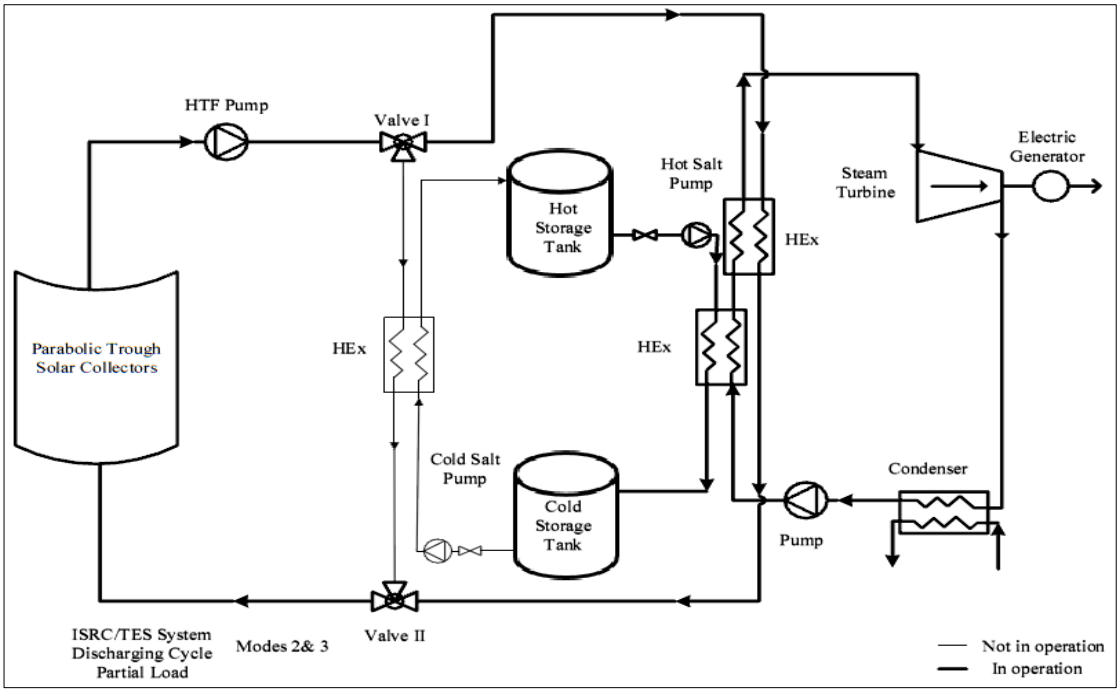

(b)

Figure 11: ISRC/TES Discharging Cycle Schematic Diagram for (a) Full load, and (b) Partial load

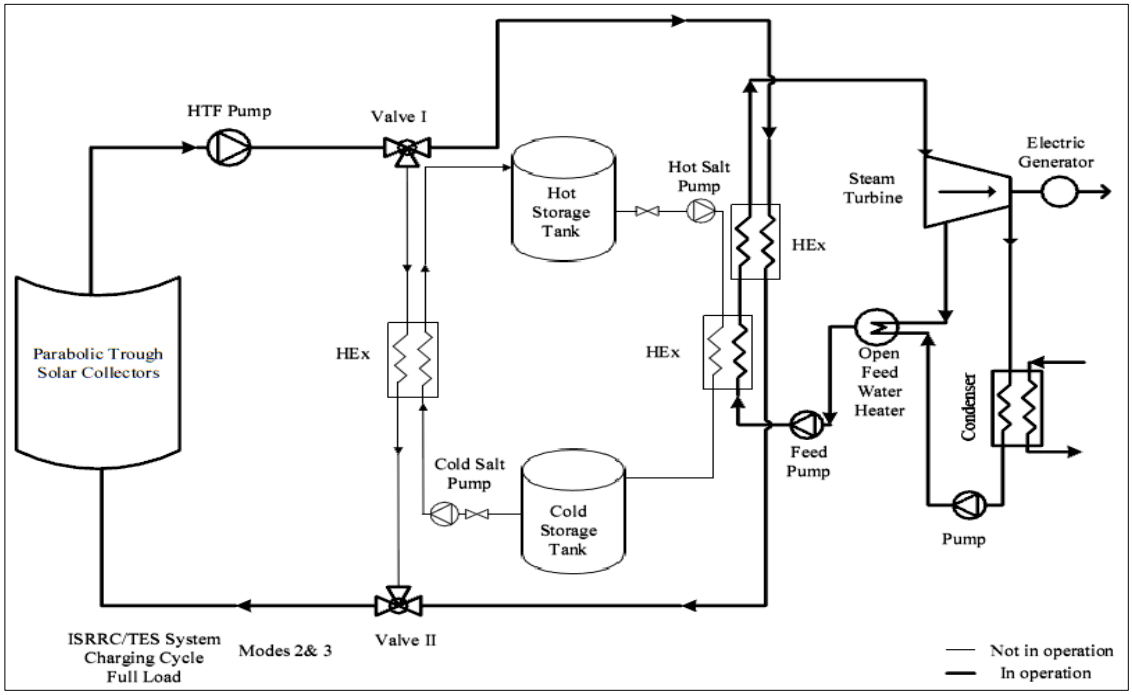

(a)

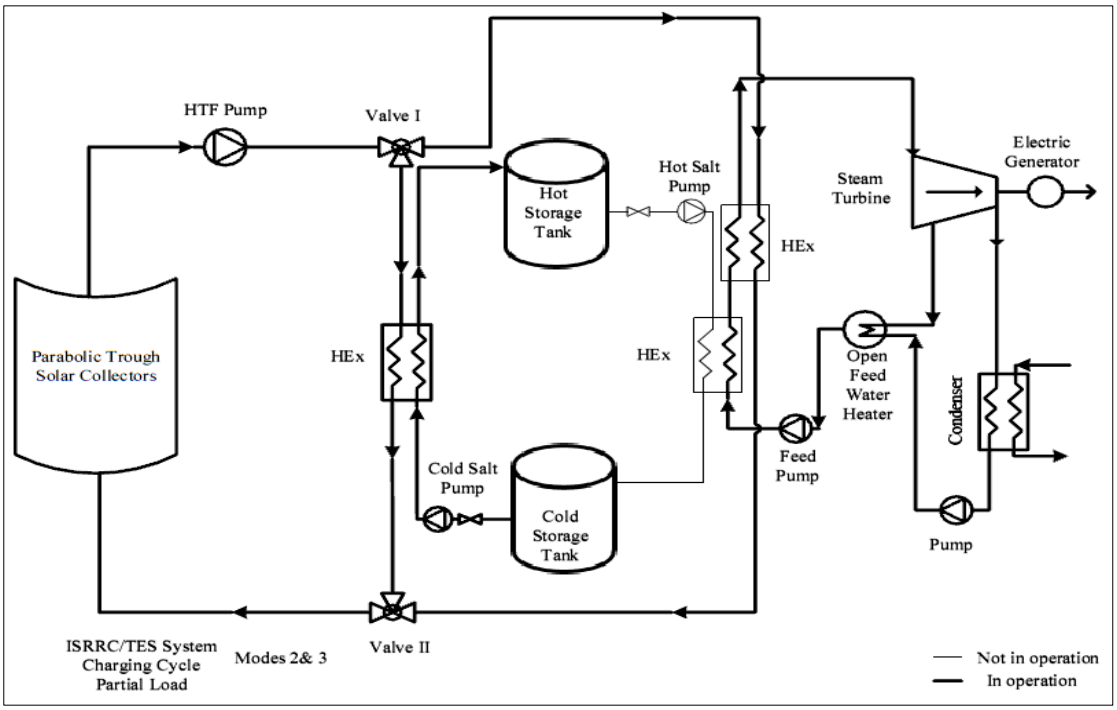

(b)

Figure 12: ISRRC/TES Charging Cycle Schematic Diagram for (a) Full load, and (b) Partial load

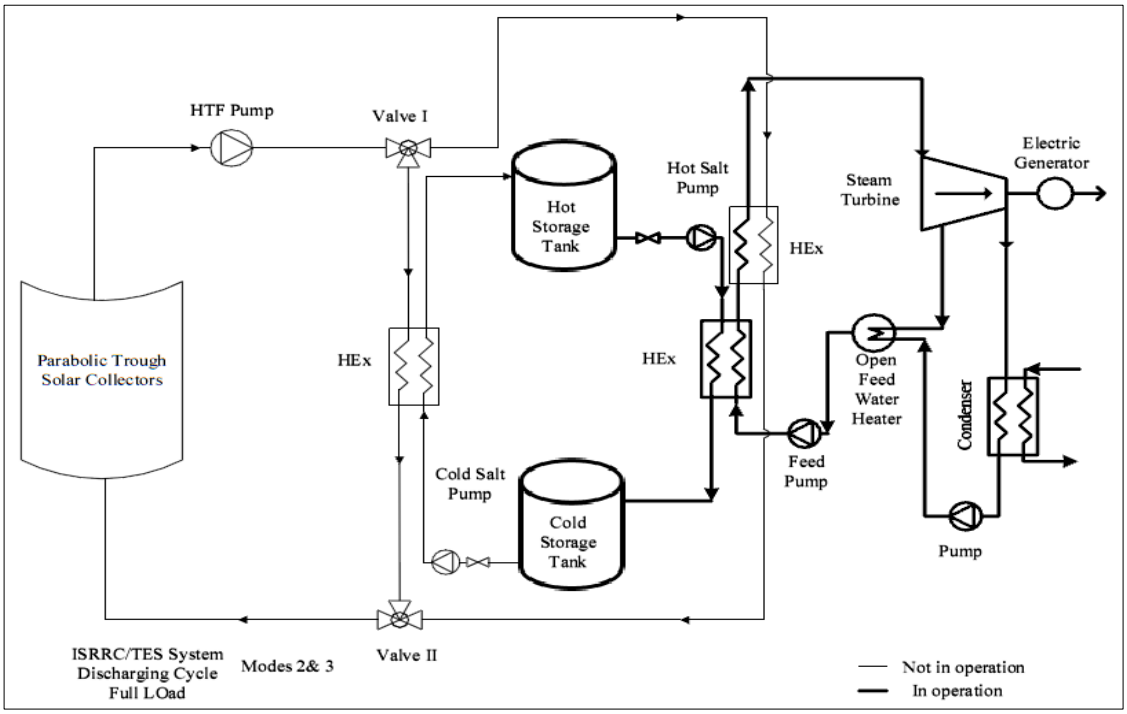

(a)

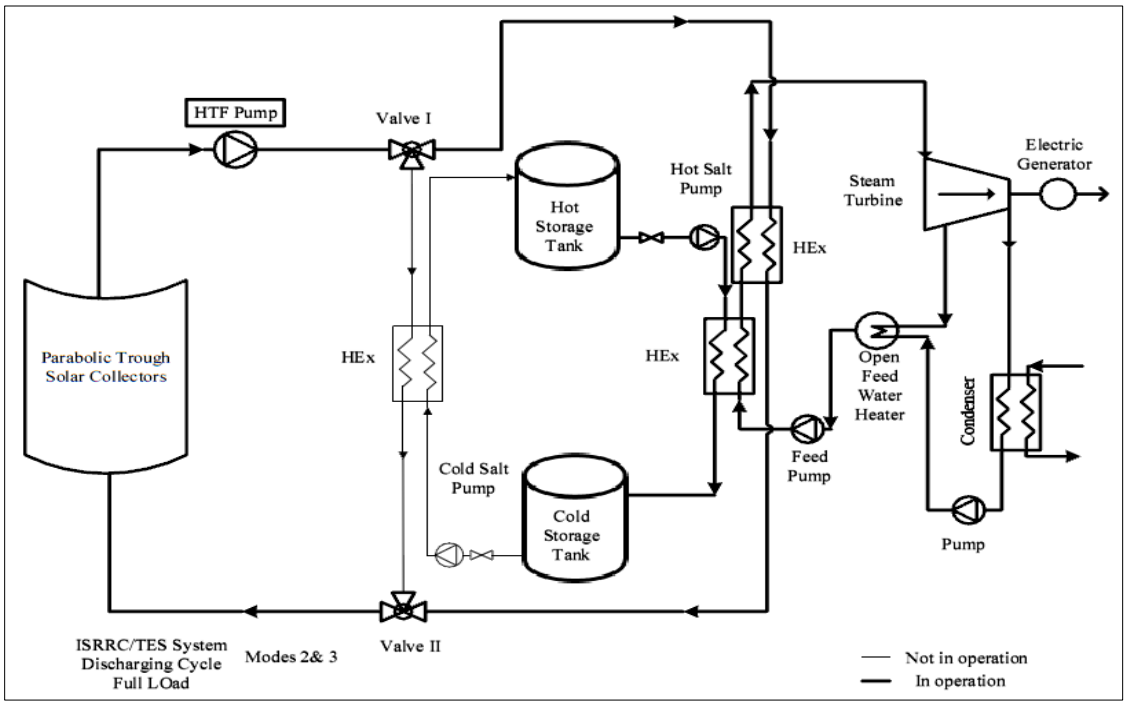

(b)

Figure 13: ISRRC/TES Discharging Cycle Schematic Diagram for (a) Full load, and (b) Partial load

Chapter 4: Results and Discussion

The following chapter presents the results and discussion of the provided system configurations and modeling parameters listed in the preceding chapter. The properties of the nanofluids are calculated, and their effect on the convective heat transfer is analyzed. The efficiency and power output of the systems are compared for different system configurations and mode of operations. Further, the use of nanofluids as a heating fluid is assessed and studied.

4.1 Meteorological data

The meteorological data is based on the city of Abu Dhabi, due to the geographical position of the city which lies on the Sun Belt which provides the use of solar energy for power production with great potential. The amount of solar radiation per day on the city of Abu Dhabi is around $18.48 MJ/m^2$, which is a considerably high amount. Figure 14 shows the variation of the time on the beam radiation for different months in the city of Abu Dhabi. It is observed that the months of June and September show the highest amount of solar beam radiation, while the month of March shows the lowest. Figure 15 shows the maximum and average beam radiation for different months. The climate in Abu Dhabi is mostly hot and dry, making the summer months very hot and uncomfortable. The variation of the time on the dry bulb temperature in the city of Abu Dhabi for different months is shown in Figure 16. It is seen that the summer months of August, June and July show the highest dry bulb temperatures with highs reaching $42\ ℃$. The maximum and average dry bulb temperatures for different months are shown in Figure 17. The high amounts of solar radiation allow for an easy and considerable change in power production, by shifting the normal power plants running on fuel into an integrated solar power production plants. Further, the geographic layout of the United Arab Emirates consists mostly of deserts, which can provide the large area needed for the installation of the PTSC solar field in order for the ISRRCs to run efficiently.

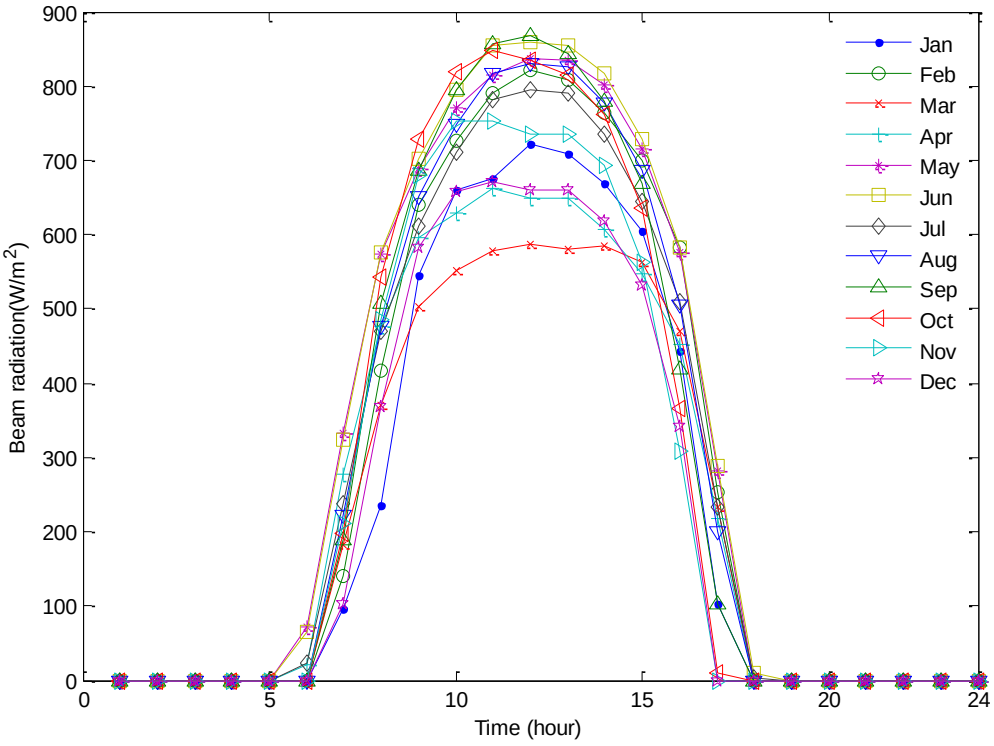

Figure 14: Effect of time on the beam radiation

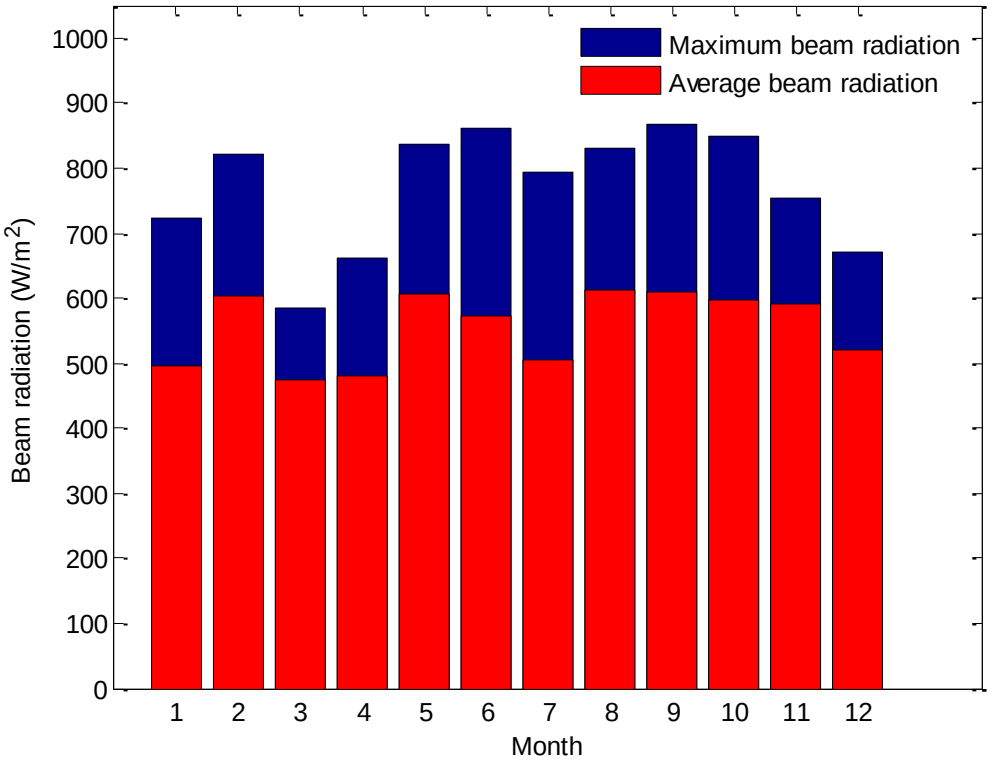

Figure 15: Maximum and average beam radiation

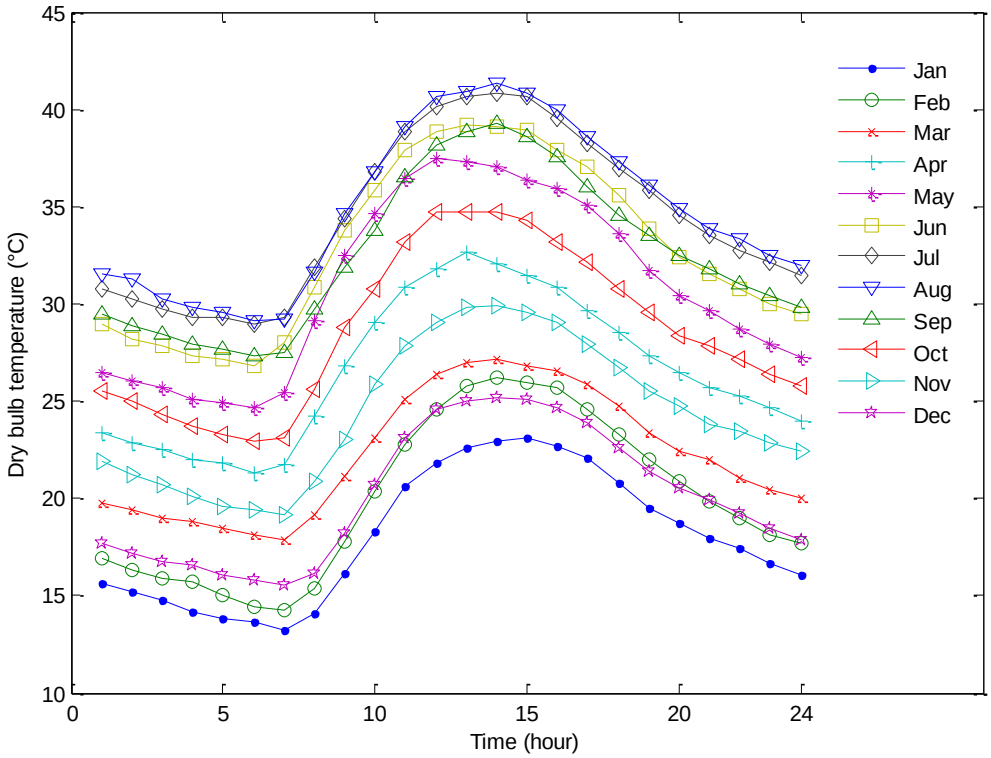

Figure 16: Effect of time on the dry bulb temperature

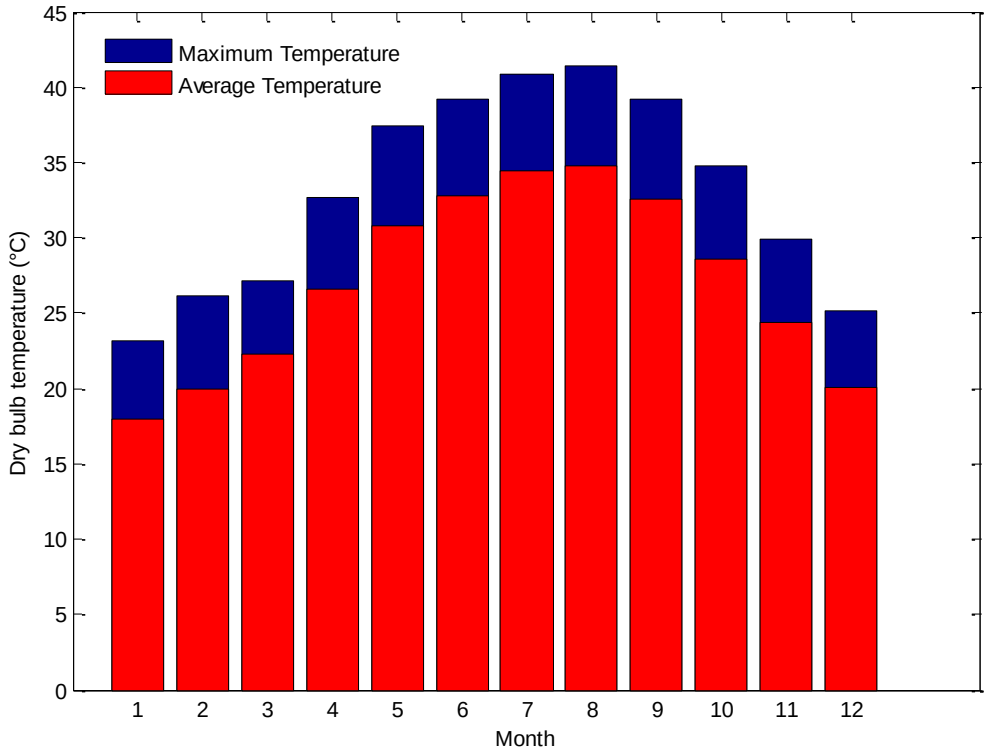

Figure 17: Maximum and average dry bulb temperatures

4.2 Heating fluid and Thermal Storage material selection

The following section shows a comparison between different heating fluids, and different TES materials in order to choose the most suitable fluid and material to carry the analysis.

4.2.1 Heating fluid selection.

Seven different heating fluids were compared in terms of annual energy output and levelized electricity cost, according the input data and design parameters provided in Tables 5-7. The heating fluids used for comparison in this study are: Therminol VP-1, Therminol 66, Therminol 59, Caloria HT 43, Dowtherm Q, Dowtherm RP, and Syltherm 800. Table 12 shows the comparison of different heat transfer fluids according to annual energy output and levelized electricity cost.

Table 12: Comparison between HTFs

HTF	Annual Energy Output	LEC
Unit	(KWh)	(c/KWh)
Caloria HT 43	477,686,400	3.92
Therminol VP-1	477,914,976	3.92
Dowtherm Q	478,991,136	3.91
Dowtherm RP	479,077,344	3.91
Therminol 59	475,040,800	3.94
Therminol 66	477,465,728	3.92
Syltherm 800	467,482,592	4.01

It is seen that Dowtherm RP shows the highest annual energy output followed by Dowtherm Q, Therminol VP-1 and Caloria HT 43 respectively. Regarding the LEC, it is also seen that Dowtherm Q, and Dowtherm RP show the least LEC, followed by Therminol VP-1 and Caloria HT 43 Respectively. Taking the previous comparisons into account, Dowtherm Q and Dowtherm RP are the most suitable heat transfer fluids to be used in this study. However, according to Table 6 the design outlet temperature of the loop is given as 391 ℃, where this temperature is higher than the operating temperatures

of Dowtherm Q and Dowtherm RP which are $-35\,℃ < T < 330\,℃\ and\ 0\,℃ < T < 330℃$ respectively. Given the temperature considerations, Therminol VP-1 is chosen as the best and most suitable heat transfer fluid to be used. Further, Syltherm 800 is also used as a heat transfer fluid in this study, in order to analyze the magnitude of enhancement that can result from adding nanoparticles to the fluid. In that sense, the most suitable and least suitable heat transfer fluids can be compared in terms of the enhancement, when nanoparticles are added.

4.2.2 TES material selection.

The Thermal Energy Storage material is important for analysis as it impacts the volume of the storage tank. For the input data and design parameters provided in Tables 5-7, a comparison between different molten salts in terms of the storage volume is done. The molten salts used are: Hitec Solar Salt, Hitec XL and Hitec. Table 13 shows a comparison between different molten salts for Thermal Energy Storage Material. The comparison was done for a thermal capacity of 2981 MW_{ht}.

Table 13: Comparison between different Salts for TES material

Molten Salt	Storage Volume
Unit	m^3
Hitec Solar Salt	44373
Hitec XL	44491
Hitec	43726

The storage volume is the smallest when Hitec salt is used as a TES material. Therefore, Hitec is used a TES material in this study. The properties of the salt are already shown in Tables 10 and 11. The molten salt in general was used, in order to take advantage of the high specific heat capacity which allows for a greater storage period and a smaller storage volume.

4.3 Nanofluids properties

The thermophysical properties of the nanofluids are calculated and compared based on the models and equations provided in the preceding chapter. However, first the

properties of the base fluids and nanoparticles alone are analyzed in order to understand the behavior of these properties with respect to temperature.

4.3.1 Base fluids properties.

The thermophysical properties of the base fluids vary with the change in temperature. This section aims to study the type of change caused by temperature on the properties of the base fluids. The correlations from sections 3.1.1.1 and 3.1.1.2 are used to calculate the properties of Therminol and Syltherm respectively. Figure 18 shows the variation of the temperature on the density of Therminol and Syltherm. It is seen that the density of the base fluids decreases as the temperature increases, implying an inversely proportional relation between the density and the temperature. Further, it is observed that the density of the Therminol is higher than that of Syltherm.

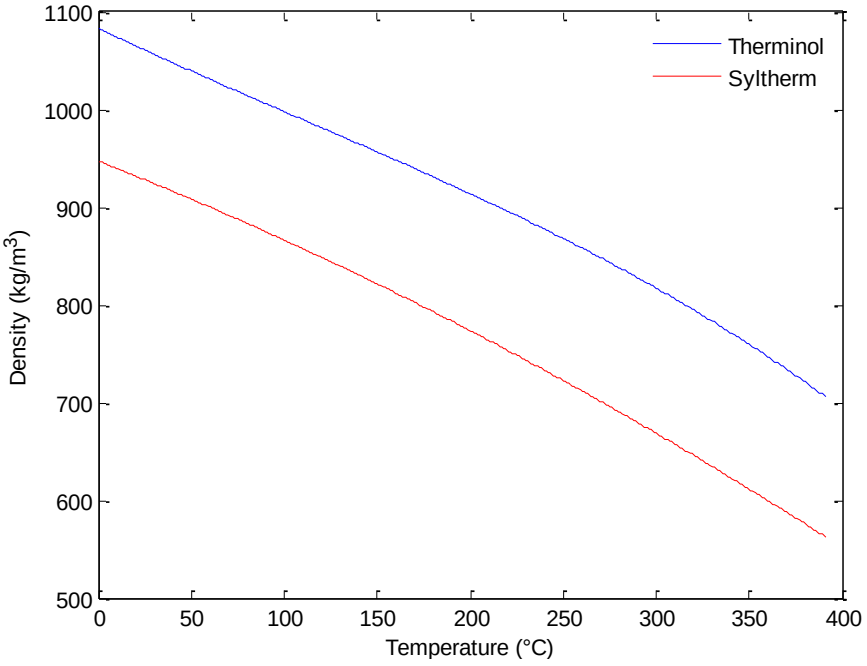

Figure 18: Effect of temperature on the density of the base fluids

The variation of the tempertaure on the specific heat capacity of Therminol and Sylthem is shown in Figure 19. It is seen that the specifc heat capacity increases with the increase of the temperature suggesting a directly proportional relation between the two. Moreover, it is observed that the specific heat capacity of Syltherm is higher than that of

Therminol only for low temperatures (below 80 ℃), then Therminol exhibits a higher specific heat capacity.

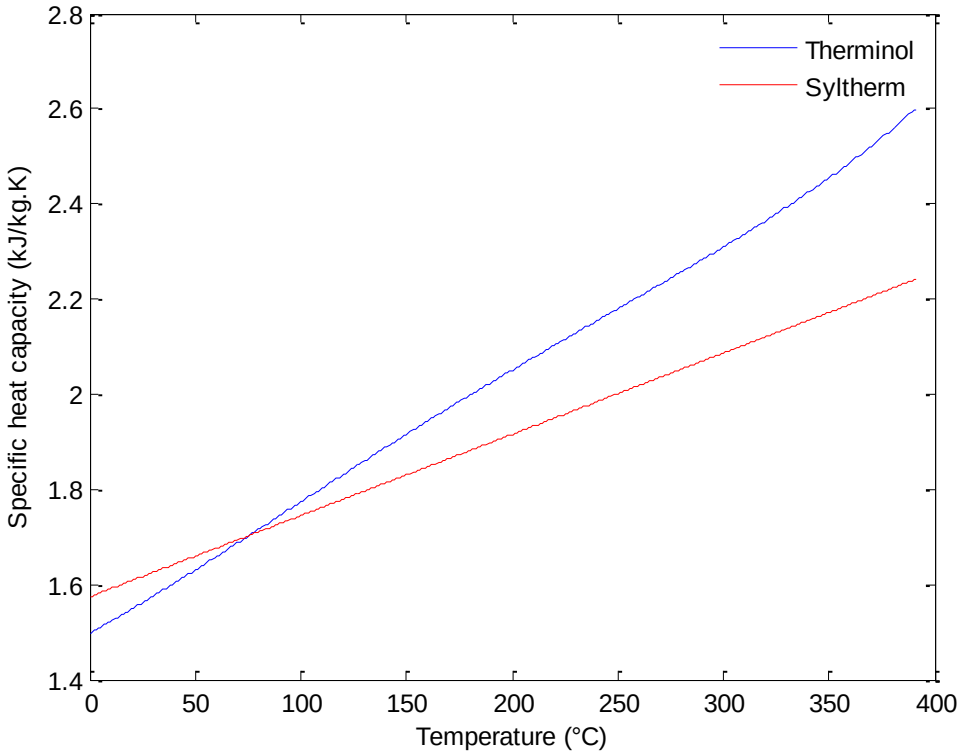

Figure 19: Effect of temperature on the specific heat capacity of the base fluids

Figure 20 shows the variation of the temperature on the thermal conductivty of Therminol and Syltherm. It is seen that the thermal conductivity decreases with the increase of temperature implying an inversly proportional relation. Further, the thermal conductivty of Therminol is higher than that of Syltherm.

The variation of the temperature on the viscosity of Therminol and Syltherm is shown in Figure 21. It is seen that the viscosity drops exponentionally with temperature increase and becomes constant at very high temperatures. In addition, it is observed that the viscosty of Syltherm is almost double that of Therminol at room temperaure, even at high temperatures the difference is still present.

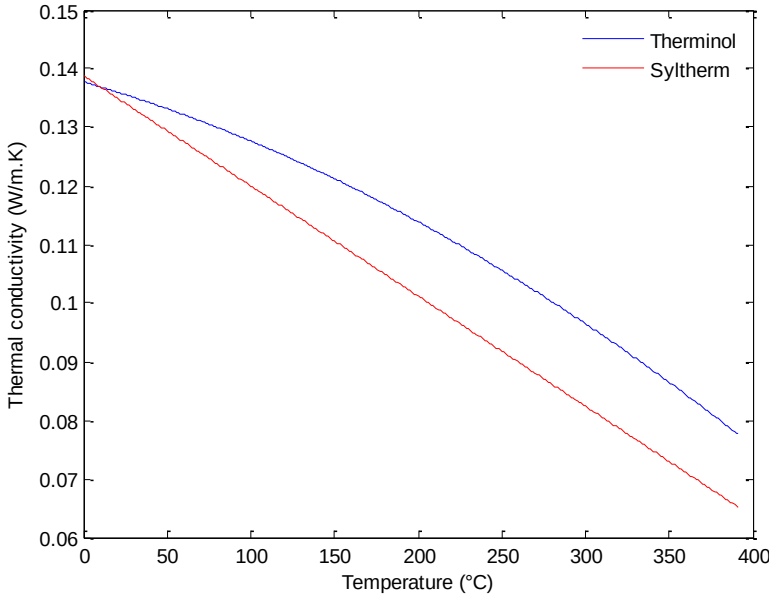

Figure 20: Effect of temperature on the thermal conductivity of the base fluids

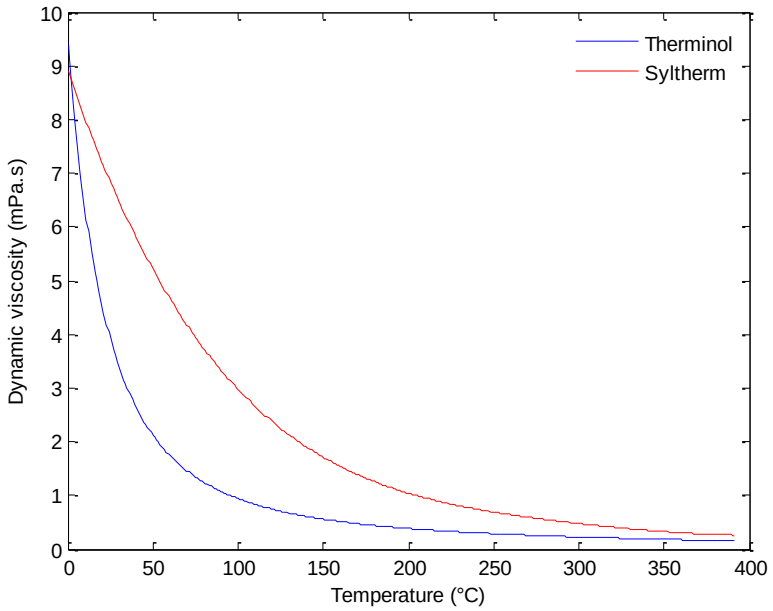

Figure 21: Effect of temperature on the dynamic viscosity of the base fluids

4.3.2 Nanoparticles properties.

The thermophysical properties of the nanoparticles and their relation with temperature are studied. From section 3.1.2, it is observed that the density of the nanoparticles is constant with respect to the temperature. The specific heat capacity of

$SWCNT$ is also constant and it is equal to$1.38\,kJ/kg\cdot K$, however the specific heat capacities of $Al_2O_3$and Cu vary with respect to the temperature.

Figure 22 shows the variation of the temperature on the specific heat capacity of Al_2O_3 and Cu nanopartciles. It is seen that similar to the base fluids, the specific heat capacity and the temperature are directly proportional. Moreover, it is observed that the specific heat capacity of $Al_2O_3$is twice as much as Cu nanoparticles.

The variation of the temperature on the thermal conductivity of Al_2O_3 and Cu nanoparticles is shown in Figure 23. It is seen that the thermal conductivity of the nanoparticles decreases with the increase in temperature. Further, because of the metallic structure of Cu nanoparticles, their thermal conductivity is 10 times that of Al_2O_3 nanoparticles.

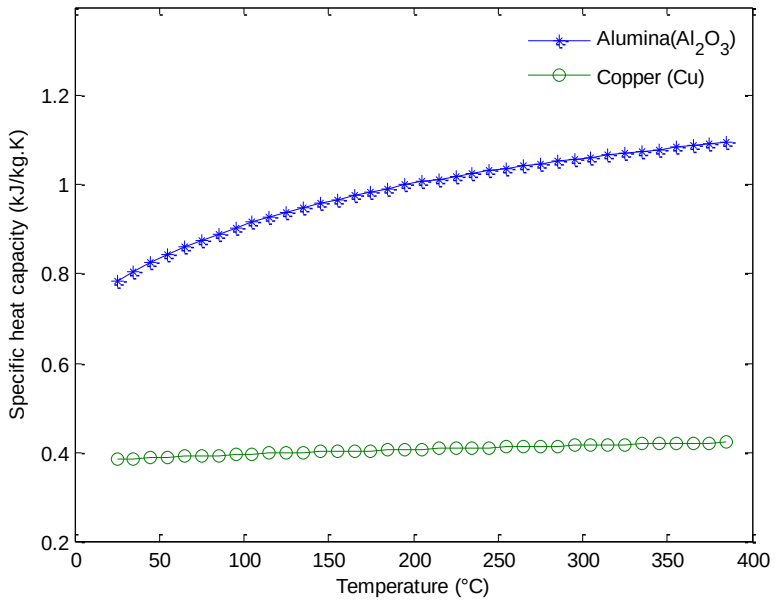

Figure 22: Effect of temperature on the specific heat capacity of $\boldsymbol{Al_2O_3}$ and $\boldsymbol{Cu}$ nanoparticels

Regarding the $SWCNT$ nanoparticles and as seen from Equation (3.17), the thermal conductivity depends on the length of the nanoparticles. Figure 24 shows the variation of the temperature on the thermal conductivity of $SWCNT$ nanoparticles for different lengths. It is seen that the thermal conductivity decreases with the increases in temperature. As for the length of the $SWCNT$, it is observed that the longer the

nanoparticle, the higher the thermal conductivity; however, for a length more than $3\mu m$, the increase in the thermal conductivity becomes almost negligible. Compared to Al_2O_3 and Cu nanopartciles, $SWCNT$ nanoparticles possess a much higher thermal conductivity even at small lengths.

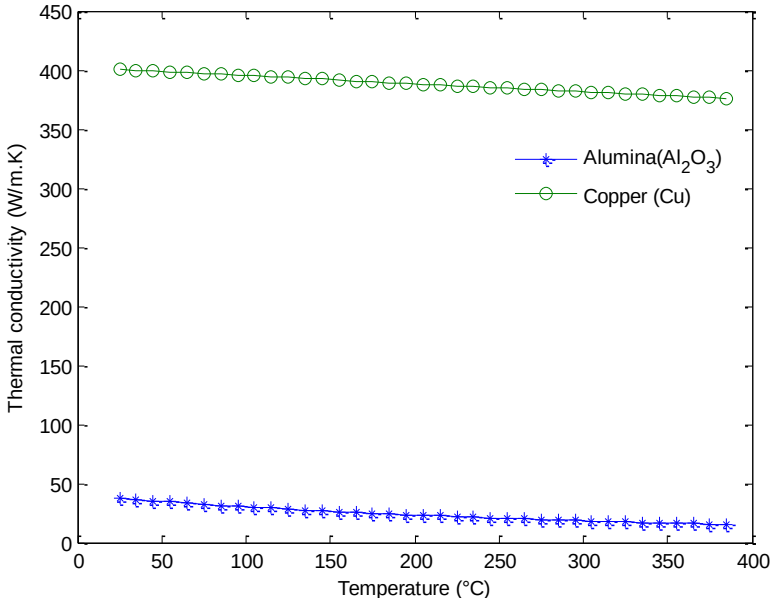

Figure 23: Effect of temperature on the thermal conductivity of $\boldsymbol{Al_2O_3}$ and $\boldsymbol{Cu}$ nanoparticels

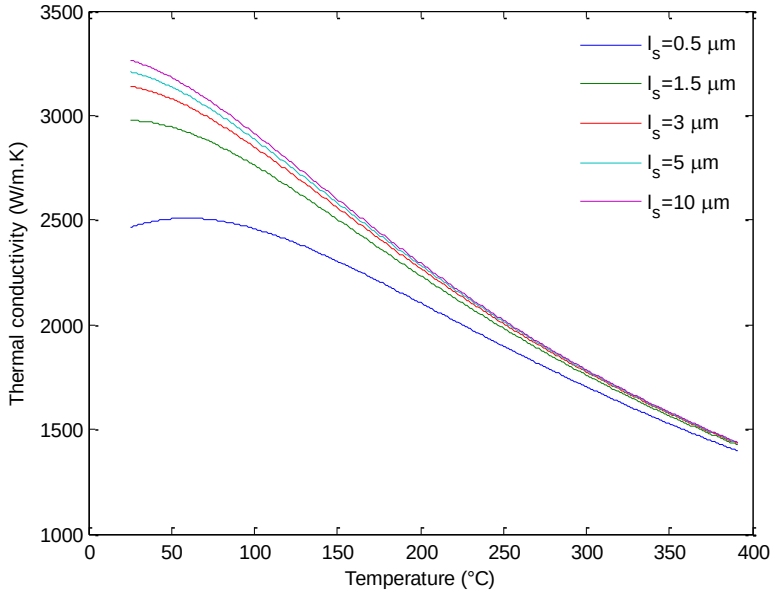

Figure 24: Effect of temperature on the thermal conductivity of $\boldsymbol{SWCNT}$ nanoparticles for different lengths

4.3.3 Nanofluids density.

The density of nanofluids depends on the density of the base fluid and the density of the nanoparticles. Since the density of the nanoparticles is higher than that of the base fluids, it is expected that adding nanoparticles to the base fluid will increase the density of the fluid. Figure 25 shows the variation of the volume fraction on the density of Therminol-based and Syltherm-based nanofluids. The density was evaluated at an average temperature between the inlet and outlet conditions specified in Table 6. This temperature is 342 ℃. It is seen that the density of the nanofluids increases with the increase in volume fraction, and Cu-based nanofluids has the highest density increase where that increase can be attributed to the high density of Cu nanoparticles.When comparing the nanofluids, it can be seen that Syltherm-based nanofluids display lower density value than that of Therminol-based nanofluids. Since the density of Syltherm is less than that of Therminol, the density of Syltherm based nanofluids is less than the density of Therminol based nanofluids.

Figure 26 shows the variation of the temperature on the density of Therminol-based and Syltherm-based nanofluids for a volume fraction 5%. It is seen that the nanofluids density decreases with the increase in temperature. This behavior is expected since the density of the base fluids decreases with the increase in temperature, while the density of the nanoparticles is constant, therefore having no contribution to the behavior of the density of nanofluids. Moreover, it is noticed that $SWCNT$-based nanofluids show the lowest increase in the density, and that is because of the density of $SWCNT$ nanoparticles which is marginally larger than the densities of the base fluids. The density of the Syltherm$/Al_2O_3$ nanofluid agrees with the results provided by [155] where the effect of the temperature on the density of Syltherm$/Al_2O_3$ nanofluid was studied.

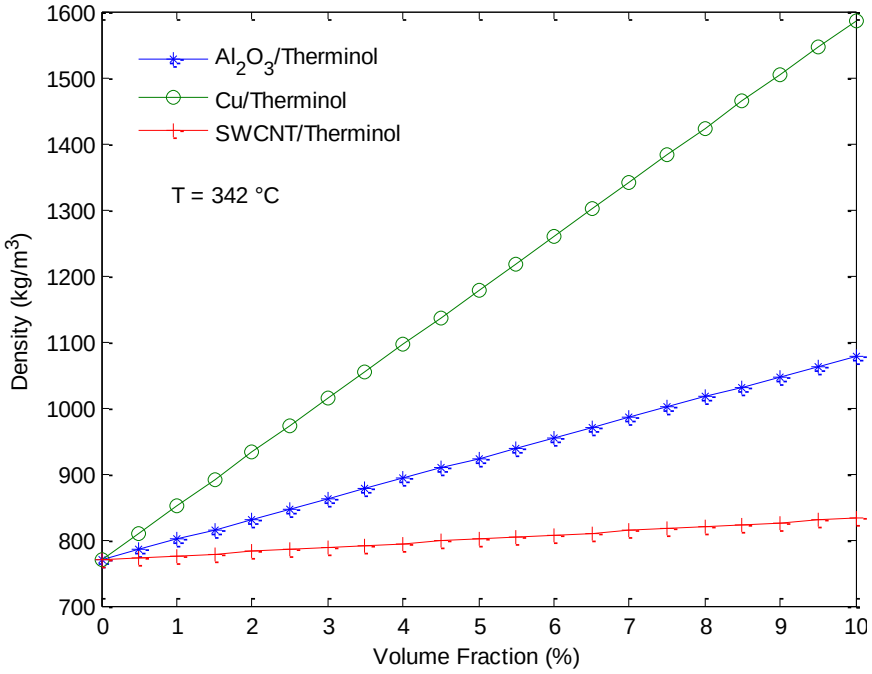

(a)

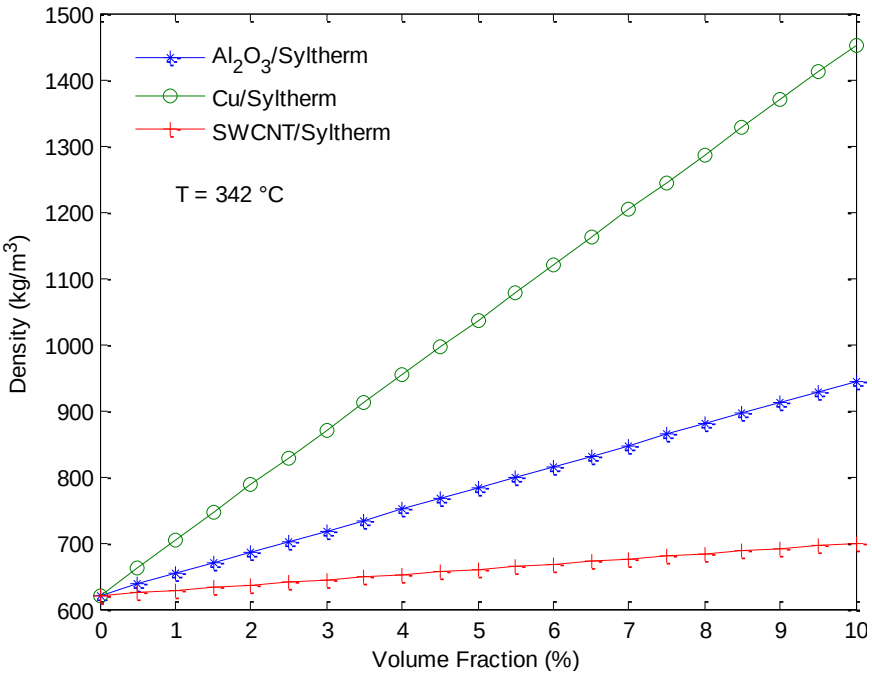

(b)

Figure 25: Effect of volume fraction on the density of (a) Therminol-based nanofluids and (b) Syltherm-based nanofluids

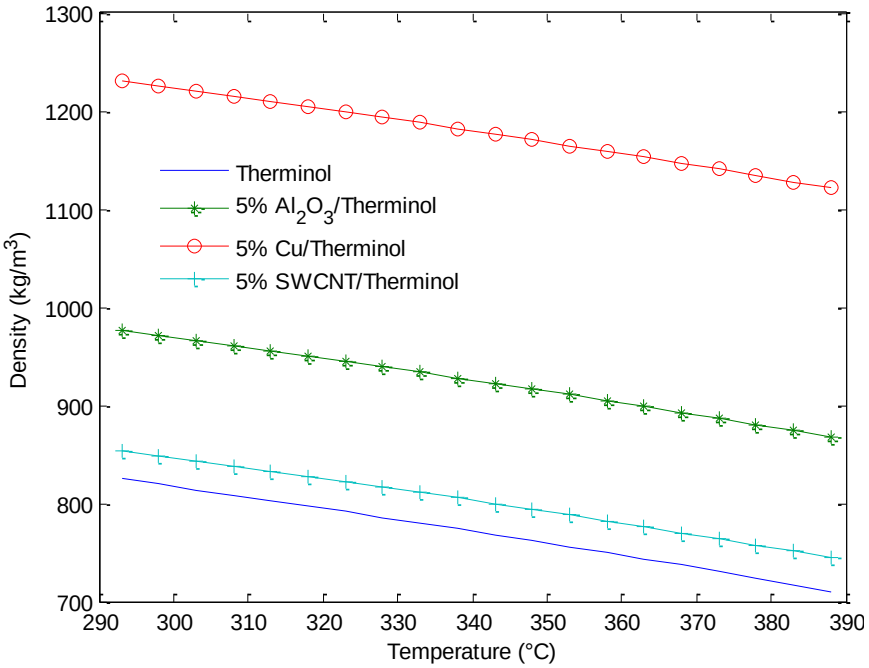

(a)

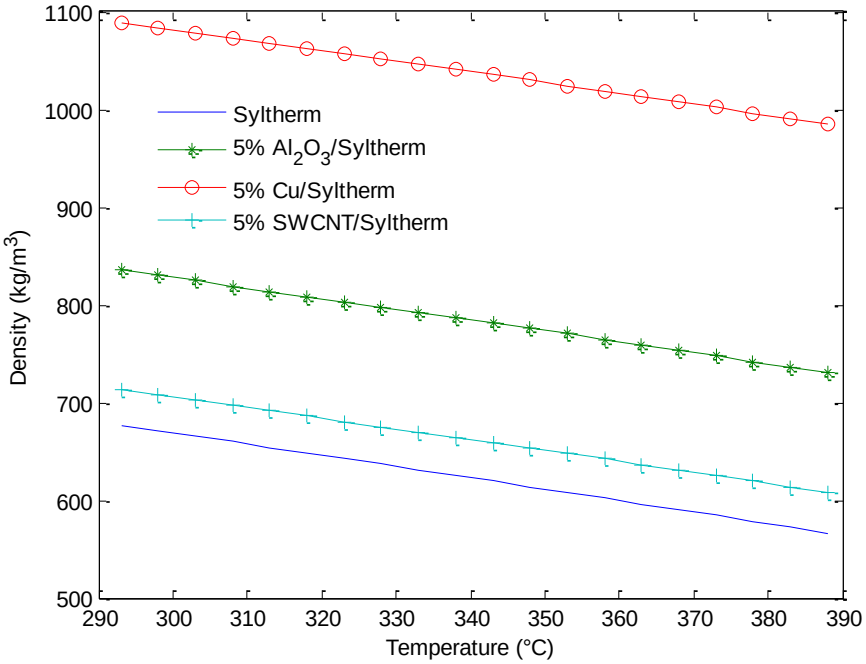

(b)

Figure 26: Effect of temperature on the density of (a) Therminol-based nanofluids and (b) Syltherm-based nanofluids ($\boldsymbol{\varphi = 5\%}$)

4.3.4 Nanofluids specific heat capacity.

The specific heat capacity of the nanofluids depends on the specific heat of the base fluid, specific heat of the nanoparticles and the volume fraction. The specific heat capacity is the amount of energy needed to change the temperature of a fluid weighing 1 kg by one degree. It is important because it affects the thermal energy storage.

Figure 27 shows the variation of the volume fraction on the specific heat capacity of Therminol-based nanofluids and Syltherm-based nanofluids for a temperature of 342 ℃. It is seen that adding nanoparticles to the base fluids decreases the specific heat capacity of the fluid. However, this decrease is considerably small for all the Therminol-based and Syltherm-based nanofluids. However, since the specific heat capacity of Syltherm is lower than that of Therminol, the specific heat capacity of Therminol-based nanofluids is higher than that of Syltherm-based nanofluids.

Figure 28 shows the variation of the temperature on the specific heat capacity of Therminol-based nanofluids and Syltherm-based nanofluids for a volume fraction of 5%. It is seen that the specific heat capacity increases with the increase in temperature. Comparing the nanofluids, $SWCNT$-based nanofluids show the least decrease in the specific heat capacity and that is because the $SWCNT$ nanoparticles have the highest specific heat capacity compared to Al_2O_3 and Cu nanoparticles. Nevertheless, while comparing other nanofluids, it is observed that the decrease in the heat capacity is considerably small. The variation of the temperature on the specific heat capacity of Syltherm/Al_2O_3 shown in Figure 28, agrees with the results provided by [155] where the effect of the temperature on the specific heat capacity of Syltherm/Al_2O_3 was investigated.

Referring to Equation (3.19) it is seen that in order to enhance the specific heat capacity of a base fluid, nanoparticles with higher specific heat capacity than the fluid are ought to be added. Otherwise, the contribution of the nanoparticles will always have a negative effect on the specific heat capacity of the nanofluids, since nanoparticles with the lower specific heat capacity are replacing the base fluid with the higher specific heat capacity resulting in a decrease in the overall specific heat capacity of the nanofluids.

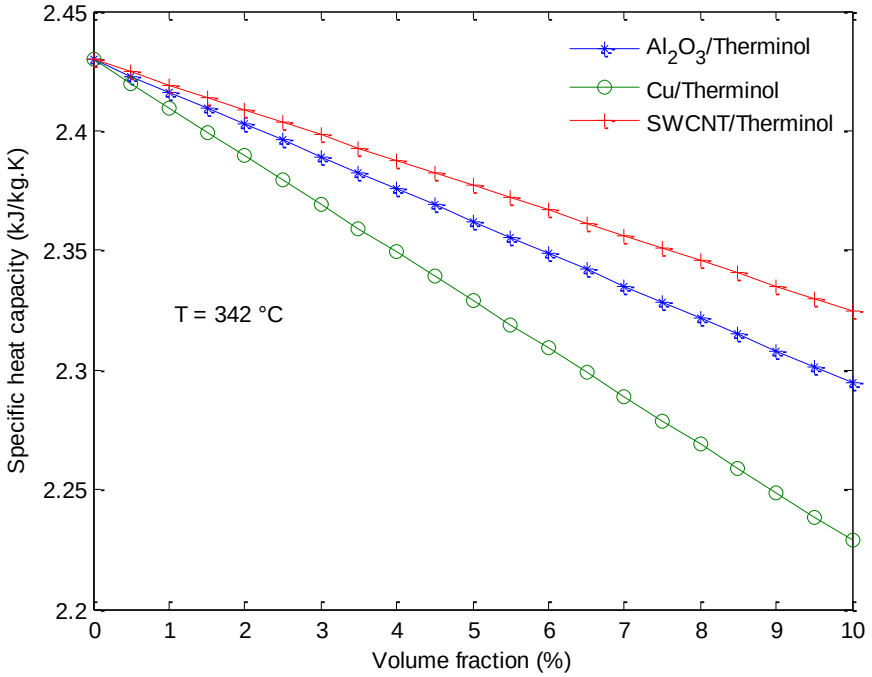

(a)

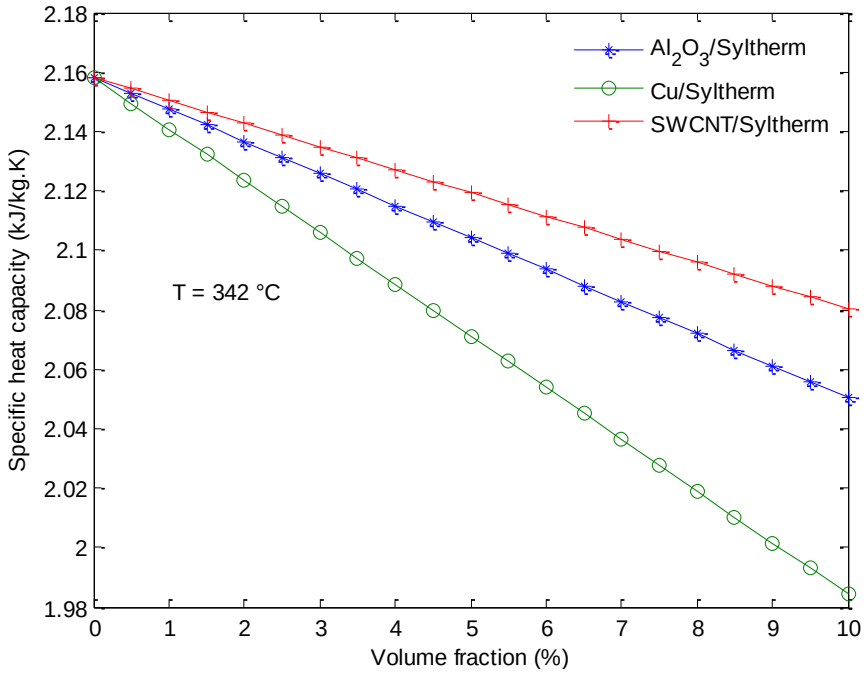

(b)

Figure 27: Effect of volume fraction on the specific heat capacity of (a) Therminol-based nanofluids and (b) Syltherm-based nanofluids

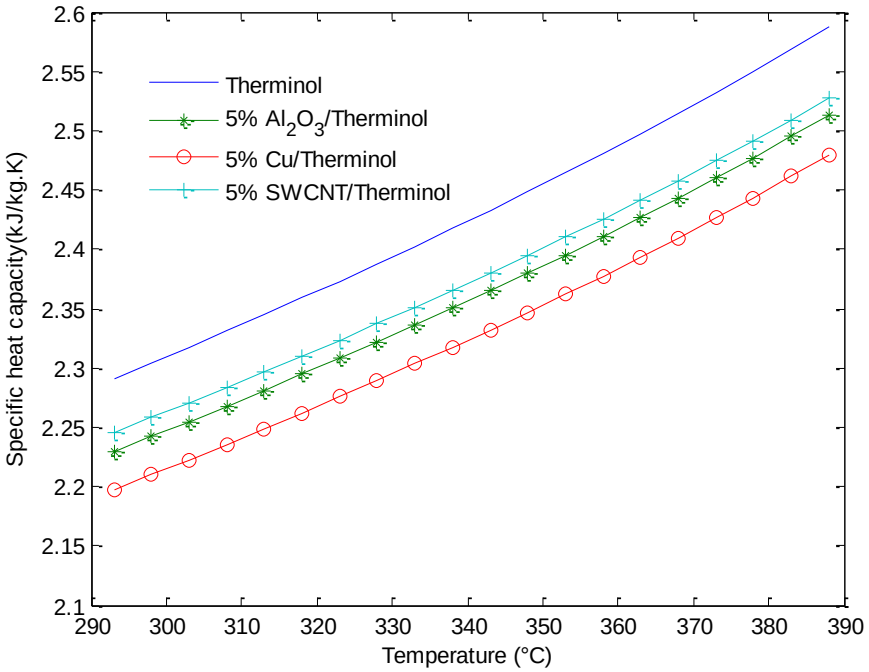

(a)

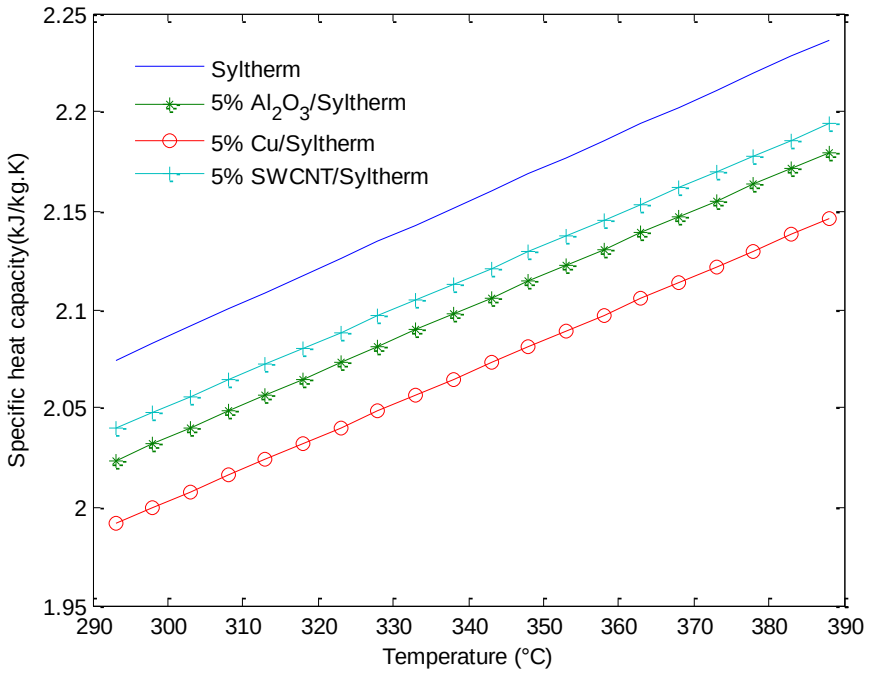

(b)

Figure 28: Effect of temperature on the specific heat capacity of (a) Therminol-based nanofluids and (b) Syltherm-based nanofluids ($\boldsymbol{\varphi = 5\%}$)

4.3.5 Nanofluids viscosity.

The viscosity of the nanofluids depends mostly on the viscosity of the base fluid and the volume fraction. Different models can be used to estimate the viscosity of the nanofluids as seen from section 3.1.5. Figure 29 shows the variation of the temperature on the viscosity of Therminol-based nanofluids using different models for a volume fraction of 3%. It is seen that most of the viscosity models are in close agreement with each other, except for the Pak and Cho model given by Equation (3.29), where it over estimates the nanofluids viscosity. The model chosen for the estimation of the nanofluids is the Batchelor model [94] because it takes into account the Brownian motion of the nanoparticles inside the fluid, which is the movement caused by the nanoparticles when they are dispersed into the nanofluids.

The effect of the nanoparticles diameter on the viscosity of the nanofluids is studied using the Avsec and Oblac model [98]. Figure 30 shows the variation of the temperature on the viscosity of Therminol based nanofluids for different nanoparticle radii and a volume fraction of 3%. It is seen that increasing the nanoparticles radius has a negligible effect on the viscosity of the nanofluids.

Figure 31 shows the variation of the temperature on the viscosity of Therminol-based nanofluids and Syltherm-based nanofluids for different volume fractions. It is seen that the viscosity of the nanofluids decreases with the increase in the temperature, and increases with the increase in the volume fraction. Since the nanoparticles material has no effect on the viscosity of the nanofluids, all Therminol-based nanofluids and Syltherm-based nanofluids share the same viscosity values at different volume fractions and temperatures. Compared to Therminol-based nanofluids, the viscosity of Syltherm-based nanofluids is much higher, and that is because of the high viscosity of Syltherm. The viscosity of the Syltherm based nanofluids agree with the results obtained from [155], where the effect of the temperature on the viscosity of Syltherm/Al_2O_3 nanofluid was studied. In addition, it is seen that the increase in the viscosity with volume fraction of Syltherm-based nanofluids is higher than that of Therminol-based nanofluids, concluding that the addition of the nanoparticles has a higher effect on Syltherm base fluid when compared to Therminol base fluid.

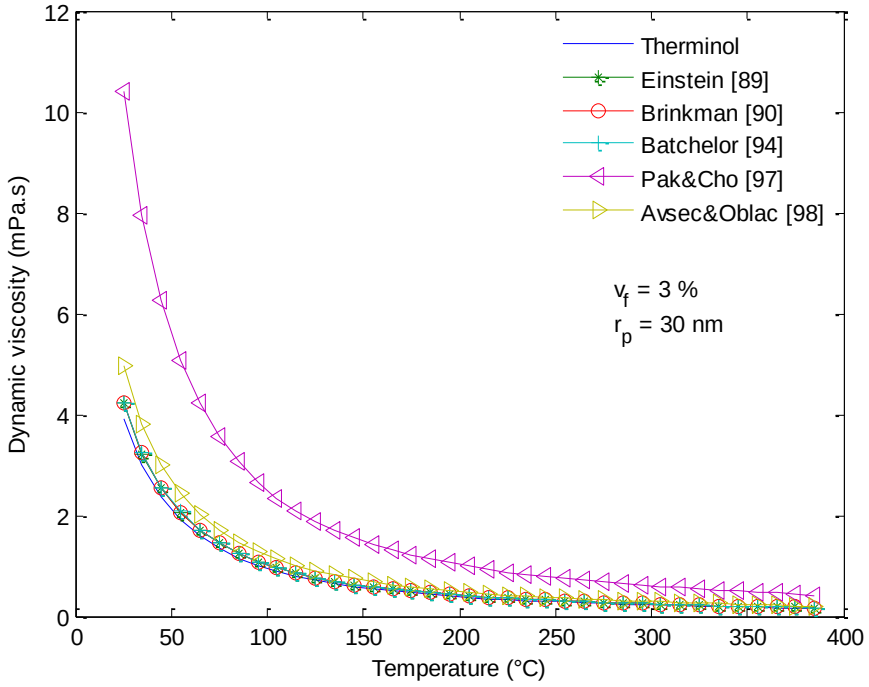

Figure 29: Effect of temperature on the dynamic viscosity of Therminol-based nanofluids for different viscosity models($\boldsymbol{\varphi = 3}$ %)

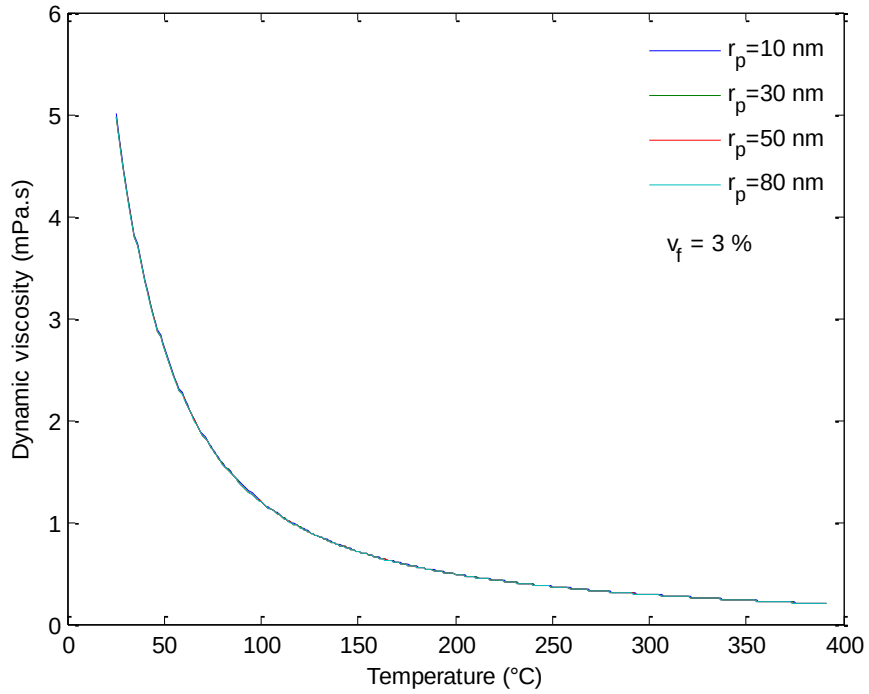

Figure 30: Effect of temperature on the dynamic viscosity of Therminol-based nanofluids for different nanoparticle radii ($\boldsymbol{\varphi = 3}$%)

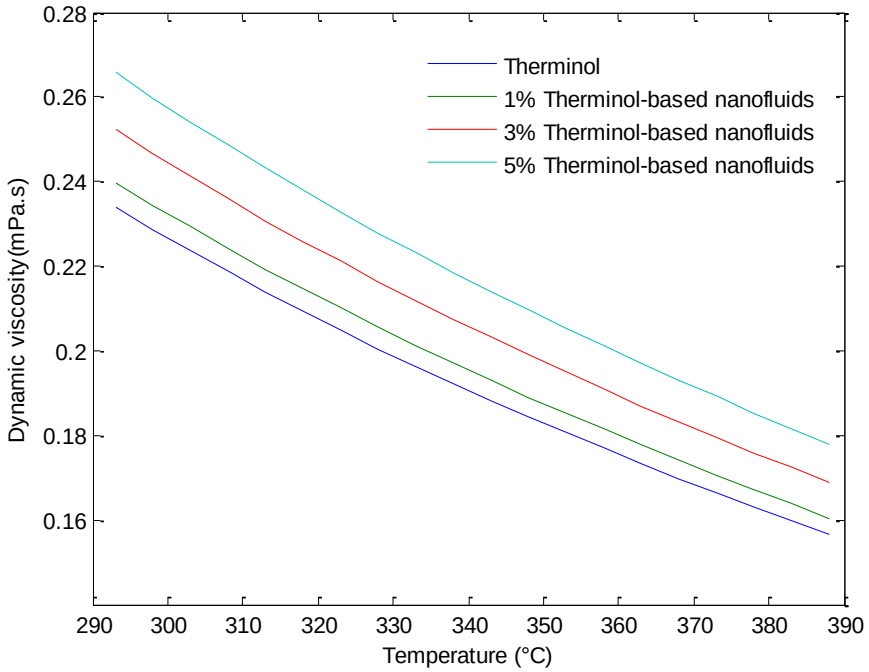

(a)

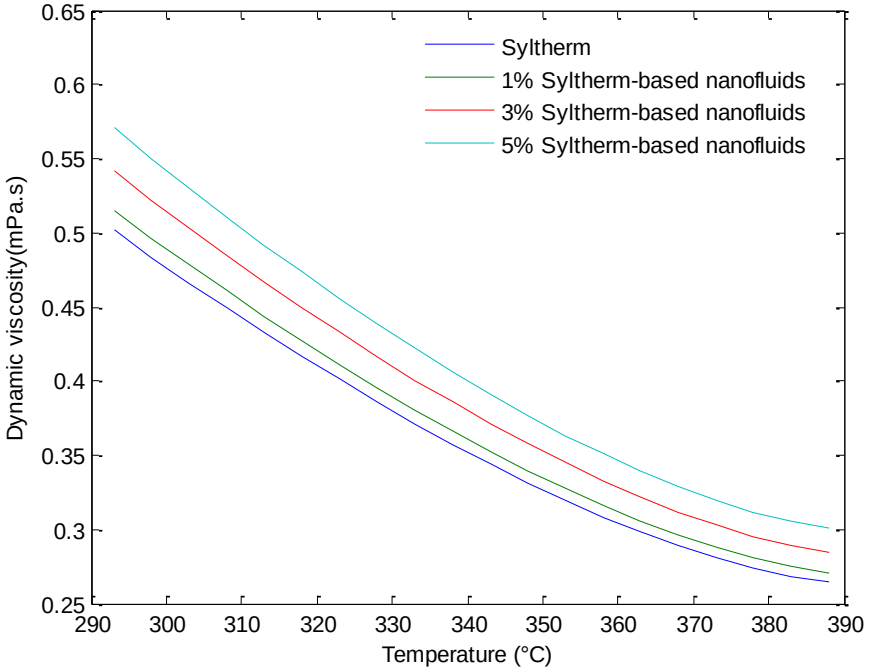

(b)

Figure 31: Effect of temperature on the dynamic viscosity of (a) Therminol-based nanofluids, and (b) Syltherm-based nanofluids for different volume fractions

4.3.6 Nanofluids thermal conductivity.

In the following section, the thermal conductivity of the nanofluids is investigated and analyzed. The main focus of adding nanoparticles to the base fluids is the thermal conductivity enhancement, and how that enhancement can be used to improve the heat transfer rate and the amount of heat absorbed by the fluid. Given the importance of the thermal conductivity, much research and experiments were done to evaluate the value of enhancement, and the mechanism behind it. Hence the analysis is divided into different sections, where the suitable thermal conductivity models are to be selected, then the effect of different parameters on the thermal conductivity of nanofluids are studied and presented.

4.3.6.1 Comparison of models.

Numerous models for the prediction of the thermal conductivity of nanofluids can be found in the literature. Section 3.1.5 shows a number of models that are applicable for the conditions provided in this study. However, in order to choose the most suitable model to carry out the analysis, a comparison is done between different models and experimental data. Figure 32 shows a comparison between the thermal conductivity of EG/Cu nanofluids with a nanoparticle radius of $3\,nm$ for various models and experimental data provided by Eastman et al. [30]. Since the base fluids used in the analysis (Therminol, Syltherm) are not widely experimented on, other base fluids are used in this section for the purpose of comparing the accuracy of the models to the experimental data. For instance, ethylene glycol is used, and its thermal conductivity is $0.253\,W/mK$. It is seen that almost all the models underestimate the thermal conductivity of EG/Cu nanofluids, however the model developed by Yu and Choi [75] is the closest in agreement with the experimental data. The models developed by Xie et al. [76] and Leong et al. [77] also, to an acceptable extent. Predict the enhancement of the thermal conductivity. These three models account for the interfacial nanolayer that is formed between the base fluids and the nanoparticles, and their being in an agreement with the experimental data proves the importance of considering the interfacial nanolayer as a significant mechanism in enhancing the thermal conductivity.

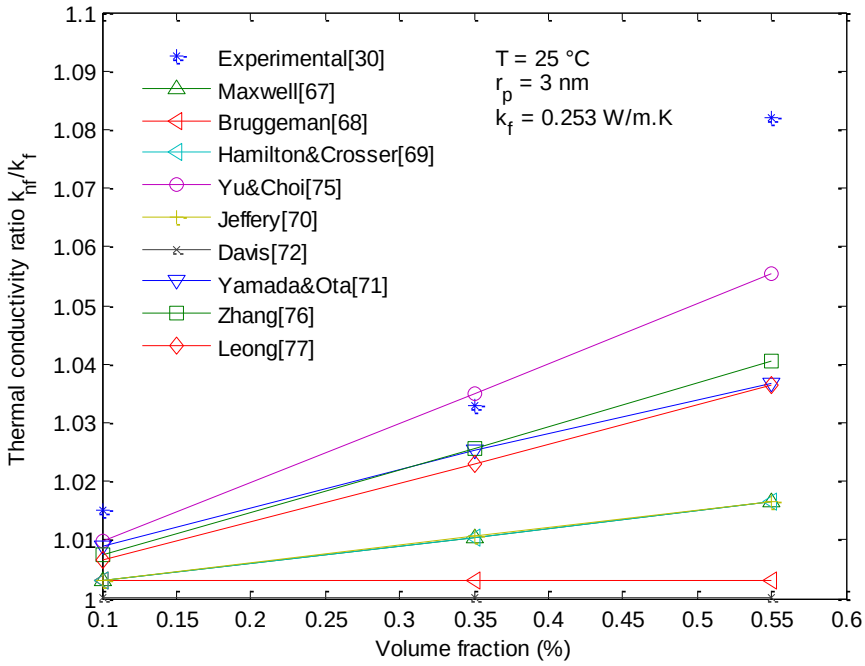

Figure 32: Comparison of experimental data [30] and various models for the thermal conductivity of EG/$\boldsymbol{Cu}$ nanofluids

Figure 33 shows a comparison between the thermal conductivity of Water/Al_2O_3 nanofluids with a nanoparticle radius of 12 nm for various models and experimental data provided by Xie et al. [31]. Again the model developed by Yu and Choi [75] is again the closest in agreement with the experimental data. While the model developed by Leong et al. [77] overestimates the enhancement of the thermal conductivity, along with the model developed by Yamada and Ota [71], the remaining models underestimate the enhancement. The models developed by Bruggeman [68] and Davis [72] fail to predict the thermal conductivity enhancement and the trend, where both models show no further enhancement with the increase of the volume fraction. The other models developed by Maxwell [67], Hamilton and Crosser [69] and Jeffery [70] all underestimate the thermal conductivity enhancement, and they almost show the same enhancement as each other. After comparing the models, the model developed by Yu and Choi [75] is chosen to calculate the thermal conductivity Cu-based and Al_2O_3-based nanofluids.

As mentioned from section 3.1.5, the models used to predict the thermal conductivity enhancement of Cu-based and Al_2O_3based nanofluids cannot predict the thermal conductivity enhancement of $SWCNT$-based nanofluids. This can be shown in

Figure 34 where the thermal conductivity models fail to predict the enhancement of Oil/CNT nanofluids provided by Xue [86].

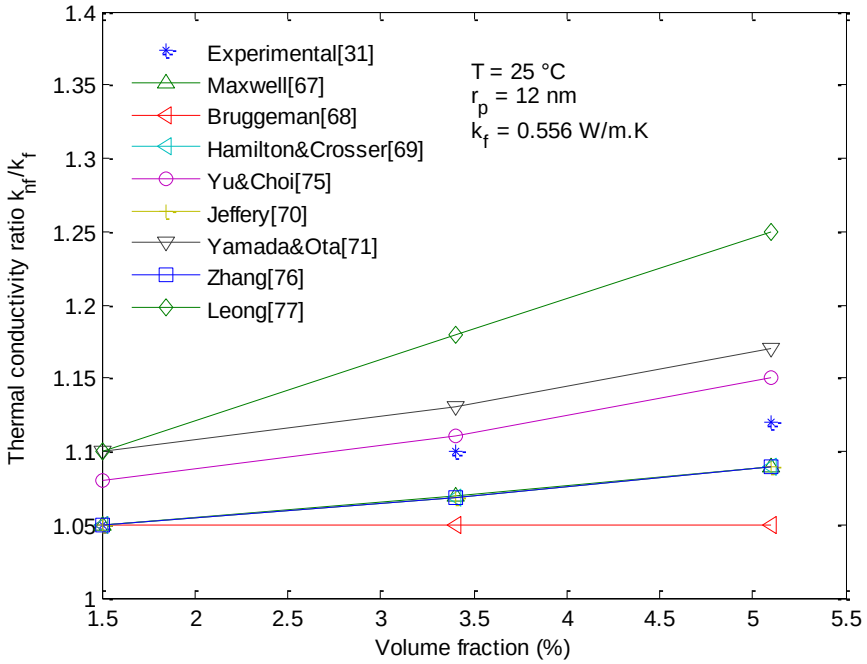

Figure 33: Comparison of experimental data [31] and various models for the thermal conductivity of Water/Al_2O_3 nanofluids

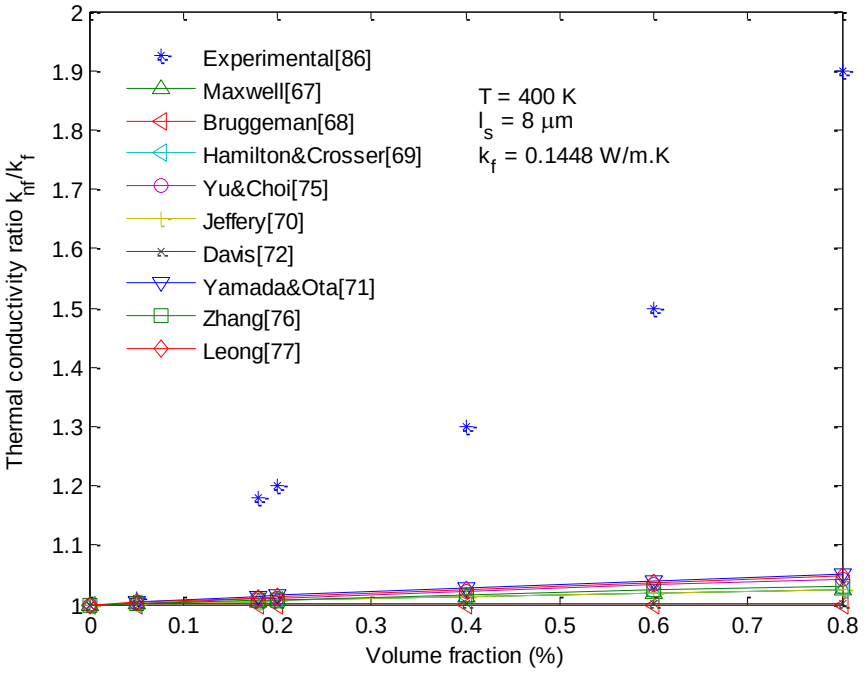

Figure 34: Comparison of experimental data [86] and various models for the thermal conductivity of Oil/CNT nanofluids

Figure 35 shows a comparison of experimental data provided by Xue [86] for Oil/CNT nanofluids and various $SWCNT$-based thermal conductivity models. The Oil has a thermal conductivity of $0.1448\ W/mK$, and the length of the $SWCNT$ is $8\ \mu m$. It is seen that models developed by Xue [86] either over predict or under predict the enhancement of the thermal conductivity depending on the distribution of the CNT in the base fluid. However, the model developed by Nan et al. [85] is in reasonable agreement with the experimental data. It also takes into account the interfacial nanolayer mechanism. Based on the previous observation, the model developed by Nan et al. [85] is chosen for the calculation of the thermal conductivity of $SWCNT$-based nanofluids.

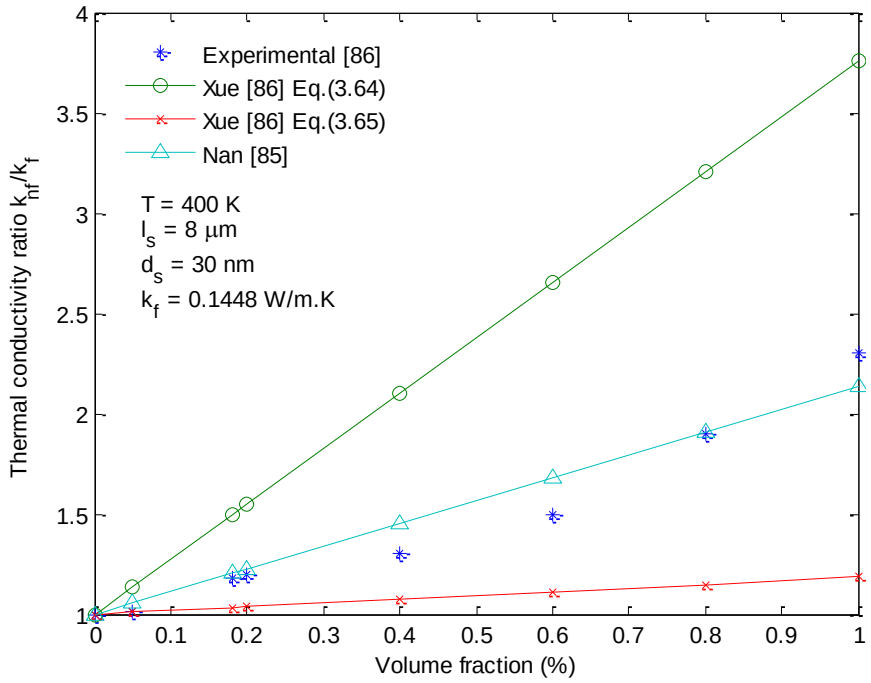

Figure 35: Comparison of experimental data and various $\boldsymbol{CNT}$-based models for the thermal conductivity of Oil/$\boldsymbol{CNT}$ nanofluids

4.3.6.2 Effect of radius, length and nanolayer thickness.

After choosing the most suitable model for the calculation of the thermal conductivity, the effect of the radius, length and nanolayer thickness of the nanoparticles on the thermal conductivity of the nanofluids are analyzed. Figure 36 shows the variation of the nanoparticles radius on the thermal conductivity ratio of Therminol/Al_2O_3 nanofluids for different nanolayer thicknesses, at a temperature of 342 ℃ and a volume fraction of 3%. It is seen that as the nanoparticles radius increase, the thermal

conductivity ratio decreases, however the thermal conductivity ratio increases with the increase in the nanolayer thickness. It is also observed that the effect of the nanoparticle radius on the thermal conductivity ratio is negligible for a radius larger than 30 nm, suggesting that an increase in the radius will not yield a decrease in the thermal conductivity ratio of nanofluids. According to [47], [52], [55], and [59] the ratio of enhancement in the thermal conductivity of nanofluids decreases with the increase in nanoparticles radius, which agrees with the results provided in Figure 36. The increase of the thermal conductivity ratio with the increase in the nanolayer thickness was also reported by [83], where the same trend obtained in the Figure 36.

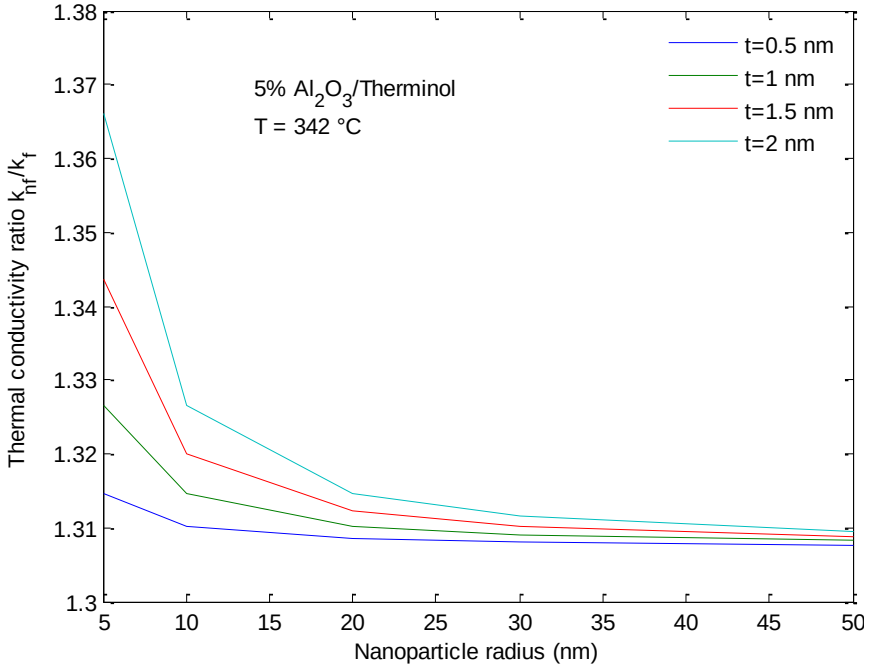

Figure 36: Effect of nanoparticle's radius on the thermal conductivity ratio of $\boldsymbol{Al_2O_3}$/Therminol nanofluids for different nanolayer thicknesses

Since the thermal conductivity of $SWCNT$ depends on the length of the CNT, the length will have an effect on thermal conductivity of $SWCNT$-based nanofluids. Figure 37 shows the variation of the volume fraction on the thermal conductivity ratio of Therminol/$SWCNT$ nanofluids for different $SWCNT$ lengths, at a diameter of 30 nm and a temperature of 342 ℃. It is seen that the length of $SWCNT$ has a huge impact on the thermal conductivity ratio, where the ratio increases with the length. For instance, the ratio increased from 3.14 to 4.53, when the length increased from 3 $\mu m$to 5 μm.

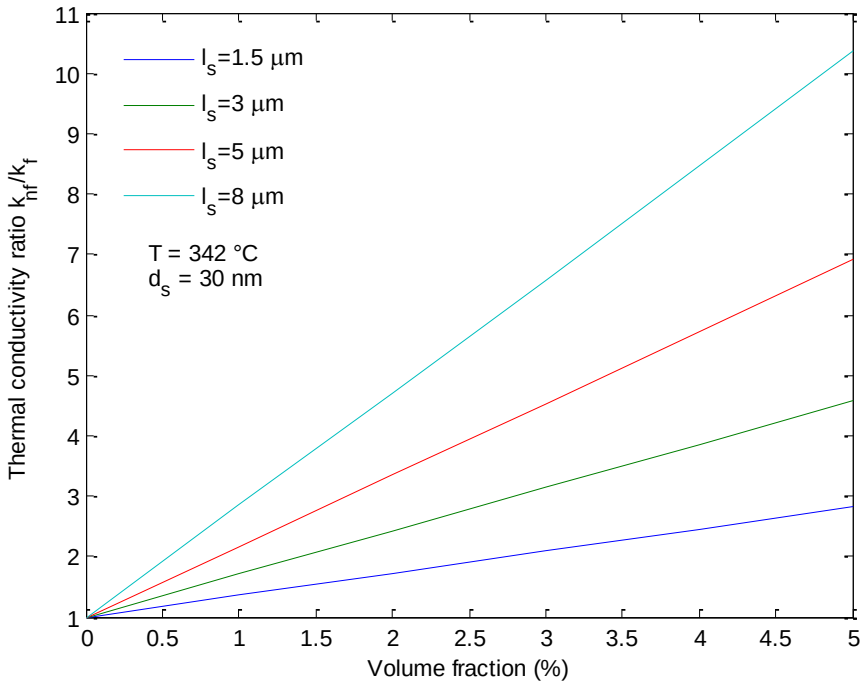

Figure 37: Effect of volume fraction on the thermal conductivity ratio of ***SWCNT***/Therminol nanofluids for different lengths

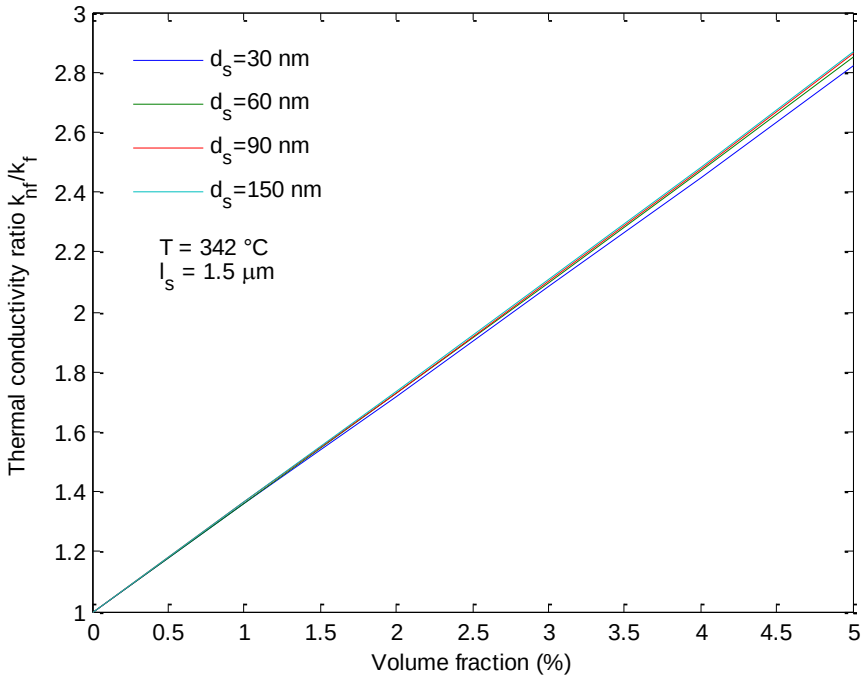

Figure 38: Effect of volume fraction on the thermal conductivity ratio of ***SWCNT***/ Therminol nanofluids for different diameters

Figure 38 shows the variation of the volume fraction on the thermal conductivity ratio of Therminol/$SWCNT$ nanofluids for different $SWCNT$ diameters, at a length of 5 μm and a temperature of 342 ℃. Unlike the length of the $SWCNT$, the diameter has a negligible effect on the thermal conductivity enhancement of $SWCNT$-based nanofluids. It is seen that for $SWCNT$-based nanofluids, the length has the major impact on the thermal conductivity, while for Cu-based and Al_2O_3-based nanofluids, the diameter or the radius affects the thermal conductivity considerably.

4.3.6.3 Effect of nanoparticles shape.

The thermal conductivity of the Cu-based and Al_2o_3-basednanofluids is affectedby the shape of these nanoparticles. The analysis is done using the Hamilton and Crosser model [69] which accounts for different nanoparticles shapes, by calculating their sphericity. Three shapes are chosen: cylinder, tetrahedron and sphere, with the following sphericity 0.5, 0.874 and 1 respectively. Figure 39 shows the variation of the volume fraction on the thermal conductivity ratio of Therminol/Al_2O_3 nanofluids for different shapes. It is seen that the shape with the smallest sphericity, exhibits the highest enhancement in thermal conductivity. Hence the nanofluids with a cylinder shaped nanoparticles show the highest thermal conductivity enhancement followed by the tetrahedron then the sphere.

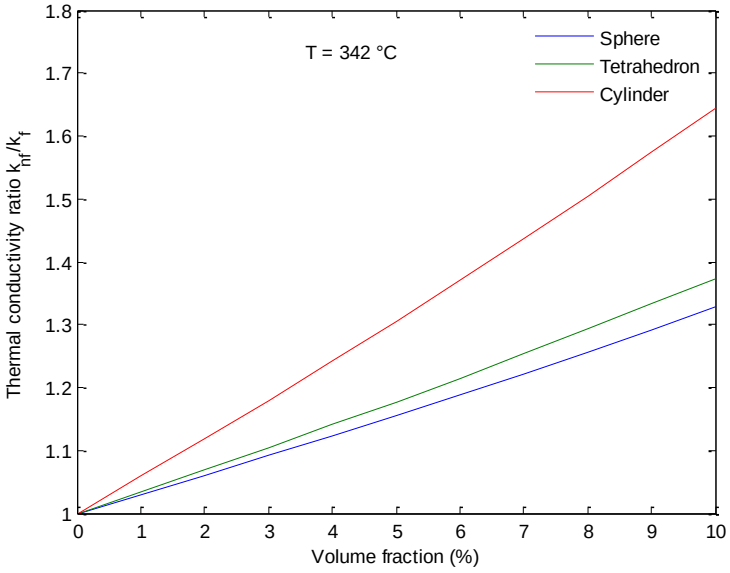

Figure 39: Effect of volume fraction on the thermal conductivity ratio of $\boldsymbol{Al_2O_3}$ /Therminol nanofluids for different nanoparticles shapes

The results shown in Figure 39, agree with the experimental data provided by [26] and [38] where elongated rods and cylindrical shaped nanoparticles showed a higher thermal conductivity enhancements compared to spherical shaped nanoparticles.

4.3.6.4 Effect of volume fraction.

The thermal conductivity of nanofluids depends greatly on the volume fraction, or the percentage of the nanoparticles added to the base fluid. Figure 40 shows the variation of the volume fraction on the thermal conductivity ratio of Therminol-based and Syltherm-based nanofluids. The temperature is taken as 342 ℃, the length of the $SWCNT$ nanoparticles is $1.5\mu m$, the diameter of all the nanoparticles is $30\ nm$, the nanolayer thickness formed by Cu-based and Al_2O_3-based nanofluids is taken as $2\ nm$, and the Al_2O_3 and Cu nanoparticles are spherically shaped. It is seen that the thermal conductivity ratio increases with the increase of the volume fraction. Interestingly, both Cu-based and Al_2O_3-based nanofluids almost share the same thermal conductivity enhancement; although the thermal conductivity of Cu nanoparticles is 10 times that of Al_2O_3 nanoparticles at room temperature. Regarding $SWCNT$-based nanofluids, the enhancement caused by the $SWCNT$ nanoparticles is considerably larger than the remaining nanofluids. The results obtained agree with the experimental data provided by [43] where $SWCNT$-based nanofluids showed the highest thermal conductivity enhancement of water base fluid, when compared to other metallic and non-metallic nanoparticles.

Figure 41 shows the variation of the temperature on the thermal conductivity of Cu-based nanofluids for a volume fraction of 5%. It is seen that the thermal conductivity of nanofluids decreases with the increase in temperature. Further, it is observed that the enhancement in the thermal conductivity of Syltherm/Cu nanofluids is more than that of Therminol/Cu nanofluids, which can be attributed to the fact that the thermal conductivity of Syltherm is less than Therminol resulting in a higher thermal conductivity enhancement. Xie et al. [31] reported that nanofluids with a smaller base fluid thermal conductivity show a higher thermal conductivity enhancement when compared to other nanofluids with a higher base fluid thermal conductivity when the same nanoparticles are added.

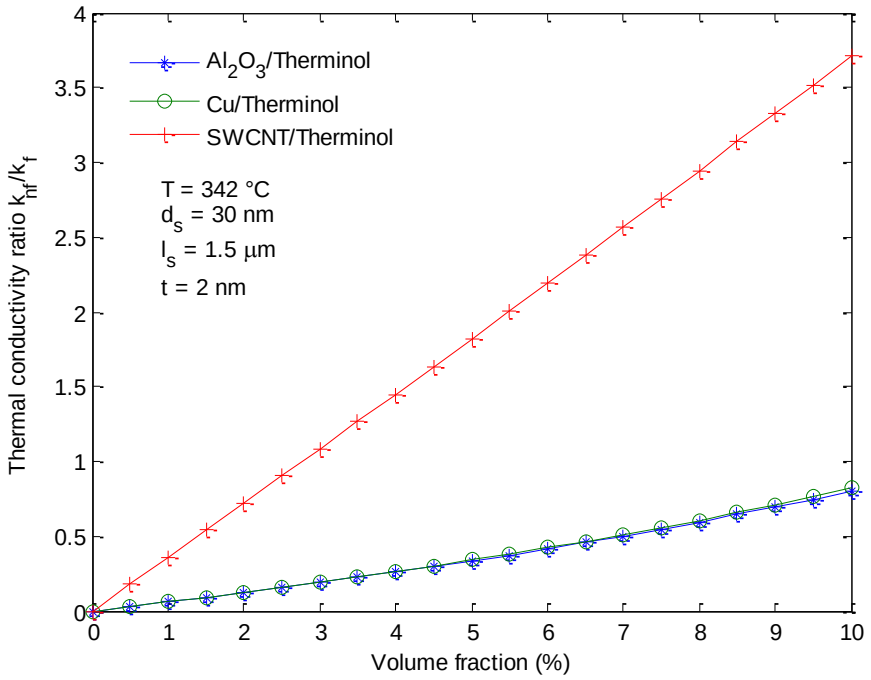

(a)

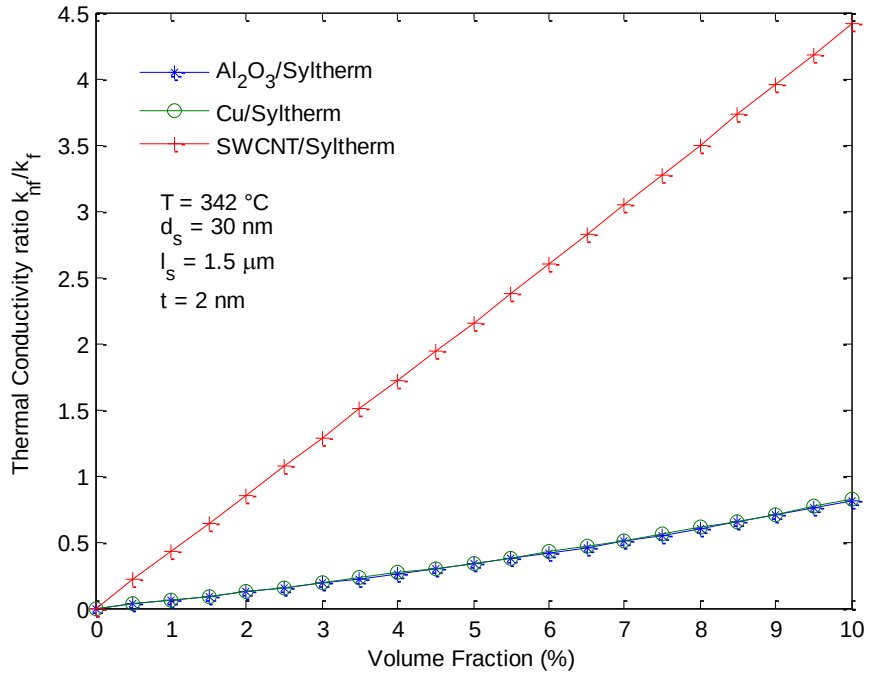

(b)

Figure 40: Effect of volume fraction on the thermal conductivity ratio of (a) Therminol-based nanofluids, and (b) Syltherm-based nanofluids

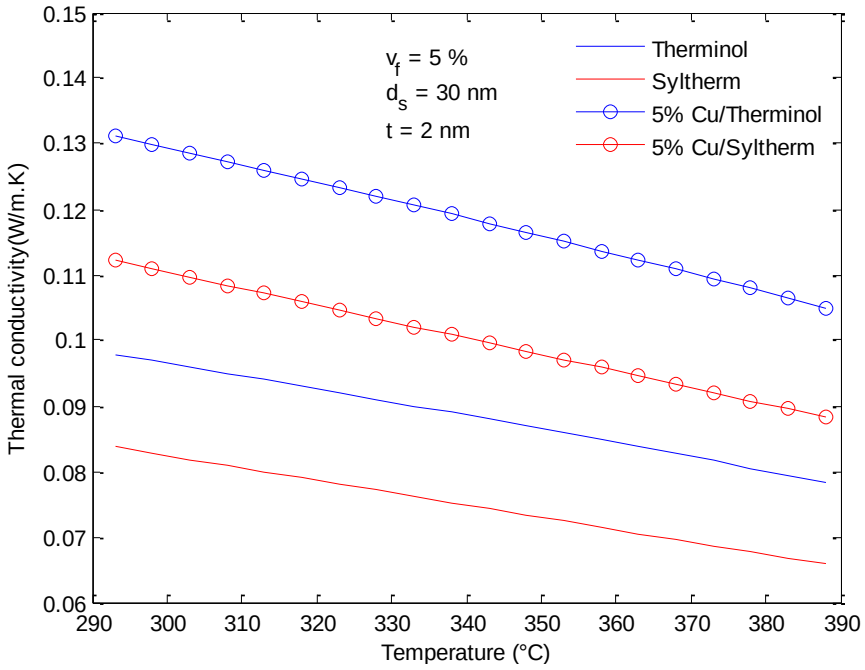

Figure 41: Effect of temperature on the thermal conductivity of $\boldsymbol{Cu}$-based nanofluids

Table 14 shows a summary of the thermophysical properties of nanofluids for different temperatures and volume fractions. From the table, it can be concluded that the density of the nanofluids increases with the volume fraction and decreases with the temperature. While the specific heat capacity of the nanofluids increases with the increase in temperature, but decreases with the increase in the volume fraction. Moreover, the viscosity of the nanofluids depends only on the viscosity of the base fluid and the volume fraction; therefore nanofluids that share the same base fluid have the same viscosity at different volume fractions. It is observed that the viscosity of nanofluids increases with the increase of the volume fraction and decreases with the increase in temperature. Further, it is seen that the thermal conductivity of nanofluids increases with the increase in volume fraction, but decreases with the increase in temperature. Comparing the base fluids, the thermal conductivity of Therminol based nanofluids is higher than that of Syltherm based nanofluids, however the ratio of thermal conductivity enhancement of Syltherm based nanofluids is higher than that of Therminol based nanofluids. In addition, the specific heat capacity of Therminol based nanofluids is higher than the specific heat capacity of Syltherm based nanofluids.

Table 14: Thermophysical properties of nanofluids for different temperatures and volume fractions

Property	Unit	$T = 293$ ℃			$T = 342$ ℃			$T = 391$ ℃		
					Therminol					
ρ	(kg/m^3)		825			770			706	
C_p	(kJ/kgK)		2.2909			2.4297			2.5993	
k	(W/mK)		0.0978			0.0881			0.0776	
μ	$(mPa \cdot s)$		0.2339			0.1891			0.1546	
					Therminol/Al_2O_3					
φ		1%	3%	5%	1%	3%	5%	1%	3%	5%
ρ	(kg/m^3)	855	915	976	800	862	923	738	800	863
C_p	(kJ/kgK)	2.278	2.253	2.229	2.416	2.389	2.362	2.584	2.554	2.524
k	(W/mK)	0.103	0.116	0.130	0.093	0.104	0.117	0.082	0.092	0.103
μ	$(mPa \cdot s)$	0.239	0.252	0.265	0.193	0.204	0.214	0.158	0.166	0.175
					Therminol/Cu					
φ		1%	3%	5%	1%	3%	5%	1%	3%	5%
ρ	(kg/m^3)	906	1068	1230	851	1014	1177	788	953	1117
C_p	(kJ/kgK)	2.272	2.234	2.197	2.409	2.369	2.329	2.577	2.533	2.490
k	(W/mK)	0.103	0.116	0.131	0.093	0.105	0.118	0.082	0.092	0.104
μ	$(mPa \cdot s)$	0.239	0.252	0.265	0.193	0.204	0.214	0.158	0.166	0.175
					Therminol/$SWCNT$					
φ		1%	3%	5%	1%	3%	5%	1%	3%	5%
ρ	(kg/m^3)	831	842	853	776	788	801	713	727	741
C_p	(kJ/kgK)	2.281	2.263	2.245	2.419	2.398	3.377	2.587	2.562	2.538
k	(W/mK)	0.129	0.193	0.257	0.119	0.183	0.248	0.109	0.173	0.238
μ	$(mPa \cdot s)$	0.239	0.242	0.265	0.193	0.204	0.214	0.158	0.166	0.175
					Syltherm					
ρ	(kg/m^3)		677			621			563	
C_p	(kJ/kgK)		2.0745			2.1582			2.2419	
k	(W/mK)		0.0837			0.0745			0.0652	
μ	$(mPa \cdot s)$		0.5020			0.3467			0.2625	
					Syltherm/Al_2O_3					
φ		1%	3%	5%	1%	3%	5%	1%	3%	5%
ρ	(kg/m^3)	708	772	835	653	718	782	595	661	727
C_p	(kJ/kgK)	2.064	2.044	2.023	2.147	2.125	2.104	2.230	2.207	2.184
k	(W/mK)	0.088	0.099	0.111	0.078	0.088	0.099	0.069	0.077	0.087
μ	$(mPa \cdot s)$	0.514	0.541	0.570	0.355	0.374	0.394	0.269	0.283	0.298
					Syltherm/Cu					
φ		1%	3%	5%	1%	3%	5%	1%	3%	5%
ρ	(kg/m^3)	759	924	1089	704	870	1036	646	814	981
C_p	(kJ/kgK)	2.057	2.024	1.991	2.140	2.106	2.071	2.223	2.187	2.150
k	(W/mK)	0.088	0.099	0.112	0.078	0.088	0.099	0.069	0.077	0.087
μ	$(mPa \cdot s)$	0.514	0.541	0.570	0.355	0.374	0.394	0.269	0.283	0.298
					Syltherm/$SWCNT$					
φ		1%	3%	5%	1%	3%	5%	1%	3%	5%
ρ	(kg/m^3)	684	698	713	629	644	660	571	588	604
C_p	(kJ/kgK)	2.067	2.053	2.039	2.150	2.134	2.119	2.233	2.216	2.198
k	(W/mK)	0.115	0.179	0.244	0.106	0.170	0.235	0.096	0.160	0.226
μ	$(mPa \cdot s)$	0.514	0.541	0.570	0.355	0.374	0.394	0.269	0.283	0.298

4.4 Convective heat transfer coefficient

This section covers the analysis of the convective heat transfer coefficient of nanofluids inside the PTSC absorber tube. After obtaining the thermophysical properties of different nanofluids, these properties are used to calculate the Reynolds number, Prandtl number, Nusselt number and finally the convective heat transfer coefficient of nanofluids.

4.4.1 Reynolds number.

The Reynolds number of the nanofluids is calculated based on the properties of the nanofluids. Figure 42 shows the variation of the temperature on the Reynolds number for Therminol-based and Syltherm-based nanofluids for a volume fraction of 5%. The fluid velocity is assumed to be $1\ m/s$, and the receiver properties are obtained from Table 5. It is seen that the Reynolds number of the nanofluids increases with the increase in temperature. Further in the case of Al_2O_3-based and Cu-based nanofluids, the Reynolds number for these nanofluids is higher than that of the base fluids. While for the $SWCNT$-based nanofluids, the Reynolds number is less than that of the base fluids. The variation in the trends of the Reynolds number of the nanofluids can be attributed to the change in the thermophysical properties of these nanofluids. For instance, for Al_2O_3-based and Cu-based nanofluids the Reynolds number is higher than Therminol and Syltherm. This trend is a result of the relation between the density's increase with volume fraction, decrease with temperature, the viscosity's decrease with temperature, and decrease with volume fraction. Hence depending on the rate of increase or decrease between the thermophysical properties of each particular nanofluid, the behavior of the Reynolds number is presented.

Figure 43 shows the variation of the volume fraction on the Reynolds number for Therminol-based and Syltherm-based nanofluids for a temperature of 342 ℃, and a velocity of $1\ m/s$. It is seen that the Reynolds number of Al_2O_3-based and Cu-based nanofluids increases with volume fraction, while the Reynolds number of $SWCNT$-based nanofluids decreases with the increase in temperature. When comparing the base fluids, it is seen that Therminol-based nanofluids display a higher Reynolds number than Syltherm-based nanofluids, indicating a more turbulent flow.

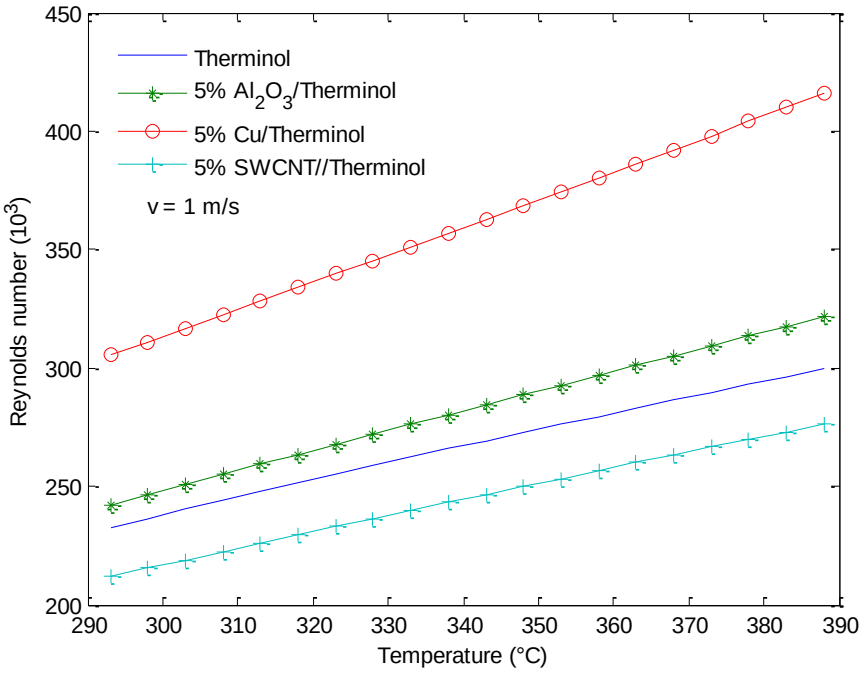

(a)

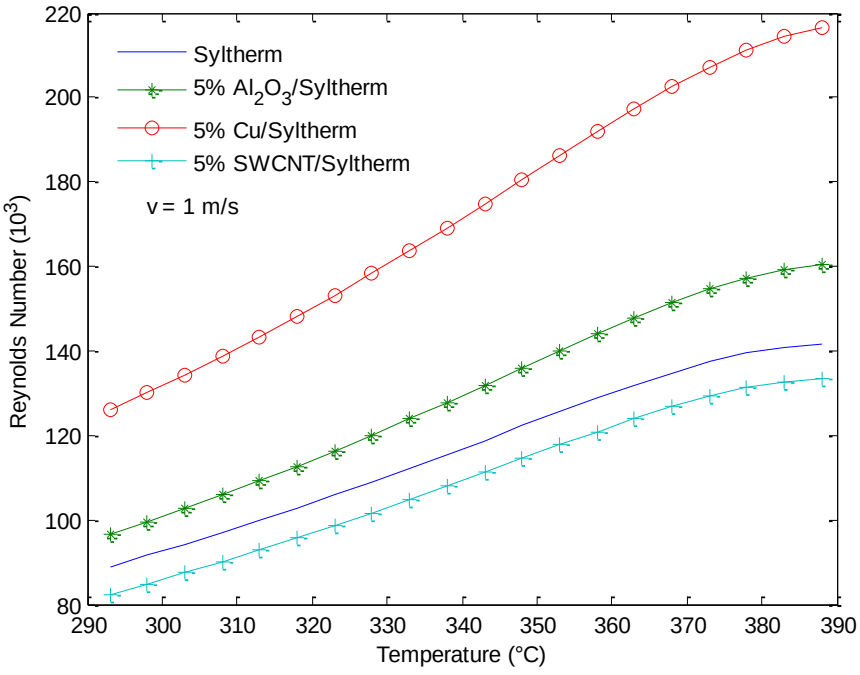

(b)

Figure 42: Effect of temperature on the Reynolds number for (a) Therminol-based nanofluids, and (b) Syltherm-based nanofluids

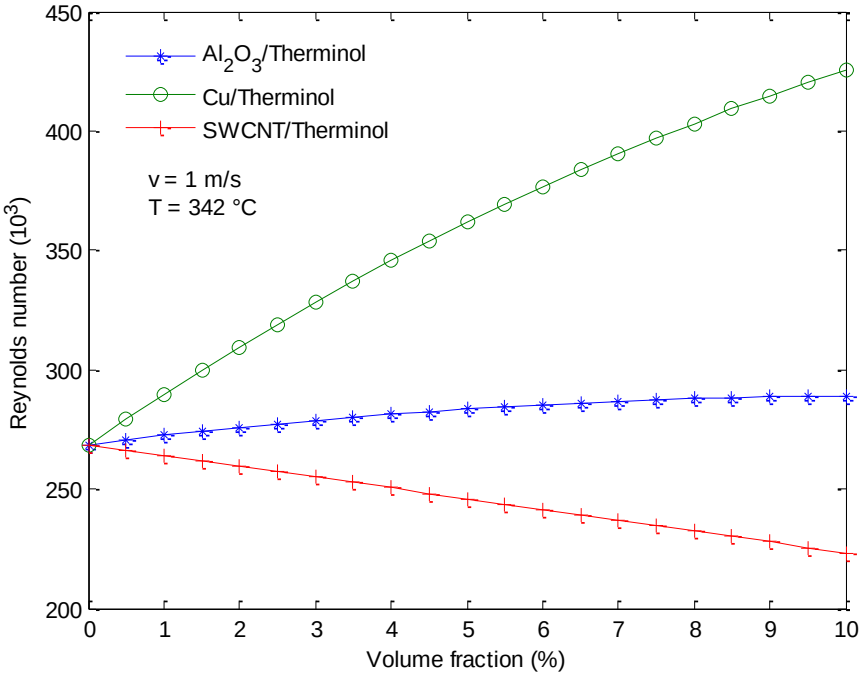

(a)

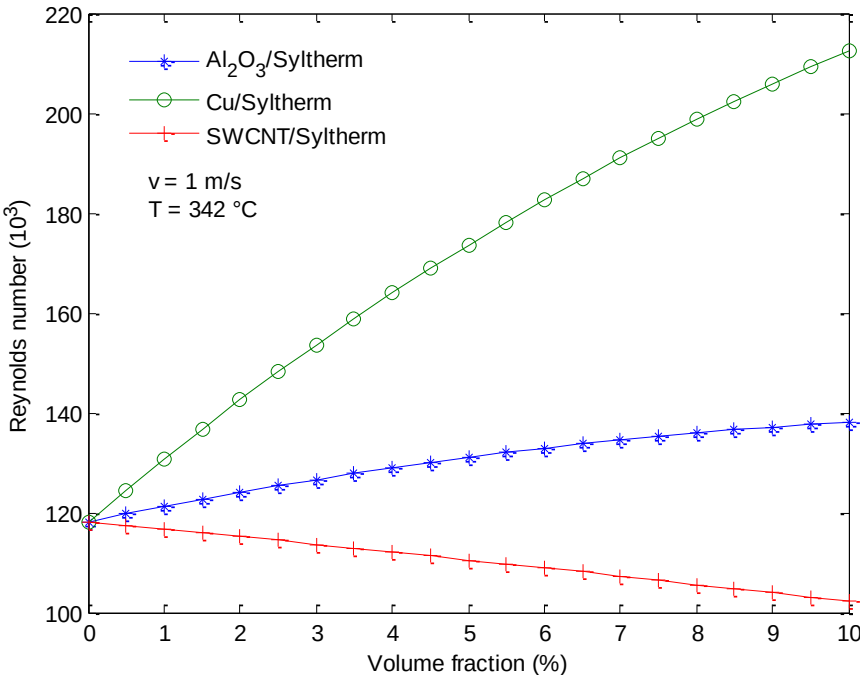

(b)

Figure 43: Effect of the volume fraction on the Reynolds number for (a) Therminol-based nanofluids, and (b) Syltherm-based nanofluids

4.4.2 Prandtl number.

The Prandtl number of the nanofluids is calculated using the specific heat capacity, thermal conductivity and viscosity of the nanofluids. Figure 44 shows the variation of the temperature on the Prandtl number for Therminol-based and Syltherm-based nanofluids for a volume fraction of 5%, and a velocity of 1 m/s. It is seen that the Prandtl number of the nanofluids decreases with the increase in temperature, and it is less than that of the base fluids. Moreover, it is seen that Prandtl number for Al_2O_3-based and Cu-based nanofluids is almost the same. The reason is that the thermal conductivity enhancement of both nanofluids is almost the same, and the viscosity is exactly the same since it does not depend on the nanoparticles, leaving the specific heat capacity which varies a little between the two nanofluids. However, this variation is not large enough to affect the Prandtl number of the two nanofluids.

Figure 45 shows the variation of the volume fraction on the Prandtl number of Therminol-based and Syltherm-based nanofluids at a temperature of 342℃, and a velocity of 1 m/s. It is seen that the Prandtl number of the nanofluids decreases with the increase in the volume fraction, and for $SWCNT$-based nanofluids it is exponential.

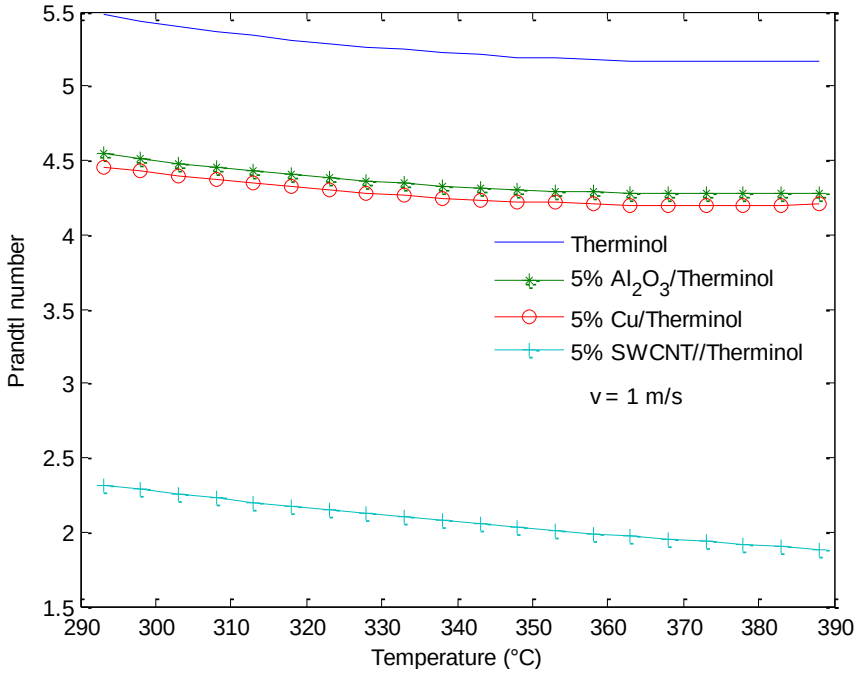

(a)

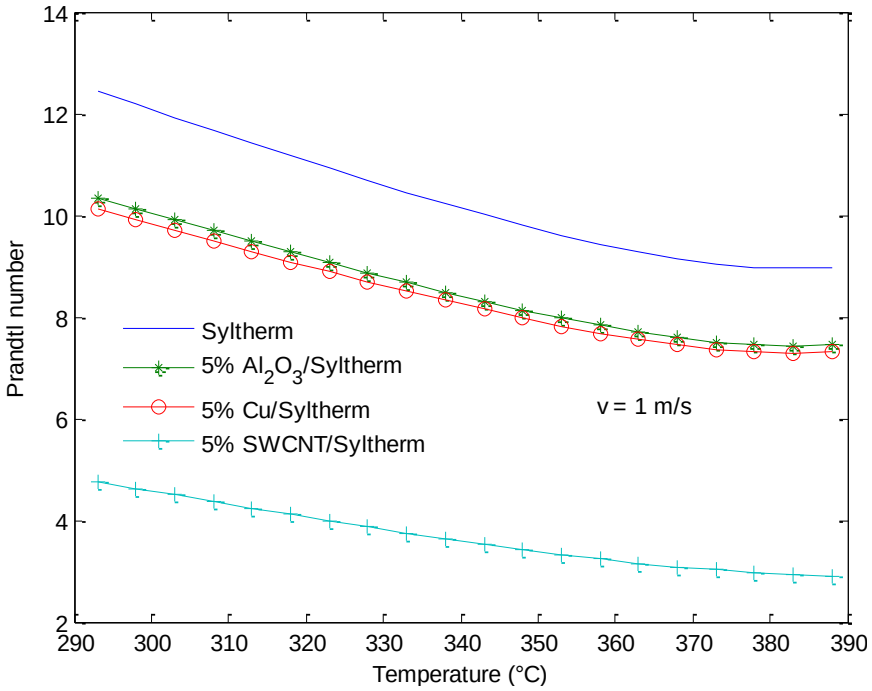

(b)

Figure 44: Effect of temperature on the Prandtl number for (a) Therminol-based nanofluids, and (b) Syltherm-based nanofluids

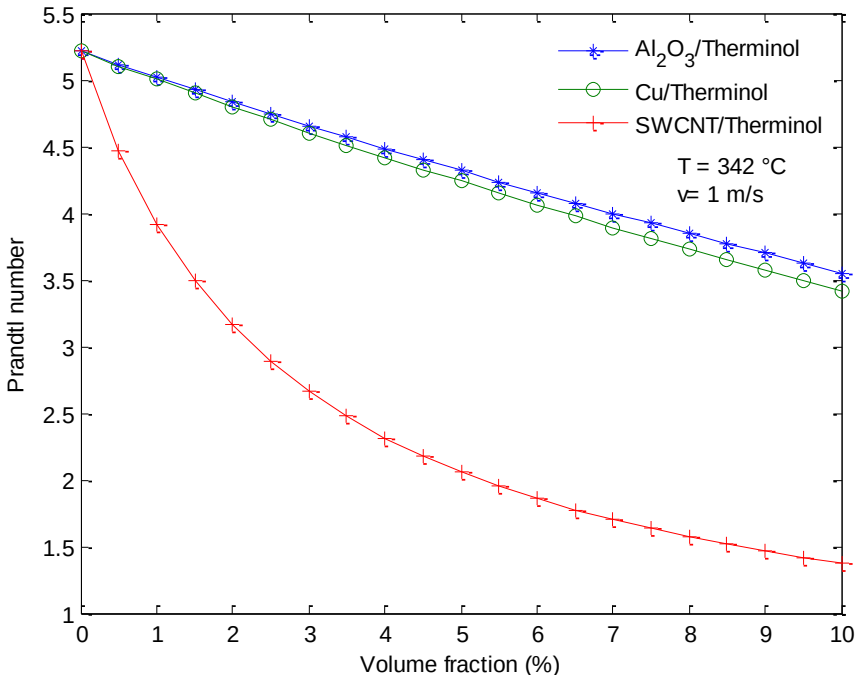

(a)

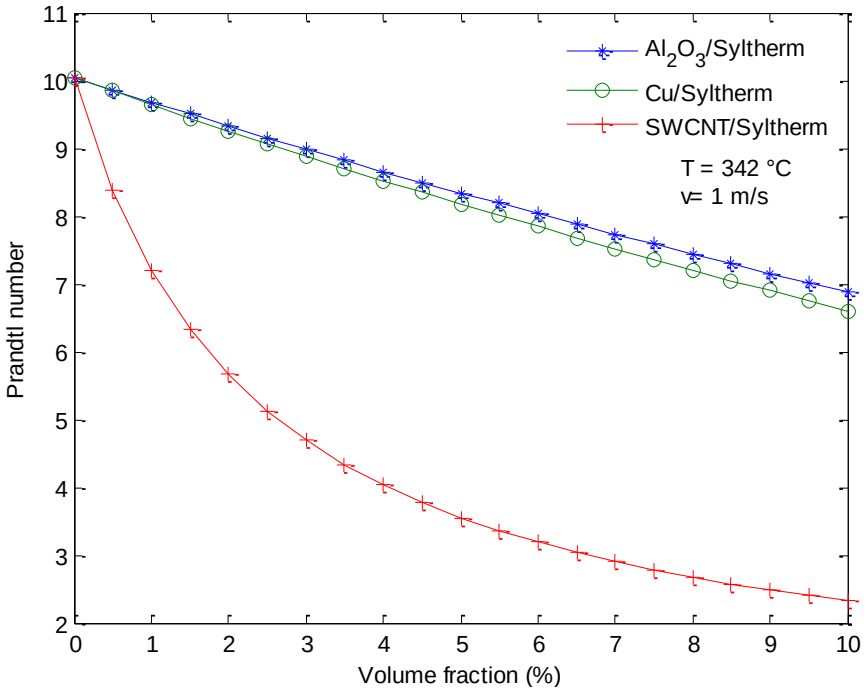

(b)

Figure 45: Effect of volume fraction on the Prandtl number for (a) Therminol-based nanofluids, and (b) Syltherm-based nanofluids

4.4.3 Heat transfer coefficient.

The convective heat transfer coefficient of the nanofluids depends on the thermophysical properties, Reynolds number, Prandtl number, and directly on the Nusselt number and flow type. The specifications of the receiver and absorber tube of the PTSC are taken from Table 5, and the equations from section 3.2 are used to calculate the convective heat transfer coefficient. The effect of the temperature, volume fraction and flow type whether laminar or turbulent on the convective heat transfer coefficient are investigated in this section.

4.4.3.1 Model validation.

In order to test the validity of the models and the carried analysis, the results obtained for the convective heat transfer coefficient are compared to experimental data published in the literature. Since the base fluids used in this study are not widely experimented on, water is used as the base fluid and the models proposed in the previous chapter are used to calculate the convective heat transfer coefficient.

Figure 46 shows the variation of the Reynolds number on the Nusselt number for Cu/Water nanofluids compared to experimental data obtained from [103]. The fluid was in turbulent flow and the volume fraction is 1 %. The experiment was done for a temperature of 25 ℃, and for a nanoparticles diameter of 15 nm. The diameter of the tube where the experiment was conducted is 10 mm. It is seen that the data calculated from the provided model is in good agreement with the experimental data, proving the validity of the model for turbulent flow and Cu-based nanofluids.

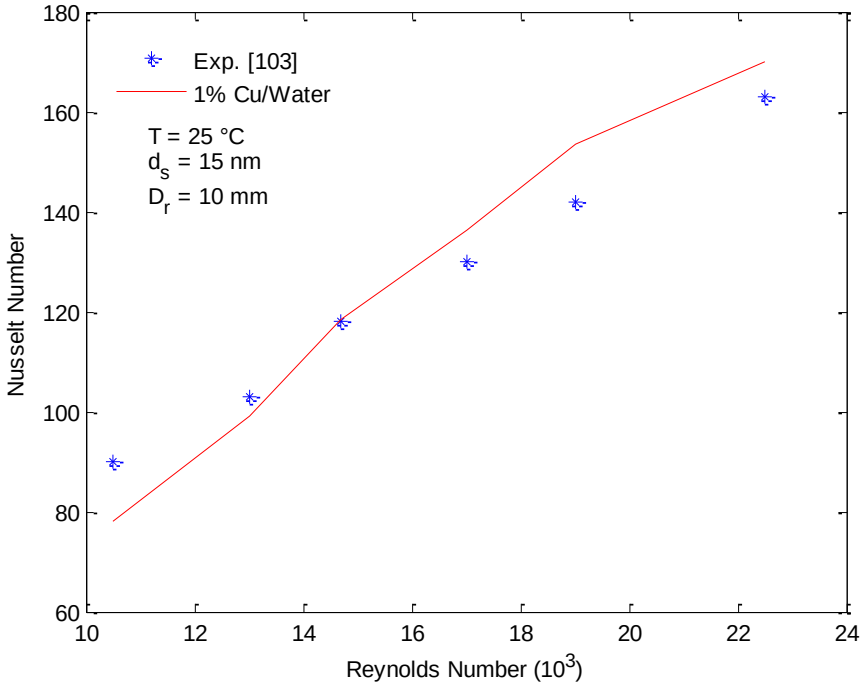

Figure 46: Effect of Reynolds number on the Nusselt number for $\boldsymbol{Cu}$/water, compared to [103]

Figure 47 shows the variation of the Reynolds number on the Nusselt number for Al_2O_3/ Water nanofluids compared to experimental data obtained from [129]. The experimental study was conducted for laminar flow and a volume fraction of 0.1 %. In addition, the temperature was kept at 25 ℃, and the nanoparticles with a diameter of 20 nm were used. The diameter of the tube where the experiment was conducted is 10 mm. It is seen that the calculated data matches the results obtained from the experimental data, proving the validity of the model for laminar flow and Al_2O_3-based nanoparticles.

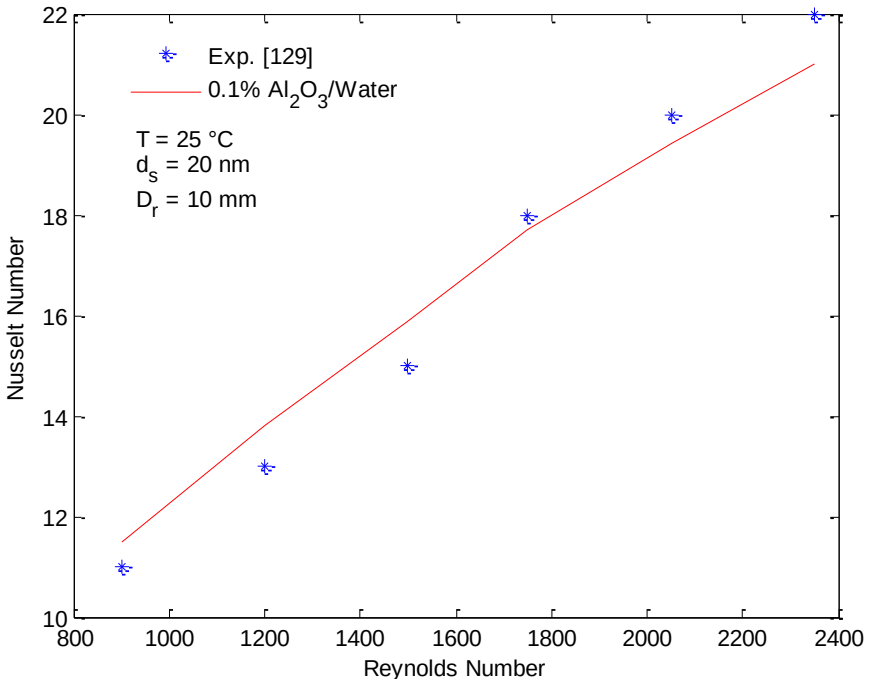

Figure 47: Effect of Reynolds number on the Nusselt number for $\boldsymbol{Al_2O_3}$/ water, compared to [129]

Figure 48 shows the variation of the Reynolds number on the heat transfer coefficient for CNT/Water nanofluids compared to experimental data obtained from [111]. The analysis was done for turbulent flow; a volume fraction of 0.24%, temperature of 25 ℃, and CNT length and diameter of 8 μm and 80 nm respectively. In addition, the diameter of the test tube was set to be 12.7 mm. It is shown that the results obtained for the CNT/Water nanofluid are in agreement with the experimental data, verifying the validity of the model for $SWCNT$-based nanofluids. While comparing $SWCNT$-based nanofluids with Cu-based and Al_2O_3-based nanofluids, the results are more accurate for Cu-based and Al_2O_3-based nanofluids because of the discrepancy of the $SWCNT$ nanoparticles provided in the literature. In other words, the $SWCNT$ nanoparticles possess a very complicated structure, and their thermal conductivity depends on that structure as well as the length and the diameter. Therefore, it is tough for analytical results to perfectly match the experimental results, because some aspects of the $SWCNT$ structure cannot be simulated.

Since the temperature dependent model for the thermophysical properties of the nanofluids, and the convective heat transfer coefficient inside the absorber tube is

verified, the effect of the volume fraction, temperature and flow type on the convective heat transfer coefficient of the nanofluids inside the PTSC absorber tube is studied.

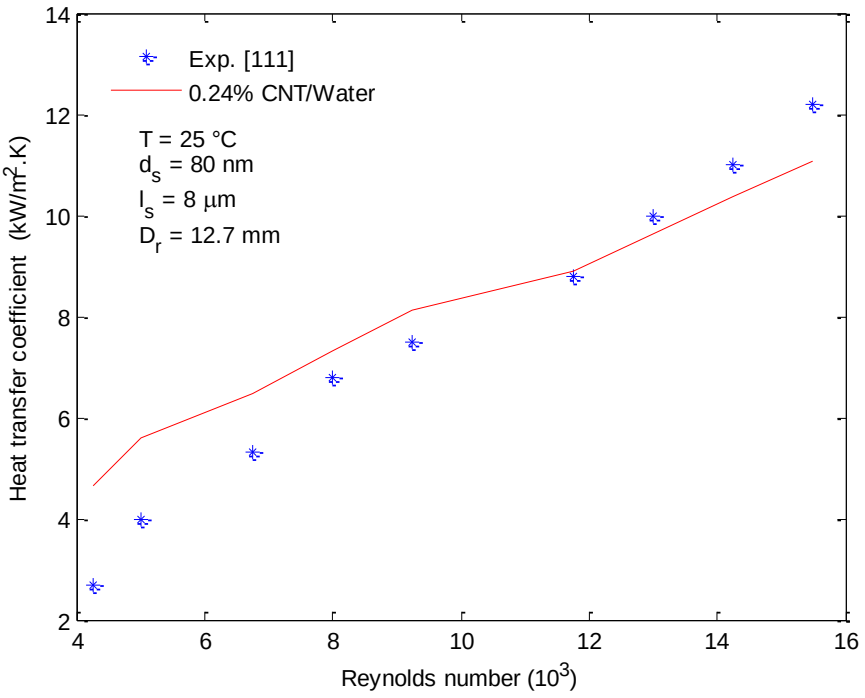

Figure 48: Effect of Reynolds number on the heat transfer coefficient for ***CNT***/ water, compared to [111]

4.4.3.2 Effect of the nanofluids on the convective heat transfer coefficient.

In order to compare the nanofluids with the base fluids, the velocity of the flow inside the PTSC absorber tube is kept constant. In this case all of the fluids will have the same velocity, however depending on their properties the Reynolds number, mass flow rate, and convective heat transfer coefficient would be different.

Figure 49 shows the variation of the volume fraction on the convective heat transfer coefficient for Therminol-based and Syltherm-based nanofluids for a temperature of $342\ ℃$, and a fluid velocity of $1\ m/s$. It is seen that the convective heat transfer coefficient of the nanofluids increases with the increase in the volume fraction. It is also observed that the $SWCNT$-based nanofluids display the highest enhancement in the heat transfer coefficient. Further, Cu-based nanofluid shows a higher enhancement in the convective heat transfer coefficient when compared to Al_2O_3- based nanofluids although both nanofluids show the same thermal conductivity enhancement.

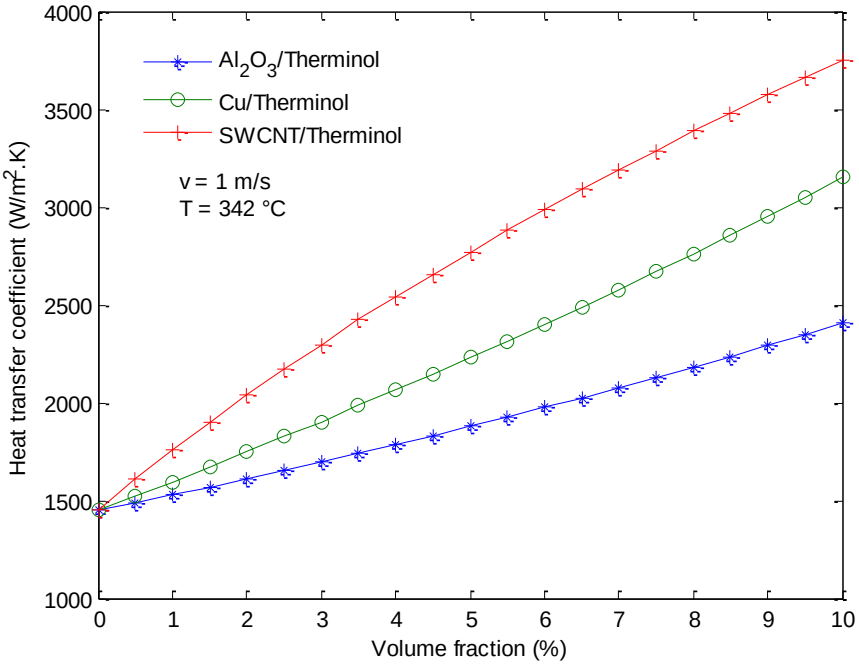

(a)

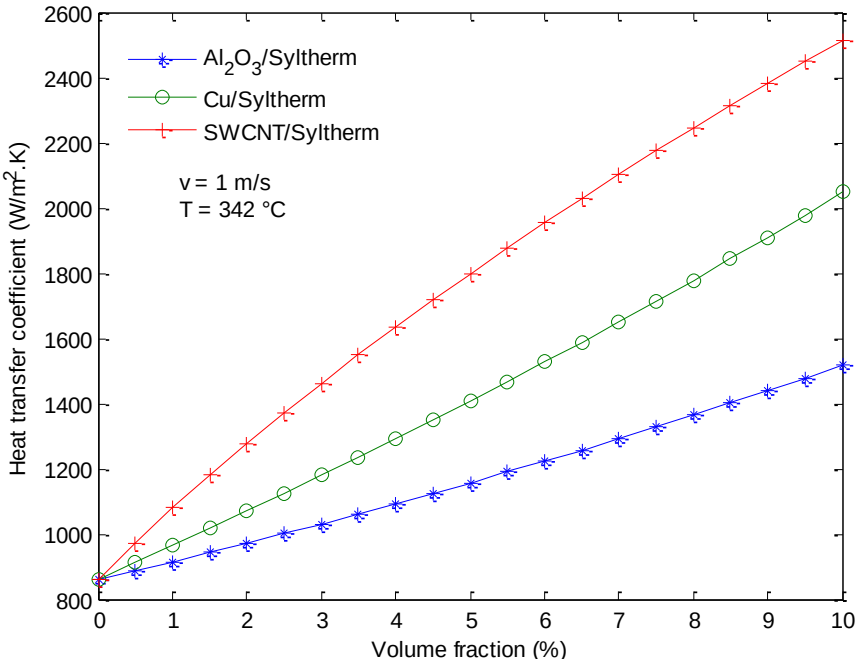

(b)

Figure 49: Effect of volume fraction on the convective heat transfer coefficient for (a) Therminol-based nanofluids, and (b) Syltherm-based nanofluids

This behavior is expected since the convective heat transfer coefficient depends on the thermophysical properties of the nanofluids and not only the thermal conductivity, and since the Cu-based nanofluids possess the high properties of metallic nanoparticles, they are prone to show a higher heat transfer coefficient enhancement when compared to non-metallic nanofluids. Even though the $SWCNT$-based nanofluids are considered to be of non-metallic base, the considerably high thermal conductivity, and the shape of $SWCNT$ nanoparticles enhance the heat transfer coefficient greatly.

Referring back to Figure 49, it is noticed that nanofluids with a small volume fraction display a lower heat transfer coefficient. Also for a high volume fraction, the heat transfer coefficient drops intensely, therefore after a set of simulations it was concluded that nanofluids with volume fractions in the range of 2% to 10% exhibits the best enhancement in the convective heat transfer coefficient regardless of the nanoparticles type, fluid velocity, and fluid type. Another consideration to ponder is that for high volume fractions, the viscosity increases greatly extracting the fluid nature of the nanofluids, as the greater number of nanoparticles force the solid like form on the nanofluids, resulting in a slow and rough fluid flow.

4.4.3.3 Effect of the temperature on the convective heat transfer coefficient.

Figure 50 shows the variation of the temperature on the convective heat transfer coefficient for Therminol-based and Syltherm-based nanofluids for a volume fraction of 5%, and a velocity of $1\ m/s$. It is seen that the temperature almost has a negligible effect on the convective heat transfer coefficient for the PTSC operating temperature range. It is noticed that for Therminol and Therminol-based nanofluids, the convective heat transfer coefficient increases to a peak value then decreases, while for Syltherm and Syltherm-based nanofluids the convective heat transfer coefficient is increasing to the peak value. When comparing Therminol-based nanofluids to Syltherm-based nanofluids, it is observed that the convective heat transfer coefficient of the Therminol-based nanofluids is higher than that of Syltherm-based nanofluids, Nevertheless, the enhancement in the heat transfer coefficient caused by adding the nanoparticles to Syltherm is higher than that of Therminol.

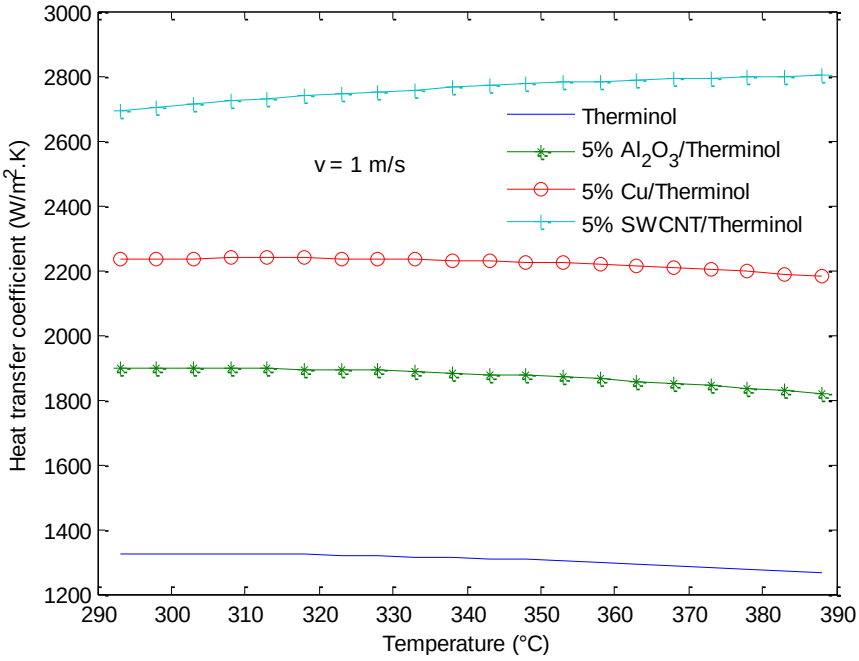

(a)

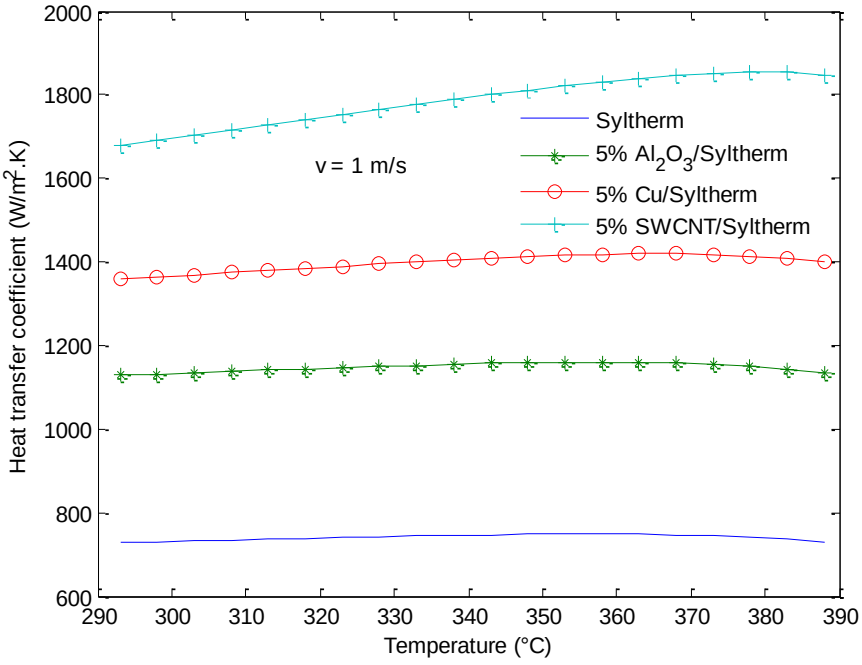

(b)

Figure 50: Effect of temperature on the convective heat transfer coefficient for (a) Therminol-based nanofluids, and (b) Syltherm-based nanofluids

4.4.3.4 Effect of the flow type on the convective heat transfer coefficient.

The convective heat transfer coefficient enhancements depends on the flow type, whether it is laminar or turbulent. Figures 51 and 52 show the variation of the Reynolds number on the convective heat transfer coefficient for Therminol-based nanofluids with a volume fraction of 3% and at a temperature of 342 ℃. Figure 51 displays a turbulent flow while a laminar flow is displayed in Figure 52. It is seen that the enhancement in the convective heat transfer coefficient decreases with the increase of the Reynolds number. However, the maximum enhancement happens in the transition phase, meaning that when the velocity of the base fluid and the nanofluids is the same, but due to the difference in thermophysical properties, the nanofluids transitions into turbulent flow while the base fluid is still experiencing laminar flow. This is can be clearly seen by comparing the Cu-based nanofluids with Therminol. The results obtained agree with the experimental data provided by [102], [103], [104] and [110] where the heat transfer coefficient increases with the addition of nanoparticles, and the enhancement in the heat transfer coefficient is greater for laminar flow rather than turbulent flow.

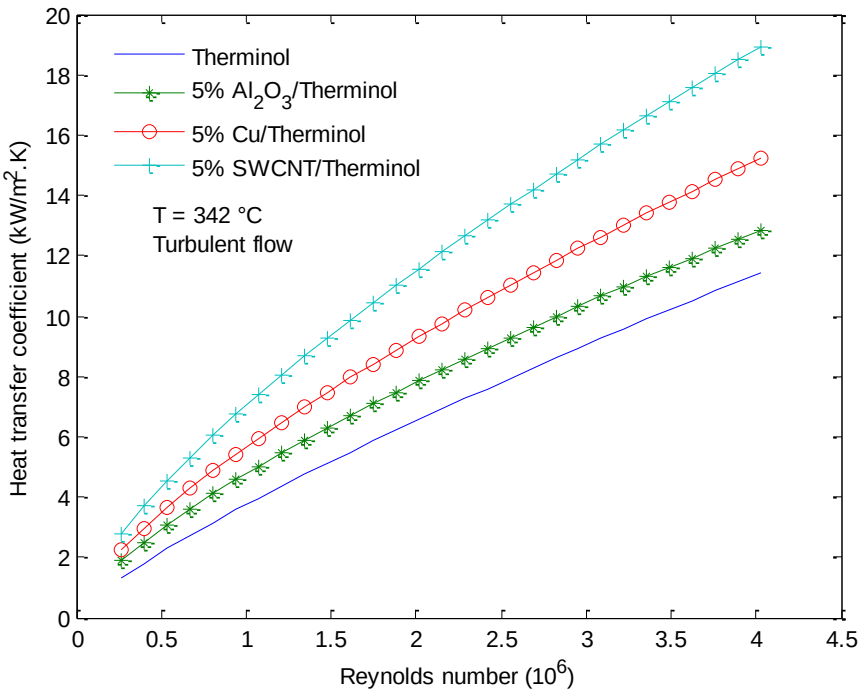

Figure 51: Effect of Reynolds number on the heat transfer coefficient for Therminol-based nanofluids (turbulent flow)

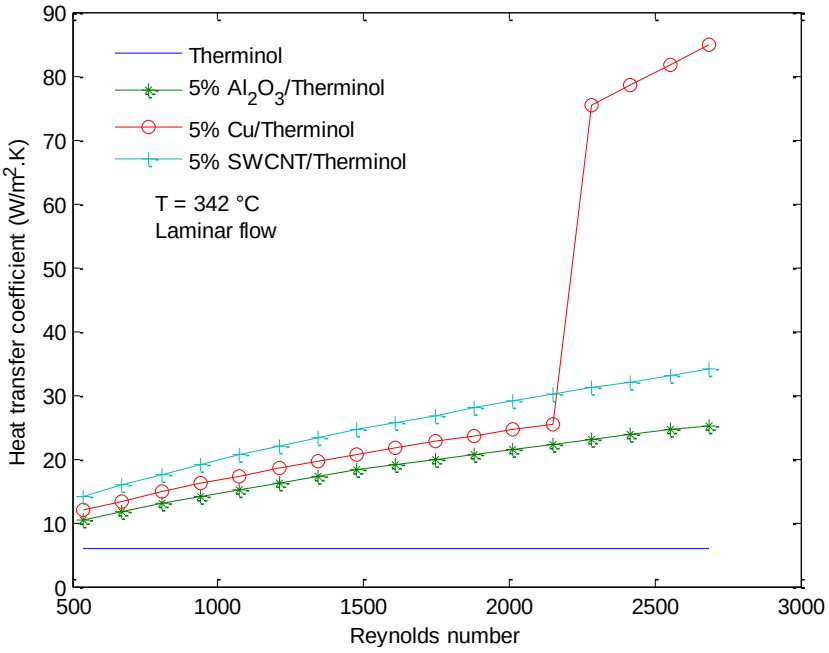

Figure 52: Effect of Reynolds number on the heat transfer coefficient for Therminol-based nanofluids (laminar flow)

4.5 Parabolic Trough Solar Collector (PTSC)

The effect of the nanofluids on the PTSC is limited to the enhancement of the overall heat transfer coefficient between the heating fluid and the PTSC, where here the variation of the heating fluid only affects the absorber tube of the PTSC, while the glass cover and the collector are unaffected by the addition of the nanoparticles to the heating fluid. After analyzing the effect of dispersing the nanoparticles on the thermophysical properties of the heating fluid and the convective heat transfer coefficient of the fluid inside the absorber tube of the PTSC, the effect of using nanofluids as a heating fluid on the power output and efficiency of the PTSC are investigated. The specifications and design parameters from Tables 5-7 are used to carry the analysis.

4.5.1 Effect of the mass flow rate on the PTSC performance.

Figure 53 shows the variation of the mass flow rate on the power output of the PTSC for Therminol-based nanofluids and Syltherm-based nanofluids for a volume fraction of 5%, and a temperature of 342 ℃.

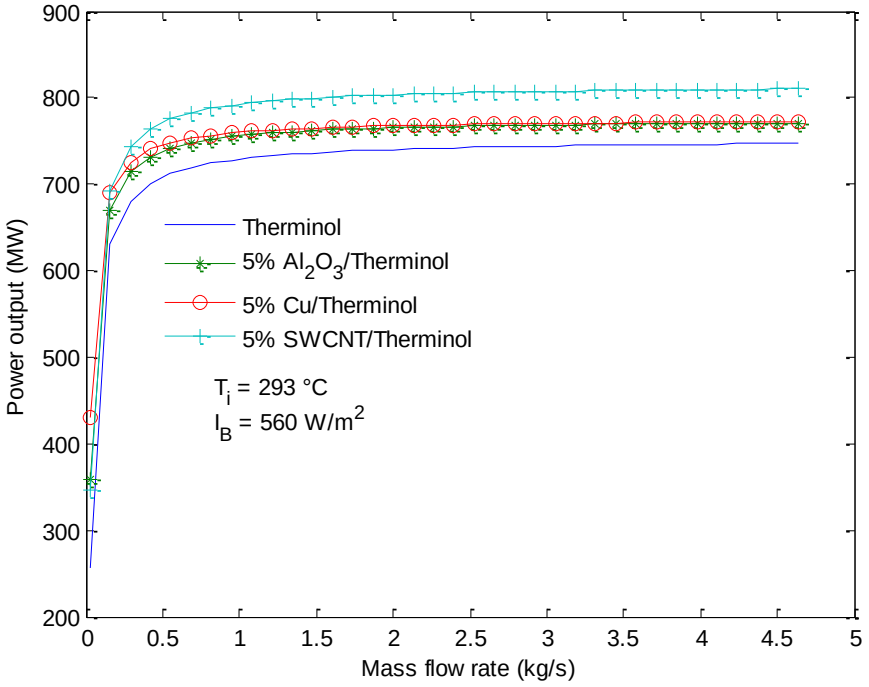

(a)

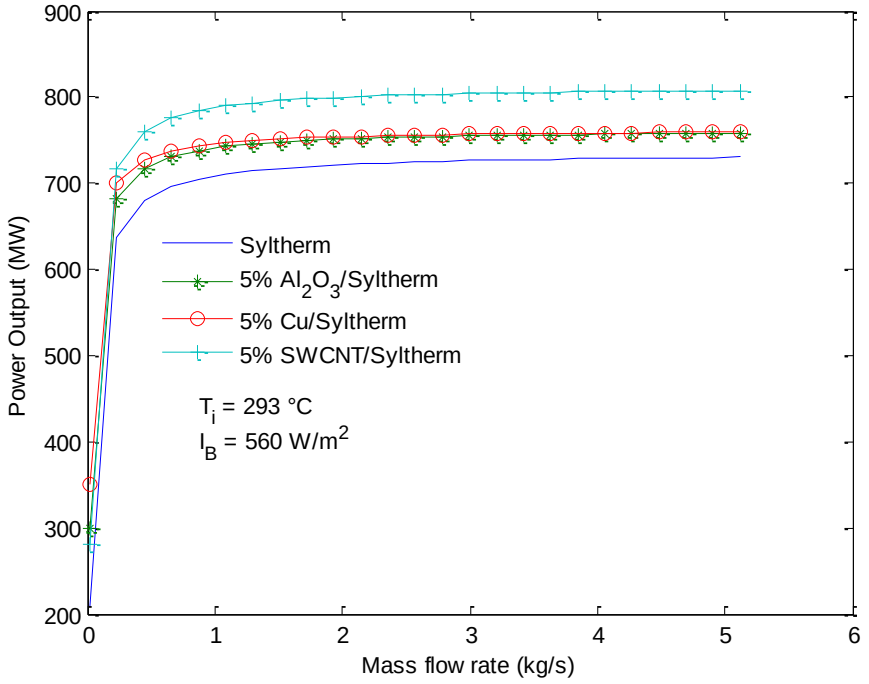

(b)

Figure 53: Effect of mass flow rate on the power output of the PTSC for (a) Therminol-based nanofluids, and (b) Syltherm-based nanofluids

It is seen that the increase in the mass flow rate yields an increase in the power output of the PTSC. However, this increase becomes negligible for a mass flow rate higher than $4\,Kg/s$ for Therminol and Therminol-based nanofluids, and higher than $5\,kg/s$ for Syltherm and Syltherm-based nanofluids. Since the energy input to the PTSC is constant, increasing the mass flow rate will result in a higher efficiency up to the mass flow rate value of which the power output becomes constant.

Figure 54 shows the variation of the mass flow rate on the efficiency of the PTSC for Therminol-based nanofluids, and Syltherm-based nanofluids for a volume fraction of 5%, and a temperature of 342 ℃. As expected, the efficiency of the PTSC increases with the increases with the mass flow rate until the peak value, where increasing the mass flow rate further would yield negligible effect on the efficiency. The previous relations agree with the work done in [179] where the mass flow rate increase resulted in an efficiency increase of the PTSC up to a peak value.

Regarding the figures, it is observed that $SWCNT$-based nanofluids show the highest enhancements in both the efficiency and power output, followed by Cu-based and Al_2O_3-based nanofluids respectively. Since the $SWCNT$-based nanofluids showed a very high thermal conductivity enhancement, it is expected for these nanofluids to display the highest enhancement in the power output and the efficiency of the PTSC.

Table 15 shows a comparison between the nanofluids and the average percentage enhancement in the PTSC efficiency and power output for a volume fraction of 5%. As seen from the table and provided in the figures, $SWCNT$-based nanofluids exhibits the highest enhancement in the efficiency and power output, which almost double the Cu-based and Al_2O_3- based nanofluids. When comparing the base fluids, it is observed that Syltherm-based nanofluids display a higher percentage of enhancements when compared to Therminol-based nanofluids. Since the thermophysical properties of Syltherm are lower than that of Therminol, it is expected that Syltherm-based nanofluids would show a higher enhancement. Nevertheless, when compared, the Therminol-based nanofluids show a higher efficiency and power output than Syltherm-based nanofluids, for any given temperature and volume fraction

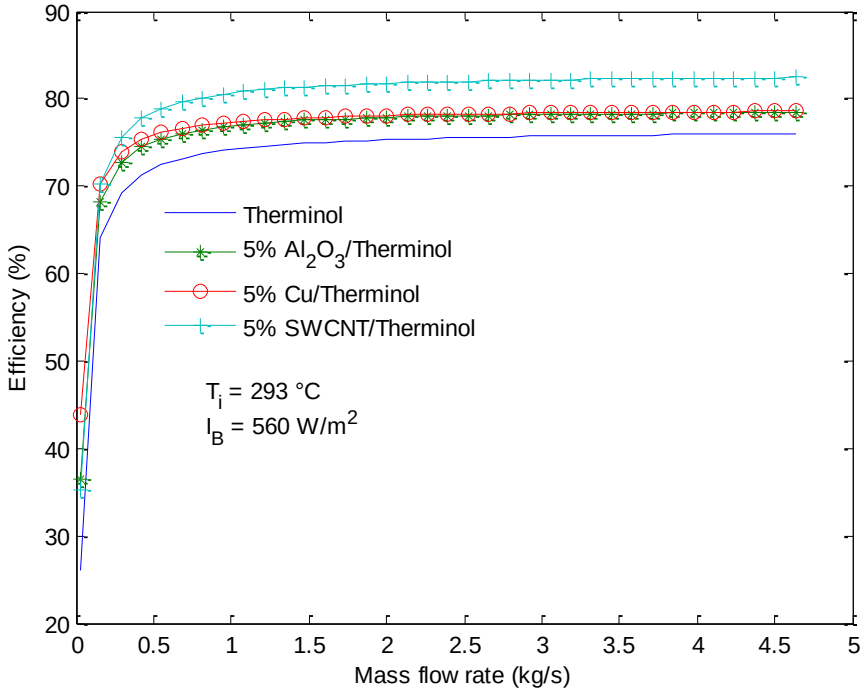

(a)

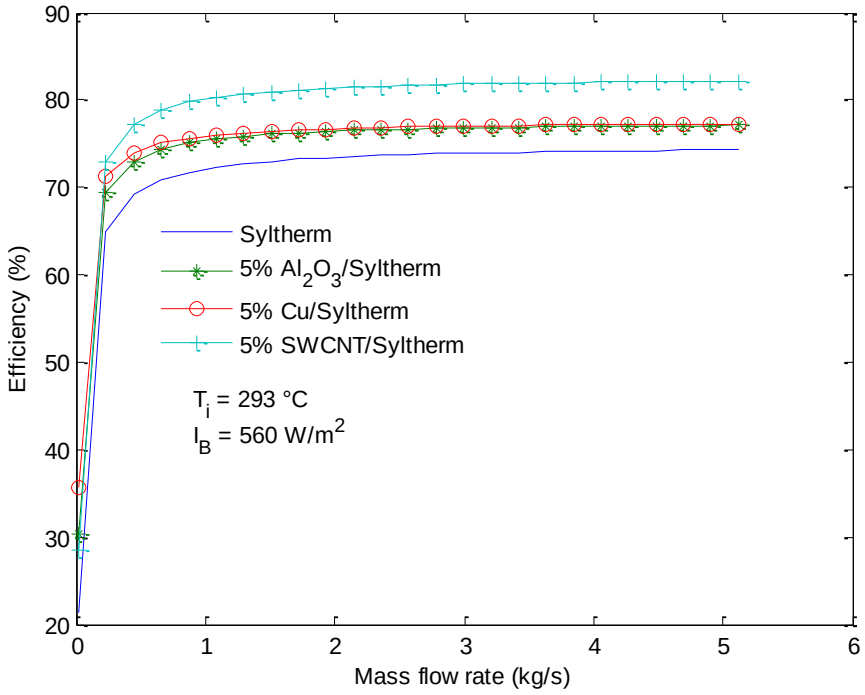

(b)

Figure 54: Effect of mass flow rate on the efficiency of the PTSC for (a) Therminol-based nanofluids, and (b) Syltherm-based nanofluids

Table 15: Average enhancement in PTSC efficiency and power output ($\boldsymbol{\varphi = 5}$%)

Nanofluid	Average enhancement in $\eta_{PTSC}, \dot{Q}_u$
Unit	(%)
Al_2O_3/Therminol	4.8588
Cu/Therminol	6.3125
$SWCNT$/Therminol	9.5623
Al_2O_3/ Syltherm	6.2388
Cu/ Syltherm	8.0297
$SWCNT$/ Syltherm	12.0853

The effect of using nanofluids as a heating fluid is studied with respect to the mass flow rate range, the thermophysical properties, and the heat transfer coefficient values acquired from the previous sections. The effect of the volume fraction on the efficiency and power output of the PTSC is considered in order to choose the most suitable nanofluid to replace the conventional heating fluid and enhance the system outputs.

4.5.2 Effect of the volume fraction on the PTSC performance.

Figure 55 shows the variation of the volume fraction on the power output of the PTSC for Therminol-based and Syltherm-based nanofluids at a temperature of 342 ℃. The mass flow rate is taken as the optimum mass flow rate from Figure 53; it is 2.5 kg/s for Therminol-based nanofluids, and 2.8 kg/s for Syltherm-based nanofluids. It is seen that the power output increases with the increase of the volume fraction for all nanofluids. However, for $SWCNT$-based nanofluids, the increase in the power output is almost negligible for a volume fraction higher than 10%. While for Al_2O_3-based and Cu–based nanofluids the power output increases with the increase in the volume fraction up to a volume fraction of more than 25%. However, the high increase in the volume fraction will have a negative effect on the thermophysical properties of the nanofluids, and will increase the cost of the nanofluids due to the addition of more nanoparticles. Therefore, it is recommended to use nanofluids with a low volume fraction, ranging between 5% and 10%.

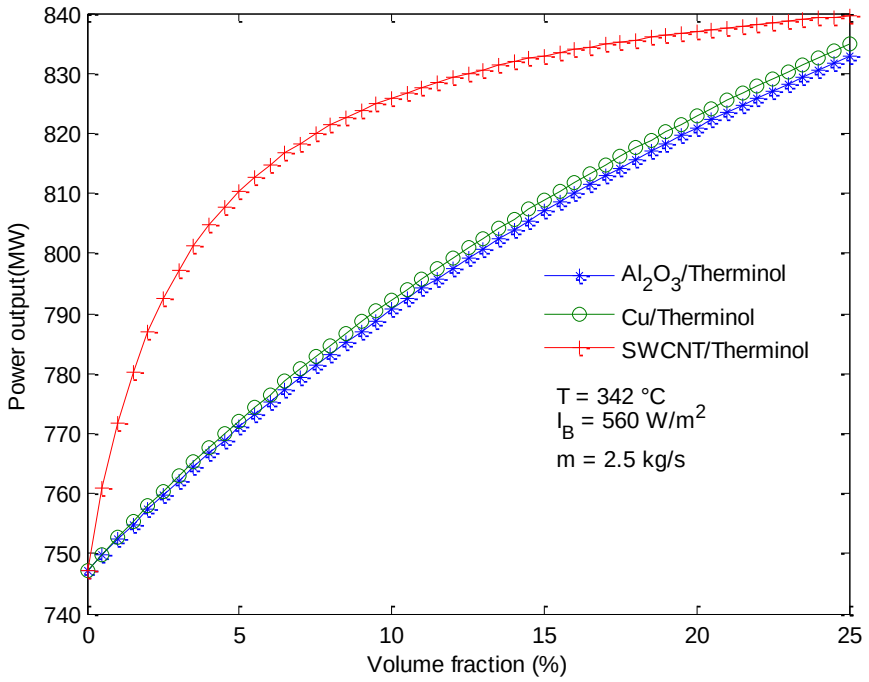

(a)

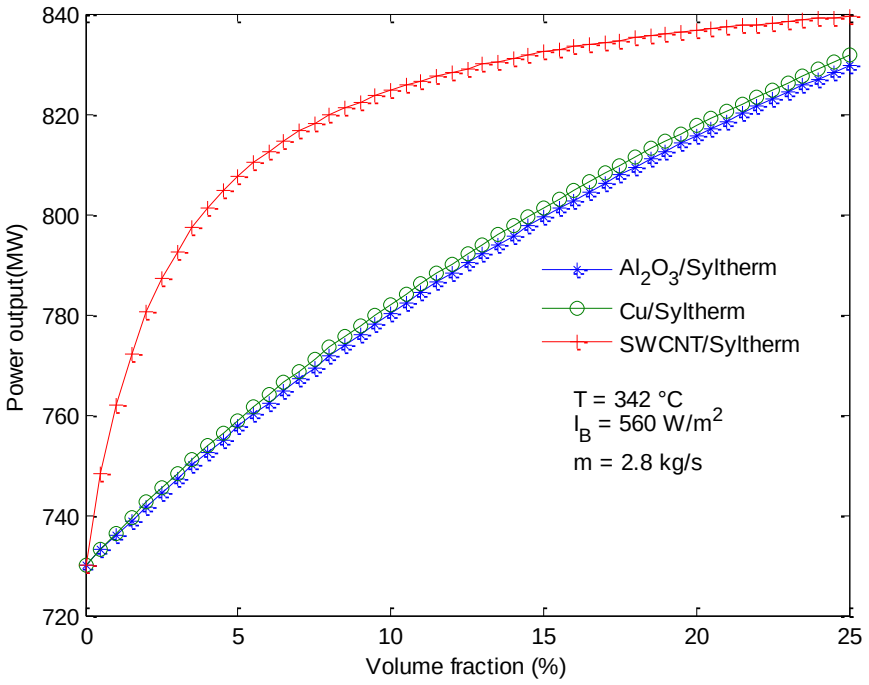

(b)

Figure 55: Effect of volume fraction on the power output of the PTSC for (a) Therminol-based nanofluids, and (b) Syltherm-based nanofluids

In addition, it is noticed that Al_2O_3-based nanofluids and Cu-based nanofluids share the same improvement in the power output of the PTSC with a slight advantage to the Cu-based nanofluids. Moreover, when compared to data provided in the literature, [158] and [159] respectively found that adding $SWCNT$ and Cu nanoparticles to the heating fluid enhances the efficiency of the PTSC, and that enhancement increases with the increase of the volume fraction which agrees with the results provided in the following figures.

4.5.3 Effect of the concentration ratio on the PTSC performance.

The concentration of the PTSC is a measure of the ratio of the aperture area to the receiver area as seen from Equation (3.108). The following analysis assumes the receiver area to be constant, and varies the concentration to study the effect of the aperture area on the power output of the PTSC.

Figure 56 shows the variation of the mass flow rate on the power output of the PTSC for Therminol-based nanofluids with a volume fraction of 5% for different concentrations, and at a temperature of 342 ℃. It is seen that the power output increases with the increase of the concentration ratio, and this is expected as the larger the aperture area, the larger the amount of solar beam radiation reflected onto the absorber tube. Moreover, it is observed that the addition of the nanoparticles increases the power output of the PTSC at any given concentration ratio. When comparing the increase in the power output, it was noticed that the enhancement in the power output is constant despite the change in the concentration ratio. For instance, the enhancement caused by Al_2O_3, Cu, and $SWCNT$ nanoparticles is 4.8%, 6.3% and 9.5% respectively for all concentration ratios.

Figure 57 shows the variation of the mass flow rate on the power output of the PTSC for Syltherm-based nanofluids with a volume fraction of 5% for different concentrations, and at a temperature of 342 ℃. Similar to Therminol-based nanofluids, it is seen the power output increase with the increase in the concentration ratio, and with the presence of the nanoparticles. The amount of the enhancement in the power output caused by the addition of Al_2O_3, Cu, and $SWCNT$ nanoparticles is 5.87%, 7.47%, and 11.84% respectively. Compared to Therminol-based nanofluids, it is observed that

Syltherm-based nanofluids show a higher percentage increase in power output, however Therminol-based nanofluids display a higher power output at any given mass flow rate and concentration ratio. Regarding the effect of the mass flow rate on the concentration ratio, it is seen that the mass flow rate has a negligible effect on the concentration ratio in the sense that for every concentration ratio provided, the mass flow increases and reaches the peak at the same value. Moreover, indicating that the mass flow rate has a negligible effect on the aperture area of the PTSC, and that it only affects the receiver.

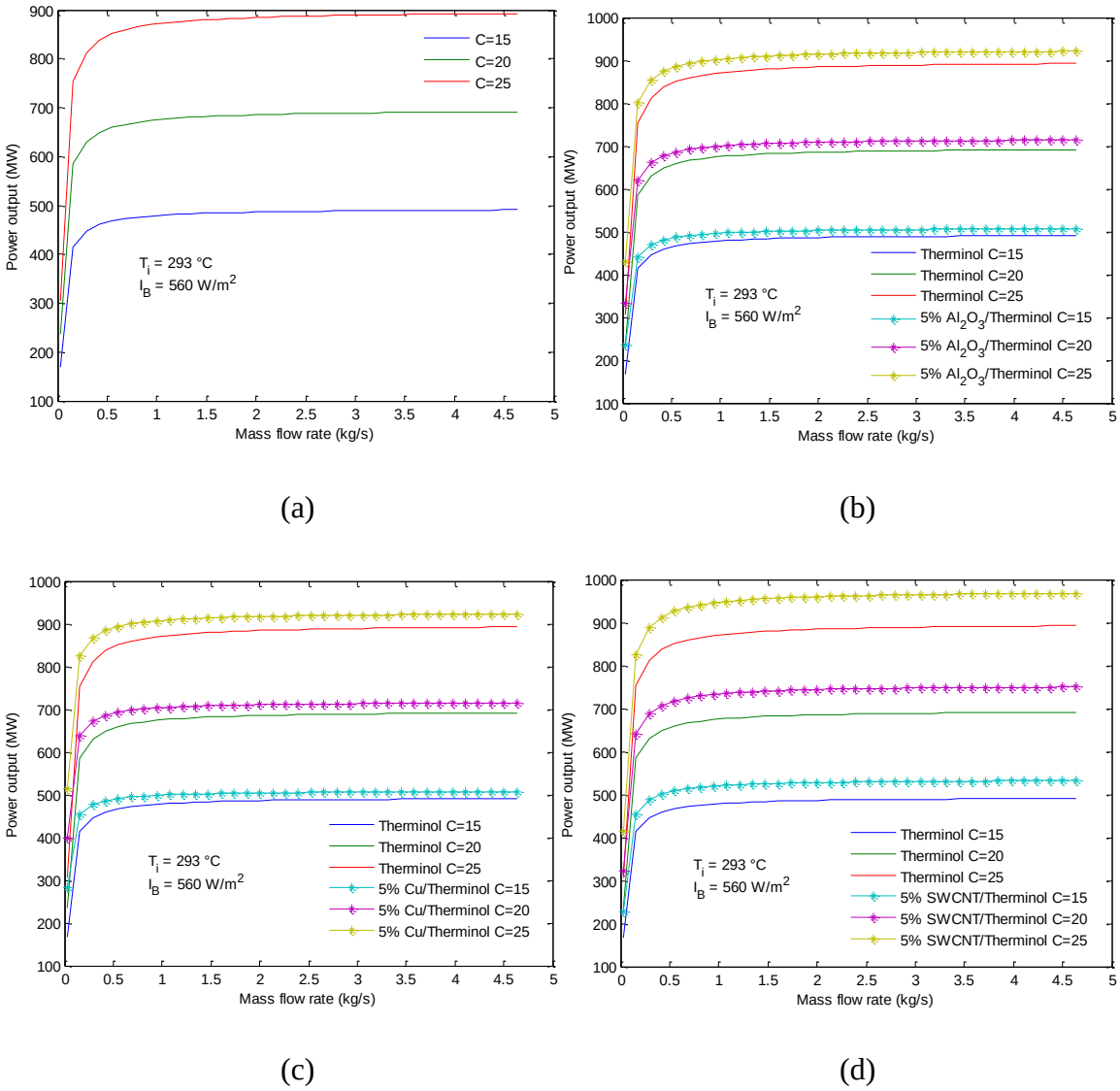

Figure 56: Effect of mass flow rate on the power output of the PTSC for different concentration for (a) Therminol, (b) **5%** $\boldsymbol{Al_2O_3}$/Therminol, (c) **5%** $\boldsymbol{Cu}$/Therminol, and (d) **5%** $\boldsymbol{SWCNT}$/Therminol

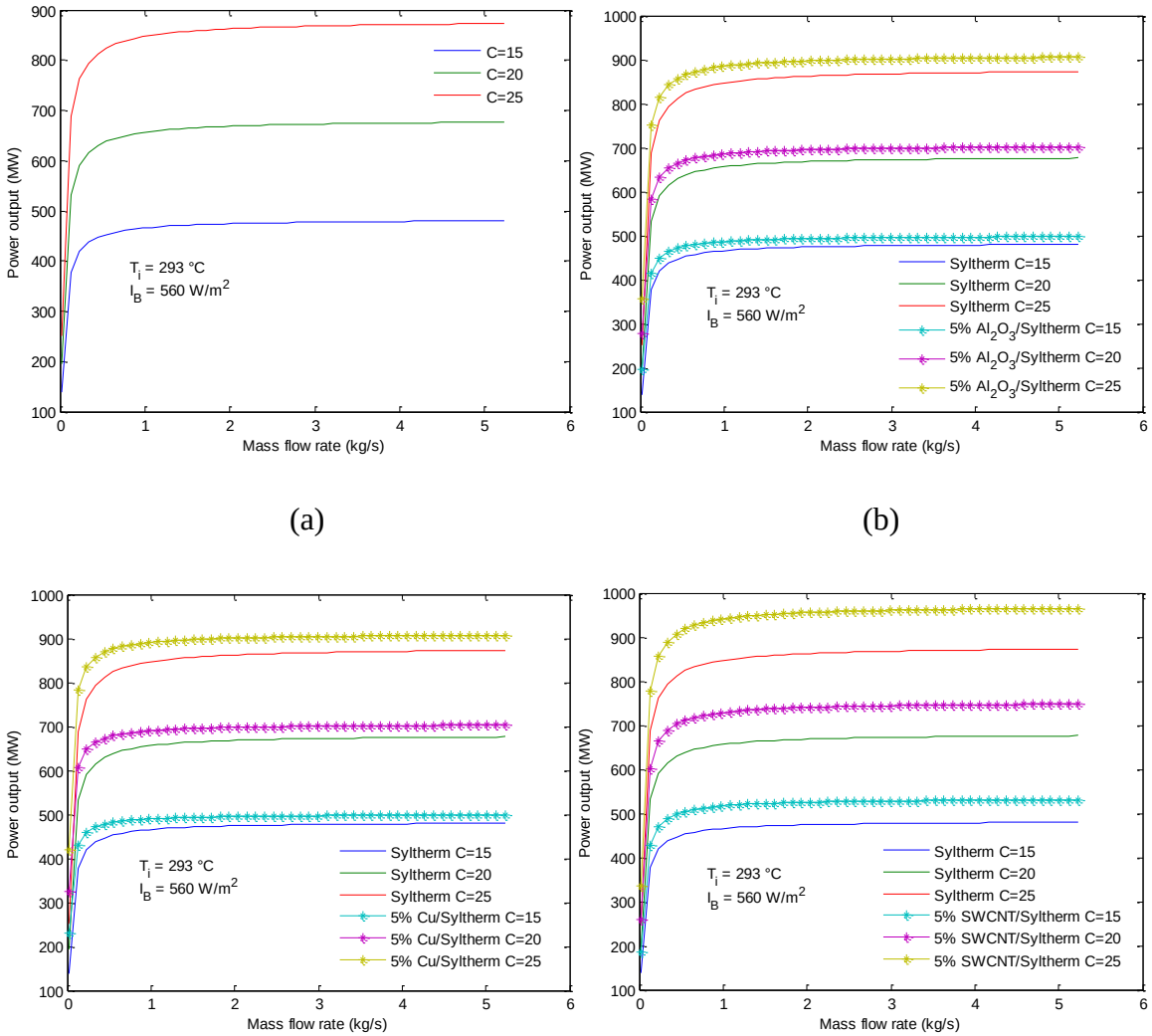

Figure 57: Effect of mass flow rate on the power output of the PTSC for different concentration for (a) Sytherm, (b) **5%** $\boldsymbol{Al_2O_3}$/Sytherm, (c) **5%** $\boldsymbol{Cu}$/Sytherm, and (d) **5%** $\boldsymbol{SWCNT}$/Sytherm

4.5.4 Effect of the beam radiation on the PTSC performance.

It is evident from the earlier finding that nanofluids are the best replacement for conventional heat transfer fluids; however the magnitude of the improvement caused by adding nanoparticles to the base fluids is still to be determined. For this case a monthly based analysis is done for the PTSC system described in the System Modeling section for the city of Abu Dhabi. In order to proceed with the analysis, the beam radiation for a monthly basis from Figure 15 is used along with the thermophysical properties and heat

transfer characteristics of Therminol-based nanofluids, and Syltherm-based nanofluids, a monthly based analysis is done for the power output of the PTSC.

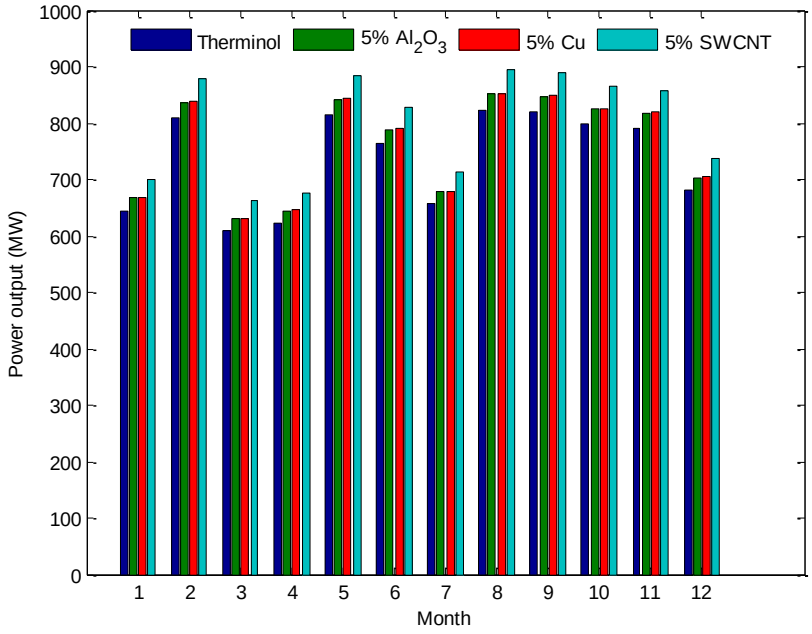

(a)

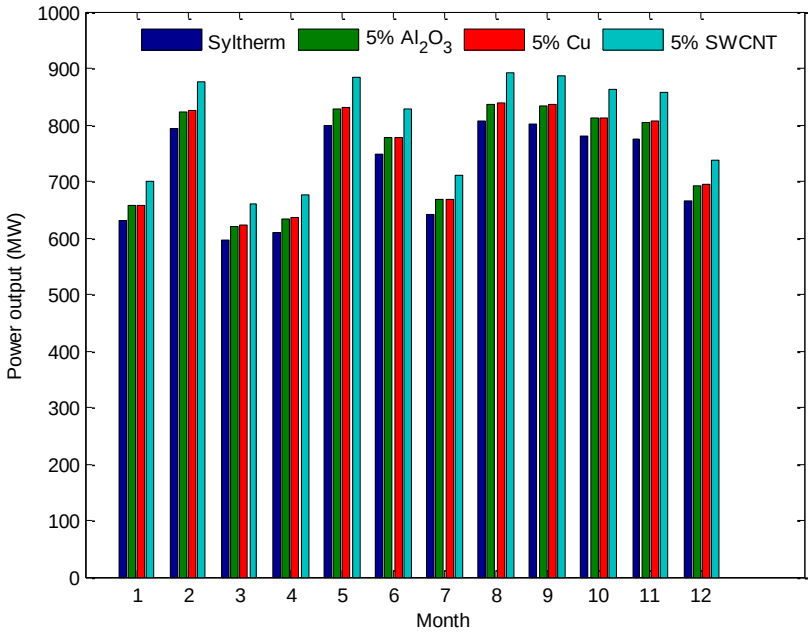

(b)

Figure 58: Effect of beam radiation on the power output of the PTSC on a monthly basis for (a) Therminol-based nanofluids and (b) Syltherm-based nanofluids

Figure 58 shows the variation of the beam radiation on the power output of the PTSC on a monthly basis for Therminol-based nanofluids and Syltherm-based nanofluids with a volume fraction of 5%. The analysis is carried for a temperature of 342 ℃, and a mass flow rate of $2.5\,kg/s$ for Therminol-based nanofluids, and a mass flow rate of $2.8\,kg/s$ for Syltherm-based nanofluids as they are the optimum mass flow rates. It is seen that the power output of the PTSC is higher when nanofluids are present, as expected from the previous discussion; $SWCNT$-based nanofluids show the highest enhancement in the power output for all the months. The percentage increase in the power output for $SWCNT$-based nanofluids is around 8.54% when compared to Therminol and 10.7% when compared to Syltherm. For Cu-based nanofluids, the percentage increase is around 3.58% when compared to Therminol and 4.2% when compared to Syltherm, while for Al_2O_3-based nanofluids the increase is 3.32% when compared to Therminol and 3.92% when compared to Syltherm. The same trend is observed where Syltherm-based nanofluids show a higher enhancement than Therminol-based nanofluids. Moreover, the month of August shows the highest power output of the PTSC, followed by September which is the month where the highest beam radiation is present.

In order to study the performance of the PTSC in depth, a daily analysis is done for a day in the month of August, where the variation of the operation time on the power output, efficiency, exergetic efficiency and entropy generation of the PTSC is analyzed. To start the analysis, the variation of the time on the beam radiation for a day in the month of August is shown in Figure 59. It is assumed that the PTSC is under operation for 8 hours, from 8:00 am until 4:00 pm. The highest beam radiation is present during the noon hours from 12:00 pm until 1:00 pm, where the sun is in its highest position and the sun rays are reflected from the collector onto the absorber tube with the least refraction. The month of August was chosen for the analysis because it showed the highest performance when compared to other months.

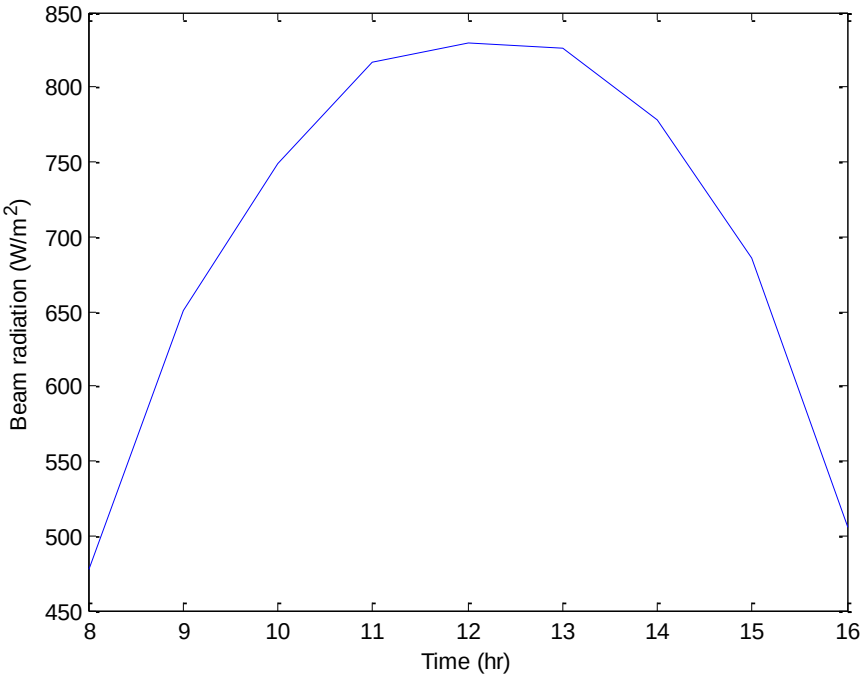

Figure 59: Effect of time on the beam radiation for a day in the month of August

Figure 60 shows the variation of the time on the power output, efficiency, exergetic efficiency, and entropy generation for Therminol-based nanofluids for a day in the month of August. The temperature is set at 342 ℃, volume fraction is 5%, and the mass flow rate is the optimum flow rate of 2.5 kg/s. It is seen that the performance of the PTSC depends heavily on the beam radiation; hence the maximum performance is present during the noon hours, while the performance decreases in the hours of the afternoon. In addition, the presence of the nanoparticles increases the power output, efficiency, exergetic efficiency, and decreases the entropy generation, improving the performance of the PTSC overall.

Similar to the analysis done for Therminol-based nanofluids, Figure 61 shows the variation of the time on the power output, efficiency, exergetic efficiency, and entropy generation for Syltherm-based nanofluids for a day in the month of August. The analysis is done for a temperature of 342 ℃, volume fraction is 5%, and an optimum mass flow rate of 2.8 kg/s. It is seen that the PTSC performance is improved when nanofluids are used. In addition, $SWCNT$-based show the highest improvement compared to Cu-based and Al_2O_3-based nanofluids. When compared to Therminol-based nanofluids, it is seen

that Syltherm-based nanofluids display a higher improvement in the performance of the PTSC, however Therminol-based nanofluids display a higher power output, efficiency, exergetic efficiency, and a lower entropy generation.

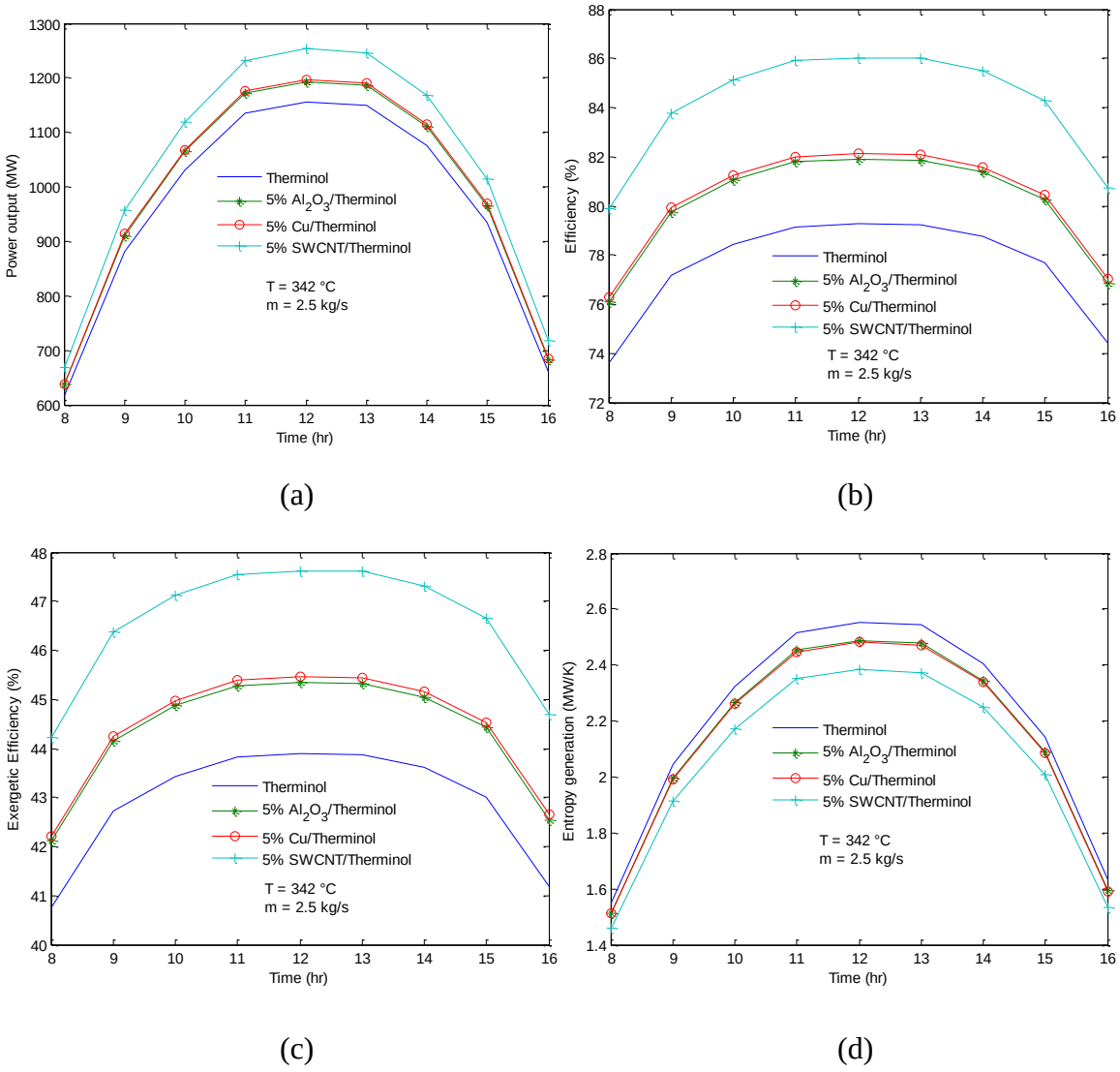

Figure 60: Effect of time on the (a) power output, (b) efficiency, (c) exergetic efficiency, and (d) entropy generation of the PTSC for Therminol-based nanofluids for a day in August

As predicted from the previous analysis, $SWCNT$-based nanofluids show the highest improvement in the PTSC performance when compared to Cu-based and Al_2O_3-based nanofluids. A comparison between the nanofluids in terms of the percentage increase in the power output and efficiencies of the PTSC, and the percentage decrease in

the entropy generation, as well as the maximum value obtained for each parameter are shown in Table 16. The maximum values are all calculated at 12:00 pm, where the maximum beam radiation is present.

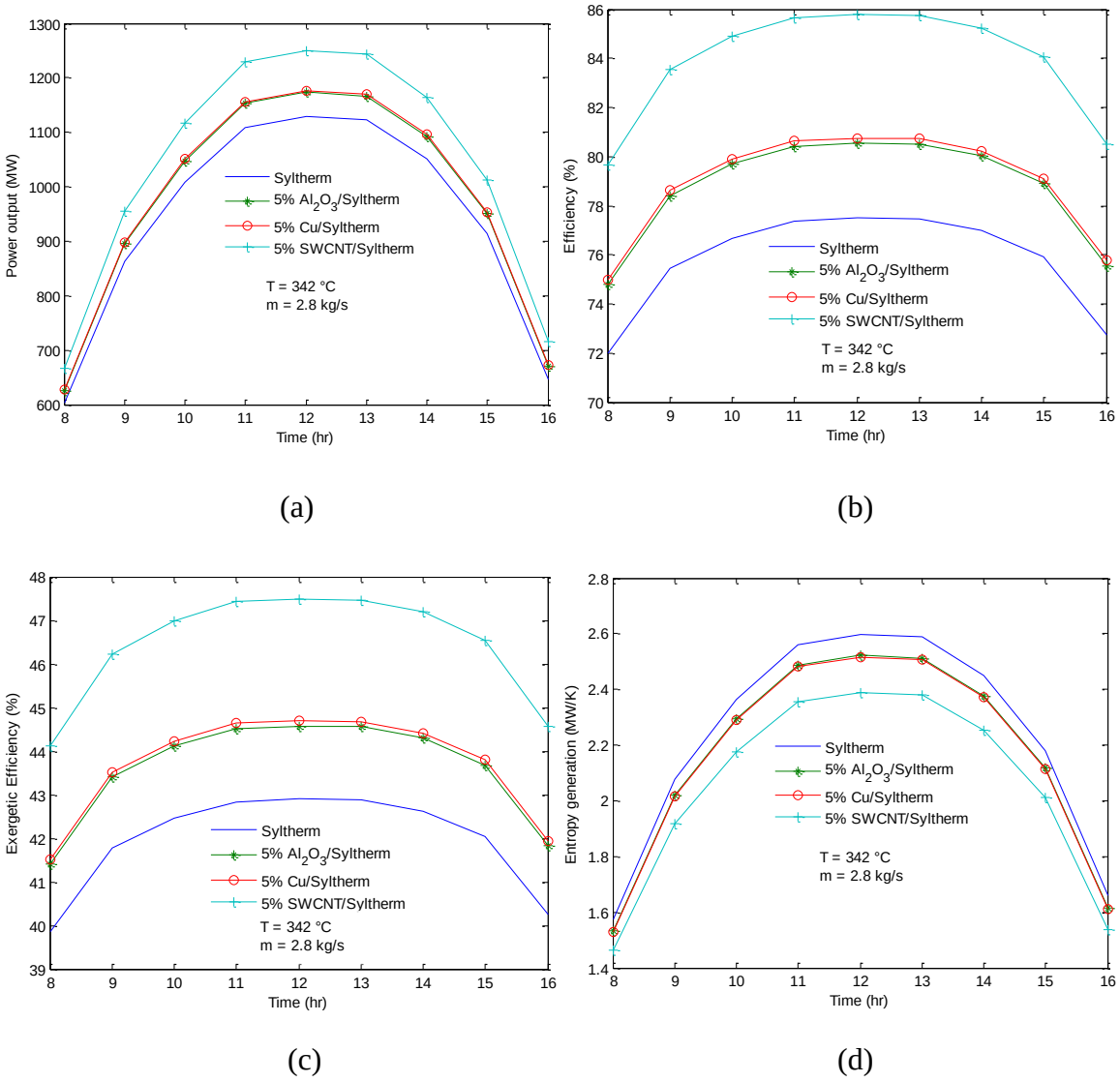

Figure 61: Effect of time on the (a) power output, (b) efficiency, (c) exergetic efficiency, and (d) entropy generation of the PTSC for Sytherm-based nanofluids for a day in August

A monthly analysis is carried comparing the effect of $SWCNT$-based nanofluids and base fluids on the performance of the PTSC regarding the power output, efficiency, exergetic efficiency, and entropy generation.

Table 16: Comparison between Therminol-based and Syltherm-based nanofluids regarding the performance of the PTSC for a day in the month of August

Parameter	Power Output (MW)		Efficiency (%)		Exergetic Efficiency (%)		Entropy Generation (MW/K)	
Fluid	% Increase	Max. Value	% Increase	Max. Value	% Increase	Max. Value	% decrease	Max. Value
Therminol	-	1155	-	79.3		43.9	-	2.554
Al_2O_3/Therminol	3.31	1193	2.57	81.9	1.42	45.3	2.59	2.488
Cu/Therminol	3.57	1196	2.77	82.1	1.53	45.5	2.80	2.483
$SWCNT$/Therminol	8.52	1253	6.60	86.1	3.66	47.6	6.95	2.384
Syltherm	-	1129	-	77.5	-	42.9	-	2.599
Al_2O_3/Syltherm	3.92	1173	2.97	80.5	1.64	44.5	2.95	2.522
Cu/Syltherm	4.20	1176	3.18	70.7	1.76	44.7	3.18	2.517
$SWCNT$/Syltherm	10.71	1250	8.12	85.8	4.49	47.5	8.52	2.390

Figure 62 shows the variation of the beam radiation on the power output of the PTSC on a monthly basis for Therminol and $SWCNT$/Therminol, Syltherm and $SWCNT$/Syltherm with a 5% volume fraction. The analysis was carried for a temperature of 342 ℃ and a mass flow rate of 2.5 kg/s for Therminol-based fluids and 2.8 kg/s for Syltherm-based fluids. It is seen that by using $SWCNT$-based nanofluids the power output was increased by 8.52% when compared to Therminol and 10.71% when compared to Syltherm.

In addition, it is seen that the highest power output is produced during the month of August contrary to September which is the month with the highest solar beam radiation, suggesting that the power output does not solely depend on the beam radiation. Moreover it is observed that $SWCNT$/Syltherm nanofluid shows a higher enhancement in power output than $SWCNT$/Therminol when compared to Syltherm and Therminol respectively, however $SWCNT$/Therminol and Therminol show a higher power output values. For instance, for the month of August the energy produced by Therminol and $SWCNT$/Therminol is 823 MW and 894 MW respectively, while the energy produced by Syltherm and $SWCNT$/Syltherm is 805 MW and 891 MW.

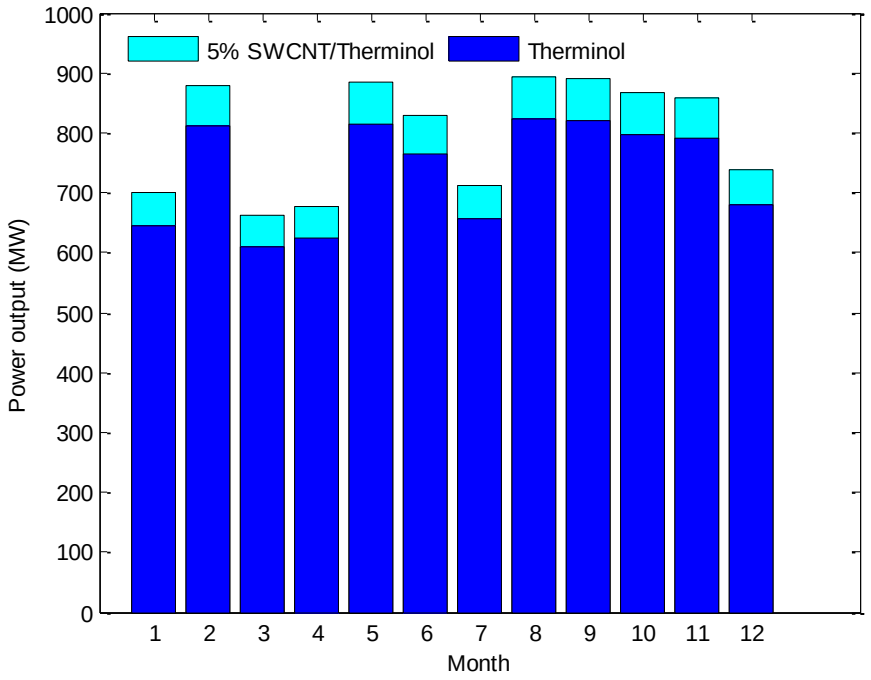

(a)

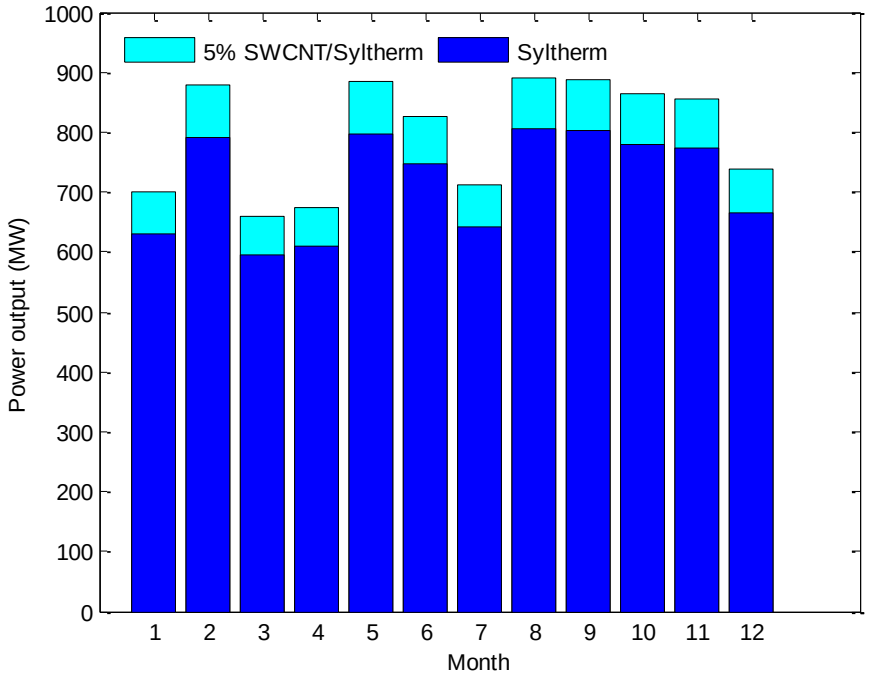

(b)

Figure 62: Effect of beam radiation on the power output of the PTSC on a monthly basis for (a) Therminol and ***SWCNT***/Therminol fluids and (b) Syltherm and ***SWCNT***/Syltherm fluids

The variation of the beam radiation on the efficiency of the PTSC on a monthly basis for Therminol and $SWCNT$/Therminol, Syltherm and $SWCNT$/Syltherm with a 5 % volume fraction is shown in Figure 63. It is seen that the presence of $SWCNT$ nanoparticles increases the efficiency of the PTSC, and this increase is around 6.4 % in average when comparing $SWCNT$/Therminol to Therminol, and around 8% when comparing $SWCNT$/Syltherm to Syltherm. It is noticed that the maximum increase in efficiency happens in the month of August where the maximum efficiency of the PTSC is present, and the minimum increase in the efficiency occurs in the month of March where the lowest value of the efficiency is present. For example, the efficiency of the PTSC in the month of August is 74.86 % and 76.52 % for Syltherm and Therminol respectively, but when $SWCNT$ nanoparticles were added, the efficiency improved to 82.87 % for SWCNT/Syltherm and 83.06 % for SWCNT/Therminol nanofluids.

Figure 64 shows the variation of the beam radiation on the exergetic efficiency of the PTSC on a monthly basis for Therminol and $SWCNT$/Therminol, Syltherm and $SWCNT$/Syltherm with a 5% volume fraction. It is seen that the addition of the nanoparticles increases the exergetic efficiency by 4.37 % and 3.56 % on average for Syltherm and Therminol respectively. The same trend is present regarding the maximum exergetic efficiency where it occurs in the month of August. For instance, the exergetic efficiency is 41.44 % and 42.36 % for Syltherm and Therminol respectively, compared to an increased efficiency of 45.88 % for Syltherm-based and 45.98 % for Therminol-based nanofluids.

Figure 65 shows the variation of the beam radiation on the entropy generation of the PTSC on a monthly basis for Therminol and $SWCNT$/Therminol, Syltherm and $SWCNT$/Syltherm with a 5 % volume fraction. It is seen that the entropy generation reduces when nanofluids are used, this decrease is around 6.54 % for $SWCNT$/Therminol compared to Therminol, and around 8 % for $SWCNT$/Syltherm compared to Syltherm. Finally, it is concluded that the use of nanofluids improves the power output of the PTSC as well as the efficiency and exergetic efficiency. In addition, nanofluids reduces the amount of entropy generated leading to an enhanced heat transfer between the heating fluid and the PTSC.

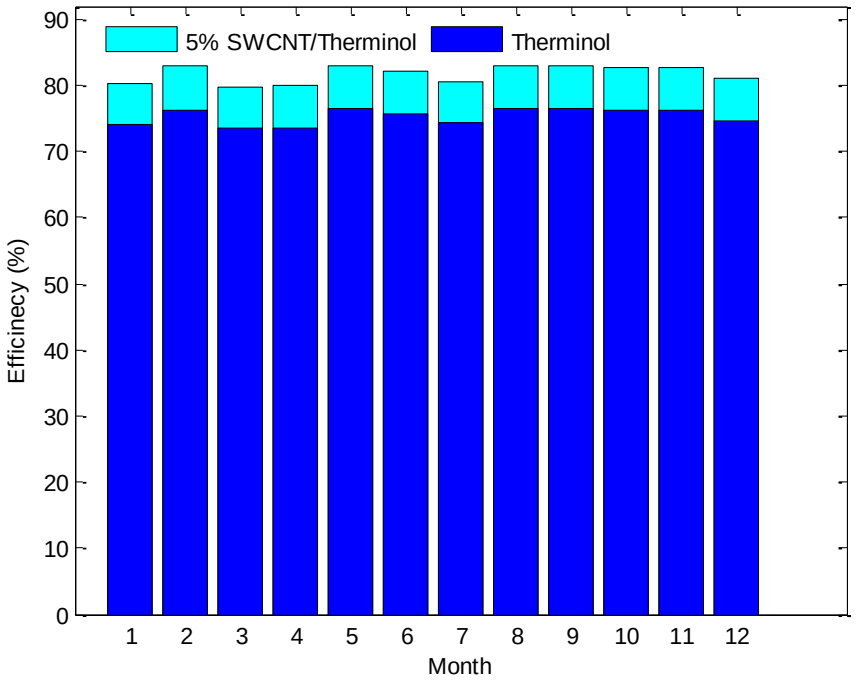

(a)

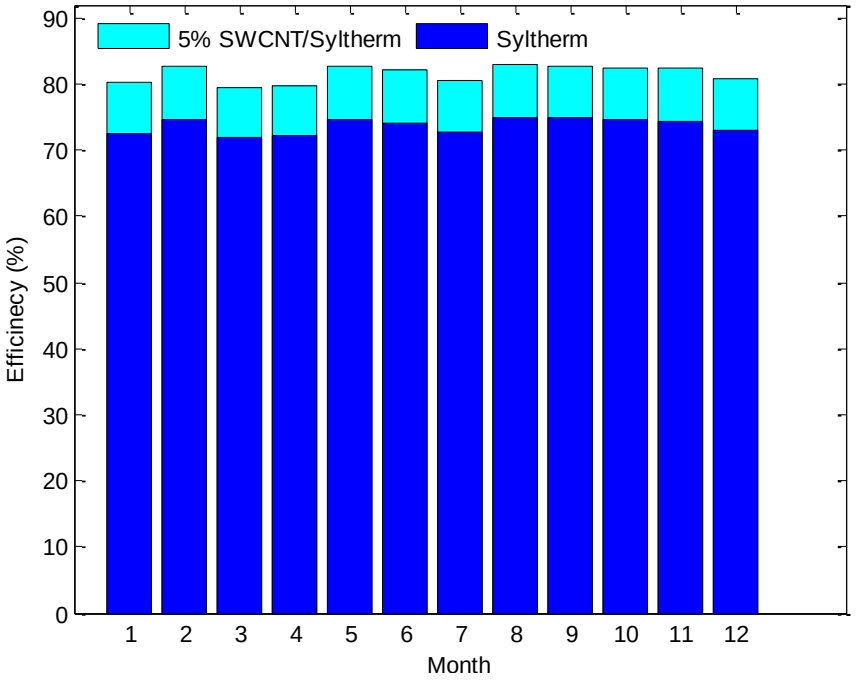

(b)

Figure 63: Effect of beam radiation on the efficiency of the PTSC on a monthly basis for (a) Therminol and ***SWCNT***/Therminol fluids and (b) Syltherm and ***SWCNT***/Syltherm fluids

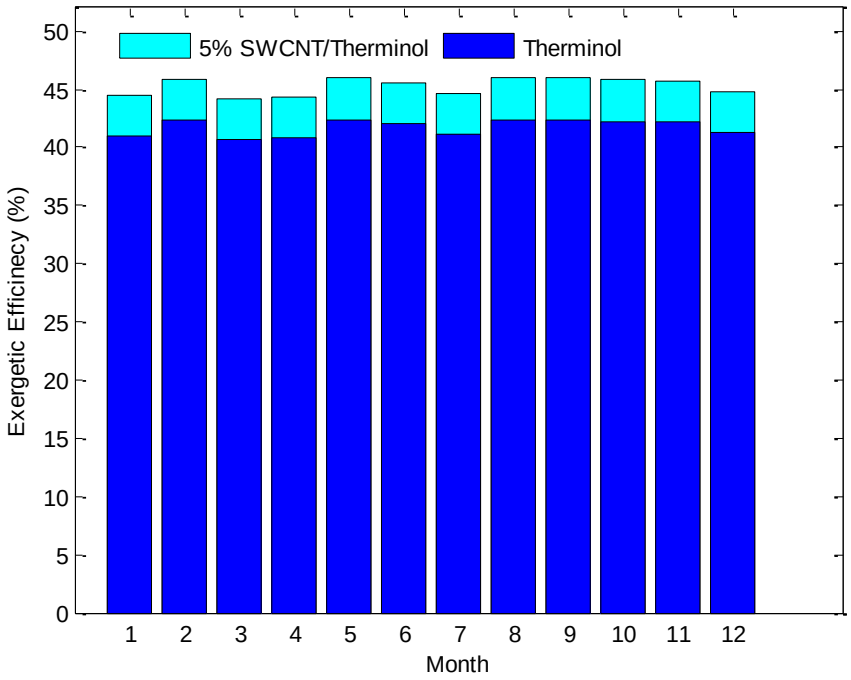

(a)

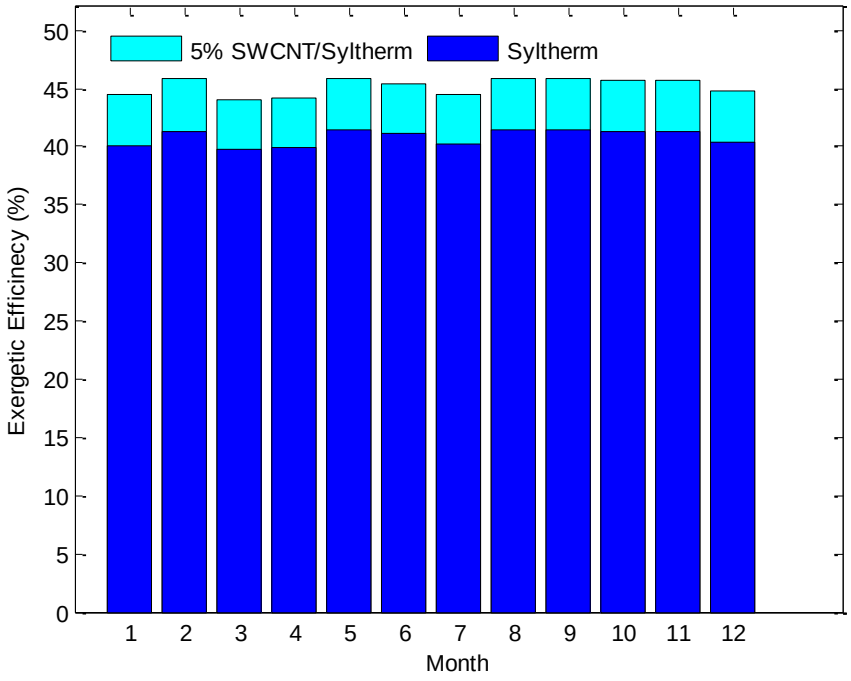

(b)

Figure 64: Effect of beam radiation on the exergetic efficiency of the PTSC on a monthly basis for (a) Therminol and ***SWCNT***/Therminol fluids and (b) Syltherm and ***SWCNT***/Syltherm fluids

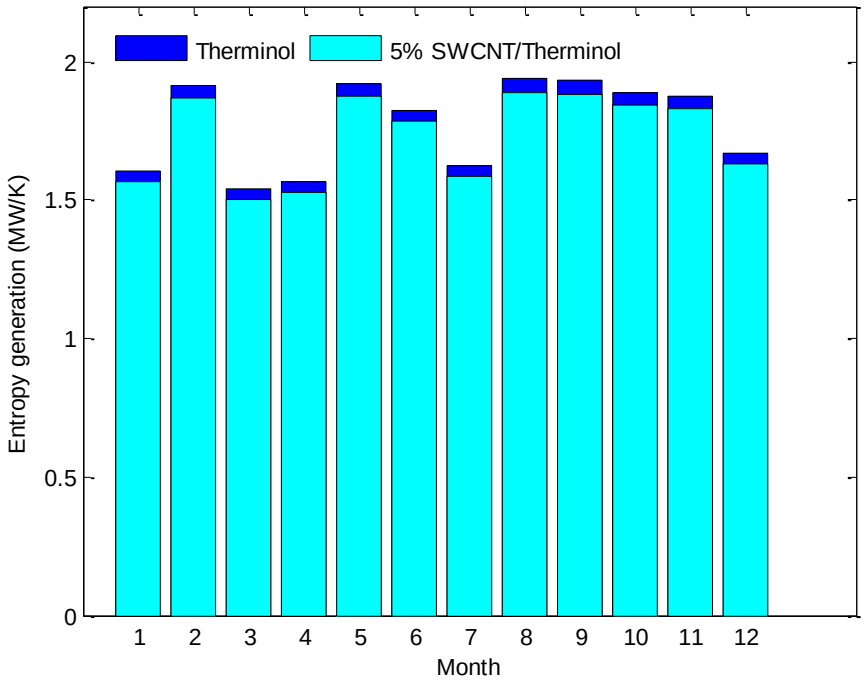

(a)

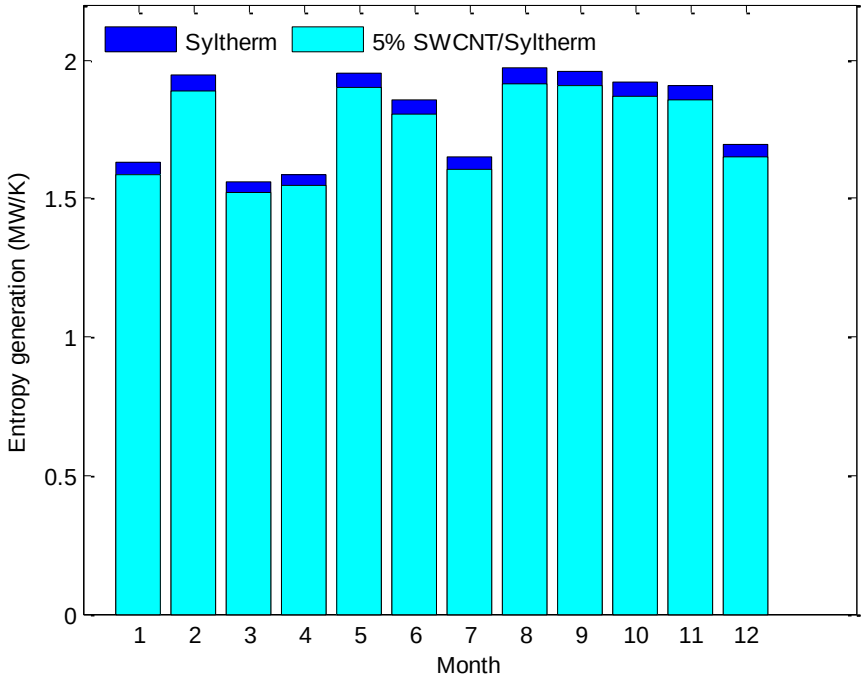

(b)

Figure 65: Effect of beam radiation on the entropy generation of the PTSC on a monthly basis for (a) Therminol and ***SWCNT***/Therminol fluids and (b) Syltherm and ***SWCNT***/Syltherm fluids

4.6 Integrated Solar-Rankine Cycle (ISRC) and Integrated Solar-Regenerative Rankine Cycle (ISRRC)

The effect of using nanofluids on the Integrated Solar-Rankine Cycle and Integrated Solar-Regenerative Rankine Cycle is investigated in this section. First a comparison between the ISRC and ISRRC is carried in order to choose the most efficient cycle; second the modes of operation are analyzed and compared for the base fluids. Third, the effect of using nanofluids as a heating fluid is studied.

4.6.1 Comparison between ISRC and ISRRC.

The power cycles are compared to each other in terms of the efficiency in order to choose the most efficient cycle for the integrated system. However, regarding the ISRRC the feed water pressure affects the efficiency of the cycle; therefore the optimum pressure is to be selected. Figure 66 shows the variation of the feed water pressure on the efficiency of the ISRRC. The analysis was carried using the input and design parameters from Tables 6, 7 and 9. It is seen that the efficiency of the ISRRC increases with the increase of the pressure, up to a pressure of 9 bar where a peak value is reached. For feed water pressure greater than 9 bar the efficiency of the ISRRC decreases. Therefore, it is observed that the optimum pressure is 9 bars, which is provided in Table 9.

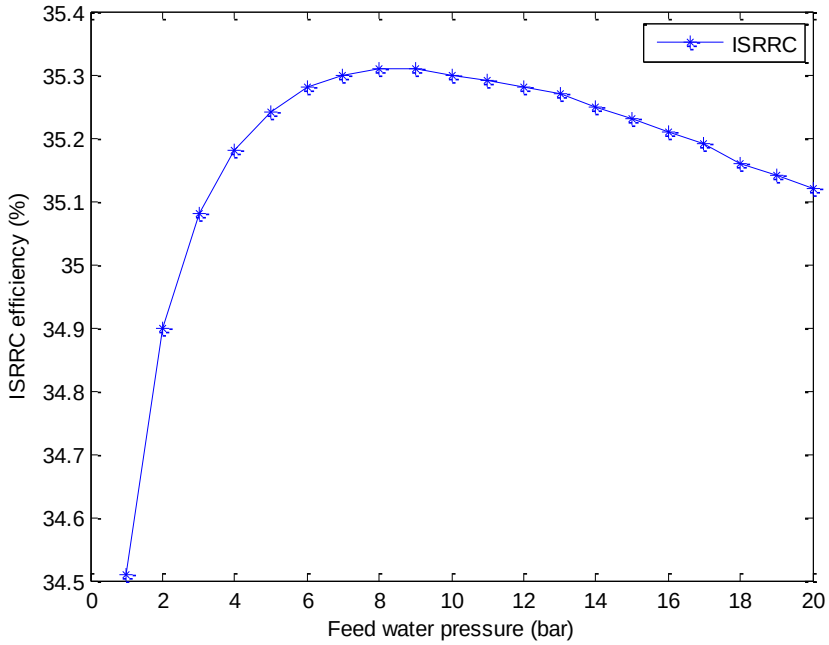

Figure 66: Effect of feed water pressure on the efficiency of the ISRRC

Subsequent to finding the optimum pressure, the optimum mass fraction extracted is determined. Figure 67 shows the variation of the feed water pressure on the mass fraction extracted of the ISRRC. It is seen that for a feed water pressure of 9 bars, the mass fraction extracted from the turbine is 0.2244.

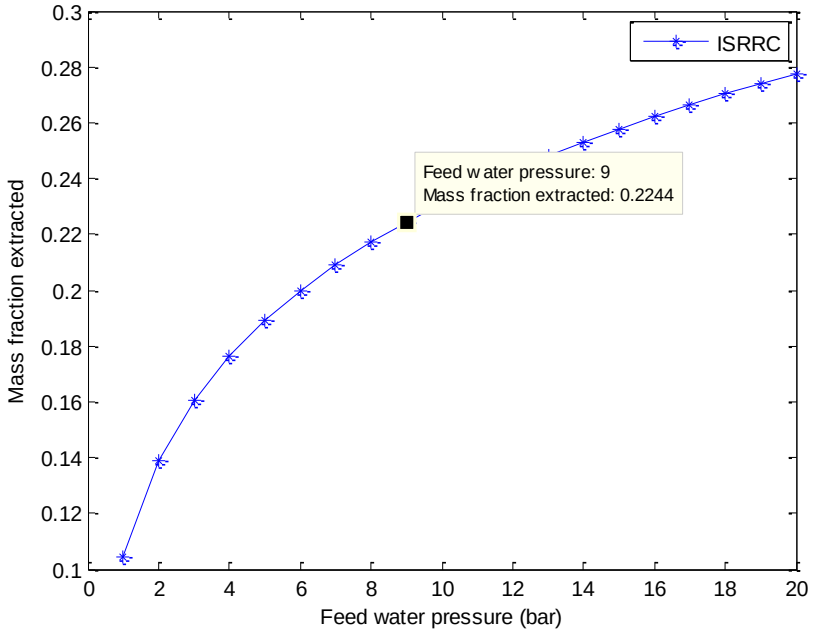

Figure 67: Effect of feed water pressure on the flash factor of the ISRRC

After optimizing the ISRRC, a comparison is done between the two power cycles. Figure 68 shows the variation of the inlet turbine temperature on the efficiency of the ISRC and ISRRC. It is seen that as the inlet turbine temperature increases, the efficiencies of the cycles increase. However, the ISRRC exhibits a higher efficiency than that of ISRC. Although the work done by the turbine of the ISRRC is less than the work done by the ISRC, the amount of heat needed to run the turbine for the ISRRC is less than that of the ISRC, resulting in a higher efficiency.

In reality, adding the feed water heater will decrease the load on the turbine, and the amount of heat needed from the solar field. In addition, most of the power plant that is run on an integrated solar system utilizes the regenerative Rankine cycle as the power cycle, nevertheless those cycles consist of multiple feed water heaters and multiple turbines. Based on the analysis done in this section, the ISRRC is chosen as power cycle for the integrated solar system.

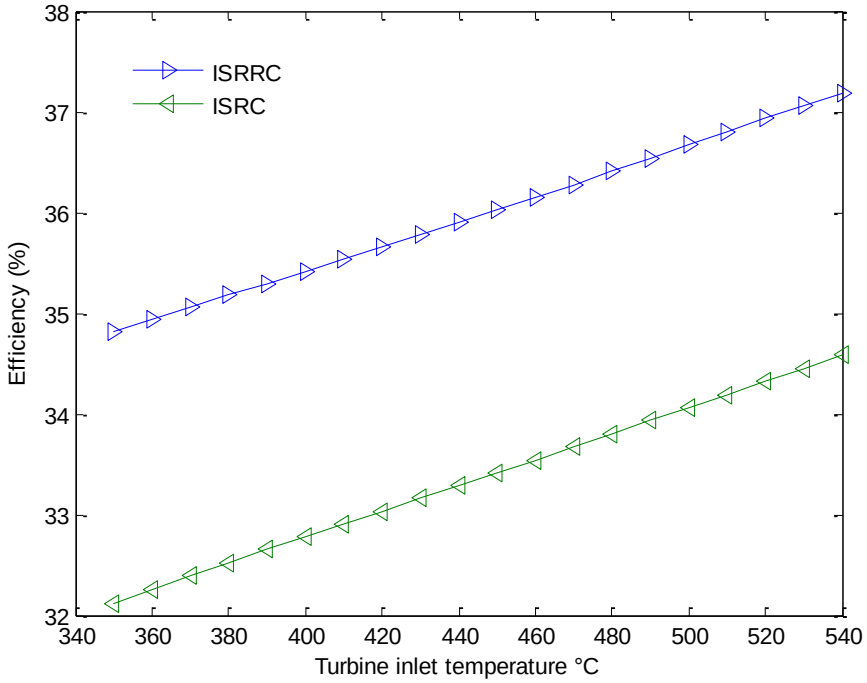

Figure 68: Effect of inlet turbine temperature on the efficiencies of the ISRC and ISRRC

4.6.2 Effect of the mass flow rate on the performance of the ISRRC.

The performance of the ISRRC depends heavily on the mass flow rate of the heating fluid inside the PTSC field, the molten salt inside the storage system, and the steam running the cycle. In turn, the mass flow rates depend on the beam radiation reflected by the collector on the absorber tube. Figure 69 shows the variation of time on the mass flow rate for a day in the month of August for Therminol, and for the 2nd mode of operation with a storage period of 7.5 hour, in order to understand the behavior of the mass flow rate with respect to plant operation time.

The mass flow rates of the heating fluid inside the PTSC, the molten salt inside the storage system, and the steam in the cycle are shown in the figure. It is seen that the mass flow rate of the heating fluid inside the PTSC increases until a peak value around noon, before decreasing to zero when the PTSC shuts down due to the lack of sun around 7:00 pm. During the high beam radiation hours (12:00 pm to 3:00 pm), it is noticed that the mass flow rate of the molten salt is in the negative values. That indicates the charging process, where some of the heating fluid is bypassed to the storage heat exchanger in order to store the heating fluid for the discharging process. The discharging process begins around 5:00 pm, when the solar intensity is low and the PTSC is struggling to

supply the demand of the generation load. Moreover, the discharging process continues until the storage period set by the mode of operation (in this case 7.5 hours) is fulfilled. Regarding, the mass flow rate in the cycle, it is seen that the mass flow rate of the steam is almost constant through the plant operation hours, with the exception of the startup and the closedown.

The behavior depicted in the last figure is the same for the rest of the months, modes of operation, and for different nanofluids, and base fluids, with the exception of the values of the mass flow rate depending on the nanofluids and the mode of operation. This variation will be covered in the following section.

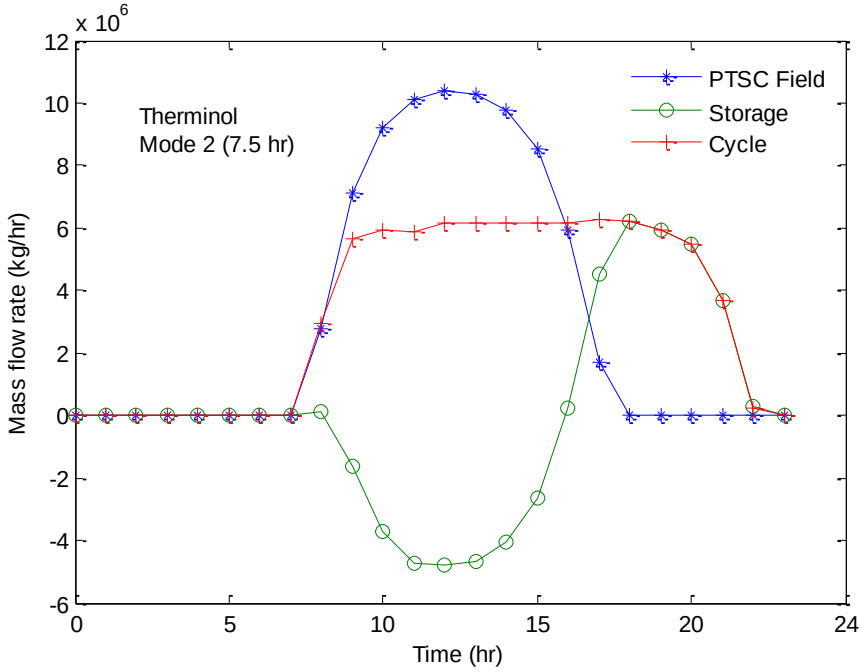

Figure 69: Effect of time on the mass flow rate for a day in August for Therminol

Figure 70 shows the variation of the beam radiation on the mass flow rate of the plant on a monthly basis for Therminol, and 2nd mode of operation. It is seen that the mass flow rate for the PTSC field, charging, discharging, and cycle are different for each month, depending on the solar intensity and beam radiation. The month of March shows the lowest mass flow rate, while the month of June shows the highest. Similar to the daily analysis, the trend of the mass flow rates with respect to the months is the same for all nanofluids, base fluids and modes of operation, with the values of the mass flow rates

being different depending on the mode of operation and the fluid. The analysis of the effect of the mass flow rates on the performance of the power plant with respect to the modes of operation is shown in the next section.

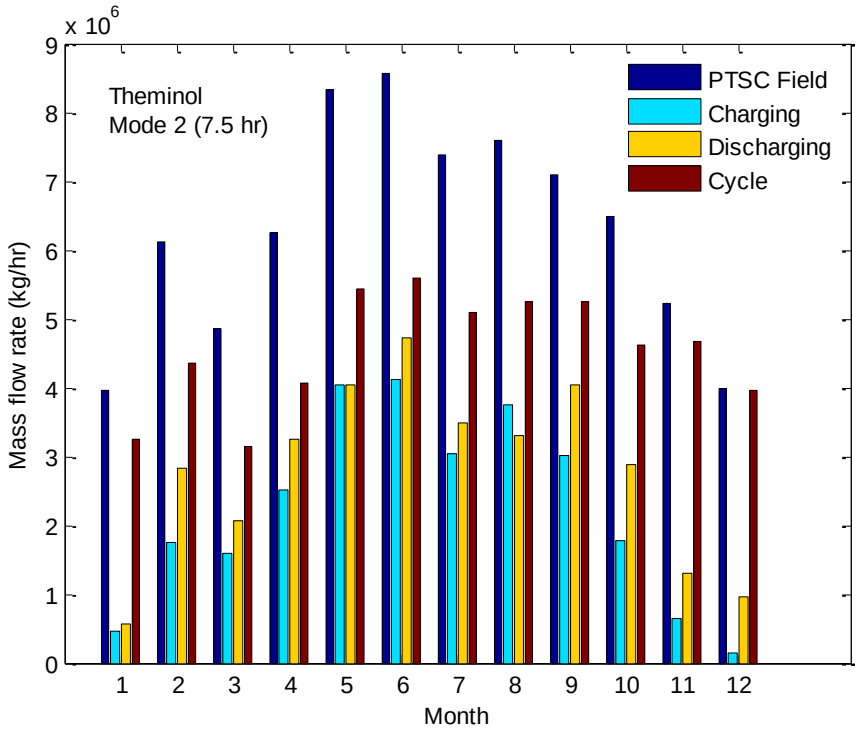

Figure 70: Effect of beam radiation on the mass flow rates of the power plant on a monthly basis for Therminol

4.6.3 Effect of the mass flow rate for different nanofluids and modes of operation.

As seen from the previous section, the mass flow rates of the heating fluid, fluid in the storage, and fluid in the cycle all depend on the beam radiation, the heating fluid, and the modes of operation. The design inputs and parameters from Tables 7, 9-11 are employed to study the annual profile of the mass flow rates with respect to time.

Figure 71 shows the variation of the time on the mass flow rates of the power plant for Therminol, and Therminol-based nanofluids for 1st mode of operation (no storage). It is seen that the mass flow rate of Therminol and Therminol-based nanofluids increases until a peak value during the high solar intensity hours (12:00 pm to 3:00 pm), then decreases until the PTSC stops operating because of the lack of the beam radiation. In addition, the mass flow of the steam inside the ISRRC follows the same trend as the

heating fluid, since this mode of operation has no storage, meaning that the operating hours are restricted to the operating hours of the PTSC from 8:00 Am until 6:00 pm.

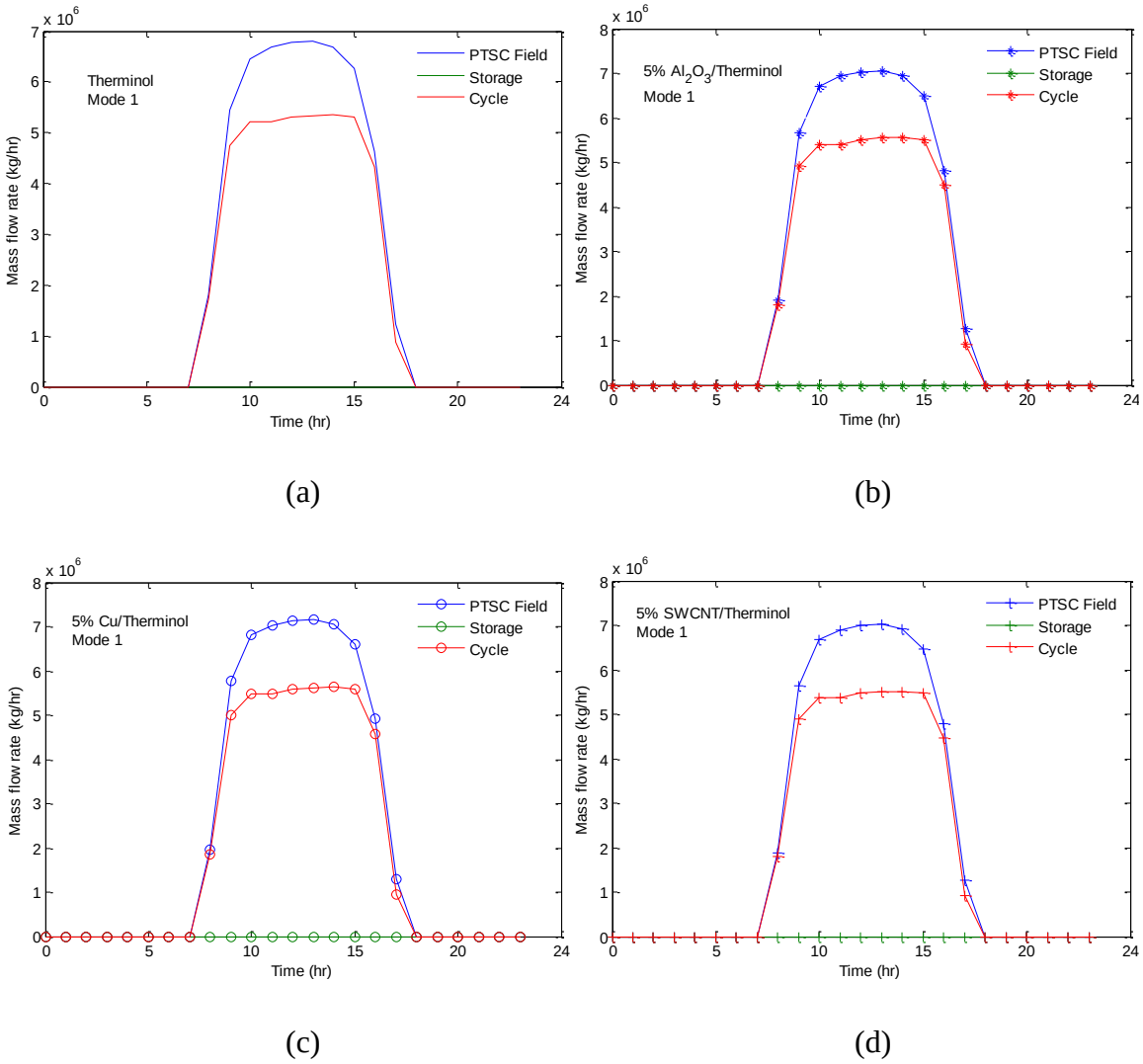

Figure 71: Effect of time on the mass flow rates of the ISRRC for the 1st mode of operation for (a) Therminol, (b) 5% $\boldsymbol{Al_2O_3}$/Therminol, (c) 5% $\boldsymbol{Cu}$/Therminol, and (d) 5% $\boldsymbol{SWCNT}$/Therminol

Figure 72 shows the variation of the time on the mass flow rates of the power plant for Syltherm, and Syltherm-based nanofluids for the 1st mode of operation (no storage). It is seen that the mass flow rates trend is the same as Figure 71, however it is noticed that the mass flow rates of the base fluids and the nanofluids inside the PTSC, and the mass flow rate of the steam in the cycle are larger when compared to Therminol, and Therminol-based nanofluids.

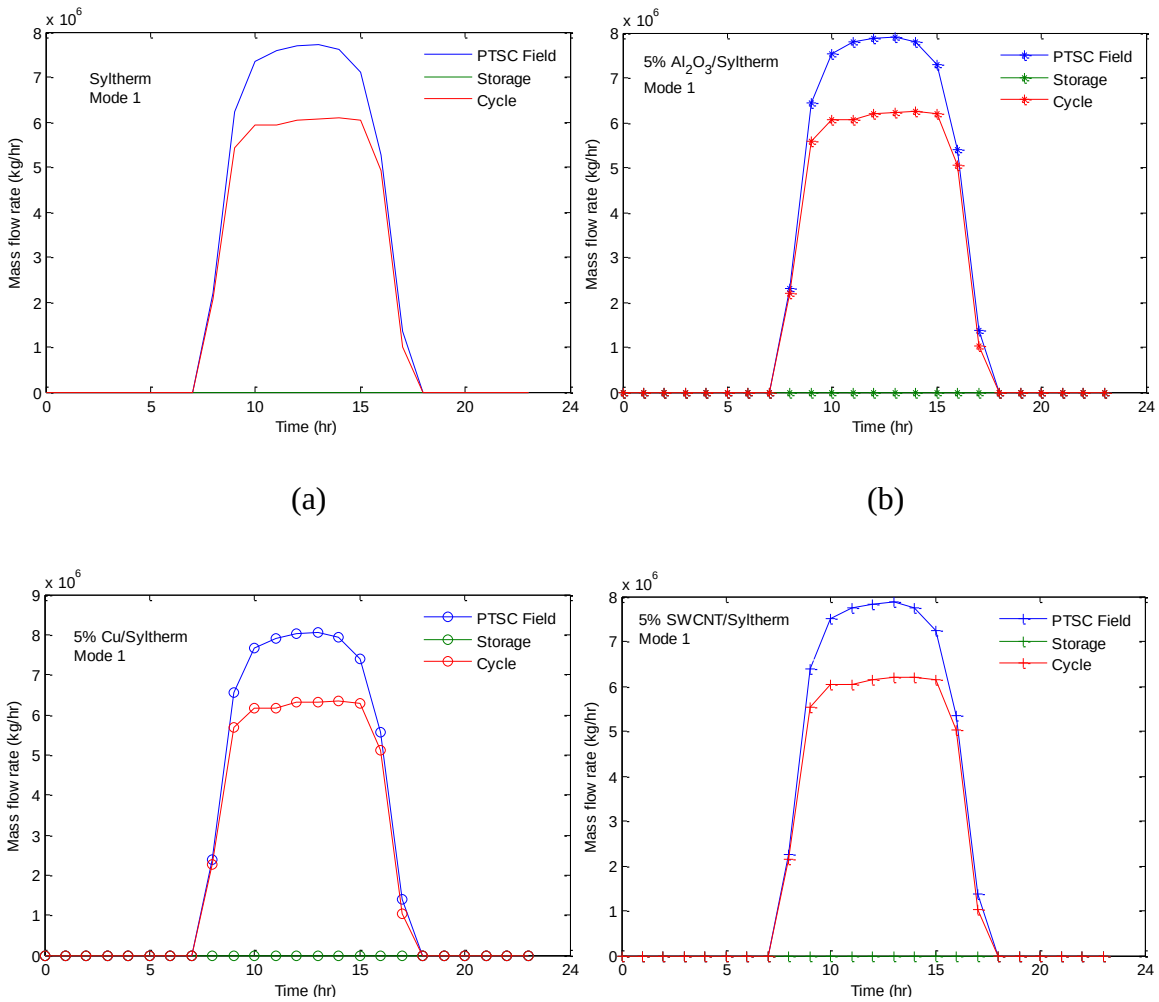

Figure 72: Effect of time on the mass flow rates of the ISRRC for the 1st mode of operation for (a) Sylthem, (b) 5% $\boldsymbol{Al_2O_3}$/Sylthem, (c) 5% $\boldsymbol{Cu}$/Sylthem, and (d) 5% $\boldsymbol{SWCNT}$/Sylthem

Figure 73 shows the variation of the time on the mass flow rates of the power plant for Therminol, and Therminol-based nanofluids for the 2nd mode of operation. It is seen that similar to Figure 69, the mass flow rate of the cycle is almost constant throughout the operation hours of the plant, while the mass flow rate of the heating fluid increases until the peak timings, then decreases with the lack of the sun. in addition, during the periods of high solar intensity part of the mass flow rate of heating fluid is routed to the storage tanks in order to charge the tanks, hence the negative values shown in the graph. The discharging cycle takes place in the hours of low solar intensity, and

when the PTSC shuts down. The hours of operation of the plant are increased from 10 hours to 16 hours, because of the presence of the storage system.

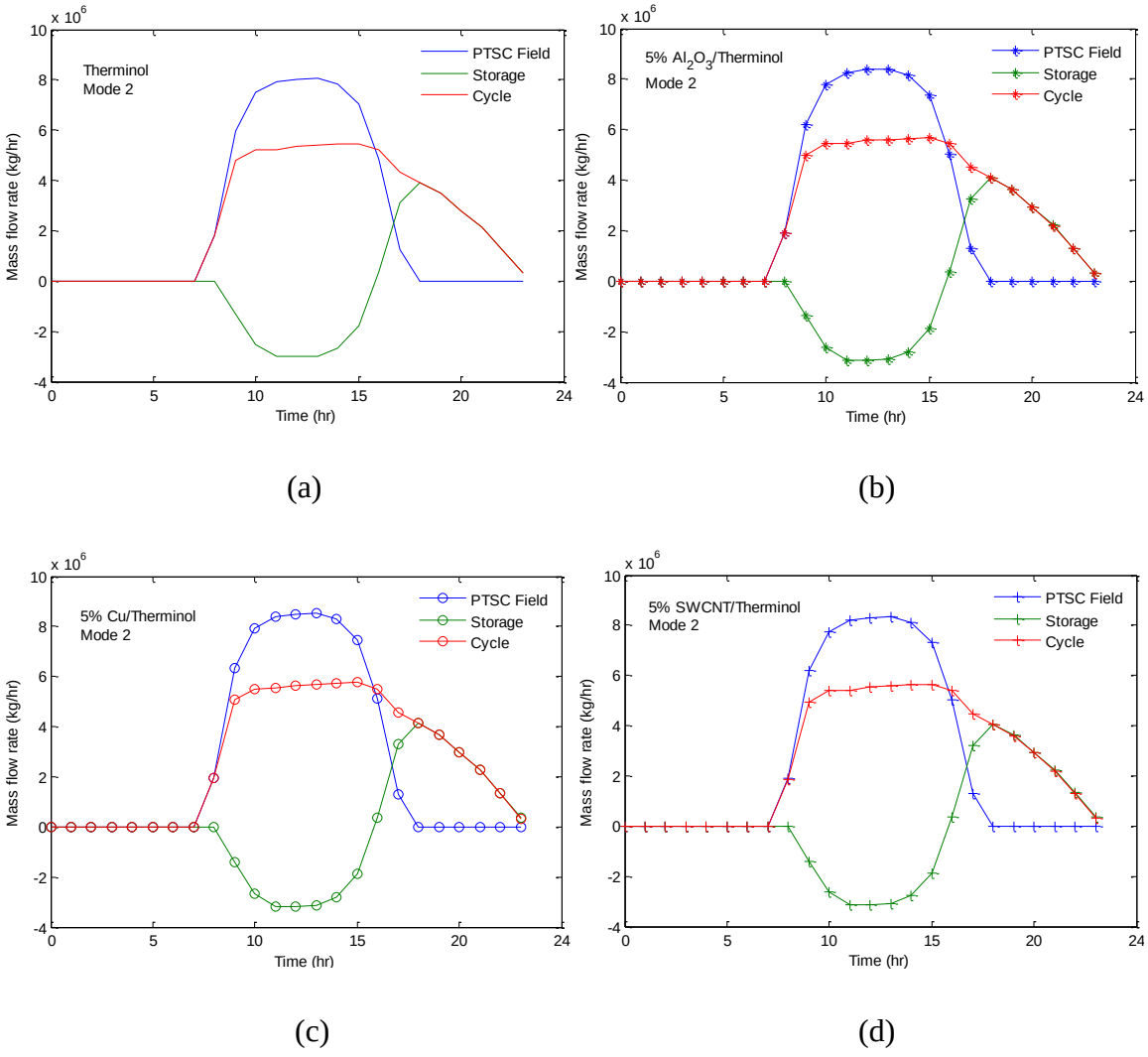

Figure 73: Effect of time on the mass flow rates of the ISRRC for the 2nd mode of operation for (a) Therminol, (b) 5% $\boldsymbol{Al_2O_3}$/Therminol, (c) 5% $\boldsymbol{Cu}$/Therminol, and (d) 5% $\boldsymbol{SWCNT}$/Therminol

Figure 74 shows the variation of the time on the mass flow rates of the power plant for Syltherm, and Syltherm-based nanofluids for the 2nd mode of operation (7.5 hours storage). It is seen that the mass flow rates trend is the same as Figure 73, however it is noticed that the mass flow rates of the base fluids and the nanofluids inside the PTSC, the mass flow rate of the charging and discharging cycles, and the mass flow rate

of the steam in the cycle are larger when compared to Therminol, and Therminol-based nanofluids.

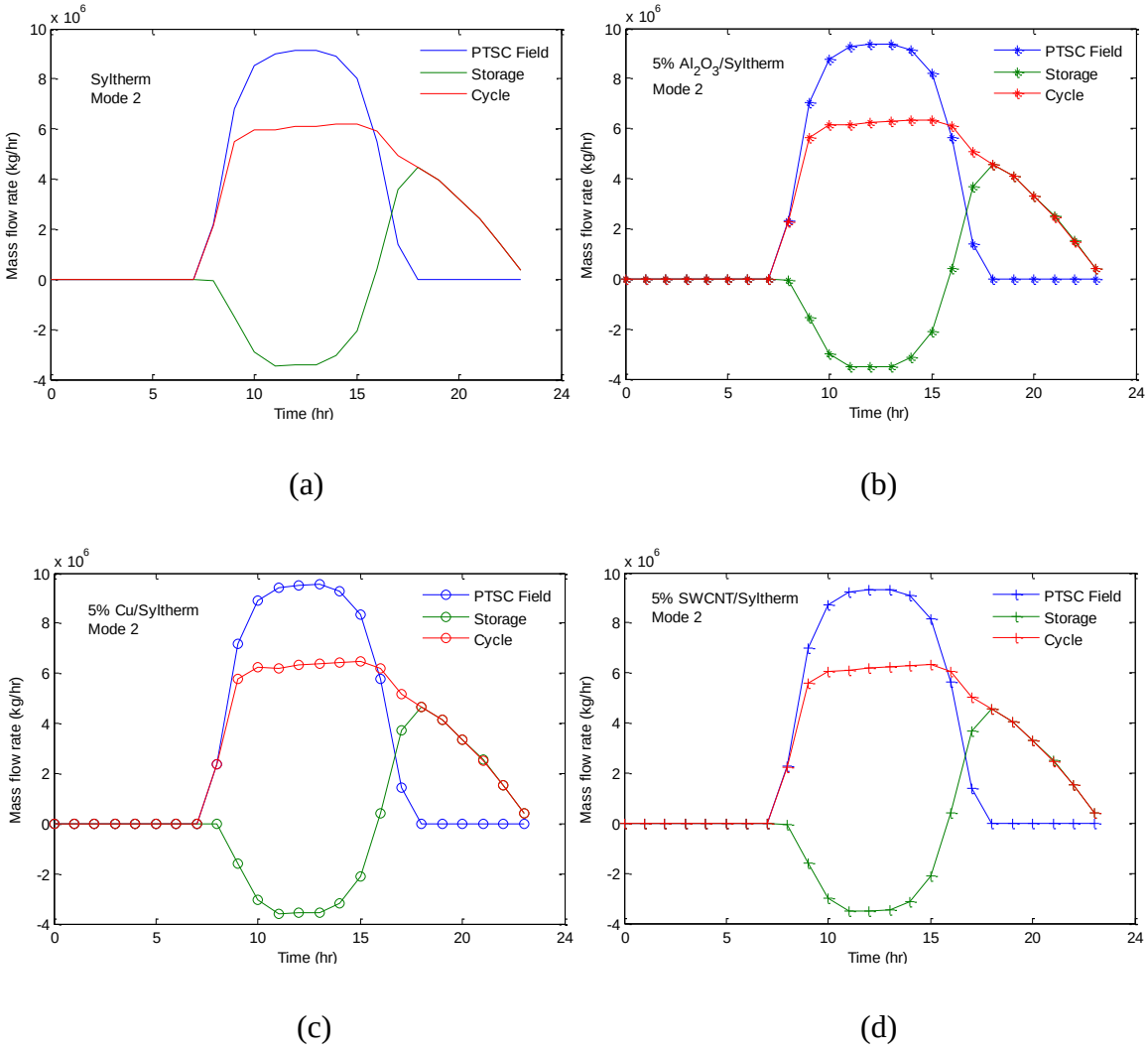

Figure 74: Effect of time on the mass flow rates of the ISRRC for the 2nd mode of operation for (a) Sylltherm, (b) 5% $\boldsymbol{Al_2O_3}$/Sylltherm, (c) 5% $\boldsymbol{Cu}$/Sylltherm, and (d) 5% $\boldsymbol{SWCNT}$/Sylltherm

Figure 75 shows the variation of the time on the mass flow rates of the power plant for Therminol, and Therminol-based nanofluids for the 3rd mode of operation (10 hours storage). When compared to the 2nd mode of operation, there is no substantial difference between the mass flow rates of the two modes of operation; however the mass flow rates for the 3rd mode operation are higher than that of the 2nd. In addition, in some

cases the discharging cycle for the 3rd mode of operation operates for a higher number of hours when compared to the 2nd mode in order to accommodate the storage load.

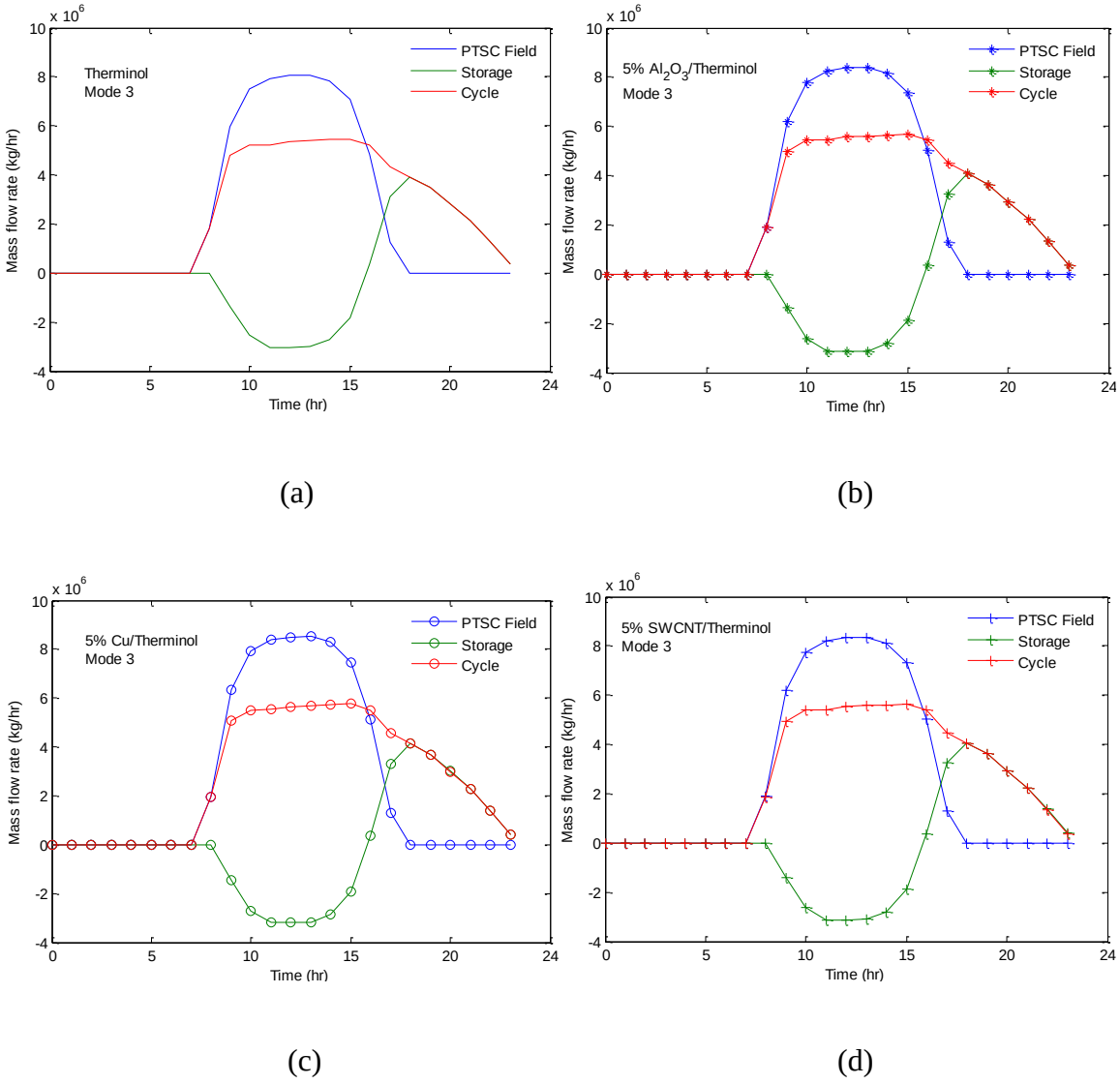

Figure 75: Effect of time on the mass flow rates of the ISRRC for the 3rd mode of operation for (a) Therminol, (b) 5% $\boldsymbol{Al_2O_3}$/Therminol, (c) 5% $\boldsymbol{Cu}$/Therminol, and (d) 5% $\boldsymbol{SWCNT}$/Therminol

Figure 76 shows the variation of the time on the mass flow rates of the power plant for Syltherm, and Syltherm-based nanofluids for the 3rd mode of operation. It is seen that the mass flow rates trend is the same as Figure 75, however it is noticed that the mass flow rates of the base fluids and the nanofluids inside the PTSC, the mass flow rate of the charging and discharging cycles, and the mass flow rate of the steam in the cycle

are larger when compared to Therminol, and Therminol-based nanofluids. Moreover, for some of the nanofluids, the discharging cycle operates for extra hours when compared to the 2nd mode of operation to accommodate the load on the storage tanks.

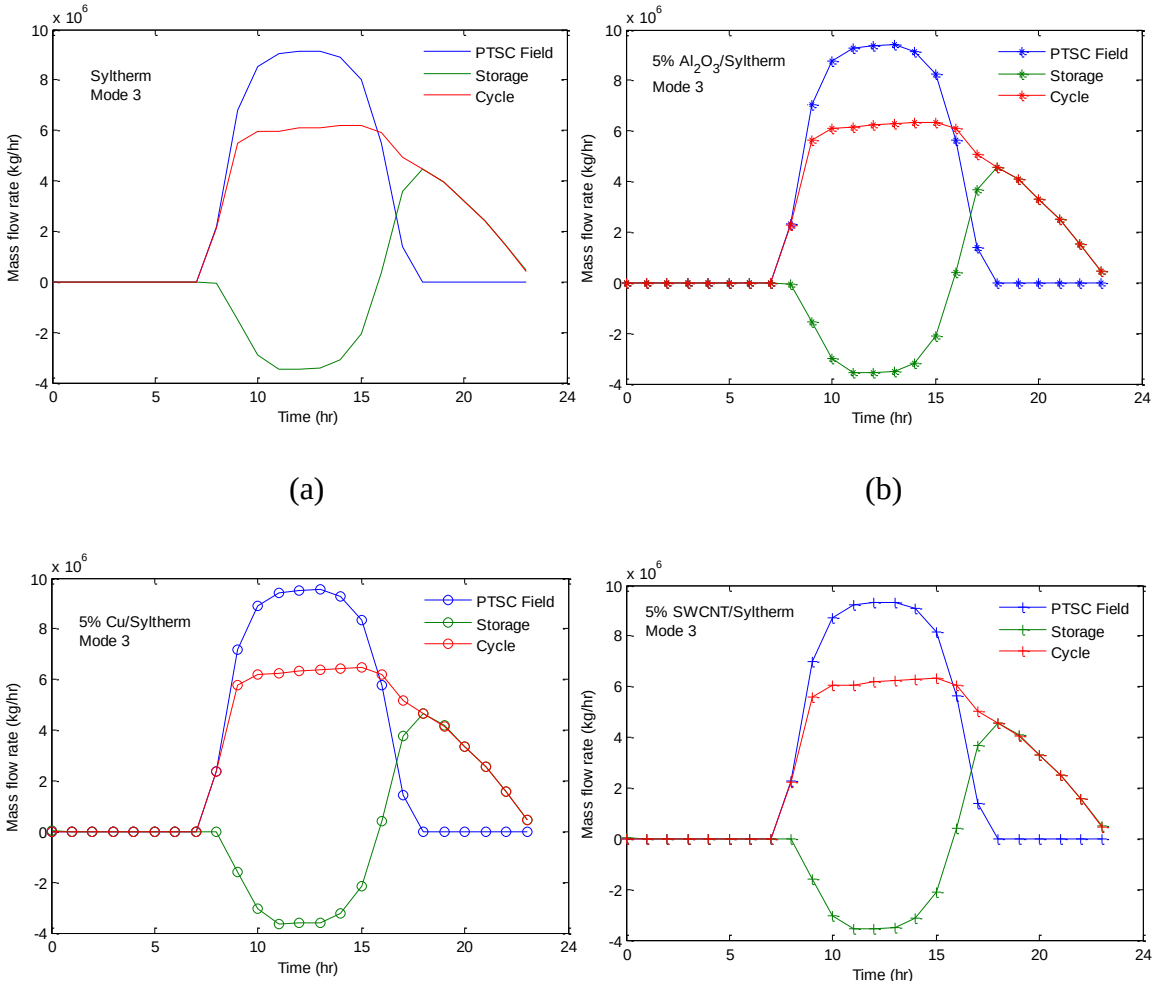

Figure 76: Effect of time on the mass flow rates of the ISRRC for the 3rd mode of operation for (a) Sylltherm, (b) 5% $\boldsymbol{Al_2O_3}$/Sylltherm, (c) 5% $\boldsymbol{Cu}$/Sylltherm, and (d) 5% $\boldsymbol{SWCNT}$/Sylltherm

Based on the mass flow rates analysis done above, the performance of the ISRRC is studied for different nanofluids and modes of operation. The analysis is shown in the following section.

4.6.4 Effect of the nanofluids on the performance of the ISRRC for different modes of operation.

The analysis for the effect of different nanofluids on the performance of the ISRRC for different modes of operation is done using the System Advisory Model (SAM) software, based on the design input and parameters from Tables 7, 9-11 and the results from the previous sections. For this analysis all the properties of the nanofluids are calculated for a volume fraction of 5%.

4.6.4.1 Effect of the nanofluids on the performance of the ISRRC for the 1st Mode of operation

The 1st mode of operation assumes no storage, meaning that the plant is under operation as long as the PTSC field is under operation. This mode will result in a shortage in the supply, as the weather data varies throughout the year, and with the absence of the storage system there is no compensation available for the power production. Figure 77 shows the variation of the month on the monthly energy output of the ISRRC for Therminol-based and Syltherm-based nanofluids for the 1st mode of operation. It is seen that using nanofluids a heating fluid increases the monthly energy output of the ISRRC, and that increase depends on the nanoparticles. For instance, Cu-based nanofluids show the highest improvement in the output energy of the ISRRC compared to $SWCNT$-based and Al_2O_3-based nanofluids. Moreover, when comparing Therminol-based and Syltherm-based nanofluids, it is observed that Therminol and Therminol-based nanofluids show a higher monthly energy output when compared to Syltherm and Syltherm-based nanofluids. However, Syltherm-based nanofluids show a higher enhancement in the monthly energy output. For example, for the month of June, the monthly energy produced for Therminol and Cu/Therminol is $37\ GWh$ and $37.3\ GWh$ respectively, while for Syltherm and Cu/Syltherm the energy output is $36.1\ GWh$ and $36.9\ GWh$ respectively.

Regarding the monthly analysis, it is noticed that the month of June displays the highest energy output, while the month of December displays the lowest. Referring back to Figure 14, it is seen that the month of June has the highest beam radiation, while the month of December has one of the lowest concluding that the energy output of the ISRRC depends directly on the beam radiation.

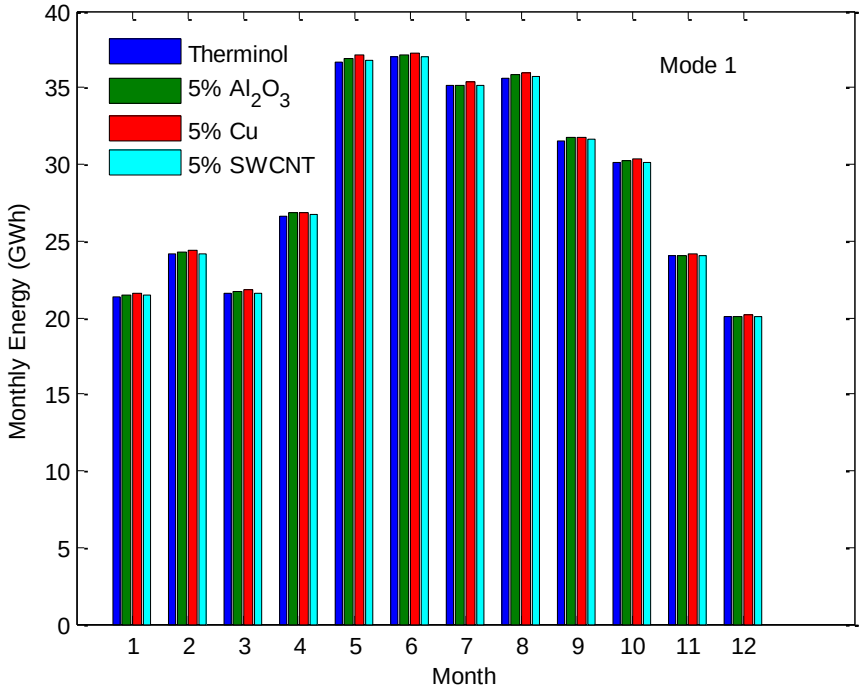

(a)

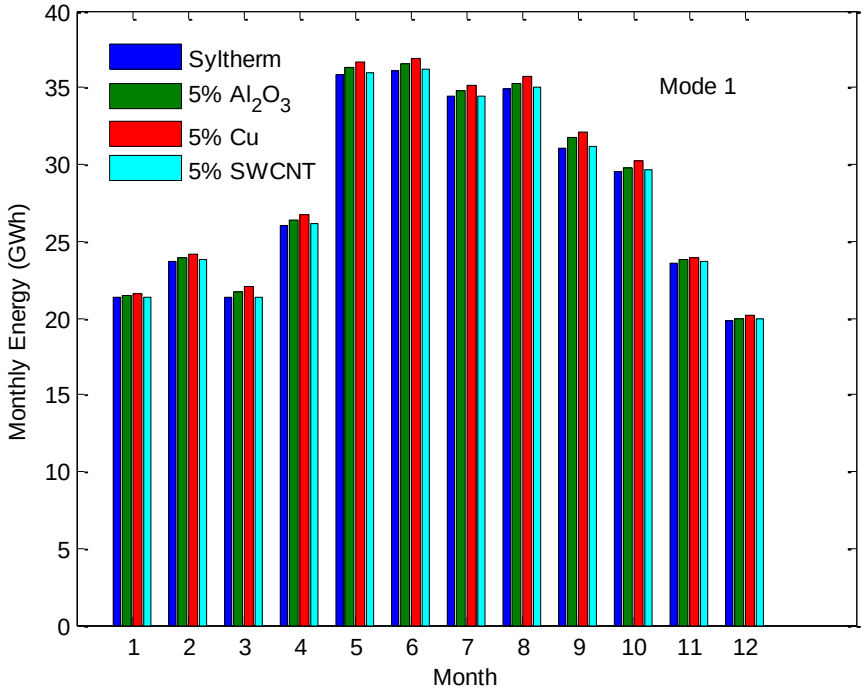

(b)

Figure 77: Variation of the month on the energy output of the ISRRC for (a) Therminol-based nanofluids, and (b) Syltherm-based nanofluids for 1st mode of operation

Table 17 shows a comparison between Therminol, Therminol-based nanofluids, Syltherm and Syltherm-based nanofluids in terms of the annual energy production, power output, and field thermal output of the ISRRC for the 1st mode of operation. As expected Cu-based nanofluids provide the highest annual energy, power output, and field thermal output when compared to $SWCNT$-based and Al_2O_3-based nanofluids. In addition, Therminol-based nanofluids display a higher annual energy, power output, and field thermal output when compared to Syltherm-based nanofluids.

Table 17: Comparison between Therminol-based and Syltherm-based nanofluids regarding the performance of the ISRRC for 1st mode of operation

Parameter	Annual Energy	Cycle Power Output	Field Thermal Output
Unit	kWh	MWh	MWh
Therminol	343,897,856	31,631	106,415
Al_2O_3/Therminol	345,199,968	31,661	106,411
Cu/Therminol	347,008,064	31,704	106,683
$SWCNT$/Therminol	344,268,704	31,682	106,556
Syltherm	337,436,608	31,688	106,486
Al_2O_3/Syltherm	341,773,472	31,772	106,777
Cu/Syltherm	345,446,880	31,821	106,955
$SWCNT$/Syltherm	338,663,392	31,767	106,913

4.6.4.2 Effect of the nanofluids on the performance of the ISRRC for the 2nd Mode of operation

The second mode of operation assumes a storage time of 7.5 hours, meaning that the storage system will compensate for the shortage in the power supply caused by the variation of the weather data by supplying the power block with heating fluid charged and stored in the system during the operation hours of the PTSC. Figure 78 shows the variation of the month on the monthly energy output of the ISRRC for Therminol-based and Syltherm-based nanofluids for the 2nd mode of operation. Similar to the 1st mode of operation it is seen the Cu-based nanofluids cause the highest improvement in the monthly energy output of the ISRRC when compared to $SWCNT$-based and Al_2O_3-based

nanofluids. Moreover, it is also seen that Therminol and Therminol-based nanofluids display a higher monthly energy output when compared to Syltherm and Syltherm-based nanofluids, nevertheless Syltherm-based nanofluids result in a higher enhancement in the monthly energy output when compared to Therminol-based nanofluids. On the contrary to the 1st mode of operation, the month of May displays the highest monthly energy output, while the month of December displays the lowest. The addition of the storage system weakens the dependency of the energy output on the beam radiation.

Table 18 shows a comparison between Therminol, Therminol-based nanofluids, Syltherm and Syltherm-based nanofluids in terms of the annual energy production, power output, and field thermal output of the ISRRC for the 2nd mode of operation. Similar to the 1st mode of operation, Cu-based nanofluids provide the highest annual energy, power output, and field thermal output when compared to $SWCNT$-based and Al_2O_3-based nanofluids. In addition, Therminol-based nanofluids display a higher annual energy, power output, and field thermal output when compared to Syltherm-based nanofluids.

Table 18: Comparison between Therminol-based and Syltherm-based nanofluids regarding the performance of the ISRRC for 2nd mode of operation

Parameter	Annual Energy	Cycle Power Output	Field Thermal Output
Unit	kWh	MWh	MWh
Therminol	477,914,976	44,091	117,840
Al_2O_3/Therminol	479,397,152	44,094	117,854
Cu/Therminol	482,669,376	44,198	118,172
$SWCNT$/Therminol	478,313,248	44,166	118,060
Syltherm	467,482,560	44,200	117,840
Al_2O_3/Syltherm	474,379,456	44,327	118,173
Cu/Syltherm	480,352,992	44,417	118,364
$SWCNT$/Syltherm	470,286,336	44,406	118,375

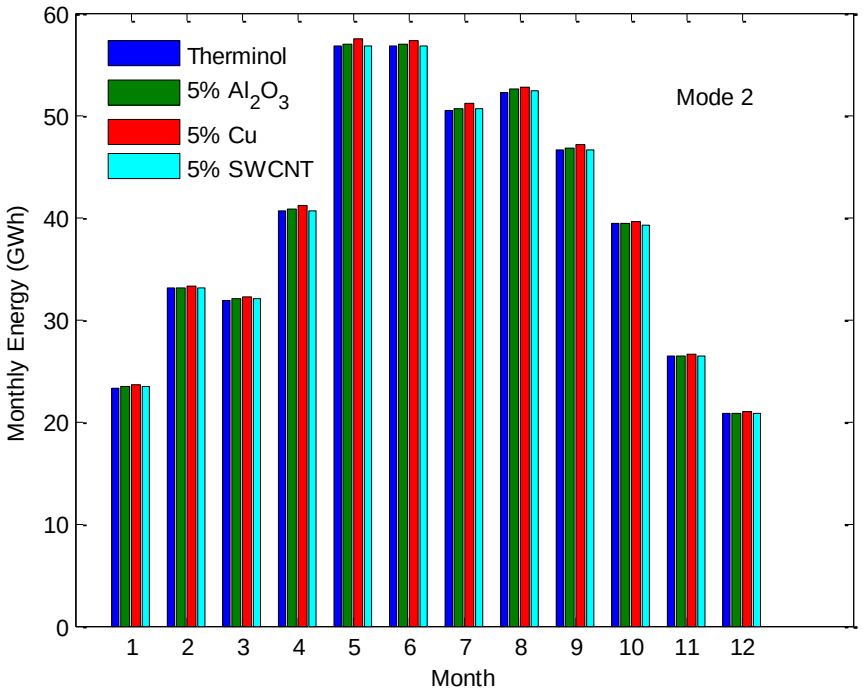

(a)

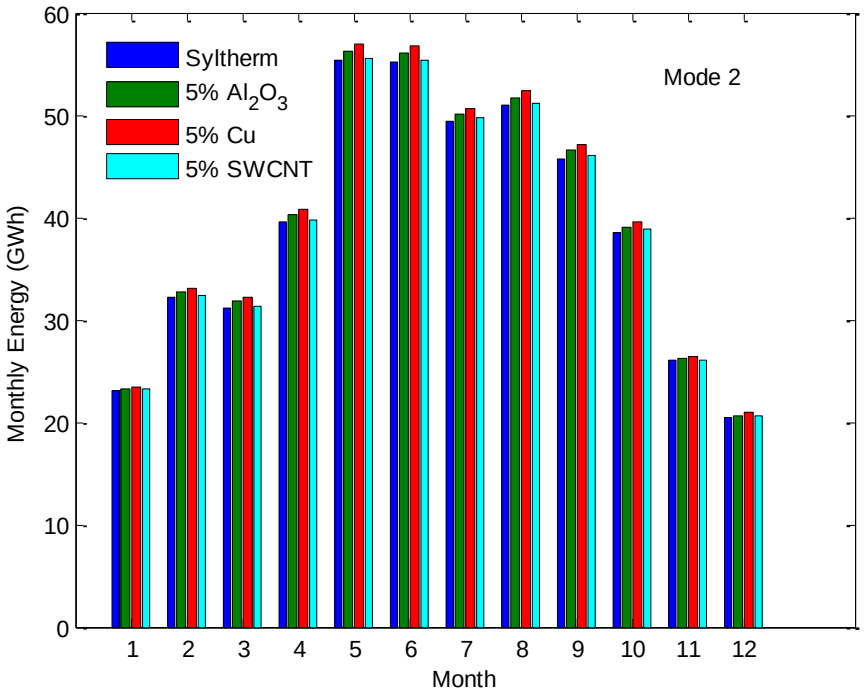

(b)

Figure 78: Variation of the month on the energy output of the ISRRC for (a) Therminol-based nanofluids, and (b) Syltherm-based nanofluids for 2ndmode of operation

4.6.4.3 Effect of the nanofluids on the performance of the ISRRC for the 3rd Mode of operation

The 3rd mode of operation assumes a storage period of 10 hours, meaning that the storage system will be able to compensate the shortage in the power supply for a period time longer than that of the 2nd mode of operation. Figure 79 shows the variation of the month on the monthly energy output of the ISRRC for Therminol-based and Syltherm-based nanofluids for the 3rd mode of operation. It is seen that the monthly energy behavior of the 3rd mode of operation is very similar to that of the 2nd mode of operation, where the month of May displays the highest energy output, and December displays the lowest. Table 19 shows a comparison between Therminol, Therminol-based nanofluids, Syltherm and Syltherm-based nanofluids in terms of the annual energy production, power output, and field thermal output of the ISRRC for the 3rd mode of operation. Similar to the 1st mode and 2nd mode of operation, Cu-based nanofluids provide the highest annual energy, power output, and field thermal output when compared to $SWCNT$-based and Al_2O_3-based nanofluids. In addition, Therminol-based nanofluids display a higher annual energy, power output, and field thermal output when compared to Syltherm-based nanofluids.

Table 19: Comparison between Therminol-based and Syltherm-based nanofluids regarding the performance of the ISRRC for 3rd mode of operation

Parameter	Annual Energy	Cycle Power Output	Field Thermal Output
Unit	kWh	MWh	MWh
Therminol	478,163,808	44,126	117,828
Al_2O_3/Therminol	479,790,240	44,139	117,844
Cu/Therminol	482,998,976	44,237	118,161
$SWCNT$/Therminol	478,700,544	44,211	118,048
Syltherm	467,911,520	44,253	117,831
Al_2O_3/Syltherm	474,679,744	44,367	118,162
Cu/Syltherm	480,515,616	44,442	118,354
$SWCNT$/Syltherm	470,639,296	44,453	118,366

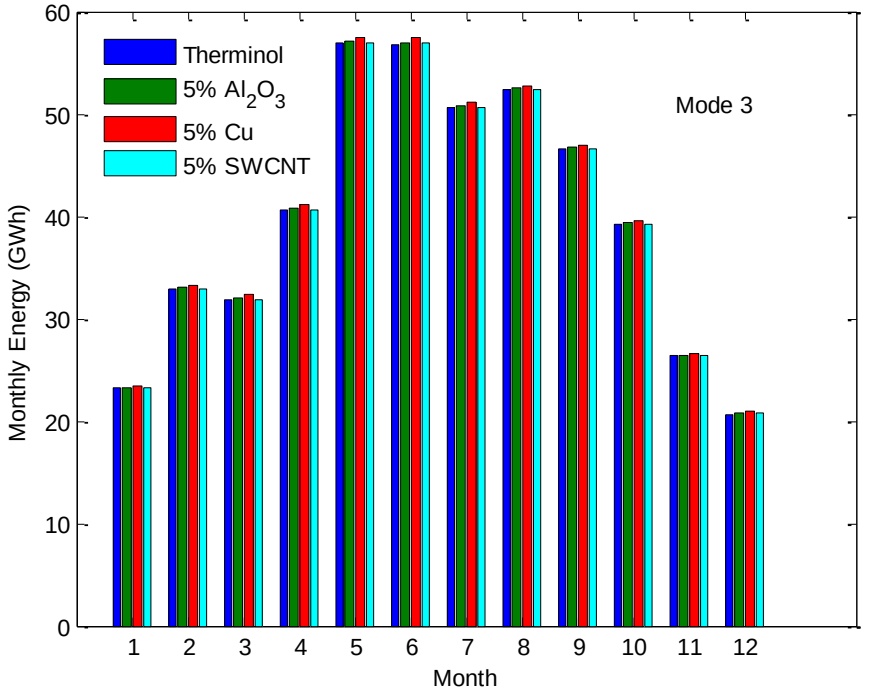

(a)

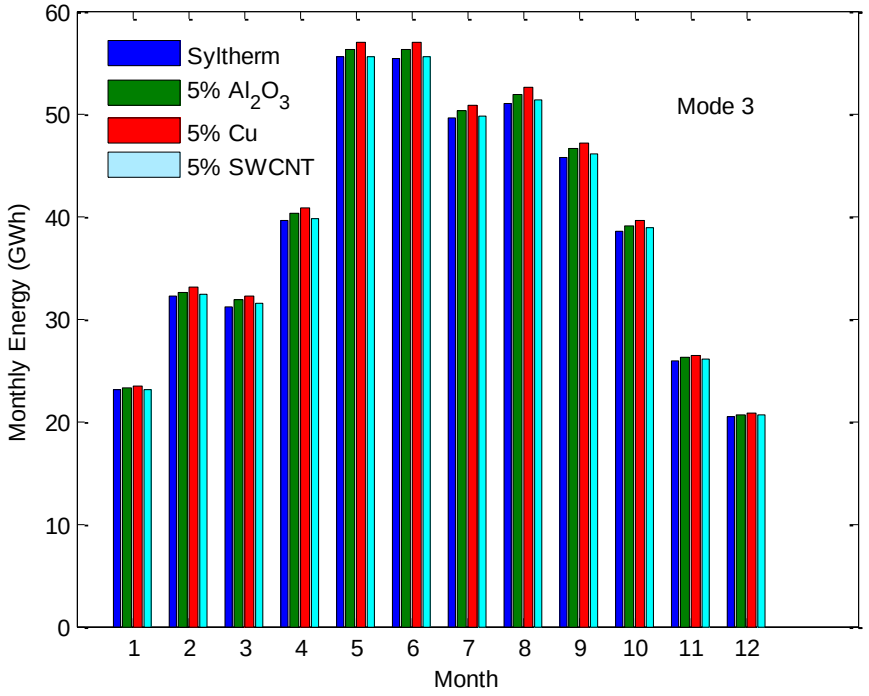

(b)

Figure 79: Variation of the month on the energy output of the ISRRC for (a) Therminol-based nanofluids, and (b) Syltherm-based nanofluids for 3rd mode of operation

4.6.4.4 Comparison of the effect of the modes of operation on the performance of the ISRRC

In order to establish the most efficient mode of operation for the ISRRC to operate at, a comparison between the 1st, 2nd, and 3rd modes of operation is done in this section. Figure 80 shows the variation of the modes of operation on the power output of the ISRRC for Therminol-based and Syltherm-based nanofluids. It is seen that the power output of the ISRRC increases considerably when comparing the 1st mode to the 2nd and 3rd. in addition, it is seen that the highest power output occurs in the 3rd mode of operation. However, when compared to the 2nd mode of operation it is seen that the increase in the electricity output is limited as seen from Tables 18 and 19.

Figure 81 shows the variation of the modes of operation on the annual energy of the ISRRC for Therminol-based and Syltherm-based nanofluids. It is seen that the 1st mode of operation results in the least annual energy production when compared to the 2nd and 3rd modes of operation. The effect of the storage system can be seen in this figure, where the existence of the storage system increases the annual energy production by around 39 % when comparing the 1st mode of operation to the 2nd and 3rd . However, one of the disadvantages of the storage system is that it has a negative effect on the overall efficiency of the system. While comparing the 2nd and 3rd modes of operation it is noticed that the annual energy increase is almost negligible, nevertheless the 3rd mode of operation displays the highest annual energy. Regarding Syltherm-based and Therminol-based nanofluids, it is shown that Therminol-based nanofluids show a higher annual energy than Syltherm-based nanofluids.

Figure 82 shows the variation of the modes of operation on the field thermal output for Therminol-based nanofluids and Syltherm-based nanofluids. It is seen that the difference in the field thermal output between the 1st mode and the 2nd and 3rd modes is not as large as the annual energy, and electricity output of the ISRRC. Since the field thermal output represents the amount of thermal energy produced by the PTSC field, the increase from the 1st mode to the modes with storage system is not significant. However, the increase is present because the excess amount of thermal output from the field is directed towards the storage system during the charging cycle. Similar to the previous trends, the 3rd mode of operation displays a slightly higher field thermal output that the 2nd mode of operation.

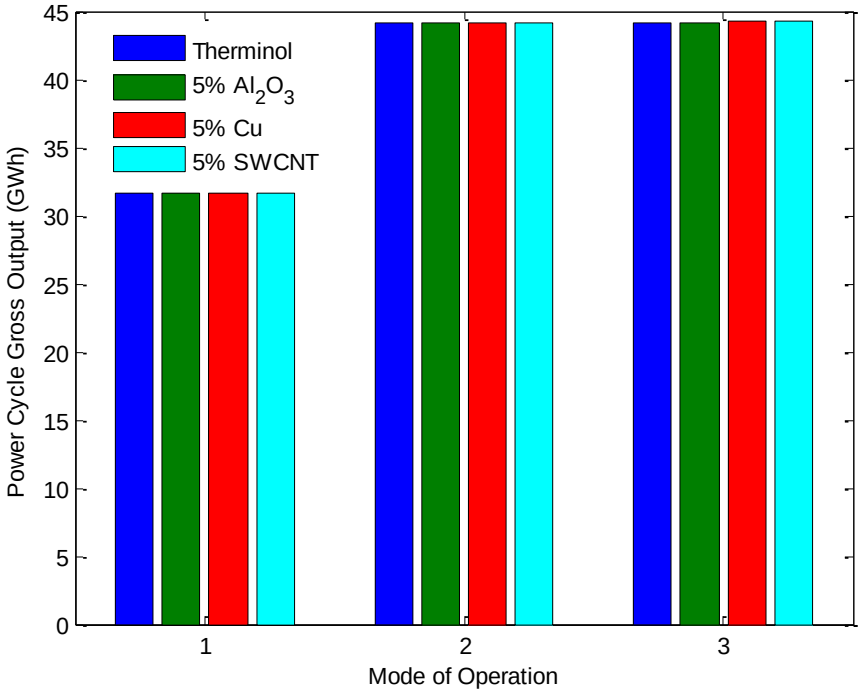

(a)

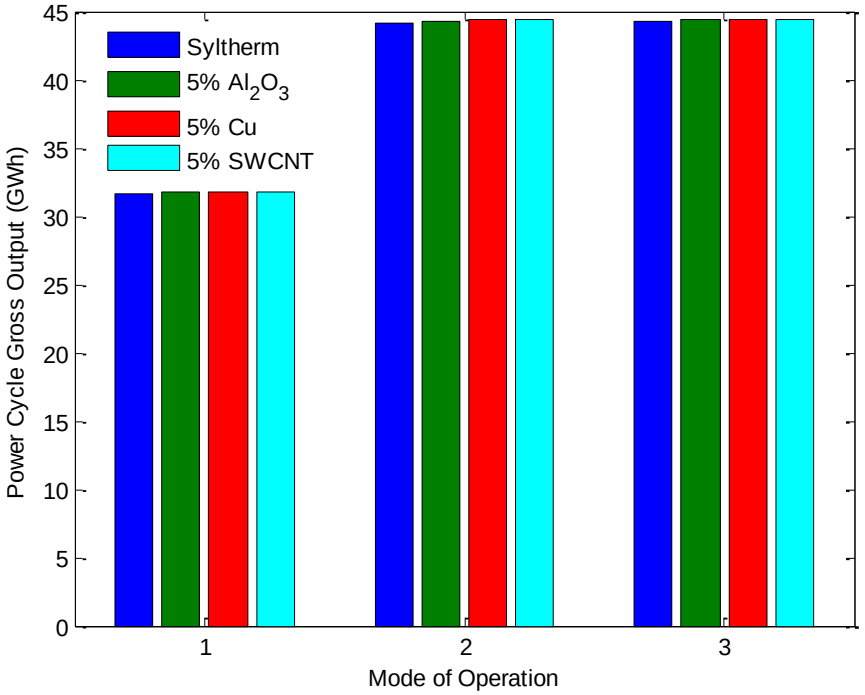

(b)

Figure 80: Effect of modes of operation on the power output of the ISRRC for (a) Therminol-based nanofluids, and (b) Syltherm-based nanofluids

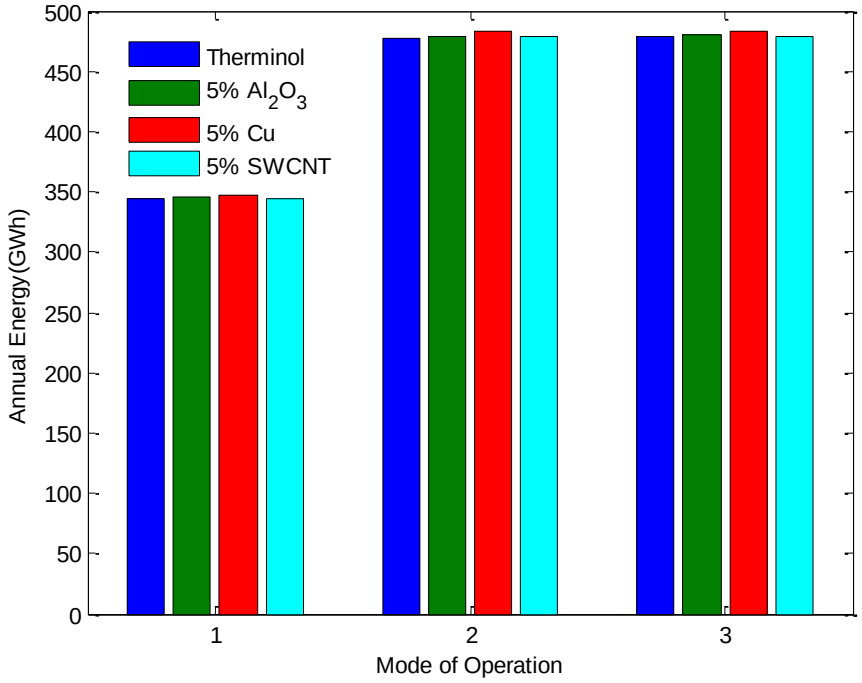

(a)

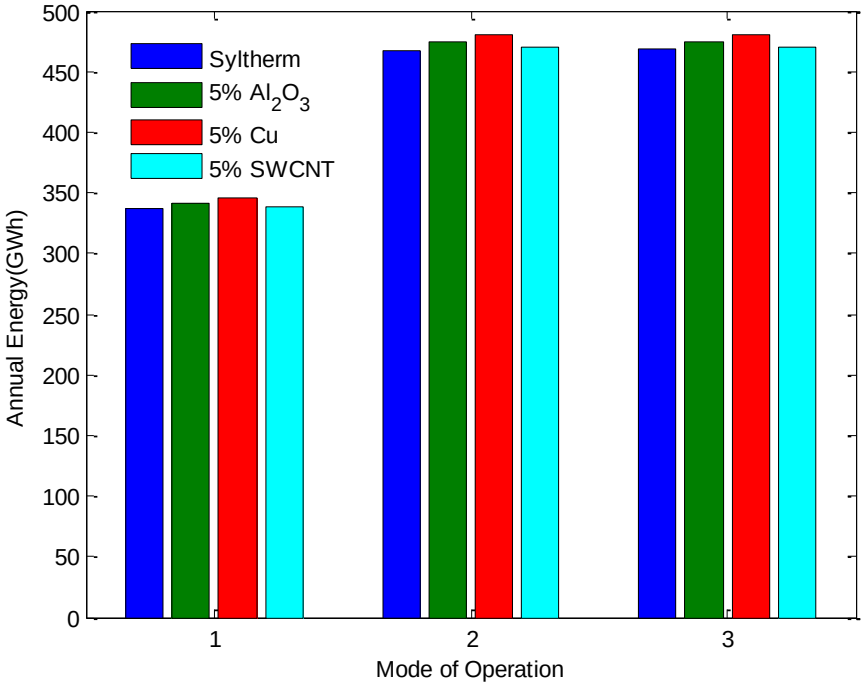

(b)

Figure 81: Effect of modes of operation on the annual energy of the ISRRC for (a) Therminol-based nanofluids, and (b) Syltherm-based nanofluids

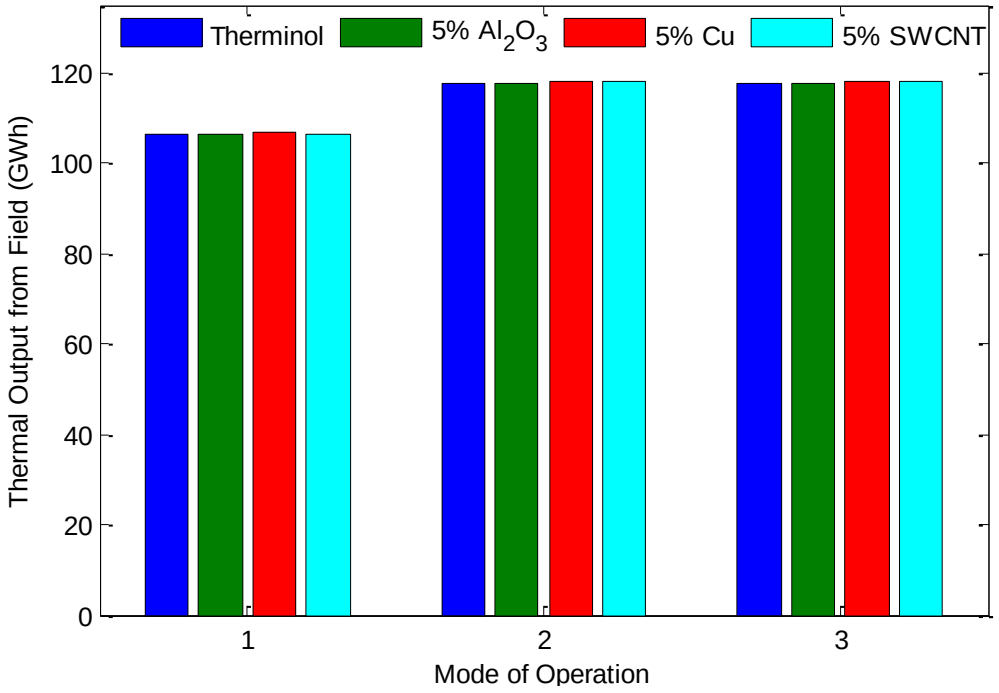

(a)

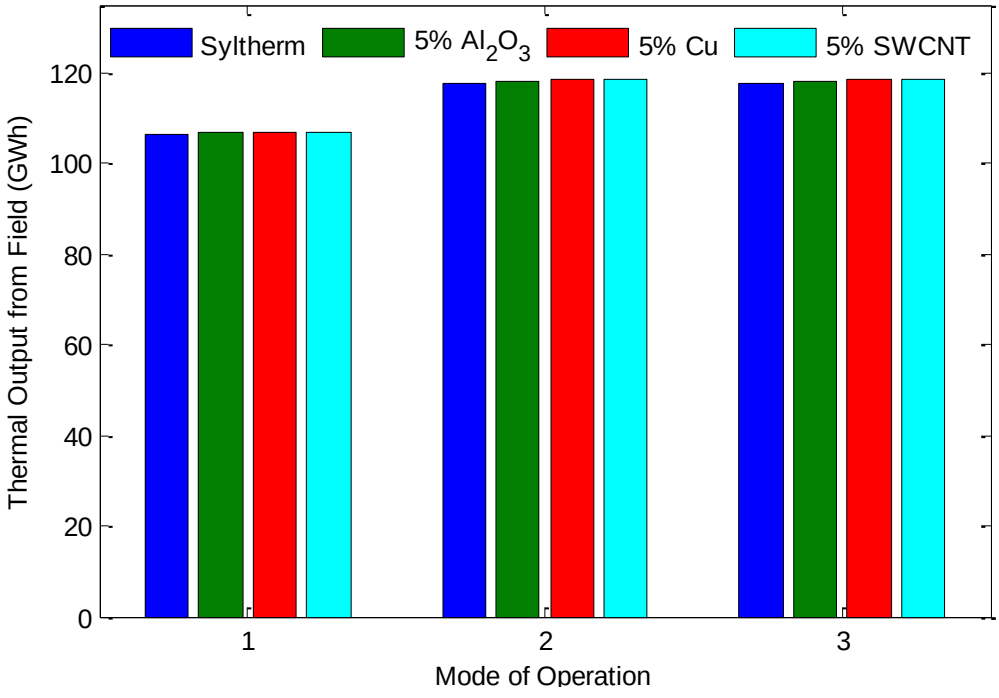

(b)

Figure 82: Effect of modes of operation on the thermal output from the field of the ISRRC for (a) Therminol-based nanofluids, and (b) Syltherm-based nanofluids

In conclusion, it is seen that Cu-based nanofluids display the highest improvement in the performance of the ISRRC, while the 3rd mode of operation is the optimum mode to operate at. However, an economic evaluation of the ISRRC for different nanofluids and modes of operations is needed in order to fully compare the effect of the nanofluids on the performance of the ISRRC. The following chapter discusses the effect of the nanofluids on the costs of the ISRRC.

Chapter 5: Economic Evaluation of the ISRRC

This chapter presents an economic evaluation of the Integrated Solar Rankine Regenerative Cycle (ISRRC) consisting of the PTSC field, Thermal Energy System, and the Regenerative Rankine Cycle. The economic analysis is carried only for the ISRRC and not the ISRC, because the efficiency of the ISRC is less than that of the ISRRC as seen from section 4.6.1. Since the technical performance of the ISRC is lower when compared to ISRRC, it is trivial that the economic evaluation will show that the ISRC configuration is not feasible.

The main idea of the thermo-economic evaluation is to compare the effect of using nanofluids on the cost of the ISRRC as the nanofluid that provides the highest improvement in the power output, might not necessarily impact the cost positively. Therefore in order to completely analyze the effect of using nanofluids, a performance model and an economic model are ought to be established and compared for different nanofluids and modes of operation.

The main objectives of the economic evaluation of the ISRRC System are to:

1. Calculate the levelized cost of electricity (LEC) for different nanofluids and modes of operation.
2. Calculate the Net Present Value (NPV)of the ISRRC for different nanofluids and modes of operation.
3. Calculate the Net Saving (NS) of the ISRRC for different nanofluids and modes of operation.
4. Compare the different nanofluids, and select the most suitable nanofluid to replace the conventional heating fluid for different modes of operation.
5. Compare the different modes of operation and select the optimum one.

In order to analyze the economic aspect of the ISRRC, an economic model is to be presented. The following sections show an economic model, followed by a comparison between the power output, LEC, NPV, and NS of the ISRRC for different nanofluids and modes of operation.

5.1 Economic model

In this following section an economic model for the ISRRC is presented. The model serves as a tool to compare the effect of using nanofluids, as it provides an overview of the capital, operational, and direct costs of the power plant. The cost analysis will determine the feasibility of utilizing nanofluids, as the increase in the performance of the ISRRC might not yield a lower cost. The model is carried for different components of the cycle, and it takes into account the capital, direct and indirect costs of the ISRRC. The chemical engineering plant cost index (CEPCI) is utilized in order to achieve a more realistic economic model. The capital investment cost of the components is multiplied by a correction factor in order to update the economic estimation of the plant. The factor is as follows:

$$f_{CEPCI} = \frac{CEPCI_{ref}}{CEPCI_{2015}} \tag{5.1}$$

where $CEPCI_{ref}$ and $CEPCI_{2015}$ stand for the reference chemical engineering plant cost index and the 2015 one respectively. The capital investment cost of the ISRRC components is provided in the following sections.

5.1.1 Steam Turbine.

The capital investment cost of the steam turbine in $US\$$ is presented by using the model developed by [173]:

$$Z_{st} = 150(\dot{m}_s w_{st})\left(1 + e^{0.096(T_{T,i}-866)}\right)\left(\frac{50000}{\dot{m}_s w_{st}}\right)^{0.67} \tag{5.2}$$

5.1.2 Heat Exchangers.

The capital investment cost of the heat exchangers in $US\$$ is presented by using the model developed by [174]:

$$Z_{He} = 1.53 + 1.27\left(\frac{T_{h,i}}{623}\right)^{2.4} 10^{3.8528+0.4242\ln\left(\frac{\dot{Q}_{He}}{0.018 LMTD_{He}}\right)} \tag{5.3}$$

where

$\dot{Q}_{He}$is the rate of heat exchanged between the fluids (kW)

$LMTD_{He}$is the log mean temperature difference in the heat exchanger (K)

$T_{h,i}$is the inlet temperature of the hot fluid (K)

Equation (5.3) can be employed to find the capital investment cost of the heat exchanger between the PTSC Field and the TES system $Z_{HE,1}$, in addition to the heat exchanger between the TES system and the power blockZ_{HE2}. The feed water heater can be assumed as a heat exchanger as the cost function of capital investment cost is not provided. Therefore, Equation (5.3) can be used to calculate the capital investment cost of the feed water heater Z_{FW}

5.1.3 Pumps.

The capital investment cost of the pumps in $US\$$ is presented by employing the model presented by [173], it is as follow:

$$Z_p = 442\left[\dot{m}_s w_p\right]^{0.71} 1.41\left[1 + \left(\frac{0.2}{1-\eta_p}\right)\right] \tag{5.4}$$

Equation (5.4) is employed to calculate the capital investment cost of the heating fluid pump in the PTSC field$Z_{\ PHTF}$, the hot storage tank pump Z_{PHST}, the cold storage tank pump Z_{PCST}, the feed water heater pump Z_{FWH}, and finally the water pump in the power blockZ_{PW}.

5.1.4 Condenser.

The capital investment cost of the condenser in $US\$$ is divided into two main components, the cost of the steam condenser and the cost of the cooling tower:

$$Z_c = Z_{sc} + Z_{ct} \tag{5.5}$$

The capital investment cost of the steam condenser in $US\$$ is adapted from [173], and it is given by:

$$Z_{sc} = 248\left(\frac{\dot{Q}_c}{2.2LMTD_c}\right) + 659\left(\frac{\dot{Q}_c}{48.1275}\right) \tag{5.6}$$

where

$\dot{Q}_c$is the rate of heat transfer in the condenser (kW)

$LMTD_c$ is the log mean temperature difference in the condenser (K)

The capital investment cost of the cooling tower in $US\$$ is adapted from [175], and it is given by:

$$Z_{ct} = 253226.835\left(\frac{\dot{Q}_c}{3600}\right)\left(-0.6936\ln\left(\frac{T_{cw,i}+T_{cw,e}}{2} - T_{wb,amb}\right) + 2.1898\right) \quad (5.7)$$

where

$T_{cw,i}$ is the inlet cooling water temperature (K)

$T_{cw,o}$ is the outlet cooling water temperature (K)

$T_{wb,amb}$ is the ambient air wet bulb temperature (K)

5.1.5 PTSC Field.

The capital investment cost of the PTSC field in $US\$$ is divided among the cost of the PTSCs, the cost of the thermal energy storage, and the cost of heating fluid. The cost function is obtained from the National Renewable Energy Laboratory (NREL) [176], and it is as follows:

$$Z_{PTSC} = A_{SA}C_{PTSC} + \dot{Q}_{tank}C_{TES} + A_{SA}C_{HTF} \quad (5.8)$$

where

C_{PTSC} is the PTSC cost constant and it equals $245\$/m^2$

C_{TES} is the TES cost constant and it equals $80\$/kWh$

C_{HTF} is the Heating Fluid cost constant and it equals $90\$/kWh$

$\dot{Q}_{tank}$ is the thermal capacity of the storage tank, and it depends on the mode of operation as seen from Tables 10 and 11.

In the case where nanofluids are used, the capital cost of the nanoparticles is to be added, the cost of the nanoparticles is provided in Table 20, along with the input parameters and design specifications used in order to carry the economic model. The prices of the nanoparticles are obtained from [180].

Table 20: Input data and design parameters for the economic model

Parameter	Symbol	Unit	Value
Construction years	y_{con}	Years	3
Decommission year	y_{dec}	Years	3
Plant life time cycle	y_{opt}	Years	25
Loan interest rate	i	%	7
Insurance rate	r_{ins}	%	1
Electricity sale price	C_{el}	$US\$/kWh$	0.07
Al_2O_3 nanoparticles price	$C_{Al_2O_3}$	$US\$/gram$	1.16
Cu nanoparticles price	C_{cu}	$US\$/gram$	1.5
$SWCNT$ nanoparticles price	C_{SWCNT}	$US\$/gram$	62
Operating hours	t_{opt}	$hour/year$	8760

5.1.6 Auxiliary Equipment.

The capital investment cost of the steam turbine, such as the pumps and the lubrication systems in $US\$$ is obtained from [177], and it is provided below:

$$Z_{st,aux} = 10^7 \left(\frac{\dot{W}_{net}}{75}\right)^{0.7} \tag{5.9}$$

5.1.7 Equipment Installation.

The equipment installation capital investment cost in $US\$$, is set to be 20% of the equipment's capital investment cost according to [178]; therefore the equipment installations cost is given by:

$$Z_{eq,ins} = 0.2 \sum Z_{eq} \tag{5.10}$$

where Z_{eq} is the summation of the capital investment cost of the equipment discussed in the previous sections.

5.1.8 Water Treatment Facility.

The capital investment cost of the water treatment facility of the steam turbine in $US\$$ is obtained from [177]:

$$Z_{wt} = 2.03 \times 10^6 \left(\frac{\dot{W}_{net}}{110}\right)^{0.8} \tag{5.11}$$

5.1.9 Operating Cost.

The operating cost of the plant can be simply calculated from the following equation:

$$Z_{opt} = \dot{W}_{net} C_{PB} + \dot{W}_{net} C_{om} \tag{5.12}$$

where

C_{PB} is the power block cost constant equal to 875 $\$/kW$.

C_{om} is the operating and maintenance cost constant equal to 60 $\$/kW$

5.1.10 Civil Engineering.

The capital investment needed for a new site infrastructure and building can be assumed to 55% of the equipment cost according to [178], therefore the civil engineering capital investment cost in $US\$$ is given by:

$$Z_{CE} = 0.55 \sum Z_{eq} \tag{5.13}$$

5.1.11 Project Engineering and Contingencies.

The cost of the indirect factors such as planning, permitting, and management of the construction in $US\$$, are estimated by [177] and are as follows:

$$Z_{ic} = 0.05 \sum Z_{eq} + Z_{eq,ins} + Z_{CE} \tag{5.14}$$

The cost of contingency issues such as technical and regulatory problems in $US\$$ is given by:

$$Z_{con} = 0.1 \sum Z_{eq} + Z_{eq,ins} + Z_{CE} \tag{5.15}$$

5.1.12 Decommissioning cost.

The cost of decommissioning the plant and returning the site into its original state in $US\$$ is given by the following equation:

$$Z_{dec} = 0.05 \sum Z_{eq} + Z_{ins,eq} + Z_{CE} \quad (5.16)$$

5.1.13 Labor cost.

The labor cost consists of the salaries paid to the plant employees. According to a study done by [177], the number of employees, their correspondent job, and salaries are provided in Table 20.

The labor cost can be calculated from the following equation:

$$Z_{labor} = 1.5 \sum SalaryN \quad (5.17)$$

Table 21: Plant positions, salary, and number of employees needed [177]

Employee	Salary ($US\$/year$)	Number of employees (N)
Power block technician	40,000	6
Solar filed technician	40,000	12
Control room operator	40,000	15
Maintenance Supervisor	48,000	2
Operation Manager	84,000	2
Plant Engineer	92,000	1
Plant Manager	95,000	1

5.1.14 Maintenance cost.

The annual maintenance cost is estimated as a percentage of the initial capital investments. For civil engineering the maintenance cost is approximated to be 1% of the initial investment.

$$Z_{mc.CE} = 0.1 Z_{CE} \quad (5.18)$$

The maintenance cost of the cycle components is approximated to be 2% of their initial investment, given by:

$$Z_{mc,eq} = 0.2Z_{eq} \tag{5.19}$$

The maintenance cost of the PTSC field is approximated to be 5% of the initial investment, given by:

$$Z_{mc,PTSC} = 0.5Z_{PTSC} \tag{5.20}$$

Therefore, the maintenance cost is given by:

$$Z_m = Z_{mc.CE} + Z_{mc,eq} + Z_{mc,PTSC} \tag{5.21}$$

5.1.15 Net Present Value (NVP).

Different methods can be applied in order to assess the performance of the ISRRC; one of these methods is the NPV. The NPV approach calculates the investment worth growth of the plant life time to evaluate the feasibility of an investment. It is established that an investment is only advisable as long as a positive NPV is present, where a negative NPV simply implies that the required investment is greater than the cash flow during the cycle life time. The net present value is acquired from [177] and it is as follows:

$$NPV = -\sum_{k=0}^{y_{con}-1} \frac{Z_{inv}}{y_{con}(1+i)^k} + \sum_{k=y_{con}}^{y_{con}+y_{opt}-1} C_{el}\dot{W}_{net} - \frac{Z_{opt}+Z_m+Z_{labor}+r_{ins}Z_{inv}}{(1+i)^k} + \sum_{k=y_{con}+y_{opt}}^{y_{con}+y_{opt}+y_{dec}-1} \frac{Z_{dec}}{y_{dec}(1+i)^k} \tag{5.22}$$

where

$y_{con}$is the number of years taken to construct the plant

$y_{opt}$is the plant life time cycle or the number of years the plant is under operation

$y_{dec}$is the number of years taken to disassemble the plant and return the site to its original condition

C_{el} is the electricity sale price in $\$/kWh$

i is the loan interest rate

r_{ins} is the annual insurance rate, which is the cote of insuring the equipment

Z_{inv} is the initial investment required for constructing the plant, it is given by :

$$Z_{inv} = Z_{st} + Z_{HE1} + Z_{HE2} + Z_{FW} + Z_{PHTF} + Z_{PHST} + Z_{PCST} + Z_{PFWH} + Z_{PW} + Z_c + Z_{PTSC} + Z_{st,aux} + Z_{CE} + Z_{ins,eq} + Z_{ic} + Z_{cont} \quad (5.23)$$

5.1.16 Net Saving (NS).

The Net Saving (NS) approach is a calculation of the money saved by employing a renewable energy source as opposed to running the plant on fossil fuels. It is primarily an indication of the cost saving in the electricity caused utilizing the PTSC as a source of generation. The Net Saving (NS) in $US\$$ can be calculated from the following equation:

$$NS = C_{withoout\ system} - C_{with\ system} \quad (5.24)$$

where

$C_{without\ System}$is the cost of electricity that would be purchased to meet the facility electric load with no renewable energy system ($).

$C_{with\ System}$is the cost of electricity purchased from the grid, assuming that the project sells electricity generated by the system in excess of the load ($).

5.1.17 Levelized Cost of Electricity (LEC).

Another approach to indicate the performance of the ISRRC is the levelized cost of electricity (LEC), which determines the minimum cost of electricity generated by the plant. The LEC is the cost of electricity which makes the NPV equals to zero, and a lower LEC implies a more cost-effective investment. The LEC is obtained from [177] and it is given by:

$$LEC = \frac{\alpha Z_{inv} + \beta Z_{dec} + Z_{opt} + Z_m + Z_{labor}}{\dot{W}_{net}} \quad (5.25)$$

where

$$\alpha = \left[\frac{(1+i)_{con}^{y}-1}{y_{con}i}\right]\left[\frac{i(1+i)_{opt}^{y}}{(1+i)_{opt}^{y}-1}\right] + r_{ins} \quad (5.26)$$

$$\beta = \left[\frac{(1+i)_{dec}^{y}-1}{y_{dec}i(1+i)_{dec}^{y-1}}\right]\left[\frac{1}{(1+i)_{opt}^{y}-1}\right] \quad (5.27)$$

5.2 Effect of the nanofluids on the cost of the ISRRC for different modes of operation.

The analysis for the cost of the ISRRC for different modes of operation and nanofluids is done based on the models, tables and assumptions provided in the system configuration and modeling section, and using the results from the previous section. A full analysis of the cost of the ISRRC for different modes of operations and nanofluids is done using the System Advisory Model (SAM) software. For the analysis in this section the properties of the nanofluids are calculated for a volume fraction of 5%, and the effect of the nanofluids on the performance of the ISRRC for different modes of operations is taken from section 4.6.4, where the annual energy output is used for comparison.

5.2.1 Effect of the nanofluids on the economic-performance of the ISRRC for the 1st mode of operation.

Starting with the 1st mode of operation that assumes no storage, Table 22 shows a comparison of the annual energy output and cost of the ISRRC for Therminol, Syltherm, Therminol-based nanofluids, and Syltherm-based nanofluids. It is seen that the presence of the nanofluids improves the annual energy, lower the levelized electricity cost, increases the cost savings, and lowers the Net Present Value of the ISRRC. According to the table Cu-based nanofluids are the most suitable nanofluids to replace Therminol and Syltherm, when the plant is operating at the 1st mode of operation. In addition, it is observed that Therminol and Therminol-based nanofluids result in a higher performance and a lower cost for the ISRRC, when compared to Syltherm and Syltherm-based nanofluids. However, Syltherm-based nanofluids show a larger improvement in the performance and the cost when compared to Therminol-based nanofluids.

Table 22: Comparison between Therminol-based and Syltherm-based nanofluids regarding the costs of the ISRRC for 1st mode of operation

Parameter	Annual Energy	LEC (Real)	Electricity cost with system	Electricity cost without system	Net Saving	Net Present Value
Unit	kWh	c/kWh	$US\$$	$US\$$	$US\$$	$US\$$
Therminol	343,897,856	3.36	-9,297,543		9,349,645	-73,160,272
Al_2O_3/Therminol	345,199,968	3.35	-9,348,415		9,400,517	-72,714,496
Cu/Therminol	347,008,064	3.33	-9,375,601		9,427,703	-72,476,272
$SWCNT$/Therminol	344,268,704	3.36	-9,304,111		9,356,213	-73,102,720
Syltherm	337,436,608	3.43	-9,059,778	52,102	9,111,880	-75,243,784
Al_2O_3/Syltherm	341,773,472	3.38	-9,205,520		9,257,622	-73,966,672
Cu/Syltherm	345,446,880	3.35	-9,332,386		9,384,488	-72,854,944
$SWCNT$/Syltherm	338,663,392	3.41	-9,094,077		9,146,179	-74,943,224

5.2.2 Effect of the nanofluids on the economic-performance of the ISRRC for the 2nd mode of operation.

Regarding the 2nd mode of operation where a storage system with a 7.5 hours storage period is available, Table 23 shows a comparison of the annual energy output and cost of the ISRRC for Therminol, Syltherm, Therminol-based nanofluids, and Syltherm-based nanofluids for the 2nd mode of operation. From the table it is seen that the addition of the nanoparticles improves the annual energy of the ISRRC, and this increase varies depending on the nanofluid. For instance, Cu-based nanofluids show the highest improvement in the annual energy, however when Therminol and Cu/TTherminol are compared together, it is seen that the addition of Cu nanoparticles has a negative effect on the net saving of the system, as it increases it as opposed to decreasing it, therefore yielding that the addition of the Cu nanoparticles to Therminol is not feasible when the ISRRC is operating at the 2nd mode of operation.

The same result applies to Al_2O_3/Therminol, where the annual energy is increased, however, the cost increases as well. In case of Therminol-based nanofluids, the only feasible option is $SWCNT$/Therminol, where the annual energy is increased, the levelized cost of electricity stays the same, but the net savings increases, and the net present value decreases making the plant more feasible.

Regarding Syltherm-based nanofluids it is seen that the addition of nanoparticles has a positive effect on the annual energy and the cost regardless of the nanoparticles used. When comparing, it is seen that Cu/Syltherm has the highest annual energy production, but it also possess the lowest net savings. Moreover, Al_2O_3/Syltherm has the second highest annual energy production, and the highest net savings yielding that Al_2O_3/Syltherm is the most feasible nanofluid to replace Syltherm when the ISRRC is operating at the 2nd mode of operation.

Table 23: Comparison between Therminol-based and Syltherm-based nanofluids regarding the costs of the ISRRC for 2nd mode of operation

Parameter	Annual Energy	LEC (Real)	Electricity cost with system	Electricity cost without system	Net Saving	Net Present Value
Unit	kWh	c/kWh	$US\$$	$US\$$	$US\$$	$US\$$
Therminol	477,914,976	3.08	-12,323,464		12,375,566	-89,121,768
Al_2O_3/Therminol	479,397,152	3.07	-12,259,894		12,311,996	-89,678,824
Cu/Therminol	482,669,376	3.05	-12,156,485		12,208,587	-90,585,000
$SWCNT$/Therminol	478,313,248	3.08	-12,358,502		12,410,604	-88,814,744
Syltherm	467,482,560	3.15	-11,925,526	52,102	11,977,628	-92,608,864
Al_2O_3/Syltherm	474,379,456	3.10	-12,319,715		12,371,817	-89,154,632
Cu/Syltherm	480,352,992	3.07	-12,101,207		12,153,309	-91,069,384
$SWCNT$/Syltherm	470,286,336	3.13	-12,176,500		12,228,602	-90,409,600

5.2.3 Effect of the nanofluids on the economic-performance of the ISRRC for the 3rd mode of operation.

Regarding the 3rd mode of operation where a storage system with 10 hours storage period, Table 24 shows a comparison of the annual energy output and cost of the ISRRC for Therminol, Syltherm, Therminol-based nanofluids, and Syltherm-based nanofluids for the 2nd mode of operation. From the table it is seen that all nanofluids have a positive effect on the annual energy, and the net saving of the plant. For Therminol-based nanofluids, it is seen that $SWCNT$/Therminol has the lowest annual energy improvement, but the highest net cost saving making the most feasible fluid to replace Therminol when the plant is operating at the 3rd mode of operation. Regarding Syltherm-based nanofluids, Cu/Syltherm displays the highest improvement in the annual energy, and the highest net

saving therefore it is chosen as the most suitable nanofluid to replace Syltherm when the plant is operating at the 3rd mode of operation.

Table 24: Comparison between Therminol-based and Syltherm-based nanofluids regarding the costs of the ISRRC for 3rd mode of operation

Parameter	Annual Energy	LEC (Real)	Electricity cost with system	Electricity cost without system	Net Saving	Net Present Value
Unit	kWh	c/kWh	$US\$$	$US\$$	$US\$$	$US\$$
Therminol	478,163,808	3.30	-12,199,230		12,251,332	-104,369,536
Al_2O_3/Therminol	479,790,240	3.29	-12,321,778		12,373,880	-103,295,648
Cu/Therminol	482,998,976	3.27	-12,222,188		12,274,290	-104,168,360
$SWCNT$/Therminol	478,700,544	3.30	-12,393,622		12,445,724	-102,666,096
Syltherm	467,911,520	3.37	-12,014,880	52,102	12,066,982	-105,984,976
Al_2O_3/Syltherm	474,679,744	3.33	-12,276,714		12,328,816	-103,690,552
Cu/Syltherm	480,515,616	3.28	-12,383,985		12,436,087	-102,750,536
$SWCNT$/Syltherm	470,639,296	3.35	-12,183,601		12,235,703	-104,506,480

5.2.4 Comparison of the effect of the nanofluids on the economic-performance of the ISRRC for different modes of operation.

The most suitable nanofluids to replace Therminol and Syltherm for each mode of operation are selected. However the most cost effective and efficient mode of operation for the ISRRC is ought to be determined. Selecting the optimum mode of operation is important because of the strong impact the mode of operation has on the performance of the ISRRC. It is somewhat trivial to realize that the 1st mode of operation is not the best mode for the ISRRC to operate on, as the presence of the storage system improves the output energy of the ISRRC and decreases the LEC. The main comparison is between the 2nd and 3rd mode of operation, where the optimum storage period is to found. Figure 83 shows the variation of the modes of operation on the LEC of the ISRRC for Therminol-based and Syltherm-based nanofluids.

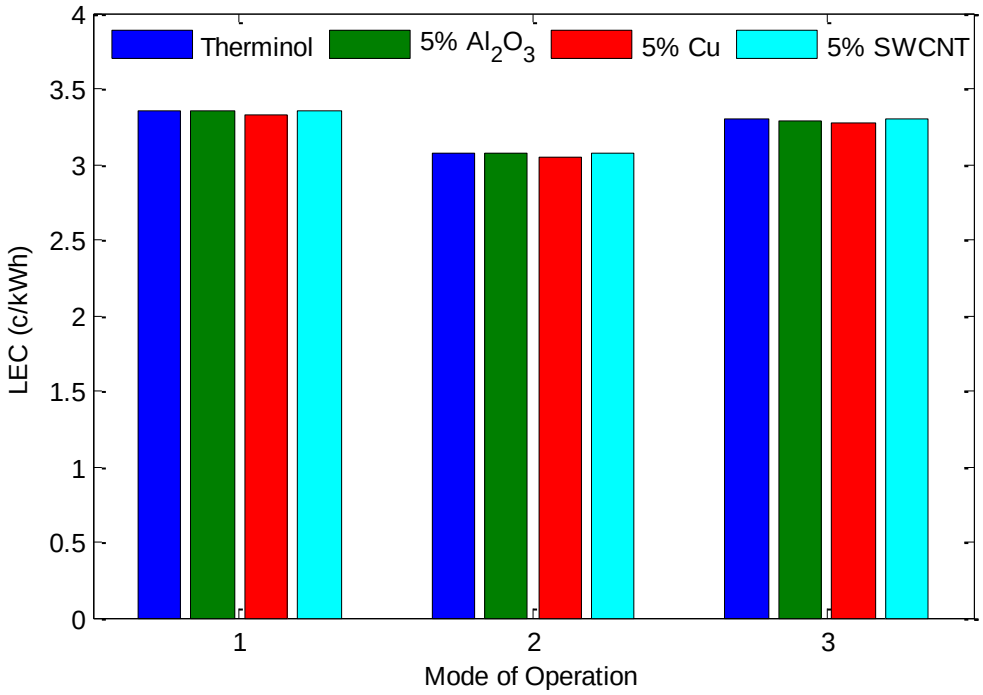

(a)

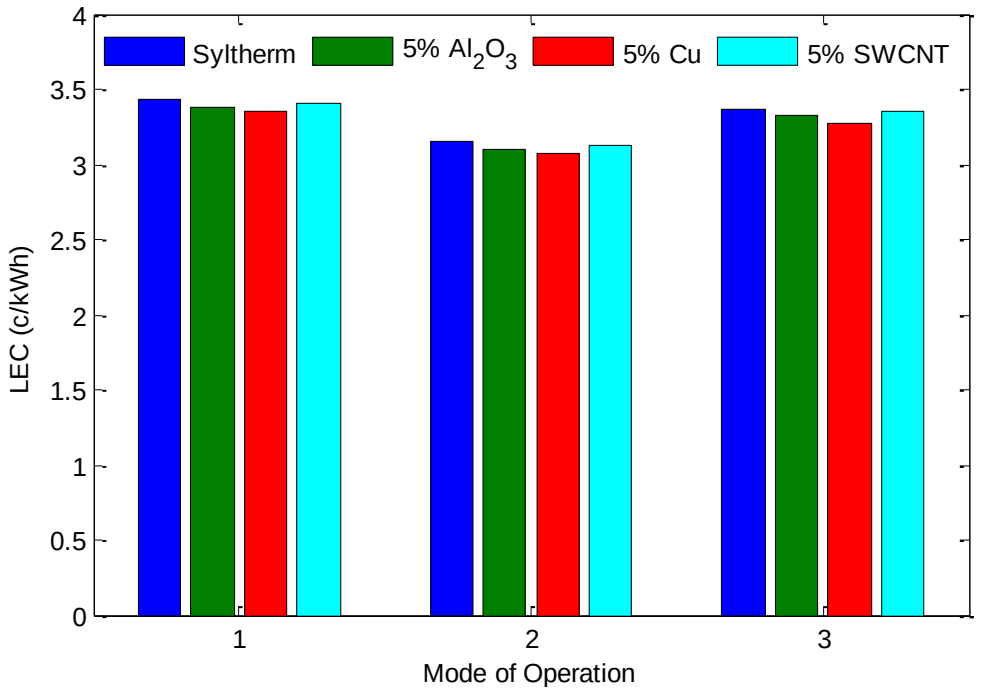

(b)

Figure 83: Effect of modes of operation on the LEC of the ISRRC for (a) Therminol-based nanofluids, and (b) Syltherm-based nanofluids

It is seen from the figure that the LEC is the lowest when the ISRRC is operating at the 2nd mode of operation. While for the 1st mode of operation and the 3rd mode of operation the LEC is almost the same. When comparing Therminol-based nanofluids and Syltherm-based nanofluids, it is observed that Therminol-based nanofluids display a lower LEC for all modes of operation, however Syltherm-based nanofluids decrease the LEC by a higher percentage.

Figure 84 shows the variation of the modes of operation on the Net Saving of the ISRRC for Therminol-based and Syltherm-based nanofluids. It is seen the 2nd mode of operation shows the highest Net Saving in the cost of the ISRRC, while the 1st mode of operation shows the lowest. When comparing Therminol-based nanofluids with Syltherm-based nanofluids, it is noticed that Therminol-based nanofluids result in a higher net savings for all modes of operation. Nevertheless, Syltherm-based nanofluids display a higher percentage increase in the cost savings.

Referring to Tables 22-24 and Figures 83 and 84, it is seen that the mode of operation where the ISRRC produces the highest annual energy is the 3rd mode of operation. However when compared to the 2nd mode of operation, it is observed that the amount of increase in the annual energy is considerably small. For example, the annual energy produced for Therminol is $477{,}914{,}976\ kWh$when operating at the 2nd mode of operation, and $478{,}163{,}808\ kWh$when operating on the 3rd mode of operation. In addition, for that small increase in the annual energy the levelized cost of electricity increase from $3.08\ c/kWh$ to $3.30\ c/kWh$. Moreover, the net saving decreases from $12{,}375{,}566\ US\$$ to$12{,}251{,}332\ US\$$. Upon the preceding findings it is recommended to operate the ISRRC at the 2nd mode of operation rather than the 3rd mode of operation, as the increase in annual energy is not feasible.

Comparing Tables 22 and 23 for the 1st mode of operation and the 2nd mode of operation respectively, it is established that operating the ISRRC on the 2nd mode of energy results in a higher annual energy, a lower levelized electricity cost, and a higher net saving because of the presence of the TES system. Therefore, it is recommended to operate the ISRRC on the 2nd mode of energy, as it is the most effective and efficient mode of operation.

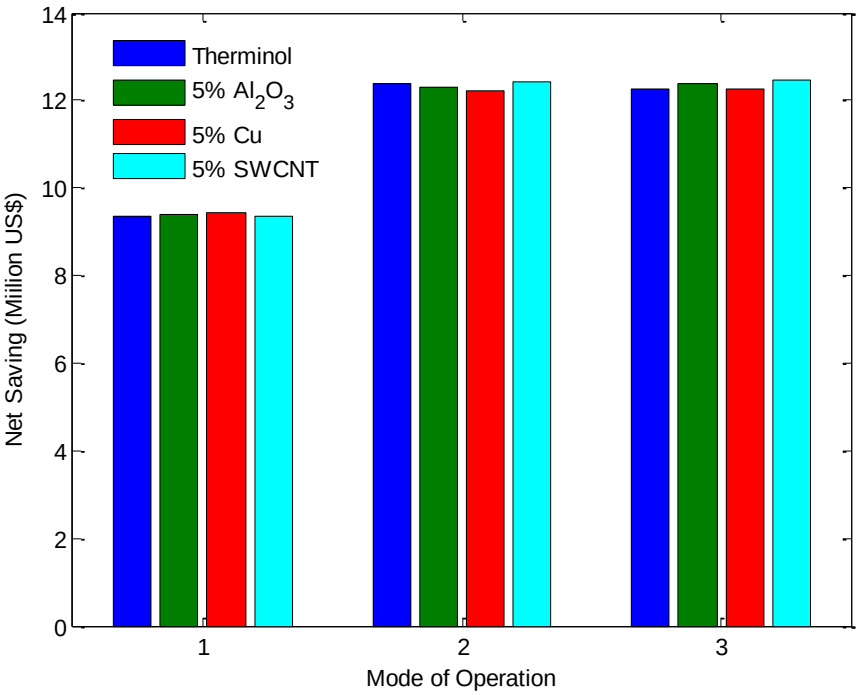

(a)

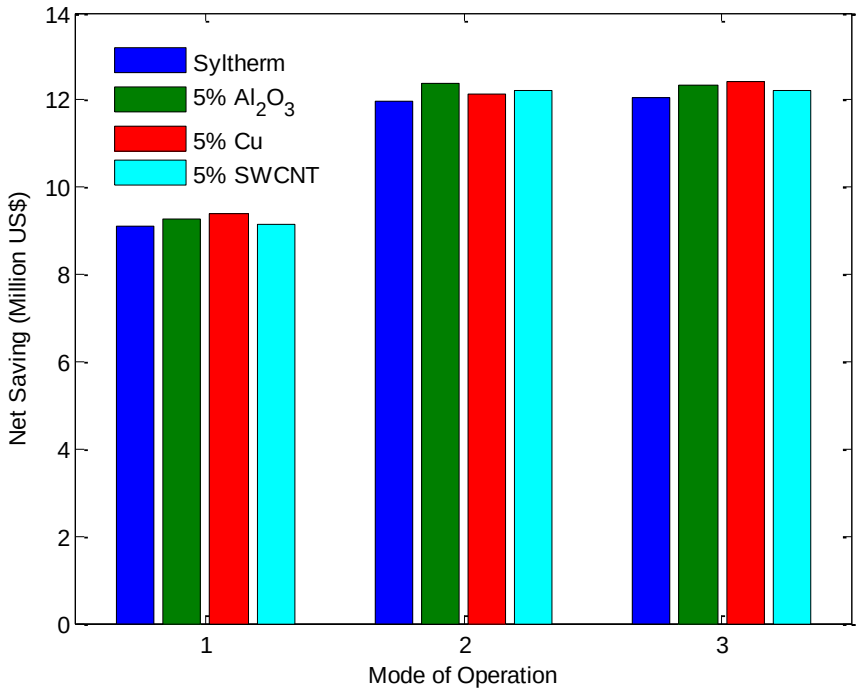

(b)

Figure 84: Effect of modes of operation on the net savings of the ISRRC for (a) Therminol-based nanofluids, and (b) Syltherm-based nanofluids

The effect of the nanofluids on the performance of the ISRRC depends on the modes of operation as seen from the preceding tables. Table 25 shows the most suitable nanofluid to replace the base fluids (Therminol and Syltherm) for different modes of operations. It is seen that for modes of operation with storage, $SWCNT$/Therminol are most suitable nanofluids, yielding that they have a positive effect on the storage system. However, for Syltherm-based nanofluids Al_2O_3-based and Cu-based nanofluids are the most suitable nanofluids to replace Syltherm. This leads to the conclusion that the relationship between the base fluid and the nanoparticles is the main motive behind the magnitude of the improvement caused by the nanofluids.

Table 25: Most suitable nanofluid to replace the base fluids for different modes of operation.

Mode of Operation	Nanofluid to replace Therminol & Syltherm	
1st mode	5% Cu/Therminol	5% Cu/Syltherm
2nd mode	5% $SWCNT$/Therminol	5% Al_2O_3/Syltherm
3rd mode	5% $SWCNT$/Therminol	5% Cu/Syltherm

5.2.5 Effect of the optimum mode of operation on the TES.

In the previous sections different modes of operation were compared, and it was established that the 2nd mode of operation is the optimum mode of operation in terms of cost and power output. However, while operating on the 2nd mode of operation it is seen that the volume of the storage tanks is rather large. The construction of the storage tank should be done using concrete in order to accommodate the large tank diameter of 53 m. Another option is to build a number of smaller storage tanks and connect them in parallel in order to extract the same flow rate from all the tanks, where the summation of the volume of the tanks should be equal to $43726\ m^3$, which is the volume specified in Table 10. In this section, the second option is explored where a number of hot and cold storage tanks are used to form the thermal energy storage system.

Three hot storage tanks and three cold storage tanks are used to substitute the hot storage tank and cold storage tank, specified in Table 10. The diameter of the tanks can be calculated from the following equation:

$$D_{tank} = \sqrt{\frac{4V_{TES}h_{tank}}{\pi}} \tag{5.28}$$

The volume and thermal capacity of the storage tanks are simply found by dividing the volume and the thermal capacity of the storage tank provided in Table 10, by the number of the storage tanks used. Table 26 shows the input and design parameters for the new thermal energy storage system for the 2nd mode of operation.

Table 26: Input design parameters for the new TES for the 2nd mode of operation

Parameter	Symbol	Unit	Value
Storage Media Type	-	-	Sensible
Storage Media	-	-	Hitec Salt
Cold Tank Temperature	T_{cold}	℃	250
Hot Tank Temperature	T_{hot}	℃	365
TES Density	ρ_{salt}	kg/m^3	1829.31
TES Specific heat	$C_{p_{salt}}$	kJ/kgK	1.56
Storage Volume	V_{TES}	m^3	14575
Tank Height	h_{tank}	m	20
Tank Diameter	D_{tank}	m	30.5
TES Thermal Capacity	$\dot{Q}_{tank}$	MWh	994
TES Capacity	$t_{storage}$	$hour$	7.5
Number of storage tanks	N_{tanks}	-	3

Figure 85 shows the schematic diagram of the charging cycle of the ISRRC for the 2nd mode of operation with the new TES system for the full load and partial load operation. It is seen from Figure 85 (b), that during high solar beam radiation timings the system operates under partial load, where the excess amount of heating fluid is directed to charge the three hot storage tanks. Valves are added before and after each tank in order to control the flow rate of the Hitec Salt entering and exiting the tanks. While when the system is under full load operation, the heating by passes the storage systems and is directed towards the power cycle as seen from Figure 85 (a).

Figure 86 shows the schematic diagram of the discharging cycle of the ISRRC for the 2nd mode of operation with the new TES system for full load and partial. It is seen in Figure 86 (a), that during the night time when the PTSC field is not in operation, the system is under full operation. The Hitec salt from the three hot storage tanks is used to heat up the water into steam, and then it is directed to the three cold storage tanks where it is stored until the charging cycle is in operation. During the low beam radiation hours the PTSC field and the storage are both under operation, where the system operates under partial load as seen in Figure 86 (b). The water from the power cycle is heated by the hot Hitec Salt from the the hot storage tanks, and then it is heated by the heating fluid from the PTSC field.

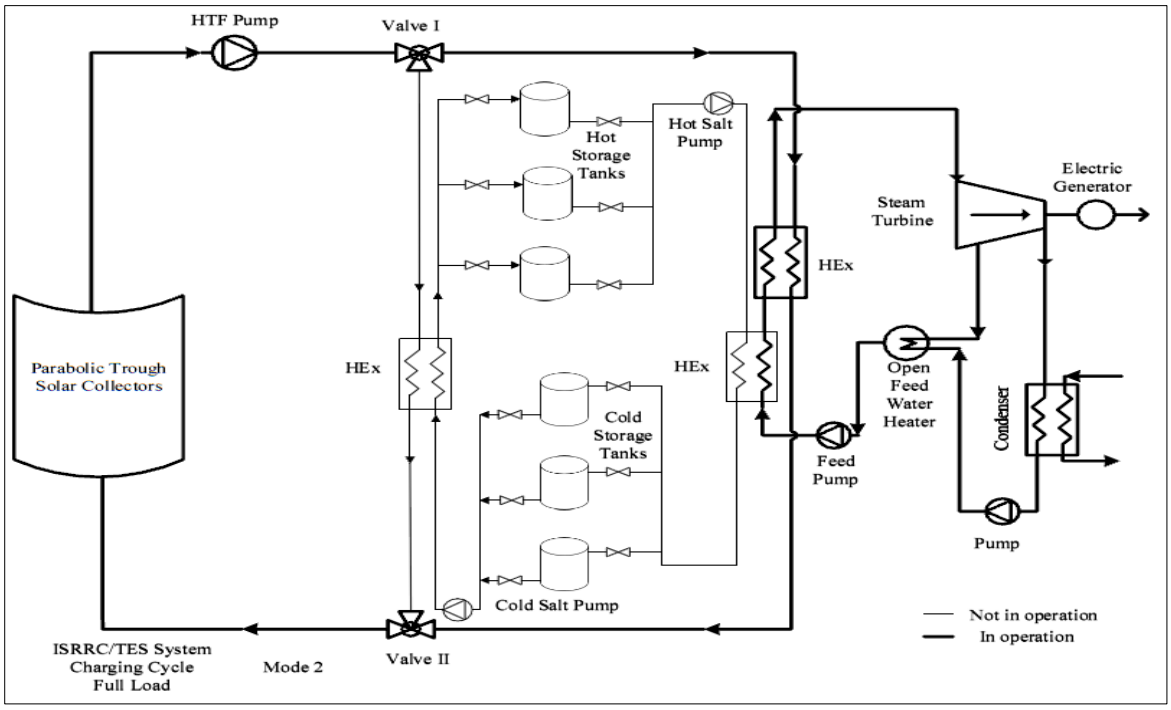

(a)

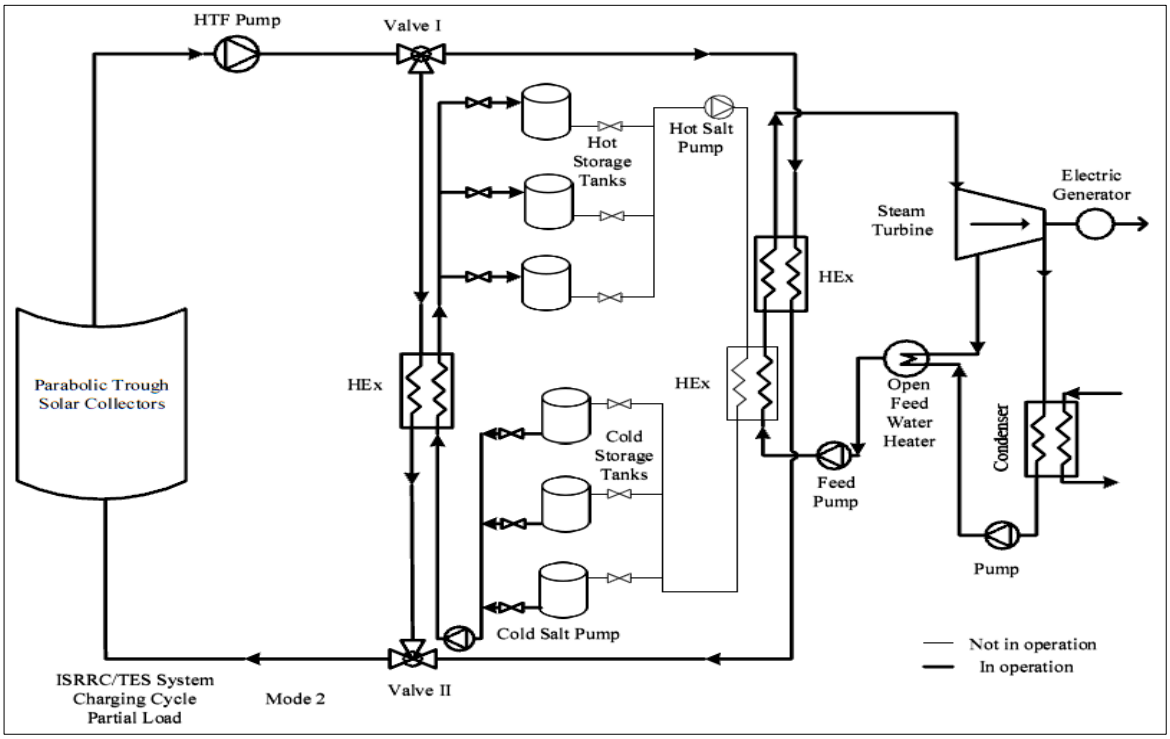

(b)

Figure 85: Schematic diagram of the charging cycle of the ISRRC with the new TES system for (a) Full load, and (b) Partial load

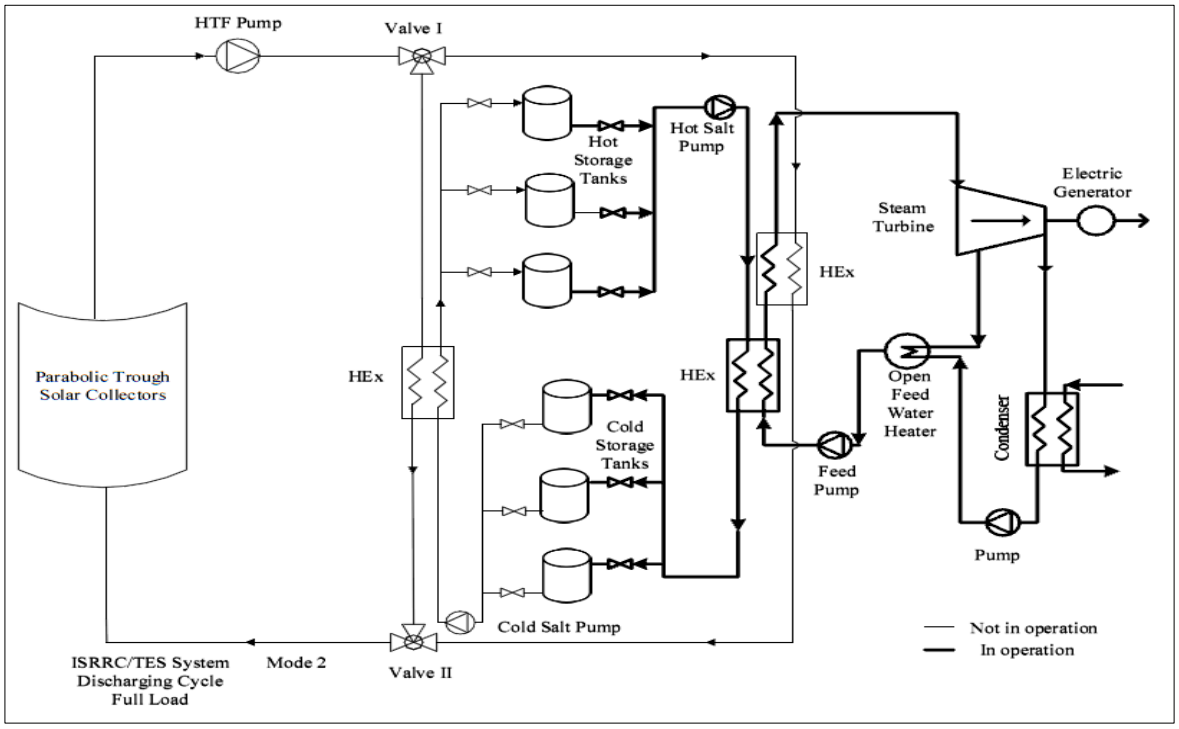

(a)

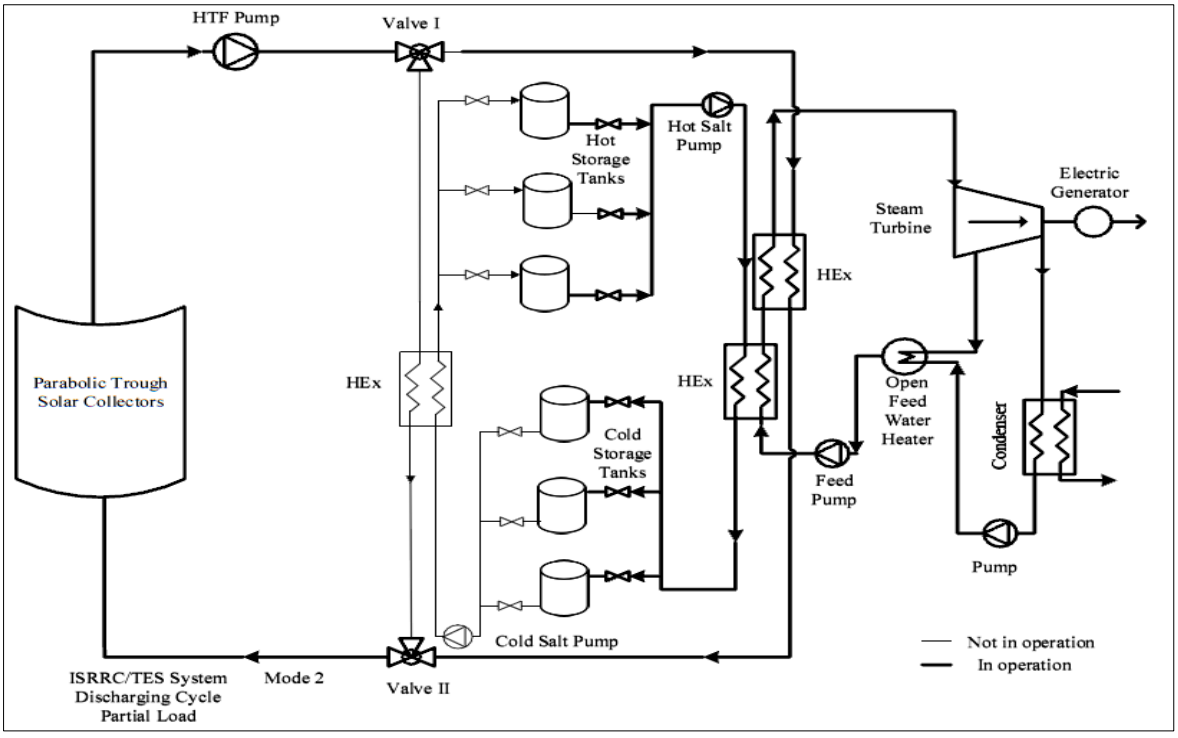

(b)

Figure 86: Schematic diagram of the discharging cycle of the ISRRC with the new TES system for (a) Full load, and (b) Partial load

In conclusion, it was shown that adding nanoparticles to the base fluids enhances the thermophysical properties of these fluids, leading to an improvement in the heat transfer coefficient. The improvement in the heat transfer coefficient inside the absorber tube, leads to an enhancement in the efficiency and energy output of the PTSC. The enhancement in the PTSC improves the energy output of the Integrated Solar Regenerative Rankine Cycle, and decreases the electricity cost as well as increases the net saving. The novelty of this work lies in studying the effect of the adding nanoparticles to conventional heating fluids on the properties of the fluids, heat transfer coefficient in the absorber tube, performance of the PTSC, and performance of the PTSC integrated system with thermal energy storage for different modes of operation.

Chapter 6: Conclusion and Recommendations

An evaluation of an integrated PTSC/TES system using nanofluids was done. The effect of adding nanoparticles to a heating fluid on the density, specific heat capacity, viscosity, and thermal conductivity was investigated. The convective heat transfer coefficient in the absorber tube of the PTSC was calculated and compared for a conventional heating fluid versus nanofluids. Further, the effect of using nanofluids as a heating fluid on the efficiency and output energy of the PTSC was studied by carrying a full energy and exergy model study. In addition, two system configurations for an ISRRC were studied and compared. Moreover, different modes of operation are analyzed and compared using conventional heating fluids and nanofluids. The conclusion and recommendations are presented in this section.

6.1 Conclusion

Therminol and Syltherm were chosen as the base fluids, while Alumina (Al_2O_3), Copper(Cu), and Single Walled Carbon Nanotubes ($SWCNT$) were chosen as the nanoparticles. It was seen that the density of the nanofluids decreases with the increase in temperature, and increases with the increase in the volume fraction. Further, since Therminol has a higher density than Syltherm, Therminol based nanofluids showed a higher density that Syltherm based nanofluids. Also, Cu-based nanofluids displayed the highest density increase compared to other nanofluids, because of the high density of Cu.

The specific heat capacity of the nanofluids increases with the increase in temperature, and decreases with the increase in volume fraction. $SWCNT$-based nanofluids showed the least decrease in the specific heat capacity when compared to other nanofluids; nonetheless the decrease caused by the addition of nanoparticles is considerably small (around 2%). Moreover, Therminol based nanofluids showed a higher specific heat capacity than that of the Syltherm nanofluids. In order to increase the specific heat capacity of the base fluids, nanoparticles with a higher specific heat capacity than the base fluids are to be added.

The viscosity of the nanofluids depends on the viscosity of the base fluids and the volume fraction, meaning that all nanofluids despite the nanoparticles added to them show the same viscosity at different volume fractions. Different viscosity models were

compared, and the Batchelor model [94] was chosen because it takes into account the Brownian motion of the nanoparticles inside the base fluid. It was seen that the viscosity of the nanofluids decreases with the increase in temperature, and increases with the increase in the volume fraction. Also, Syltherm based nanofluids show a higher viscosity than that of Therminol based nanofluids. Further, increasing the nanoparticles diameter showed no effect on the viscosity of the nanofluids.

Different models for the prediction of the thermal conductivity of the nanofluids were compared to experimental data and each other. The Yu and Choi model [75] was chosen for calculating the thermal conductivity of Cu and Al_2O_3- based nanofluids, while the model developed by Nan et al. [85] was chosen to calculate the thermal conductivity of $SWCNT$-based nanofluids. It was seen that the thermal conductivity of the nanofluids decreases with the increase in temperature, and increases with the increase in volume fraction. $SWCNT$-based nanofluids showed the highest enhancement in the thermal conductivity when compared to Cu and Al_2O_3-based nanofluids that showed the same enhancement as each other. Moreover, Therminol based nanofluids showed a higher thermal conductivity when compared to Syltherm based nanofluids, however Syltherm based nanofluids showed a higher enhancement in the thermal conductivity. In addition, it was seen that thermal conductivity of nanofluids decreases with the increase in the nanoparticles radius, and increases with the increase in the nanolayer thickness of $Cu\ and\ Al_2O_3$-based nanofluids. Moreover, it was seen that nanoparticles with the least sphericity show the highest enhancement in the thermal conductivity. Regarding the $SWCNT$-based nanofluids, it was seen that the increase in the length of the $SWCNT$ nanoparticles increases the thermal conductivity of the nanofluids, while increasing the diameter showed negligible effect on the thermal conductivity.

The Reynolds number of Therminol and Syltherm based nanofluids increases with the increase in temperature. $Cu\ and\ Al_2O_3$-based nanofluids show a higher Reynolds number when compared to the base fluids, while $SWCNT$-based nanofluids show a lower Reynolds number. The increase in the volume fraction results in an increase in the Reynolds number of $Cu\ and\ Al_2O_3$-based nanofluids, and a decrease in $SWCNT$-based nanofluids. The Prandtl number of the nanofluids decreases with the increase in the

temperature and volume fraction. The Prandtl number is the same for Cu and Al_2O_3-based nanofluids. The convective heat transfer coefficient of the nanofluids increases with the increase in the volume fraction, and the increase in temperature up to a certain temperature where a constant line is present. It was concluded that the best enhancement in the heat transfer coefficient happens between a volume fraction of 2% and 10%. $SWCNT$-based nanofluids show the highest enhancement in the heat transfer coefficient followed by Cu-based nanofluids and Al_2O_3-based nanofluids. Moreover, Therminol based nanofluids show a higher heat transfer coefficient when compared to Syltherm based nanofluids, however Syltherm based nanofluids show a higher heat transfer coefficient enhancement. In addition, the enhancement in the heat transfer coefficient decreases with the increase in the Reynolds number, and the highest enhancement is shown in the transition phase between laminar and turbulent flow.

The effect of the volume fraction on the enhancement of the efficiency and power output of PTSC was studied. It was seen that the efficiency and power output of the PTSC increase with the increase in the mass flow rate until an optimum mass flow rate value where the efficiency and power output are maximum. Using nanofluids increased the efficiency and power output of the PTSC, and the maximum increase occurred while using $SWCNT$-based nanofluids. Therminol-based nanofluids showed a higher efficiency and power output when compared to Syltherm-based nanofluids; however Syltherm based nanofluids showed a higher enhancement. Moreover, it was established that $SWCNT$-based nanofluids with a volume fraction of 5% were a suitable nanofluid to use for analyzing the PTSC system.

A monthly-based analysis of the PTSC for the city of Abu Dhabi was done for comparison between $SWCNT$-based nanofluids and conventional heating fluids. The months of May and August showed the highest efficiency and power output of the PTSC for all fluids. It was seen that using nanofluids increases the efficiency and the power output of the PTSC regardless of the beam radiation value. Moreover, the exergetic efficiency was increased, and the exergy destruction was decreased when nanofluids were utilized. Further, the entropy generation dropped in the presence of nanofluids. Therminol-based nanofluids showed a higher efficiency, power output, exergetic

efficiency and a lower entropy generation when compared to Syltherm-based nanofluids; however Syltherm based nanofluids showed a higher enhancement in the energetic and exergetic efficiencies, and the power output and a higher detraction in the entropy generation.

While comparing the ISRC and ISRRC it was seen that the efficiency of the ISRRC is higher. Although the work done by the turbine of the ISRC is greater than that of the ISRRC, however the amount of energy needed to power the ISRRC is less than that of the ISRC making it more efficient.

The mass flow rates of the heating fluid inside the PTSC, the molten salt inside the storage system, and the steam inside the cycle have a significant effect on the performance of the ISRRC. In addition, the mass flow rates are affected by the modes of operation. For modes of operation with storage (modes 2 &3), the mass flow rate of the heating fluid in the PTSC increases until a peak value where the solar intensity is at its highest, for these hours a part of the flow rate is routed in order to charge the storage system. The discharging cycle begins when the PTSC shuts down for the lack of beam radiation, and it is supplied until the storage load is satisfied.

The addition of the nanoparticles yielded a positive effect on the annual energy of the ISRRC, for all the nanofluids. The effect on the net saving of the ISRRC was either positive or negative depending on the nanofluids, and the mode of operation. For the 1st mode of operation, it was concluded that $5\%\ Cu$-based nanofluids are the best replacement for Therminol and Syltherm. However, for the 2nd and 3rd modes of operation $5\%\ SWCNT$-based nanofluids were the most suitable replacement for Therminol, while $5\%\ Al_2O_3$-based nanofluids and $5\%\ Cu$-based nanofluids were the most suitable replacement for Syltherm for the 2nd and 3rd modes of operation respectively.

Regarding the modes of operation, it was concluded that the most efficient and cost effective mode of operation for the ISRRC is the 2nd mode of operation, with a 7.5 hours of storage. It showed the lowest LEC and the highest net saving compared to the

other modes of operation, and for all nanofluids. The presence of the storage system leads to increase in the plant operation hours, increasing the annual energy produced.

6.2 Recommendations

It is recommended to carry the provided analysis for different types of base fluids and nanoparticles, as the enhancement of the fluid differs depending on the interaction between the nanoparticles and the base fluids. In addition, different models for the prediction of the thermophysical properties can be utilized in order to produce the most accurate and precise results. Moreover, experimental procedures are a must in order to compare the accuracy of the results, and study the magnitude of enhancement provided by adding nanoparticles to base fluids.

In order to further increase the efficiency and power output of the PTSC, nanomaterials can be utilized to serve as a material for the absorber tube, or the reflective collector of the PTSC. Using nanomaterials will increase the amount of heat captured by the absorber tube and reflected by the collector, hence increasing the efficiency and power output of the PTSC. In addition, nanomaterials can be used in the TES in order to increase the specific heat capacity of the fluid, resulting in less heat loss while storing and higher freezing temperature in the case of Molten Salts.

Further, the effect of using nanofluids can be studied on different solar harvesting systems such as the flat plate collector, and the Linear Fresnel as the enhancement in the nanofluids is higher while low Reynolds number and mass flow rate are present.

Moreover, a detailed exergy-economic cost analysis of the ISRRC is recommended in order to study the system from an exergetic-economic point of view, and establish the amount of saving presented by using nanofluids as a heating fluid.

Finally, the results obtained from this research can form the basis for further research towards the fulfillment of the UAE's goal toward sustainable and renewable energy production methods.

References

[1] J. Adeoye, Y. Amha, V. Poghosyan, K. Torchyan and H. Arafat, "Comparative LCA of Two Thermal Energy Storage Systems for Shams1 Concentrated Solar Power Plant: Molten Salt vs. Concrete", *Journal of Clean Energy Technologies*, pp. 274-281, 2014.

[2] D. Reiche, "Renewable Energy Policies in the Gulf countries: A case study of the carbon-neutral "Masdar City" in Abu Dhabi", *Energy Policy*, vol. 38, no. 1, pp. 378-382, 2010.

[3] T. Mezher, G. Dawelbait and Z. Abbas, "Renewable energy policy options for Abu Dhabi: Drivers and barriers", *Energy Policy*, vol. 42, pp. 315-328, 2012.

[4] G. Vidican, L. McElvaney, D. Samulewicz and Y. Al-Saleh, "An empirical examination of the development of a solar innovation system in the United Arab Emirates", *Energy for Sustainable Development*, vol. 16, no. 2, pp. 179-188, 2012.

[5] S. Kalogirou, "A detailed thermal model of a parabolic trough collector receiver", *Energy*, vol. 48, no. 1, pp. 298-306, 2012.

[6] V. Reddy, S. Kaushik and S. Tyagi, "Exergetic analysis and performance evaluation of parabolic trough concentrating solar thermal power plant (PTCSTPP)", *Energy*, vol. 39, no. 1, pp. 258-273, 2012.

[7] G. Kumaresan, R. Sridhar and R. Velraj, "Performance studies of a solar parabolic trough collector with a thermal energy storage system", *Energy*, vol. 47, no. 1, pp. 395-402, 2012.

[8] J. Feldhoff, K. Schmitz, M. Eck, L. Schnatbaum-Laumann, D. Laing, F. Ortiz-Vives and J. Schulte-Fischedick, "Comparative system analysis of direct steam generation and synthetic oil parabolic trough power plants with integrated thermal storage", *Solar Energy*, vol. 86, no. 1, pp. 520-530, 2012.

[9] D. Lobón, L. Valenzuela and E. Baglietto, “Modeling the dynamics of the multiphase fluid in the parabolic-trough solar steam generating systems”, *Energy Conversion and Management*, vol. 78, pp. 393-404, 2014.

[10] H. Al-Ansary and O. Zeitoun, “Numerical study of conduction and convection heat losses from a half-insulated air-filled annulus of the receiver of a parabolic trough collector”, *Solar Energy*, vol. 85, no. 11, pp. 3036-3045, 2011.

[11] R. Padilla, G. Demirkaya, D. Goswami, E. Stefanakos and M. Rahman, “Heat transfer analysis of parabolic trough solar receiver”, *Applied Energy*, vol. 88, no. 12, pp. 5097-5110, 2011.

[12] İ. Yılmaz and M. Söylemez, “Thermo-mathematical modeling of parabolic trough collector”, *Energy Conversion and Management*, vol. 88, pp. 768-784, 2014.

[13] M. Li and L. Wang, “Investigation of evacuated tube heated by solar trough concentrating system”, *Energy Conversion and Management*, vol. 47, no. 20, pp. 3591-3601, 2006.

[14] S. Tyagi, S. Wang, M. Singhal, S. Kaushik and S. Park, “Exergy analysis and parametric study of concentrating type solar collectors”, *International Journal of Thermal Sciences*, vol. 46, no. 12, pp. 1304-1310, 2007.

[15] M. Öztürk, N. Bezir and N. Özek, “Optical, Energetic and Exergetic Analyses of Parabolic Trough Collectors”, *Chinese Physics Letters*, vol. 24, no. 7, pp. 1787-1790, 2007.

[16] M. Mazloumi, M. Naghashzadegan and K. Javaherdeh, “Simulation of solar lithium bromide–water absorption cooling system with parabolic trough collector”, *Energy Conversion and Management*, vol. 49, no. 10, pp. 2820-2832, 2008.

[17] F. Cabrera, A. Fernández-García, R. Silva and M. Pérez-García, “Use of parabolic trough solar collectors for solar refrigeration and air-conditioning applications”, *Renewable and Sustainable Energy Reviews*, vol. 20, pp. 103-118, 2013.

[18] D. Abueidda and M. Gadalla, "Thermodynamic Analysis of an Integrated Solar-Based Multi-Stage Flash Desalination System", in *Proceedings of the ASME 2012 International Mechanical Engineering Congress & Exposition*, Houston, Texas, USA, 2012.

[19] F. Al-Sulaiman, I. Dincer and F. Hamdullahpur, "Exergy modeling of a new solar driven trigeneration system", *Solar Energy*, vol. 85, no. 9, pp. 2228-2243, 2011.

[20] S. Kuravi, J. Trahan, D. Goswami, M. Rahman and E. Stefanakos, "Thermal energy storage technologies and systems for concentrating solar power plants", *Progress in Energy and Combustion Science*, vol. 39, no. 4, pp. 285-319, 2013.

[21] Y. Tian and C. Zhao, "A review of solar collectors and thermal energy storage in solar thermal applications", *Applied Energy*, vol. 104, pp. 538-553, 2013.

[22] C. Zhao and Z. Wu, "Thermal property characterization of a low melting-temperature ternary nitrate salt mixture for thermal energy storage systems", *Solar Energy Materials and Solar Cells*, vol. 95, no. 12, pp. 3341-3346, 2011.

[23] U. Herrmann, B. Kelly and H. Price, "Two-tank molten salt storage for parabolic trough solar power plants", *Energy*, vol. 29, no. 5-6, pp. 883-893, 2004.

[24] S. Choi, Z. Zhang, W. Yu, F. Lockwood and E. Grulke, "Anomalous thermal conductivity enhancement in nanotube suspensions", *Applied Physics Letters*, vol. 79, no. 14, p. 2252, 2001.

[25] H. Masuda, A. Ebata, K. Teramae and N. Hishinuma, "Alterlation of thermal conductivity and viscosity of liquid by dispersing ultra-fine particles (Dispersion of g-Al2O3, SiO2, and TiO2 ultra-fine particles)", *Japan Journal of Thermophysical Properties*, vol. 7, no. 4, pp. 227-233, 1993.

[26] Y. Xuan and Q. Li, "Heat transfer enhancement of nanofluids", *International Journal of Heat Fluid Flow*, vol. 21, pp. 58-64, 2000.

[27] J. Eastman, U. Choi, S. Li, L. Thompson and S. Lee, "Enhanced Thermal Conductivity through the Development of Nanofluids", *MRS Proc.*, vol. 457, 1996.

[28] X. Wang, X. Xu and S. S. Choi, "Thermal Conductivity of Nanoparticle - Fluid Mixture", *Journal of Thermophysics and Heat Transfer*, vol. 13, no. 4, pp. 474-480, 1999.

[29] S. Lee, S. Choi, S. Li and J. Eastman, "Measuring Thermal Conductivity of Fluids Containing Oxide Nanoparticles", *Journal of Heat Transfer*, vol. 121, no. 2, p. 280, 1999.

[30] J. Eastman, S. Choi, S. Li, W. Yu and L. Thompson, "Anomalously increased effective thermal conductivities of ethylene glycol-based nanofluids containing copper nanoparticles", *Applied Physics Letters*, vol. 78, no. 6, p. 718, 2001.

[31] H. Xie, J. Wang, T. Xi, Y. Liu, F. Ai and Q. Wu, "Thermal conductivity enhancement of suspensions containing nanosized alumina particles", *J. Appl. Phys.*, vol. 91, no. 7, p. 4568, 2002.

[32] M. Biercuk, M. Llaguno, M. Radosavljevic, J. Hyun, A. Johnson and J. Fischer, "Carbon nanotube composites for thermal management", *Applied Physics Letters*, vol. 80, no. 15, p. 2767, 2002.

[33] H. Xie, H. Lee, W. Youn and M. Choi, "Nanofluids containing multiwalled carbon nanotubes and their enhanced thermal conductivities", *J. Appl. Phys.*, vol. 94, no. 8, p. 4967, 2003.

[34] H. Patel, S. Das, T. Sundararajan, A. Sreekumaran Nair, B. George and T. Pradeep, "Thermal conductivities of naked and monolayer protected metal nanoparticle based nanofluids: Manifestation of anomalous enhancement and chemical effects", *Applied Physics Letters*, vol. 83, no. 14, p. 2931, 2003.

[35] D. Wen and Y. Ding, "Effective Thermal Conductivity of Aqueous Suspensions of Carbon Nanotubes (Carbon Nanotube Nanofluids)", *Journal of Thermophysics and Heat Transfer*, vol. 18, no. 4, pp. 481-485, 2004.

[36] M. Assael, I. Metaxa, J. Arvanitidis, D. Christofilos and C. Lioutas, “Thermal Conductivity Enhancement in Aqueous Suspensions of Carbon Multi-Walled and Double-Walled Nanotubes in the Presence of Two Different Dispersants”, *International Journal of Thermophysics*, vol. 26, no. 3, pp. 647-664, 2005.

[37] T. Hong, H. Yang and C. Choi, “Study of the enhanced thermal conductivity of Fe nanofluids”, *J. Appl. Phys.*, vol. 97, no. 6, p. 064311, 2005.

[38] S. Murshed, K. Leong and C. Yang, “Enhanced thermal conductivity of TiO2—water based nanofluids”, *International Journal of Thermal Sciences*, vol. 44, no. 4, pp. 367-373, 2005.

[39] M. Liu, M. Ching-Cheng Lin, I. Huang and C. Wang, “Enhancement of thermal conductivity with carbon nanotube for nanofluids”, *International Communications in Heat and Mass Transfer*, vol. 32, no. 9, pp. 1202-1210, 2005.

[40] C. Li and G. Peterson, “Experimental investigation of temperature and volume fraction variations on the effective thermal conductivity of nanoparticle suspensions (nanofluids)”, *J. Appl. Phys.*, vol. 99, no. 8, p. 084314, 2006.

[41] M. Liu, M. Lin, C. Tsai and C. Wang, “Enhancement of thermal conductivity with Cu for nanofluids using chemical reduction method”, *International Journal of Heat and Mass Transfer*, vol. 49, no. 17-18, pp. 3028-3033, 2006.

[42] M. Chopkar, P. Das and I. Manna, “Synthesis and characterization of nanofluid for advanced heat transfer applications”, *ScriptaMaterialia*, vol. 55, no. 6, pp. 549-552, 2006.

[43] Y. Hwang, Y. Ahn, H. Shin, C. Lee, G. Kim, H. Park and J. Lee, “Investigation on characteristics of thermal conductivity enhancement of nanofluids”, *Current Applied Physics*, vol. 6, no. 6, pp. 1068-1071, 2006.

[44] Y. Hwang, H. Park, J. Lee and W. Jung, “Thermal conductivity and lubrication characteristics of nanofluids”, *Current Applied Physics*, vol. 6, pp. e67-e71, 2006.

[45] E. Pop, D. Mann, Q. Wang, K. Goodson and H. Dai, "Thermal Conductance of an Individual Single-Wall Carbon Nanotube above Room Temperature", *Nano Letters*, vol. 6, no. 1, pp. 96-100, 2006.

[46] S. Jana, A. Salehi-Khojin and W. Zhong, "Enhancement of fluid thermal conductivity by the addition of single and hybrid nano-additives", *ThermochimicaActa*, vol. 462, no. 1-2, pp. 45-55, 2007.

[47] S. Kim, S. Choi and D. Kim, "Thermal Conductivity of Metal-Oxide Nanofluids: Particle Size Dependence and Effect of Laser Irradiation", *Journal of Heat Transfer*, vol. 129, no. 3, p. 298, 2007.

[48] D. Yoo, K. Hong and H. Yang, "Study of thermal conductivity of nanofluids for the application of heat transfer fluids", *ThermochimicaActa*, vol. 455, no. 1-2, pp. 66-69, 2007.

[49] A. Amrollahi, A. Hamidi and A. Rashidi, "The effects of temperature, volume fraction and vibration time on the thermo-physical properties of a carbon nanotube suspension (carbon nanofluid)", *Nanotechnology*, vol. 19, no. 31, p. 315701, 2008.

[50] L. Chen, H. Xie, Y. Li and W. Yu, "Nanofluids containing carbon nanotubes treated by mechanochemical reaction", *ThermochimicaActa*, vol. 477, no. 1-2, pp. 21-24, 2008.

[51] H. Xie and L. Chen, "Adjustable thermal conductivity in carbon nanotube nanofluids", *Physics Letters A*, vol. 373, no. 21, pp. 1861-1864, 2009.

[52] P. Warrier and A. Teja, "Effect of particle size on the thermal conductivity of nanofluids containing metallic nanoparticles", *Nanoscale Res Lett*, vol. 6, no. 1, p. 247, 2011.

[53] Y. Kameya and K. Hanamura, "Enhancement of solar radiation absorption using nanoparticle suspension", *Solar Energy*, vol. 85, no. 2, pp. 299-307, 2011.

[54] M. Liu, M. Lin and C. Wang, "Enhancements of thermal conductivities with Cu, CuO, and carbon nanotube nanofluids and application of MWNT/water nanofluid on a water chiller system", *Nanoscale Res Lett*, vol. 6, no. 1, p. 297, 2011.

[55] G. Colangelo, E. Favale, A. de Risi and D. Laforgia, "Results of experimental investigations on the heat conductivity of nanofluids based on diathermic oil for high temperature applications", *Applied Energy*, vol. 97, pp. 828-833, 2012.

[56] Y. Gan and L. Qiao, "Optical Properties and Radiation-Enhanced Evaporation of Nanofluid Fuels Containing Carbon-Based Nanostructures", *Energy Fuels*, vol. 26, no. 7, pp. 4224-4230, 2012.

[57] Y. Gan and L. Qiao, "Radiation-enhanced evaporation of ethanol fuel containing suspended metal nanoparticles", *International Journal of Heat and Mass Transfer*, vol. 55, no. 21-22, pp. 5777-5782, 2012.

[58] B. Barbés, R. Páramo, E. Blanco, M. Pastoriza-Gallego, M. Piñeiro, J. Legido and C. Casanova, "Thermal conductivity and specific heat capacity measurements of Al2O3 nanofluids", *Journal of Thermal Analysis and Calorimetry*, vol. 111, no. 2, pp. 1615-1625, 2012.

[59] A. Tesfamicha and A. D. Woldeyo, "Effect of Particle Size on Effective Thermal Conductivity of Nanofluids", *Asian J. of Scientific Research*, vol. 6, no. 2, pp. 339-345, 2013.

[60] B. Gu, B. Hou, Z. Lu, Z. Wang and S. Chen, "Thermal conductivity of nanofluids containing high aspect ratio fillers", *International Journal of Heat and Mass Transfer*, vol. 64, pp. 108-114, 2013.

[61] Z. Haddad, C. Abid, H. Oztop and A. Mataoui, "A review on how the researchers prepare their nanofluids", *International Journal of Thermal Sciences*, vol. 76, pp. 168-189, 2014.

[62] R. Sadri, G. Ahmadi, H. Togun, M. Dahari, S. Kazi, E. Sadeghinezhad and N. Zubir, “An experimental study on thermal conductivity and viscosity of nanofluids containing carbon nanotubes”, *Nanoscale Res Lett*, vol. 9, no. 1, p. 151, 2014.

[63] A. Starace, J. Gomez, J. Wang, S. Pradhan and G. Glatzmaier, “Nanofluid heat capacities”, *J. Appl. Phys.*, vol. 110, no. 12, p. 124323, 2011.

[64] D. Shin and D. Banerjee, “Enhanced Specific Heat Capacity of Nanomaterials Synthesized by Dispersing Silica Nanoparticles in Eutectic Mixtures”, *Journal of Heat Transfer*, vol. 135, no. 3, p. 032801, 2013.

[65] P. Mishra, S. Mukherjee, S. Nayak and A. Panda, “A brief review on viscosity of nanofluids”, *International Nano Letters*, vol. 4, no. 4, pp. 109-120, 2014.

[66] Y. Shokrlu and T. Babadagli, “Viscosity reduction of heavy oil/bitumen using micro- and nano-metal particles during aqueous and non-aqueous thermal applications”, *Journal of Petroleum Science and Engineering*, vol. 119, pp. 210-220, 2014.

[67] J. Maxwell, “An Elementary Treatise on Electricity”, *Science*, vol. -3, no. 80, pp. 14-14, 1882.

[68] D. Bruggeman, "Berechnung verschiedener physikalischer Konstanten von heterogenen Substanzen. I. Dielektrizitätskonstanten und Leitfähigkeiten der Mischkörper aus isotropen Substanzen", *Ann. Phys.*, vol. 416, no. 7, pp. 636-664, 1935.

[69] R. Hamilton and O. Crosser, “Thermal Conductivity of Heterogeneous Two-Component Systems”, *Ind. Eng. Chem. Fund.*, vol. 1, no. 3, pp. 187-191, 1962.

[70] D. Jeffrey, “Conduction through a Random Suspension of Spheres”, *Proceedings of the Royal Society A: Mathematical, Physical and Engineering Sciences*, vol. 335, no. 1602, pp. 355-367, 1973.

[71] E. Yamada and T. Ota, “Effective thermal conductivity of dispersed materials”, *Warme- und Stoffubertragung*, vol. 13, no. 1-2, pp. 27-37, 1980.

[72] R. Davis, “The effective thermal conductivity of a composite material with spherical inclusions”, *International Journal of Thermophysics*, vol. 7, no. 3, pp. 609-620, 1986.

[73] D. Kumar, H. Patel, V. Kumar, T. Sundararajan, T. Pradeep and S. Das, “Model for Heat Conduction in Nanofluids”, *Phys. Rev. Lett.*, vol. 93, no. 14, 2004.

[74] Y. Xuan, Q. Li and W. Hu, “Aggregation structure and thermal conductivity of nanofluids”, *AIChE J.*, vol. 49, no. 4, pp. 1038-1043, 2003.

[75] W. Yu and S. Choi, “The Role of Interfacial Layers in the Enhanced Thermal Conductivity of Nanofluids: A Renovated Maxwell Model”, *Journal of Nanoparticle Research*, vol. 5, no. 12, pp. 167-171, 2003.

[76] H. Xie, M. Fujii and X. Zhang, “Effect of interfacial nanolayer on the effective thermal conductivity of nanoparticle-fluid mixture”, *International Journal of Heat and Mass Transfer*, vol. 48, no. 14, pp. 2926-2932, 2005.

[77] K. Leong, C. Yang and S. Murshed, “A model for the thermal conductivity of nanofluids – the effect of interfacial layer”, *Journal of Nanoparticle Research*, vol. 8, no. 2, pp. 245-254, 2006.

[78] Y. Xuan, Q. Li, X. Zhang and M. Fujii, “Stochastic thermal transport of nanoparticle suspensions”, *J. Appl. Phys.*, vol. 100, no. 4, p. 043507, 2006.

[79] R. Prasher, P. Bhattacharya and P. Phelan, “Brownian-Motion-Based Convective-Conductive Model for the Effective Thermal Conductivity of Nanofluids”, *Journal of Heat Transfer*, vol. 128, no. 6, p. 588, 2006.

[80] L. Gao and X. Zhou, “Differential effective medium theory for thermal conductivity in nanofluids”, *Physics Letters A*, vol. 348, no. 3-6, pp. 355-360, 2006.

[81] S. Murshed and C. de Castro, “Predicting the Thermal Conductivity of Nanofluids—Effect of Brownian Motion of Nanoparticles”, *J Nanofluids*, vol. 1, no. 2, pp. 180-185, 2012.

[82] B. Xiao, Y. Yang and L. Chen, “Developing a novel form of thermal conductivity of nanofluids with Brownian motion effect by means of fractal geometry”, *Powder Technology*, vol. 239, pp. 409-414, 2013.

[83] H. Jiang, H. Li, Q. Xu and L. Shi, “Effective thermal conductivity of nanofluids considering interfacial nano-shells”, *Materials Chemistry and Physics*, vol. 148, no. 1-2, pp. 195-200, 2014.

[84] C. Nan, Z. Shi and Y. Lin, “A simple model for thermal conductivity of carbon nanotube-based composites”, *Chemical Physics Letters*, vol. 375, no. 5-6, pp. 666-669, 2003.

[85] C. Nan, G. Liu, Y. Lin and M. Li, "Interface effect on thermal conductivity of carbon nanotube composites",*Appl. Phys. Lett.*, vol. 85, no. 16, p. 3549, 2004.

[86] Q. Xue, “Model for thermal conductivity of carbon nanotube-based composites”, *Physica B: Condensed Matter*, vol. 368, no. 1-4, pp. 302-307, 2005.

[87] H. Patel, K. Anoop, T. Sundararajan and S. Das, “Model for thermal conductivity of CNT-nanofluids”, *Bulletin of Materials Science*, vol. 31, no. 3, pp. 387-390, 2008.

[88] R. Pasrija and S. Srivastava, “The interfacial layer effect on thermal conductivity of CNT nanofluids”, *Current Science*, vol. 107, no. 6, 2014.

[89] A. Einstein, “EineneueBestimmung der Moleküldimensionen”, *Ann. Phys.*, vol. 324, no. 2, pp. 289-306, 1906.

[90] H. Brinkman, “The Viscosity of Concentrated Suspensions and Solutions”, *J. Chem. Phys.*, vol. 20, no. 4, p. 571, 1952.

[91] I. Krieger, “A Mechanism for Non-Newtonian Flow in Suspensions of Rigid Spheres”, *Journal of Rheology*, vol. 3, no. 1, p. 137, 1959.

[92] N. Frankel and A. Acrivos, “On the viscosity of a concentrated suspension of solid spheres”, *Chemical Engineering Science*, vol. 22, no. 6, pp. 847-853, 1967.

[93] T. Lundgren, "Slow flow through stationary random beds and suspensions of spheres", *Journal of Fluid Mechanics*, vol. 51, no. 02, p. 273, 1972.

[94] G. Batchelor, "The effect of Brownian motion on the bulk stress in a suspension of spherical particles", *Journal of Fluid Mechanics*, vol. 83, no. 01, p. 97, 1977.

[95] A. Graham, "On the viscosity of suspensions of solid spheres", *Applied Scientific Research*, vol. 37, no. 3-4, pp. 275-286, 1981.

[96] T. Kitano, T. Kataoka and T. Shirota, "An empirical equation of the relative viscosity of polymer melts filled with various inorganic fillers", *RheolActa*, vol. 20, no. 2, pp. 207-209, 1981.

[97] B. Pak and Y. Cho, "Hydrodynamic and heat transfer study of dispersed fluids with submicron metallic oxide particles", *Experimental Heat Transfer*, vol. 11, no. 2, pp. 151-170, 1998.

[98] J. Avsec and M. Oblak, "The calculation of thermal conductivity, viscosity and thermodynamic properties for nanofluids on the basis of statistical nanomechanics", *International Journal of Heat and Mass Transfer*, vol. 50, no. 21-22, pp. 4331-4341, 2007.

[99] C. Nguyen, F. Desgranges, G. Roy, N. Galanis, T. Maré, S. Boucher and H. AngueMintsa, "Temperature and particle-size dependent viscosity data for water-based nanofluids – Hysteresis phenomenon", *International Journal of Heat and Fluid Flow*, vol. 28, no. 6, pp. 1492-1506, 2007.

[100] T. Tsai, H. Chien and P. Chen, "Improvement on thermal performance of a disk-shaped miniature heat pipe with nanofluid", *Nanoscale Res Lett*, vol. 6, no. 1, p. 590, 2011.

[101] C. Tsai, H. Chien, P. Ding, B. Chan, T. Luh and P. Chen, "Effect of structural character of gold nanoparticles in nanofluid on heat pipe thermal performance", *Materials Letters*, vol. 58, no. 9, pp. 1461-1465, 2004.

[102] D. Wen and Y. Ding, "Experimental investigation into convective heat transfer of nanofluids at the entrance region under laminar flow conditions", *International Journal of Heat and Mass Transfer*, vol. 47, no. 24, pp. 5181-5188, 2004.

[103] Y. Xuan and Q. Li, "Investigation on Convective Heat Transfer and Flow Features of Nanofluids", *Journal of Heat Transfer*, vol. 125, no. 1, p. 151, 2003.

[104] S. Zeinali Heris, S. Etemad and M. Nasr Esfahany, "Experimental investigation of oxide nanofluids laminar flow convective heat transfer", *International Communications in Heat and Mass Transfer*, vol. 33, no. 4, pp. 529-535, 2006.

[105] Y. Yang, Z. Zhang, E. Grulke, W. Anderson and G. Wu, "Heat transfer properties of nanoparticle-in-fluid dispersions (nanofluids) in laminar flow", *International Journal of Heat and Mass Transfer*, vol. 48, no. 6, pp. 1107-1116, 2005.

[106] W. Lai, B. Duculescu, P. Phelan and R. Prasher, "Convective heat transfer with nanofluids in a single 1.02-mm tube", in *Proceedings of ASME International Mechanical Engineering Congress and Exposition (IMECE 2006)*, 2006.

[107] Y. Ding, H. Alias, D. Wen and R. Williams, "Heat transfer of aqueous suspensions of carbon nanotubes (CNT nanofluids)", *International Journal of Heat and Mass Transfer*, vol. 49, no. 1-2, pp. 240-250, 2006.

[108] S. Zeinali Heris, M. Nasr Esfahany and S. Etemad, "Experimental investigation of convective heat transfer of Al2O3/water nanofluid in circular tube", *International Journal of Heat and Fluid Flow*, vol. 28, no. 2, pp. 203-210, 2007.

[109] K. Anoop, T. Sundararajan and S. Das, "Effect of particle size on the convective heat transfer in nanofluid in the developing region", *International Journal of Heat and Mass Transfer*, vol. 52, no. 9-10, pp. 2189-2195, 2009.

[110] M. Hojjat, S. Etemad, R. Bagheri and J. Thibault, "Convective heat transfer of non-Newtonian nanofluids through a uniformly heated circular tube", *International Journal of Thermal Sciences*, vol. 50, no. 4, pp. 525-531, 2011.

[111] A. Cárdenas Gómez, A. Hoffmann and E. BandarraFilho, "Experimental evaluation of CNT nanofluids in single-phase flow", *International Journal of Heat and Mass Transfer*, vol. 86, pp. 277-287, 2015.

[112] B. Sun, W. Lei and D. Yang, "Flow and convective heat transfer characteristics of Fe2O3–water nanofluids inside copper tubes", *International Communications in Heat and Mass Transfer*, vol. 64, pp. 21-28, 2015.

[113] M. Mehrali, E. Sadeghinezhad, M. Rosen, A. Akhiani, S. TahanLatibari, M. Mehrali and H. Metselaar, "Heat transfer and entropy generation for laminar forced convection flow of graphenenanoplatelets nanofluids in a horizontal tube", *International Communications in Heat and Mass Transfer,* vol. 66, pp. 23-31, 2015.

[114] S. Venkatachalapathy, G. Kumaresan and S. Suresh, "Performance analysis of cylindrical heat pipe using nanofluids – An experimental study", *International Journal of Multiphase Flow,* vol. 72, pp. 188-197, 2015.

[115] G. Roy, C. Nguyen and P. Lajoie, "Numerical investigation of laminar flow and heat transfer in a radial flow cooling system with the use of nanofluids", *Superlattices and Microstructures*, vol. 35, no. 3-6, pp. 497-511, 2004.

[116] S. Maïga, C. Nguyen, N. Galanis and G. Roy, "Heat transfer behaviours of nanofluids in a uniformly heated tube", *Superlattices and Microstructures,* vol. 35, no. 3-6, pp. 543-557, 2004.

[117] S. Maïga, S. Palm, C. Nguyen, G. Roy and N. Galanis, "Heat transfer enhancement by using nanofluids in forced convection flows", *International Journal of Heat and Fluid Flow*, vol. 26, no. 4, pp. 530-546, 2005.

[118] A. Khaled and K. Vafai, "Heat transfer enhancement through control of thermal dispersion effects", *International Journal of Heat and Mass Transfer*, vol. 48, no. 11, pp. 2172-2185, 2005.

[119] J. Buongiorno, "Convective Transport in Nanofluids", *Journal of Heat Transfer*, vol. 128, no. 3, p. 240, 2006.

[120] S. El Bécaye Maïga, C. Tam Nguyen, N. Galanis, G. Roy, T. Maré and M. Coqueux, "Heat transfer enhancement in turbulent tube flow using Al2O3 nanoparticle suspension", *International Journal of Numerical Methods for Heat & Fluid Flow*, vol. 16, no. 3, pp. 275-292, 2006.

[121] S. Heris, M. Esfahany and G. Etemad, "Numerical Investigation of Nanofluid Laminar Convective Heat Transfer through a Circular Tube", *Numerical Heat Transfer, Part A: Applications*, vol. 52, no. 11, pp. 1043-1058, 2007.

[122] A. Behzadmehr, M. Saffar-Avval and N. Galanis, "Prediction of turbulent forced convection of a nanofluid in a tube with uniform heat flux using a two phase approach", *International Journal of Heat and Fluid Flow*, vol. 28, no. 2, pp. 211-219, 2007.

[123] R. Mansour, N. Galanis and C. Nguyen, "Effect of uncertainties in physical properties on forced convection heat transfer with nanofluids", *Applied Thermal Engineering*, vol. 27, no. 1, pp. 240-249, 2007.

[124] V. Bianco, F. Chiacchio, O. Manca and S. Nardini, "Numerical investigation of nanofluids forced convection in circular tubes", *Applied Thermal Engineering*, vol. 29, no. 17-18, pp. 3632-3642, 2009.

[125] M. Ayatollahi, S. Nasiri and A. Kasaeian, "Convection Heat Transfer Modeling of AG Nanofluid Using Different Viscosity Theories", *IIUM Engineering Journal*, vol. 13, no. 1, 2012.

[126] R. Vajjha and D. Das, "A review and analysis on influence of temperature and concentration of nanofluids on thermophysical properties, heat transfer and pumping power", *International Journal of Heat and Mass Transfer*, vol. 55, no. 15-16, pp. 4063-4078, 2012.

[127] B. Salman, H. Mohammed and A. Kherbeet, "Heat transfer enhancement of nanofluids flow in microtube with constant heat flux", *International Communications in Heat and Mass Transfer*, vol. 39, no. 8, pp. 1195-1204, 2012

[128] S. Azimi and M. Kalbasi, "Numerical study of dynamic thermal conductivity of nanofluid in the forced convective heat transfer", *Applied Mathematical Modelling*, vol. 38, no. 4, pp. 1373-1384, 2014.

[129] A. Moghadassi, E. Ghomi and F. Parvizian, "A numerical study of water based Al2O3 and Al2O3–Cu hybrid nanofluid effect on forced convective heat transfer", *International Journal of Thermal Sciences*, vol. 92, pp. 50-57, 2015.

[130] M. Turkyilmazoglu, "Anomalous heat transfer enhancement by slip due to nanofluids in circular concentric pipes", *International Journal of Heat and Mass Transfer*, vol. 85, pp. 609-614, 2015.

[131] H. Hassan and S. Harmand, "Effect of using nanofluids on the performance of rotating heat pipe", *Applied Mathematical Modelling*, vol. 39, no. 15, pp. 4445-4462, 2015.

[132] G. Saha and M. Paul, "Heat transfer and entropy generation of turbulent forced convection flow of nanofluids in a heated pipe", *International Communications in Heat and Mass Transfer*, vol. 61, pp. 26-36, 2015.

[133] P. Zadeh, T. Sokhansefat, A. Kasaeian, F. Kowsary and A. Akbarzadeh, "Hybrid optimization algorithm for thermal analysis in a solar parabolic trough collector based on nanofluid", *Energy*, vol. 82, pp. 857-864, 2015.

[134] M. Moghaddami, A. Mohammadzade and S. Esfehani, "Second law analysis of nanofluid flow", *Energy Conversion and Management*, vol. 52, no. 2, pp. 1397-1405, 2011.

[135] M. Ghanbarpour and R. Khodabandeh, "Entropy generation analysis of cylindrical heat pipe using nanofluid", *ThermochimicaActa*, vol. 610, pp. 37-46, 2015.

[136] A. Mwesigye and Z. Huan, "Thermodynamic analysis and optimization of fully developed turbulent forced convection in a circular tube with water–Al2O3 nanofluid", *International Journal of Heat and Mass Transfer*, vol. 89, pp. 694-706, 2015.

[137] H. Tyagi, P. Phelan and R. Prasher, "Predicted Efficiency of a Low-Temperature Nanofluid-Based Direct Absorption Solar Collector", *J. Sol. Energy Eng.*, vol. 131, no. 4, p. 041004, 2009.

[138] Y. He, S. Wang, J. Ma, F. Tian and Y. Ren, "Experimental Study on the Light-Heat Conversion Characteristics of Nanofluids", *Nanoscience and Nanotechnology Letters*, vol. 3, no. 4, pp. 494-496, 2011.

[139] Y. Li, H. Xie, W. Yu and J. Li, "Investigation on Heat Transfer Performances of Nanofluids in Solar Collector", *MSF*, vol. 694, pp. 33-36, 2011.

[140] R. Taylor, P. Phelan, T. Otanicar, R. Adrian and R. Prasher, "Nanofluid optical property characterization: towards efficient direct absorption solar collectors", *Nanoscale Res Lett*, vol. 6, no. 1, p. 225, 2011.

[141] T. Otanicar and J. Golden, "Comparative Environmental and Economic Analysis of Conventional and Nanofluid Solar Hot Water Technologies", *Environmental Science & Technology*, vol. 43, no. 15, pp. 6082-6087, 2009.

[142] R. Saidur, T. Meng, Z. Said, M. Hasanuzzaman and A. Kamyar, "Evaluation of the effect of nanofluid-based absorbers on direct solar collector", *International Journal of Heat and Mass Transfer*, vol. 55, no. 21-22, pp. 5899-5907, 2012.

[143] R. Taylor, P. Phelan, T. Otanicar, C. Walker, M. Nguyen, S. Trimble and R. Prasher, "Applicability of nanofluids in high flux solar collectors", *J. Renewable Sustainable Energy*, vol. 3, no. 2, p. 023104, 2011.

[144] S. Ladjevardi, A. Asnaghi, P. Izadkhast and A. Kashani, "Applicability of graphite nanofluids in direct solar energy absorption", *Solar Energy*, vol. 94, pp. 327-334, 2013.

[145] T. Otanicar, P. Phelan, R. Prasher, G. Rosengarten and R. Taylor, "Nanofluid-based direct absorption solar collector", *J. Renewable Sustainable Energy*, vol. 2, no. 3, p. 033102, 2010.

[146] V. Khullar, H. Tyagi, P. Phelan, T. Otanicar, H. Singh and R. Taylor, "Solar Energy Harvesting Using Nanofluids-Based Concentrating Solar Collector", *Journal of Nanotechnology in Engineering and Medicine*, vol. 3, no. 3, p. 031003, 2012.

[147] M. Karami, M. AkhavanBahabadi, S. Delfani and A. Ghozatloo, "A new application of carbon nanotubes nanofluid as working fluid of low-temperature direct absorption solar collector", *Solar Energy Materials and Solar Cells*, vol. 121, pp. 114-118, 2014.

[148] L. Mercatelli, E. Sani, D. Fontani, G. Zaccanti, F. Martelli and P. Ninni, "Scattering and absorption properties of carbon nanohorn-based nanofluids for solar energy applications", *Journal of the European Optical Society: Rapid Publications*, vol. 6, 2011.

[149] T. Paul, A. Morshed, E. Fox, A. Visser, N. Bridges and J. Khan, "Enhanced Thermal Performance of Ionic Liquid-Al2O3 Nanofluid as Heat Transfer Fluid for Solar Collector", in *ASME 2013 7th International Conference on Energy Sustainability*, MN,USA, 2013.

[150] V. Khullar and H. Tyagi, "A study on environmental impact of nanofluid-based concentrating solar water heating system", *International Journal of Environmental Studies*, vol. 69, no. 2, pp. 220-232, 2012.

[151] T. Yousefi, F. Veysi, E. Shojaeizadeh and S. Zinadini, "An experimental investigation on the effect of Al2O3–H2O nanofluid on the efficiency of flat-plate solar collectors", *Renewable Energy*, vol. 39, no. 1, pp. 293-298, 2012.

[152] T. Yousefi, F. Veisy, E. Shojaeizadeh and S. Zinadini, "An experimental investigation on the effect of MWCNT-H2O nanofluid on the efficiency of flat-plate solar collectors", *Experimental Thermal and Fluid Science*, vol. 39, pp. 207-212, 2012.

[153] Z. Said, R. Saidur, N. Rahim and M. Alim, "Analyses of exergy efficiency and pumping power for a conventional flat plate solar collector using SWCNTs based nanofluid", *Energy and Buildings*, vol. 78, pp. 1-9, 2014.

[154] M. Alim, Z. Abdin, R. Saidur, A. Hepbasli, M. Khairul and N. Rahim, "Analyses of entropy generation and pressure drop for a conventional flat plate solar collector using different types of metal oxide nanofluids", *Energy and Buildings*, vol. 66, pp. 289-296, 2013.

[155] T. Sokhansefat, A. Kasaeian and F. Kowsary, "Heat transfer enhancement in parabolic trough collector tube using Al2O3/synthetic oil nanofluid", *Renewable and Sustainable Energy Reviews*, vol. 33, pp. 636-644, 2014.

[156] V. Khullar and H. Tyagi, "Application of Nanofluids as the Working Fluid in Concentrating Parabolic Solar Collectors", in *37th National and 4th International Conference on Fluid Mechanics and Fluid Power*, 2010.

[157] A. de Risi, M. Milanese and D. Laforgia, "Modelling and optimization of transparent parabolic trough collector based on gas-phase nanofluids", *Renewable Energy*, vol. 58, pp. 134-139, 2013.

[158] A. Kasaeian, S. Daviran, R. Azarian and A. Rashidi, "Performance evaluation and nanofluid using capability study of a solar parabolic trough collector", *Energy Conversion and Management*, vol. 89, pp. 368-375, 2015.

[159] S. Ghasemi and G. Mehdizadeh Ahangar, "Numerical analysis of performance of solar parabolic trough collector with Cu-Water nanofluid", *International Journal of Nano Dimension*, vol. 5, no. 3, pp. 233-240, 2013.

[160] S. Wu, H. Wang, S. Xiao and D. Zhu, " ", *Procedia Engineering*, vol. 31, pp. 240-244, 2012.

[161] B. Jo and D. Banerjee, "Study of High Temperature Nanofluids Using Carbon Nanotubes (CNT) for Solar Thermal Storage Applications", in *ASME 2010 4th International Conference on Energy Sustainability*, Arizona, USA, 2010.

[162] H. Kwak, D. Shin and D. Banerjee, "Enhanced Sensible Heat Capacity of Molten Salt and Conventional Heat Transfer Fluid Based Nanofluid for Solar Thermal Energy Storage System", in *ASME 2010 4th International Conference on Energy Sustainability*, Arizona, USA, 2010.

[163] B. Dudda and D. Shin, "Investigation of Molten Salt Nanomaterials as Thermal Energy Storage in Concentrated Solar Power", in *ASME 2012 International Mechanical Engineering Congress & Exposition*, Texas, USA, 2012.

[164] A. Zabalegui, D. Lokapur and H. Lee, "Nanofluid PCMs for thermal energy storage: Latent heat reduction mechanisms and a numerical study of effective thermal storage performance", *International Journal of Heat and Mass Transfer*, vol. 78, pp. 1145-1154, 2014.

[165] X. Wang, X. Li, Y. Xu and D. Zhu, "Thermal energy storage characteristics of Cu–H2O nanofluids", *Energy*, vol. 78, pp. 212-217, 2014.

[166] D. Choi, J. Lee, H. Hong and Y. Kang, "Thermal conductivity and heat transfer performance enhancement of phase change materials (PCM) containing carbon additives for heat storage application", *International Journal of Refrigeration*, vol. 42, pp. 112-120, 2014.

[167] [Online]. Available: http://twt.mpei.ac.ru/tthb/hedh/htf-vp1.pdf.

[168] [Online]. Available: http://www.loikitsdistribution.com/files/syltherm-800-technical-data-sheet.pdf.

[169] T. Miller, S. Zinkle and B. Chin, "Strength and fatigue of dispersion-strengthened copper", *Journal of Nuclear Materials*, vol. 179-181, pp. 263-266, 1991.

[170] Linn, J.K. and J.C. Zimmerman, "*A Method for Calculating Shadows Cast by Two-axis Tracking Solar Collector*s", Report SAND79-0190, Sandia National Laboratories, Albuquerque NM, November, 1979.

[171] S. Kalogirou, *Solar energy engineering*. Burlington, MA: Elsevier/Academic Press, 2009.

[172] A. Bejan, *Heat transfer*. New York: John Wiley & Sons, 1993.

[173] C. Frangopoulos, “Introduction to Enviromics: Design , Analysis and Improvement of Energy System”, in Proceedings of the ASME Advanced Energy System Divisions, 1991, pp. 49-54.

[174] R. Turton, Analysis, synthesis, and design of chemical processes. Upper Saddle River, N.J.: Prentice Hall PTR, 1998.

[175] R. Boehm, Design analysis of thermal systems. New York: Wiley, 1987.

[176] C. Ho, G. Kolb, C. Turchi and M. Mehos, Current and Future Costs for Parabolic Trough and Power Tower Systems in the US Market, 1st ed. Perpignan: National Renewable Energy Laboratory, 2010.

[177] J. Spelling, “Hybrid Solar Gas-Turbine Power Plants”, Ph.D. Dissertation, KTH Royal Institute of Technology, 2013.

[178] S. Pelster, 'Enviromic Modeling and Optimization of Advanced Combined Cycle Power Plants', Ph.D, EcolePolytechniqueFédérale, Lausanne, 1998.

[179] A. Al Hammadi, “Integrated Renewable Energy Options for HVAC-Cooling Systems”, American University of Sharjah, 2013.

[180] Us-nano.com, 'US Research Nanomaterials, The Advanced Nanomaterials Provider', 2015. [Online]. Available: http://www.us-nano.com/home.

Vita

Adnan Alashkar was born in 1990 in Damascus, Syria. He started his education at the International School of Choueifat in Damascus, where he graduated in the year 2008. He then moved to the United Arab Emirates to join the American University of Sharjah to start his undergraduate studies, where he graduated in January 2013. His degree was a Bachelor of Science in Mechanical Engineering.

Mr. Alashkar began his graduate studies at the American University of Sharjah, for a Master's of Science in Mechanical Engineering, where he received Graduate Studies Assistantship Award. During his M.Sc., Mr. Alashkar worked as a lab assistant in the Department of Mechanical Engineering.